Title
Self-sustainable Autonomous Soft Robots: from Actuators to Sensors and Energy Storage

Author
Zhao, Yusen

Publication Date
2022

Peer reviewed|Thesis/dissertation

UNIVERSITY OF CALIFORNIA

Los Angeles

Self-sustainable Autonomous Soft Robots:

from Actuators to Sensors and Energy Storage

A dissertation submitted in partial satisfaction of the

requirements for the degree Doctor of Philosophy

in Materials Science and Engineering

by

Yusen Zhao

2022

ABSTRACT OF THE DISSERTATION

Self-sustainable Autonomous Soft Robots:

from Actuators to Sensors and Energy Storage

by

Yusen Zhao

Doctor of Philosophy in Materials Science and Engineering

University of California, Los Angeles, 2022

Professor Ximin He, Chair

Soft robotics with intrinsic mechanical compliancy and intelligence features is emerging and pushing the boundaries of conventional robots. To be smarter, reliable, and self-sustainable, soft robots require new soft materials capable of autonomous sensing and actuating with embodied energy. Polymers, especially tissue-like hydrogels, show immense promise owing to their softness, simple and tunable synthesis, multi-functionalities, and stimuli-responsiveness. Currently, tremendous attempts have been made using these materials to develop flexible/stretchable devices as robotic components, but these approaches severely compromise mechanical properties and desired functionalities, such as actuation, sensation, mobility, and energy/power density. My dissertation focuses on designing new soft materials for next-generation bioinspired autonomous robots.

In Chapter 1, the state-of-the-art of soft robotic materials and system design will be discussed. The design principles of photoresponsive polymers, and conducting hydrogels and polymers were

elucidated, followed by the motivation of the current study related to autonomous actuators, flexible electronics, and energy storage.

In Chapters 2 and 3, the photo-responsive smart materials were developed for artificial phototropism and self-sustained oscillation. An in-depth understanding of the mechanism of autonomous motion, actuator characterizations, and potential applications in energy harvesting and oscillatory locomotion were investigated.

In Chapter 4, the design principle and synthetic innovation of highly stretchable conducting hydrogels and polymers were discussed. Constructing new conducting materials with intrinsic stretchability was used for piezoresistive sensing and proprioceptive actuation.

In Chapter 5, we developed oriented and hierarchical conducting hydrogels with controlled microstructures. We explored applications in flexible and stretchable energy storage devices with bending, stretching, and long-term cyclic stability.

In Chapter 6, we summarized the progress made in autonomous actuators, sensors, and energy storage. We provided perspectives of novel materials in use of such applications.

The dissertation of Yusen Zhao is approved.

Yu Huang

Qibing Pei

Lihua Jin

Ximin He, Committee Chair

University of California, Los Angeles

2022

Dedicated to my parents Yan Zhao and Jinrong Zhao

and my friends

For their unconditional love and support

TABLE OF CONTENTS

List of Figures

ACKNOWLEDGMENTS

Time flies and more than five years of my doctoral life have come to an end. I cannot help looking back at how my dreams have materialized into reality at UCLA. Life in the Professor He group is fullfilling and interesting. I learned polymer science from scratch, followed the postdoc's teachings, and then got interesting results from the work and expanded them into standalone projects. Since then, I have carried out projects that have never been reported before, facing unprecedented challenges, preparing new materials with novel methods, learning and building different instruments for characterizations, and demonstrating the potential applications of these new materials. Meanwhile, I witness the group keeps expanding from a small group to a group with diverse research directions, collaborations, and group members from various research expertise.

First and foremost, I want to acknowledge my research advisor Prof. Ximin He for her time and effort: organized, responsive, patient, and able to work things through. She helped me overcome numerous obstacles during my research. I am also deeply grateful to Prof. Yu Huang, Qibing Pei, and Lihua Jin for serving as my committee members and providing their guidance and expertise in my research.

Second, I would like to thank Prof. Lihua Jin, Prof. Laurent Pilon, Prof. Zhiyuan He, Dr. Xuan Chen, Dr. Qiaofeng Li, Dr. Yu Qiu, Dr. Zihang Peng, Dr. Shucong Li, Wenzhong Yan, Lecheng Ruan, for the academic collaboration, supportive discussion, and guidance. This dissertation would not have been possible without their tremendous support.

Third, I would like to thank my other group members for their academic and psychological support along the way. They are Dr. Xiaoshi Qian, Dr. Cheolgyu Kim, Dr. Yunyun Yang, Dr. Mutian Hua, Dr. Shuwang Wu, Dr. Bowen Yao, Dr. Yanfei Ma, Dong Wu, Yichen Yan, Sidi Duan, Pengju Shi, Zixiao Liu, Yousif Alsaid, Bozhen Zhang, Chiao-Yueh Lo, Yucheng Zhang, and so on. I miss the days we worked together in the last five years. I am glad that I met you and I hope we keep in touch.

Lastly, I would like to thank my family for their unwavering support, and patience throughout this journey. I would like to thank my parents Yan Zhao and Jirong Zhao, my sister Jiahua Yan, and my cat Anne. My entire academic career would not have been possible without their continuous love and support.

Vita

2017 B.S., Materials Science and Engineering, Tsinghua University, Beijing, China
Dual Degree in Economics, Tsinghua University, Beijing, China

2017 - 2022 Ph.D. Student, Materials Science and Engineering, University of California, Los Angeles, CA, USA

PUBLICATIONS

Journal Publications

Zhao, Y., Lo, C. Y., Ruan, L., Pi, C. H., Kim, C., Alsaid, Y., & He, X. (2021). Somatosensory actuator based on stretchable conductive photothermally responsive hydrogel. *Science Robotics*, 6(53).

Zhao, Y., Xuan, C., Qian, X., Alsaid, Y., Hua, M., Jin, L., & He, X. (2019). Soft phototactic swimmer based on self-sustained hydrogel oscillator. *Science Robotics*, 4(33).

Qian, X., **Zhao, Y.(co-first)**, Alsaid, Y., Wang, X., Hua, M., Galy, T., Gopalakrishna, H., Yang, Y., Cui, J., Liu, N., Marszewski, M., Pilon, L., Jiang, H., & He, X. (2019). Artificial phototropism for omnidirectional tracking and harvesting of light. *Nature Nanotechnology*, 14(11).

Zhao, Y., Zhang, B., Yao, B., Qiu, Y., Peng, Z., Zhang, Y., Alsaid, Y., Frenkel, I., Youssef, K., Pei, Q., & He, X. (2020). Hierarchically Structured Stretchable Conductive Hydrogels for High-Performance Wearable Strain Sensors and Supercapacitors. *Matter*, 1–15.

Lo, C. Y., **Zhao, Y. (co-first)**, Kim, C., Alsaid, Y., Khodambashi, R., Peet, M., & He, X. (2021). Highly stretchable self-sensing actuator based on conductive photothermally-responsive hydrogel. *Materials Today*.

Yan, Y., **Zhao, Y. (co-first)**, Alsaid, Y., Yao, B., Zhang, Y., Wu, S., & He, X. (2021). Artificial Phototropic Systems for Enhanced Light Harvesting Based on a Liquid Crystal Elastomer. *Advanced Intelligent Systems*, 3(10), 2000234.

Zhao, Y., Alsaid, Y., Yao, B., Zhang, Y., Zhang, B., Bhuskute, N., Wu, S., & He, X. (2020). Wood-Inspired Morphologically Tunable Aligned Hydrogel for High-Performance Flexible All-Solid-State Supercapacitors. *Advanced Functional Materials*, 30(10).

Zhang, Y., **Zhao, Y. (co-first)**, Wu, D., Xue, J., Qiu, Y., Liao, M., Pei, Q., Goorsky, M. S., & He, X. (2019). Homogeneous Freestanding Luminescent Perovskite Organogel with Superior Water Stability. *Advanced Materials*, 31(37).

Yang, Y., **Zhao, Y. (co-first)**, Liu, J., Nie, Z., Ma, J., Hua, M., Zhang, Y., Cai, X., & He, X. (2020). Flexible and Transparent High-Dielectric-Constant Polymer Films Based on Molecular Ferroelectric-Modified Poly(Vinyl Alcohol). *ACS Materials Letters*, 2(5), 453–460.

Review Publications

Zhao, Y., Hua, M., Yan, Y., Wu, S., Alsaid, Y., & He, X. (2021). Stimuli-Responsive Polymers for Soft Robotics. *Annual Review of Control, Robotics, and Autonomous Systems*, 5.

Book Chapter

Lo, C., **Zhao, Y.**, Ma, Y., Wu, S., Alsaid, Y., Peet, M., Fisher, R., Marvi, H., Aukes, D., Berman, S., He, X., Bioinspired sensors and actuators based on stimuli-responsive hydrogels for underwater soft robotics. Chapter 5 in Bioinspired Sensing, Actuation, and Control in Underwater Soft Robotic Systems, D. A. Paley, N. M. Wereley (eds.), *Springer Nature*, 2020

1 Introduction

1.1. Soft robotics

Soft robotics has emerged as a research field pushing the boundaries of conventional robots. Numerous noticeable achievements have been made recently, including the granular jamming gripper[1], continuum fiber robot[2], worm robot[3] jumping robot, integrated octobot[4], self-oscillating swimmer[5], and flying robot[6], among many others. The use of soft matter with low Young's modulus allows for mechanical compliance and continuous deformability in robots; soft matter can facilely conform to the surfaces of objects and adapt to unstructured environment[7]. Such soft systems are particularly important for wearable devices, drug delivery[8], surgery[9], and rehabilitation[10].

Several key features merit consideration for a soft system that can be used practically, including produced force, deformation strain, response rate, energy density, function, scaling, auxiliary equipment, and reliability. However, trade-offs between these parameters usually exist and researchers are expected to balance them in specific working scenarios. It is highly desirable to achieve enhanced performance without sacrificing other characteristics. In addition, researchers can take inspiration from the actuation principle from biological systems and develop novel actuation functionalities by biomimicking[11]. To accomplish more advanced robotic locomotion with autonomy, it is also highly desired to achieve a highly compact system that incorporates a sensory-actuation feedback loop with minimal manual control, realizing a proprioceptive (self-perception) soft robot. Other challenges for future soft robots design include reducing robots tethering, and combining onboard battery/remote powering, actuator, sensing, control, and other regulation strategies[12].

Studies of **soft actuation** incorporate working mechanisms, material designs, and control systems to enable completely soft and functional robots. The working mechanism of actuation is closely related to the material selection while determining the performance and potential applications as well. Although soft actuators can be made using stiff materials through geometrical design in the

form of mesh, foam, springs, and wires, the current thesis does not focus on this type of actuator, because of limited strains and fewer degrees of freedom for complex functionalities[13]. For intrinsically soft actuators, efforts have been made to develop pneumatic actuators, hydraulic actuators, and stimuli-responsive polymers-based actuators. Among them, stimuli-responsive polymers have the potential to trigger self-sustained and autonomous motion, which provides a higher level of autonomy without human intervention.

Soft robotics also provides opportunities for **sensing**-actuation unification. Defined by their specific working mechanisms, these sensors and actuators are all single-function units, still unable to realize sensation and actuation simultaneously. Therefore, add-on functionalities to soft robots have been employed to physically integrate the two individual components by welding, 3D printing, embedding or laminating sensors and actuators. Fabricating such heterogeneous multi-material systems typically involves complex integrating processes with multiple molding and lamination steps and complicated connection terminals. These physically-integrated systems with various material interfaces also have potential stress concentration and adhesion issues. In terms of robotic performance, the sensing and actuation functionalities are predefined with constrained flexibility when handling complex dynamic environments. It would be highly advantageous to develop a multifunctional monolithic material containing chemically integrated sensing and actuation components at the molecular level, rather than the system level.

Regarding the energy source of the soft robotics, traditional hydraulic actuators and pneumatic actuators suffer from requiring tethered tubing to provide air or fluid inflation, auxiliary equipment, and predefined actuation. To tackle these, a few examples of untethered pneumatic actuators have been reported, based on the evaporation of low boiling point solvent and the production of gas from chemical reactions[14]. In addition, there are still many challenges to be addressed to realize miniaturized untethered soft robots, which require scale-down while carrying components including batteries, capacitors, electronic controller, motors, and pumps onboard.

1.2. Photoresponsive smart polymers for actuators

Stimuli-responsive polymers present an area of soft robots witnessing rapid innovation. Stimuli-responsive polymers are a class of materials that can change chemical and physical properties in response to external stimuli including heat, light, pH, humidity, magnetic fields, and electric fields.[15] Tremendous research has focused on improving characteristics without sacrificing performance in different smart materials including liquid crystal materials, hydrogels, shape-memory polymers, electroactive polymers, magnetic polymers, and thermal expansion actuators (Figure 1.1).

One advantage of stimuli-responsive polymers is that the actuation performance and robotic locomotion are largely determined by the molecular modulation and chemical modification of the smart polymers. Demonstrating uniquely tunable performance, stimuli-responsive polymers are promising as artificial muscles, grippers, locomotive robots, swimming robots, and even flying robots. In addition, the stimulus can be customized when designing the robot for different demands. For example, an electric stimulus is advantageous when fabricating a highly compact system with accurate control, but usually requires bulky electrical connections for powering and computation. Smart polymers stimulated by heat, light, and magnetic fields can be operated in an untethered pathway; this design greatly improves miniaturization since the robot is fueled through external stimuli rather than onboard equipment. Magnetic fields can penetrate through materials and most biological tissues, but bulky external instrument limits the open area application.

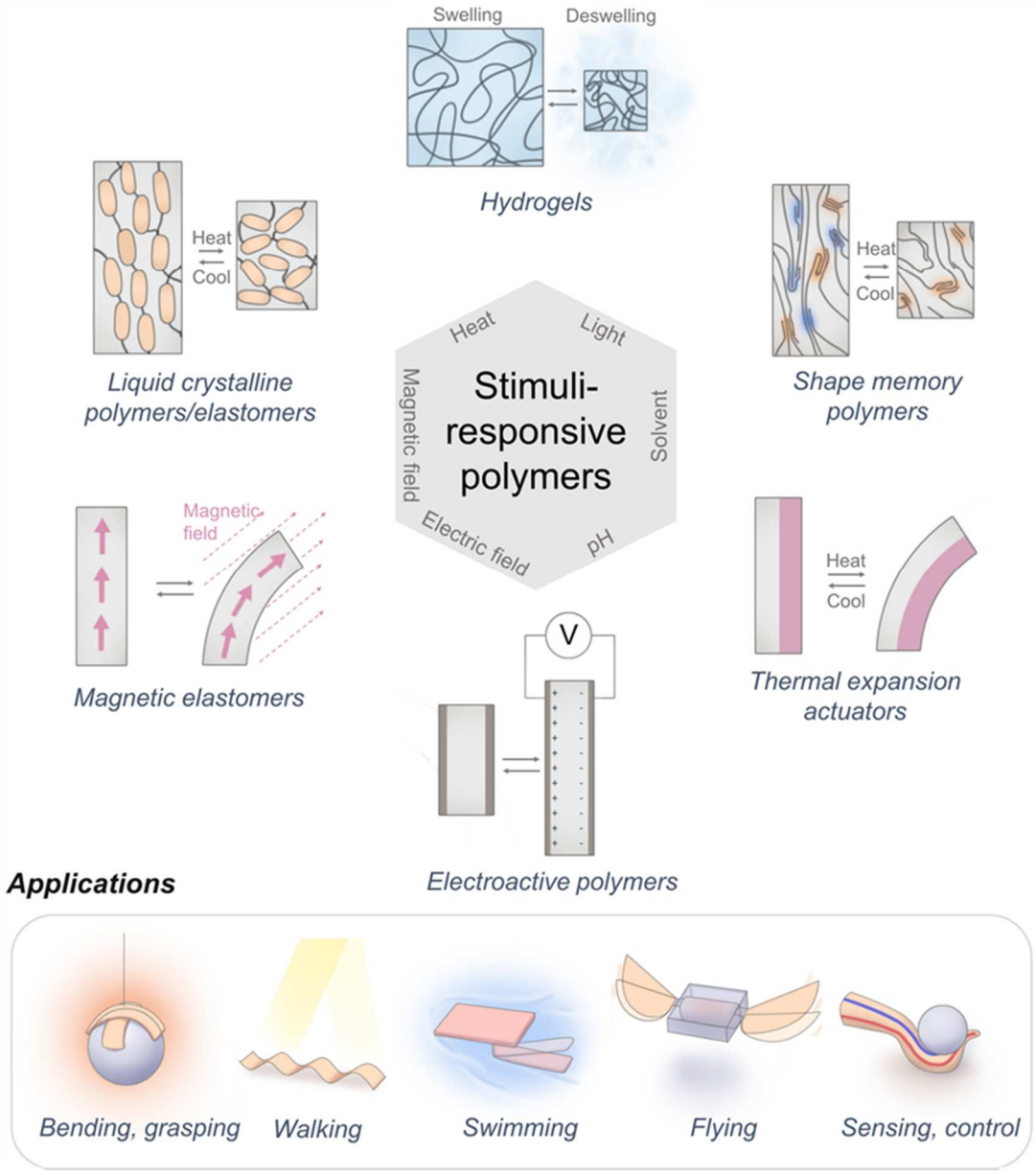

Figure 1.1 Stimuli-responsive polymers and applications in soft robotics.

Polymer type	Electric field	Heat	Light	Chemical (solvent, pH)	Magnetic field
Liquid crystal polymers, polymer networks, and elastomers	•	•	•	•	
Hydrogels	•	•	•	•	•
Shape memory polymers	•	•	•		
Magnetic elastomers					•
Dielectric elastomers	•				
Ionic polymer–metal composites	•				
Ionic conducting polymers	•				
Thermal expansion actuators	•	•	•		

Table 1. Stimuli-responsive polymers and their stimulated signals.

1.3. Photoresponsive hydrogels

Hydrogels are three-dimensional hydrophilic polymeric networks containing high water content. In soft robotics and biomimetic applications, hydrogels have received considerable attention due to the following reasons: 1) Hydrogels can swell and deswell under stimulation by water diffusion in or out of the hydrogel mesh, which can produce large volumetric change without a tethered external power. 2) Hydrogels exhibit comparable moduli (kPa) to biological tissues and organs.

Stimuli-responsive hydrogels can respond to temperature, light, electrical/magnetic fields, chemical stimuli, pH, redox reactions, and biomolecules. Here, we will particularly focus on photoresponsive hydrogels, which have more robotic-related investigation in academia than other mechanisms. One approach is to use *photoisomerization* by incorporating photoswitchable azobenzene or spiropyran molecules into the hydrogel system. The supramolecular interactions change at different temperatures due to hydrogel volume changes. However, the actuation rates of these systems are still limited to tens of minutes to a few hours[16].

To further improve light responsiveness, *photothermal* actuation has been widely utilized due to heat localization, high energy conversion efficiency, fast response, programmability, and complex shape morphing. Photoresponsive hydrogels can be realized by embedding light absorbers in a thermoresponsive hydrogel. Common light absorbers include graphene oxide, carbon nanotube, gold nanoparticles[17–19]. The thermally responsive hydrogels are largely dependent on the hydrophilicity and hydrophobicity change at different temperatures. Some hydrogels containing

both hydrophilic (e.g. amide and carboxyl) and hydrophobic (e.g. methyl ethyl and propyl) groups possess lower critical solution temperature (LCST)[20]. Below the LCST, the hydrogel is hydrophilic and absorbs water. Conversely, when the temperature is above LCST, the hydrogel is hydrophobic and expels water out of the network due to the increased entropy, resulting in volume shrinkage. Poly(N-isopropylacrylamide) (PNIPAAm) with LCST behavior is one of the most widely developed thermally responsive hydrogels for soft actuators **(**Figure 1.2**)**. Research interests involve material design of photoresposnive hydrogel for high response rate and ratio, large actuation stress, as well as robotic design, such as bending, grasping, and underwater walking.

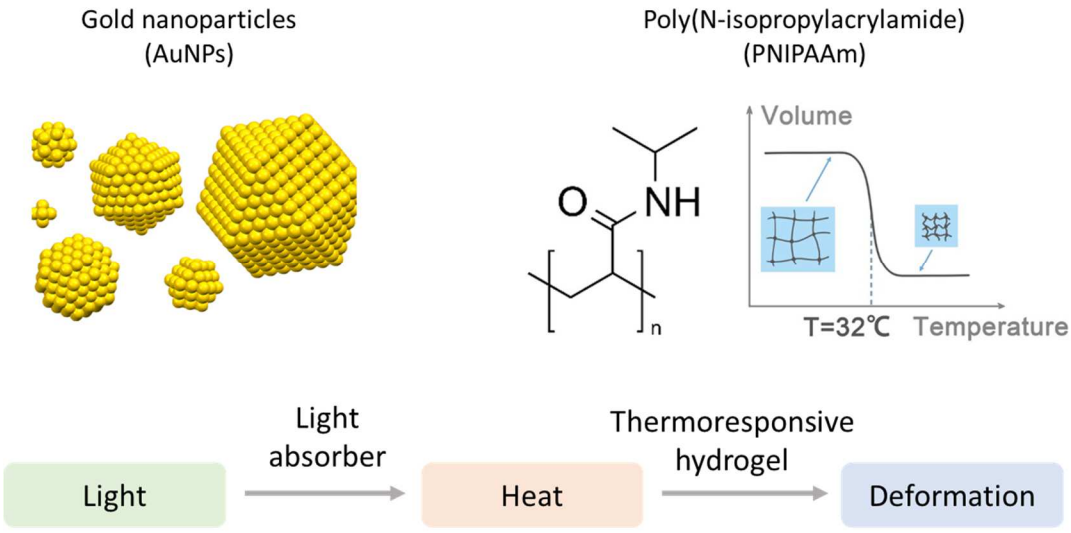

Figure 1.2 Photoresponsive hydrogels by integrating photothermal absorbers (i.e. AuNPs) and thermoresponsive hydrogels (i.e. PNIPAAm).

1.4. Liquid crystal elastomers (LCEs) and liquid crystal networks (LCNs)

Liquid crystals (LC) are a state of matter that has positional and/or rotational orientation in their molecular arrangement. Liquid crystalline materials including liquid crystal polymers (LCPs), liquid crystal elastomers (LCEs) and liquid crystal polymer networks (LCNs) have been studied as promising shape-morphing materials in response to external stimuli. In this section, we will mainly focus on LCEs that respond to temperature and light.

1.4.1. Thermally responsive LCEs

Under heating, the liquid crystal moieties undergo a transition from an anisotropic phase to an isotropic phase, which changes the system from an ordered state to a disordered state. The structural unit of LC materials is a tightly packed rod-like mesogen. In the case of typically uniaxially aligned LC materials, the average spacing of mesogens is reduced along the orientation direction and increased in the perpendicular direction. As a result, the material contracts along the oriented direction and expands in the perpendicular direction (Figure 1.3). Specifically, LCP with a main-chained uncrosslinked polymer has a low actuation ratio. LCNs with a moderate to densely crosslinked network and T_g above room temperature usually have a molecular ordering change of <5%. By contrast, LCEs that contain a variety of flexible chains and have below-room-temperature T_g can largely deform (more than 40%) above the phase transition temperature. The chemical design of liquid crystalline materials is expanded in White and Broer's paper[21].

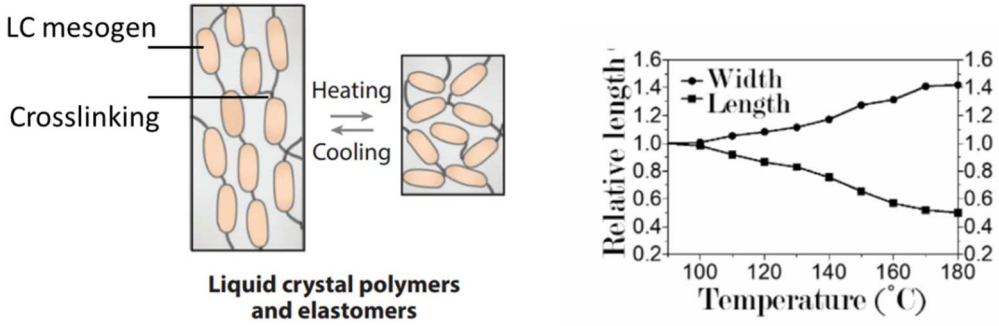

Figure 1.3. The actuation mechanism of liquid crystalline elastomers.

1.4.2. Photoresponsive LCEs

Light as a remote, directionally controllable, and clean energy source has been used to trigger light actuation in LC materials. The properties including wavelength, intensity, and polarization can be customized for specific demands with spatial and temporal control. The deformation of LC materials can be triggered by either photochemical reactions or photothermal heating. The *photochemical reaction* is obtained by the incorporation of photochromic molecules, such as

azobenzene[22], spiropyran[23], or fulgide derivative[24]. For example, the azobenzene molecule has a *trans* form with a rod-like shape in the dark state and a *cis* form with bent a shape under UV irradiation. For LC materials with incorporated azobenzene guest molecules, the *trans-cis* photo-isomerization of azobenzene under UV light decreases the average molecule length and destabilizes the alignment of entire LC phases, leading to anisotropic-isotropic phase change. In other words, the effect of configuration change of small molecules can be largely amplified to produce macroscopic deformation, with minimal energy needed to induce the photochemical reaction isothermally. However, LC material actuated by photochemical actuation is unable to autonomously relax upon turning off the UV light stimulus. Usually the recovery process requires illumination with visible light of another wavelength; one solution to address this issue is to specifically select a wavelength that overlaps the absorption range of *cis-trans* and *trans-cis* configuration[25]. In addition, the light extinguished distance is usually around 10μm, making it difficult to actuate thick actuator.

The *photothermal effect* provides an alternative and efficient means of photoactuation, by converting photonic energy to heat. The photothermal effect can occur with high spatiotemporal resolution and negligible loss. Photothermal agents (light absorbers) can be added inside or on the surface of LCEs. The elevation of temperature induces the phase transition of LCE from the anisotropic state to the isotropic state. The light absorbers can be carbon nanomaterials[26], polydopamine[27], and metal nanoparticles[28].

There have been numerous light-induced LCE soft robots such as grippers, walkers, swimmers, and self-sustained oscillators. With photo-actuation, the control circuit and power supply can be removed from the body. Therefore, the photoresponsive LCE enables researchers to design untethered, battery-free, and small-scaled soft robots. In this case, a relatively low light intensity (a few tens of sun) is sufficient to penetrate throughout the film and a large actuation strain can be

achieved. Compared to other materials, the molecular alignment of LCEs allows for precise control of actuation modes, leading to more versatile robotic motion and task execution.

1.5. Conducting polymer hydrogels (CPH) for sensors and energy storage devices

Conjugated polymers are polymers with alternating single and double bonds along the polymer chain, which endows the polymer with unique electronic conduction. Classic conducting polymers include polyaniline (PAni)[29], polypyrrole (PPy)[30], and poly(3,4-ethylenedioxythiophene) (PEDOT)[31] Conducting polymers (CPs) offer promising alternatives as conductive and piezo-resistivity fillers due to their neuron-like electrical conductivity. CPs are typically stiff and lack stretchability due to their huge, planar electron conjugating system and rigid molecular chains. One route to address the issues of elasticity and flexibility is to homogeneously incorporate interconnected CPs in soft, flexible matrices like hydrogels. As-made stretchable CPH can be used for conductors, soft sensors, and energy storage devices, such as electrodes of supercapacitors and batteries.

1.6. Motivation and Scope of Research

The emerging soft materials have been making profound and far-reaching technological and societal impacts. For instance, flexible and stretchable materials are sought to bridge the gap between humans and machines, and biologically-inspired soft robots have the unique potential of approaching their natural models in both performance and capabilities. These require material innovation and systematic design of multi-components in one robot, including energy storage and conversion units, actuators, sensors, and control tools that are built from novel materials of new properties.

Currently, the actuation unit of the soft robots is comprised of pneumatic actuators, hydraulic actuators, and dielectric elastomer actuators. However, they suffer from tethered connections and bulky external power supplies. Alternatively, smart polymers with intrinsic deformation capability in response to the environment have received considerable attention both in academia and industry.

By chemical and morphological optimization, smart polymers can be demonstrated with desired responsiveness, delivered force, and capability to autonomously interact with the environment, which has the potential for revolutionary actuating materials.

Additionally, truly autonomous robots require abilities of sensing and interact with their surroundings. However, the enhancement of electrical conduction will conflict with high mechanical stretchability in typical stretchable conductive materials. Despite tremendous efforts, the development of sensor on-demand still possesses a long-standing bottleneck.

The third important aspect of the robotic design is precisely how the energy is harvested and stored throughout the robotic system. It is necessary to enable the energy storage device to be flexible and stretchable. However, the energy storage devices such as batteries and supercapacitors suffer from reduced electrochemical performance under cyclic mechanical bending and stretching due to the disconnection of previously constructed networks. There remains a universal and generalized method to address this trade-off.

Therefore, to tackle these three important challenges, this research will focus on developing 1) smart stimuli-responsive polymers to develop autonomous light-responsive actuators with multi-functionalities, 2) stretchable conducting hydrogels for sensors, and 3) flexible/stretchable energy storage devices.

2. Artificial phototropism for energy harvesting

2.1. Introduction

Plants can self-orient to face light sources perpendicularly, known as phototropism, for energy harvesting and reproduction. All their direction of locomotion is strictly determined by the direction of an environmental stimulus, namely, tropistic movement, in contrast to nastic movement, which is a non-directional response to stimuli and is simply determined by organism anatomy. In tropistic movement, organisms not only sense and respond to the stimuli positions but also spontaneously and constantly adjust their movements to tightly follow the signal directions. This presents the intelligence of self-regulation via the feedback control inherent in the dynamic interactions between their bodies and the stimulus. However, most artificial materials actuate as a nastic movement. Achieving synthetic tropistic behavior that can steadily track input energy has proved a daunting challenge.

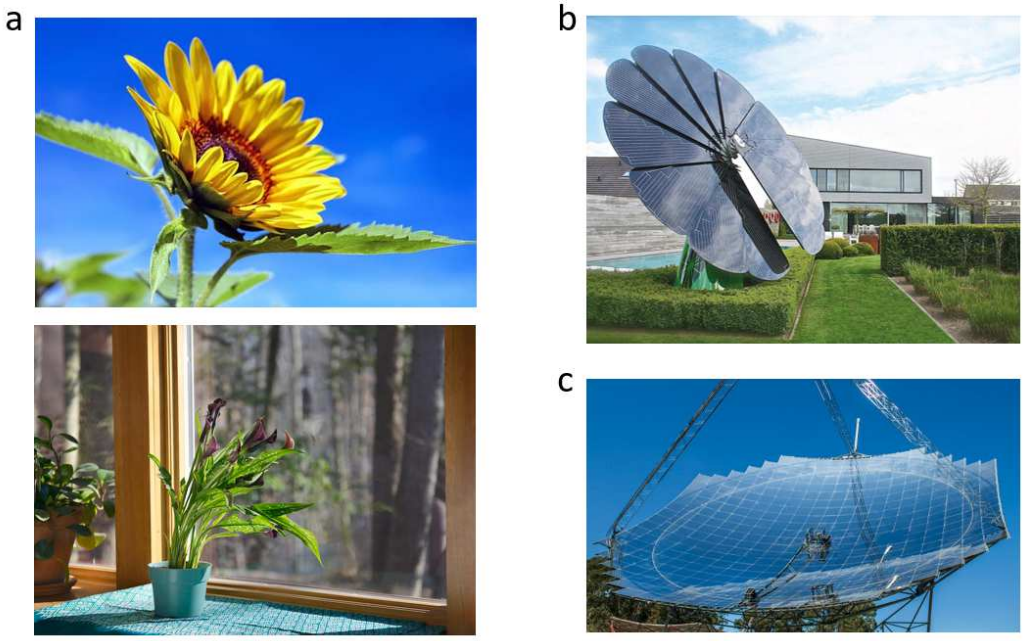

Figure 2.1. Phototropism in nature and industry.

a. Sunflower and plants with phototropism behavior, b. Smartflower solar panel, c. Solar Concentrator Dish 97% sunlight into steam (Australia)

Phototropism is developed by many plants as a strategy to recover the oblique-incidence energy-density loss (OEL), the input power density reduction when emissive energy projects on a surface obliquely. The loss can be enormous when the incident angle is large (for example, 75% loss at 75° incidence). By maintaining normal incidence, sunflowers raise the temperature of floral discs to attract more pollinators with warmth and show an effective recovery of the input loss caused by oblique illumination if no phototropism was present.

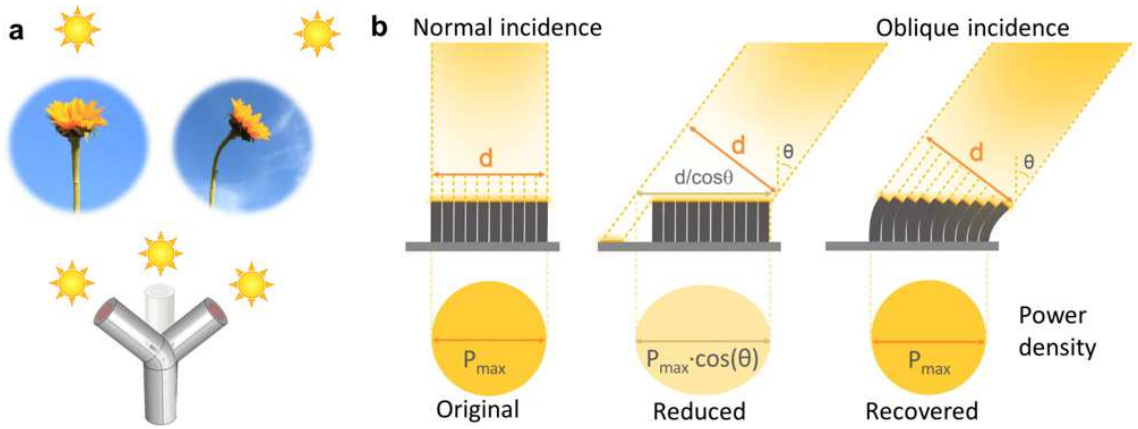

Figure 2.2. Tracking of pillar arrays compensates for the energy loss from oblique angle illumination

Artificial phototropism, if realized, may provide an efficient solution to overcome this universal OEL issue faced by almost all existing optical and electromagnetic devices. As a bioinspired concept illustrates in Figure 2.2, when a surface is covered with sunflower-like pillars that can bend towards the light source and maintain normal incidence, the original maximum power density ($P_{max} = P_0$) can be restored. The capability to harness tropistic behaviour autonomously, without external instruction and power supply (for example, via electromechanically programmed systems), would enable highly efficient energy-harvesting platforms that can adapt autonomously to complex ambient environments. However, current state-of-the-art photoactuations remain primarily nastic, unable to sense, track and harvest the emissive energy from varying incident directions self-adaptively.

2.2. Proposed method

We propose a general principle of creating artificial phototropism with a series of reversibly photoresponsive polymers. These phototropic systems, termed sunflower-like biomimetic omnidirectional tracker (SunBOT), can autonomously and instantaneously detect and track incident light in three-dimensional space at broad ambient temperatures with high accuracy and fast response, without auxiliary power supply or human intervention.

We leverage the capabilities of reversibly photoresponsive soft materials that shrink on illumination and adopt the symmetric stem-like cylindrical pillar shape for the design of SunBOTs. Like a stem, SunBOTs bend towards stimuli due to the asymmetric deformation between the illuminated high-temperature region and the shaded low-temperature region.

Unlike previously reported nastic motions, which are sensitive to the intensity of the stimuli and/or the ambient temperature, the rigorous self-regulating mechanism generates similar temperature gradients in SunBOTs under different illumination powers and environment conditions, which guarantees a stable and accurate aiming at broad power and temperature ranges. When the illumination is turned off or changes position, the bent SunBOT immediately recovers its original shape or quickly adjusts its orientation to accommodate the position of a new stimulus, to perform another tropistic cycle in real time

2.3. Experimental and characterization Section

2.3.1. Chemicals and materials

N-isopropylacrylamide (NIPAAM), N,N'-Methylenebisacrylamide (bis-AAm), sodium citrate dihydrate, chloroauric acid, acetic acid, allyl disulfide, 3(trimethoxysilyl)propyl methacrylate (TPM) were purchased from Sigma Aldrich. 2-hydroxy-2-methyl-1-phenyl-1-propanone (Darocur 1173, photo-initiator for temperature-responsive hydrogel) was purchased from TCI America. Dimethyl sulfoxide (DMSO), ethanol, hydrazine monohydrate, and hexane were purchased from Fisher Scientific. Sylgard 184 Silicone Elastomer kits were purchased from Ellsworth Adhesives.

Graphene oxide (GO) was purchased from Graphene Supermarket. All the chemicals, except NIPAAM, which was recrystallized from hexane, were used as received.

2.3.2. Fabrication of PNIPAAm-based SunBOTs

The poly(N-isopropylacrylamide) (PNIPAAM) hydrogel precursor solution was prepared with 40 vol% NIPAAM monomer, 2 vol% crosslinker bis-AAm, 0.5 vol% UV-initiator Darocur 1173 in DMSO, followed by adding photo-absorbers (i) AuNPs or (ii) rGO respectively for fabricating SunBOTs based on AuNP-PNIPAAM or rGO-PNIPAAM. (i) For AuNP-incorporated SunBOT (AuNP-SunBOT), 0.8 wt% AuNPs and 0.1 vol% allyl disulfide were added into the PNIPAAM precursor solution in DMSO, where the allyl disulfide serves as a linker between AuNP and the hydrogel matrix via hydrogen bonds. (ii) For rGO-incorporated SunBOT (rGO-SunBOT), 0.3 wt% rGO were added to the PNIPAAM precursor solution in DMSO. The mixture solution was then poured into the PDMS mold and covered with a TPM-treated glass slide, followed by UV curing for 60 seconds. The cured gel structure was carefully pulled out from the mold, yielding a SunBOT, then immersed in the DI water to remove DMSO. For rGO-SunBOTs, the gel structure was soaked in 0.33M hydrazine aqueous solution to reduce GO to reduced-GO (rGO). If not specifically identified, the fully hydrated SunBOT (single pillar) has a diameter of 1 mm and a length of 10-20 mm at room temperature; each fully hydrated pillar in the SunBOT arrays has a diameter of 0.5 mm at room temperature.

2.3.3. Fabrication of PDMAEMA-based SunBOT

To synthesize PDMAEMA hydrogel, 30 vol% 2-(dimethylamino)ethyl methacrylate (DMAEMA), 1 wt% N,N'-Methylenebisacrylamide (bis-AAm), 3 wt% Acrylamide, 1 wt% Irgacure 2959 are mixed to form an aqueous solution. The prepolymer solution is cast between two glass slides with a defined gap using spacers. The precursor solution is cured under UV light for 20 minutes. The cured gel is carefully peeled off from the glass slide and soaked in water for 5 hours to remove the excess unreacted monomers. The as-prepared hydrogel is cut into thin strips for further use.

Subsequently, to incorporate polyaniline (PANi) into the as-prepared PDMAEMA hydrogel, we use the in-situ polymerization method. Typically, 91.2 μL (0.1 M) of aniline monomer is dissolved in 5 mL of a 1M HCl aqueous solution to form Solution A. The PDMAEMA hydrogel strips are placed into solution A for 2 hours. After the two-hour soaking, 228 mg of ammonium persulfate (APS) (with a mole-concentration the same as that of aniline) is dissolved in another 5 mL of 1M HCl aqueous solution, to form Solution B. Mix solution B into Solution A under stirring at room temperature for 8 hours to grow polyaniline on the PDMAEMA gel. Then, the PANi-incorporated PDMAEMA gel is taken out of the solution and placed in water to remove excess reactants. The PANi-PDMAEMA is further cut into the desired shape and used as testing. The dimension of the PANi-PDMAEMA pillar for the test is 2.3 cm in length and 0.97 mm in thickness.

2.3.4. Fabrication of PAM-co-PNIPAAm-based SunBOT

To synthesize PAM-co-PNIPAAm hydrogel, a 300mg mixture of acrylamide (AM) and N-isopropylacrylamide (NIPAAm) in a 2:1 mol ratio respectively was dissolved in 600 μL of DMSO. 10 mg of N,N'-Methylenebisacrylamide (bis-AAm) and 5μL Darocur 1173 photoinitiator are mixed into this mixture to complete the prepolymer solution. The solution is cast between a silane-treated glass coverslip and a pillar-shaped PDMS mold with a predefined pillar width and then cured under UV light for 2 minutes. The cured gel is carefully removed from the pillar-shaped PDMS mold and soaked in DI water for 5 hours to remove excess unreacted monomers and DMSO. Subsequently, to enable photothermal response, the PAM-co-PNIPAAm pillars are coated with polypyrrole (PPy) using $FeCl_3$ – mediated oxidative chemical vapor deposition. The as-prepared PAM-co-PNIPAAm pillars are immersed in 1% $FeCl_3$ aqueous solution for 1 hour and then placed inside a vacuum-sealed desiccator alongside pyrrole monomer. After 20 min the PAM-co-PNIPAM pillars were removed after visibly turning black due to the deposited PPy on the surface. The pillars are again soaked in DI water for 5 hours to remove excess $FeCl_3$. The pillar dimensions used for testing were 1 cm in length and 1 mm in thickness.

2.3.5. Fabrication of LCE-based SunBOTs

The preparation of LCE pillar follows the procedures from Yakacki et al.[32] The diacrylate mesogen, RM257 (i.e., 4-(3-Acryloyloxypropyloxy)-benzoesure 2-methyl-1,4-phenylester) (0.6261g) was dissolved in toluene and heated to 85 □ to form a homogeneous solution. After fully dissolution, 0.035 g PETMP (i.e., pentaerythritol tetra(3-mercaptopropionate)) and 0.137 g EDDET (i.e., 2,2'-(ethylenedioxy)diethanethiol) were added into stirring RM257 solution dropwise. Then, 0.0399 g of light absorber Indigo and 0.186 g of toluene were added to form solution A. The Michael addition reaction catalyst (0.00567 g of DPA) and photo-initiator (0.01158g of HHMP) were mixed in 0.372g of toluene to form solution B. Solution A and B were mixed. Then, the solution was injected into a glass capillary tube and kept in an 85 □ oven for 24 hours to evaporate the solvent and complete the reaction. When finishing the reaction, the LCE fiber was removed from the glass capillary tube. Then, the fiber was clamped and stretched 3 times of initial length. The fiber was cured under UV light for 4 hours to fix the LCE fiber in a mono-domain state. The dimension of the LCE pillar is 1 cm in length and 0.67 mm in diameter.

2.3.6. Fabrication of the phototropic and the non-phototropic solar panel device

PVC tape (Topzone) adhered to one side of the LCE. On the other side of the LCE Sharpie ink was homogeneously applied. The tape was used to fix the LCE legs on a glass substrate and solar panel on top of the device. For the non-phototropic device, the solar panel was simply put horizontally on the bench. Silver wire (99.95% pure, 0.005" diameter, Surepure Chemetals) was used to connect the solar panel to the Keithley 2450 Sourcemeter, which was used to record the I-V curve of the solar panel.

2.3.7. Setup and instrumentation for real-time tracking of light at various angles in 3D spherical space

A 532-nm continuous wave laser (Genesis MX STM-Series), with a beam diameter of 1 mm and a maximum power of 1 W was used as a monochromatic light source. Without further tuning of the

beam width, the laser is termed the “spot light” as it shines on samples with a smaller diameter of illumination. A beam expander (10x) was used to expand the laser beam diameter to 10 mm, which is termed the “area light”.

A white light source equipped with a collimator was designed and fabricated to serve as a broadband light source (50 mm in diameter, maximum power of 1 W). An optical power meter (Newport 1830-C) was used to calibrate the power output of the light sources. The SunBOT was immersed in a water bath inside a glass container with precise temperature control (0.1 □).

A solar simulator (Asahi spectra HAL-320W solar simulator with TOU-1-31 telecentric uniform illumination unit) was used to mimic sunlight operation. One sun checker (CS-40, Asahi spectra) was used to calibrate the light intensity. A protractor was used to calibrate the light angle.

Zenith Incident Angle Control: The variation of the zenith incident angles (Figure 2.3a) of the laser in the vertical plane was controlled by using a set of mirrors in between the laser (or the beam expander) and the SunBOT. The variation of the incident angles of the white light in the vertical plane was controlled by using a fixture that positions the light source to achieve different vertical angles to the SunBOT sample.

Azimuthal Incident Angle Control: The variation of the azimuthal incident angles (Figure 2.3b) of all light sources in the horizontal plane was achieved by turning a rotary stage with the SunBOT placed at its center point.

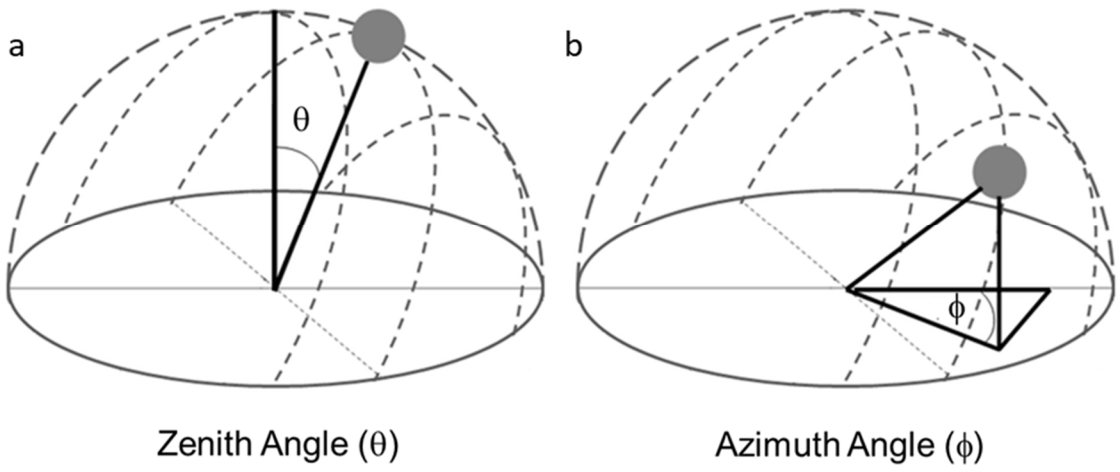

Figure 2.3 Schematics of zenith angle (a) and azimuth angle (b). The tracking accuracy is defined by comparing the pillar bending angle and the light incident angle, i.e., the final tracked angle/incident angle. Every bending angle under each different incident angle was carefully measured for more than twenty repetitive experiments by a computer tracking algorism and manual double checking.

2.3.8. UV-Vis-IR absorption of the AuNP-PNIPAAM and rGO-PNIPAAM

The absorption spectrum of the AuNP was characterized by UV-Vis Spectrometer from Ocean Optics (USB4000).

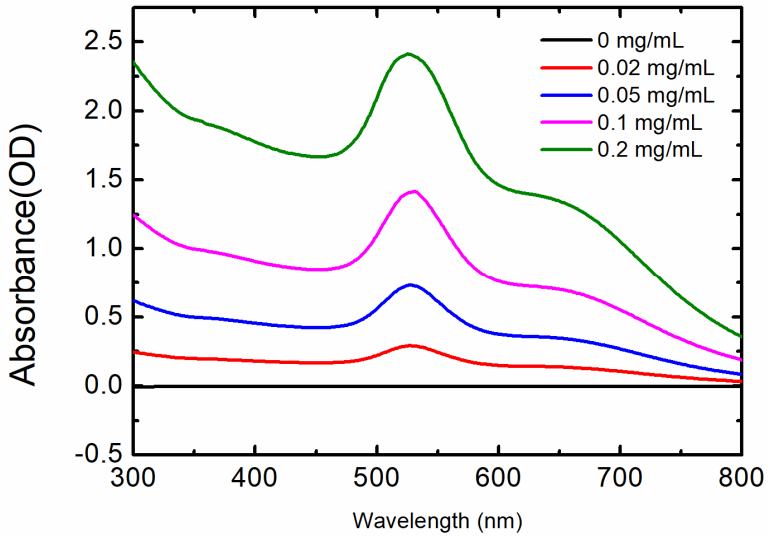

Figure 2.4 The absorbance of the AuNPs dispersed in water with different concentrations.

The absorptance of the AuNP-PNIPAAM and rGO-PNIPAAM was characterized by the UV-Vis-NIR spectrometer (Shimadzu 3101-PC with an integrating sphere (Shimadzu ISR 3100)).

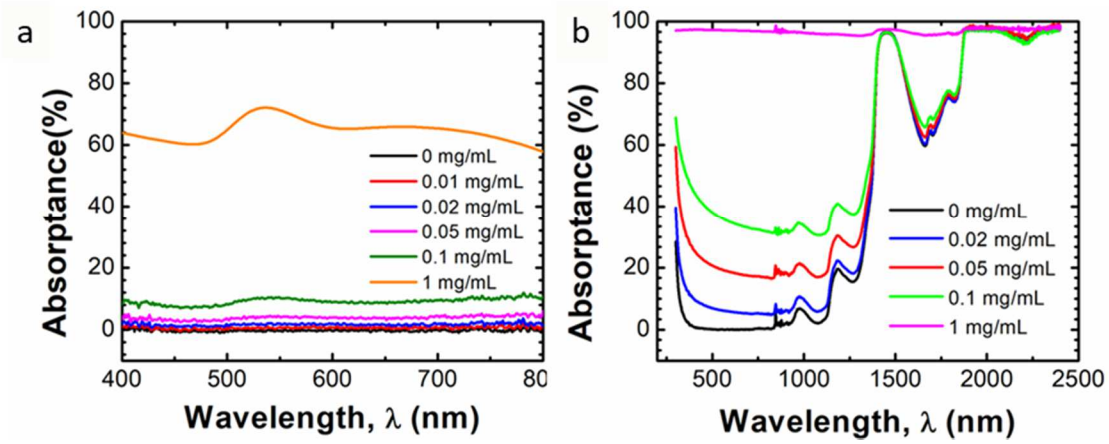

Figure 2.5 The absorptance of the AuNP-PNIPAAM hydrogel (a) and rGO-PNIPAAM hydrogel (b).

2.3.9. Mechanical properties

Mechanical properties of the AuNP-PNIPAAM and rGO-PNIPAAM in swollen states were characterized using a dynamic mechanical analyzer (DMA, TA Instruments, Q800).

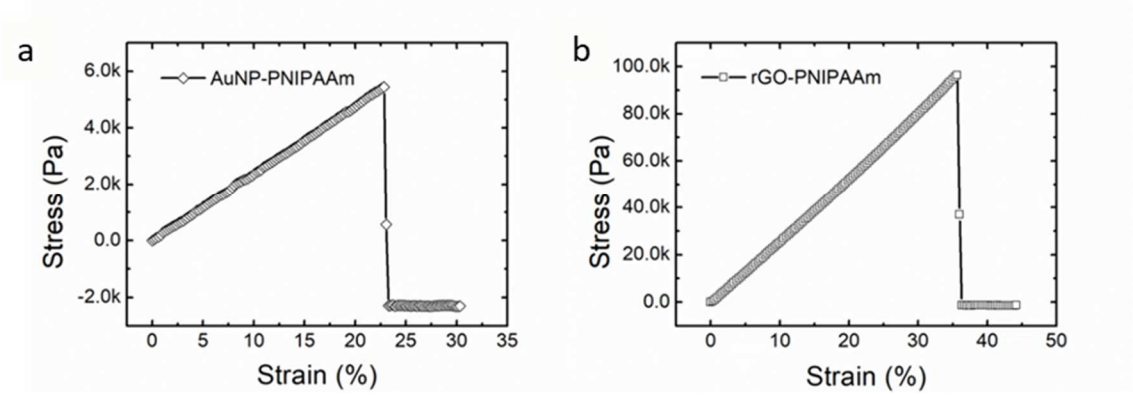

Figure 2.6 The stress-strain curves of the AuNP-PNIPAAM hydrogel (a) and rGO-PNIPAAM (b).

2.3.10. Swelling ratio and kinetics

To systematically investigate the tracking mechanism and to control the tracking speed of SunBOTs, we increased the water diffusivity of the hydrogel by tuning the pore size and the crosslinking density of the AuNP-PNIPAAM hydrogel network *via* a chemical linker, which resulted in distinct tracking kinetics.

The swelling ratio and swelling kinetics were characterized by recording and measuring the volume changes of hydrogels in a water bath using an optical microscope. The hydrogel sample was a section cut from the SunBOT pillar, in a cylindrical shape (1 mm in diameter, 1.5 mm in length). The fully swollen hydrogel cylinder at room temperature was placed in an empty container. Hot water of a well-controlled, specific temperature in the range of 35-60^{o}C was injected into the container to fully cover and heat the hydrogel to the specific temperature; simultaneously, the hydrogel volume change upon instant heating was recorded. The volume change was characterized by measuring the dimension changes in the time-lapse of the recorded video. Both the AuNP-PNIPAAM hydrogels with and without allyl disulfide, respectively in the thermal-diffusion-dominated SunBOT and the mass-diffusion-dominated SunBOT, are shown in Figure 2.7. Thermal diffusion-dominated SunBOT was used for the following applications due to its fast diffusion over time.

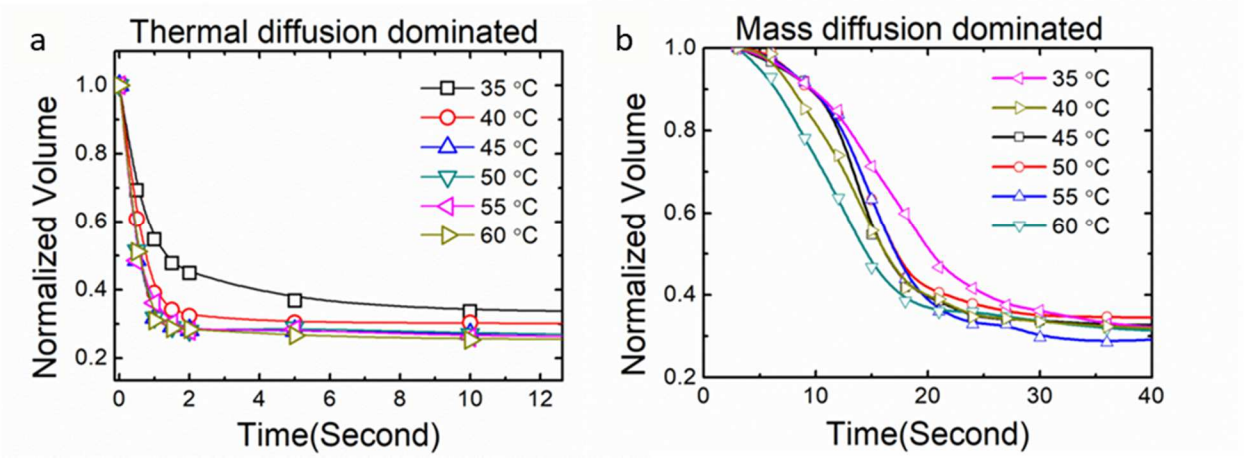

Figure 2.7 Measured swelling ratios and kinetics of the AuNP-PNIPAAM hydrogels in the thermal-diffusion-dominated SunBOT (a) and the mass-diffusion-dominated SunBOT (b).

2.3.11. Characterization of the omnidirectional solar vapor generator

The SunBOT array (5 x 7) was designed to contain micro-pillars of 300-μm diameter and 1-mm height with 700 μm spacing. The pillars would become wider (500 μm in diameter and 500 μm spacing) in diameter after washing off the solvent DMSO with water. The SunBOT array with a 70% filling ratio was fabricated by the same method but with a different mold. The SunBOT array is maintained floating at the water/air interface of a water reservoir inside a container placed on a precision scale (USS-DBS8). The light sources were illuminated on the SunBOT array with different oblique angles. The vapor generation was characterized by the mass reduction recorded by the precision scale.

2.4. Results and discussion

2.4.1. Design principle and operation mechanism

Plants track light through photoreceptors in their stems that detect the incident light and lead to cell elongation on the shaded side, due to a distribution gradient of growth factor (*e.g.,* auxin) between the illuminated and the shaded side[33]. To mimic the biological asymmetric growth, we leverage the capabilities of photo-thermo-responsive soft materials that shrink upon illumination and adopt the symmetric stem-like cylindrical pillar shape for the design of SunBOTs. Like a stem, SunBOTs

bend toward stimuli due to the asymmetric deformation between the illuminated high-temperature region and the shaded low-temperature region, as shown in Figure 2.8.

Similar to sunflowers, the photo-tracking process of SunBOTs involves four steps: (i) detection, (ii) actuation, (iii) aiming, and (iv) recovery, as shown in Figure 2.8. (i) Upon illumination, the SunBOT detects the incident light *via* surface plasmon resonance of the incorporated nano-photo-absorbers, which can be customized for various applications (*e.g.,* gold nanoparticles (AuNPs) and/or reduced graphene oxide (rGO) for monochromatic (532 nm) and broadband light sources, respectively) and (ii) actuates toward the source due to local heating and asymmetric deformation. The asymmetric deformation is induced by establishing an appropriate temperature gradient across the pillar, where the illuminated front-side temperature (T_f) is greater than the hydrogel's lower temperature solution temperature (LCST) while the shaded back-side temperature (T_b) remains below the LCST. This illuminated-side shrinkage results in a bending effect similar to what is observed in plant stems. (iii) As soon as the SunBOT aims at the light source, it spontaneously terminates the actuation motion. The aiming as a self-regulated actuation is modulated by the negative feedback loop inherent in the tight hydrogel-stimuli interactions. The localized exposure to incident photonic energy results in local shrinkage of the hydrogel and mechanical bending of the SunBOT pillar, which consequently blocks the light as overshooting protection, allowing the hydrogel to re-swell and repeat the cycles automatically, resulting in a steady state of aiming.

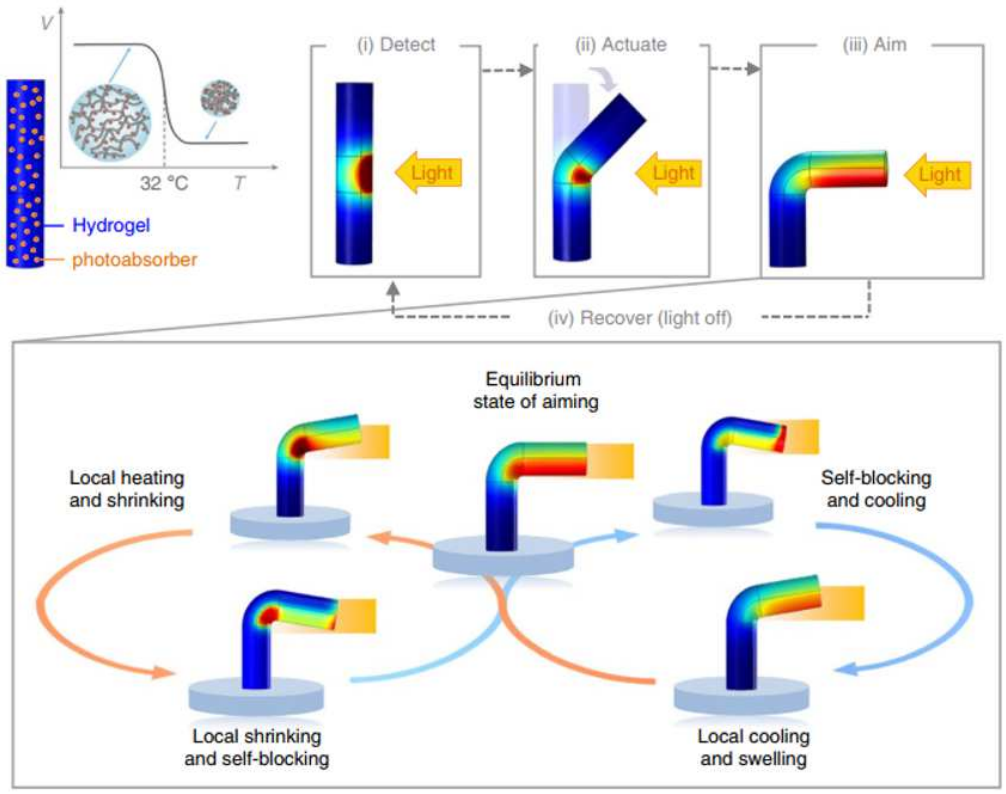

Figure 2.8 SunBOT design and phototropic mechanism. The steady state of aiming is regulated by a built-in negative feedback loop with self-shading capability.

This self-shading effect is proven by the measured temperature evolution, as both T_f and T_b converge to be tight around the LCST. Different from previously reported nastic motion, which is sensitive to the intensity of the stimuli and/or the ambient temperature, the rigorous self-regulating mechanism generates similar temperature gradients in SunBOTs under different illumination powers and environment conditions, which guarantee stable and accurate aiming at broad power and temperature ranges. (iv) When the illumination is turned off or changes position, the bent SunBOT immediately recovers its original shape or quickly adjusts its orientation to accommodate the position of a new stimulus, performing another tropistic cycle in real-time.

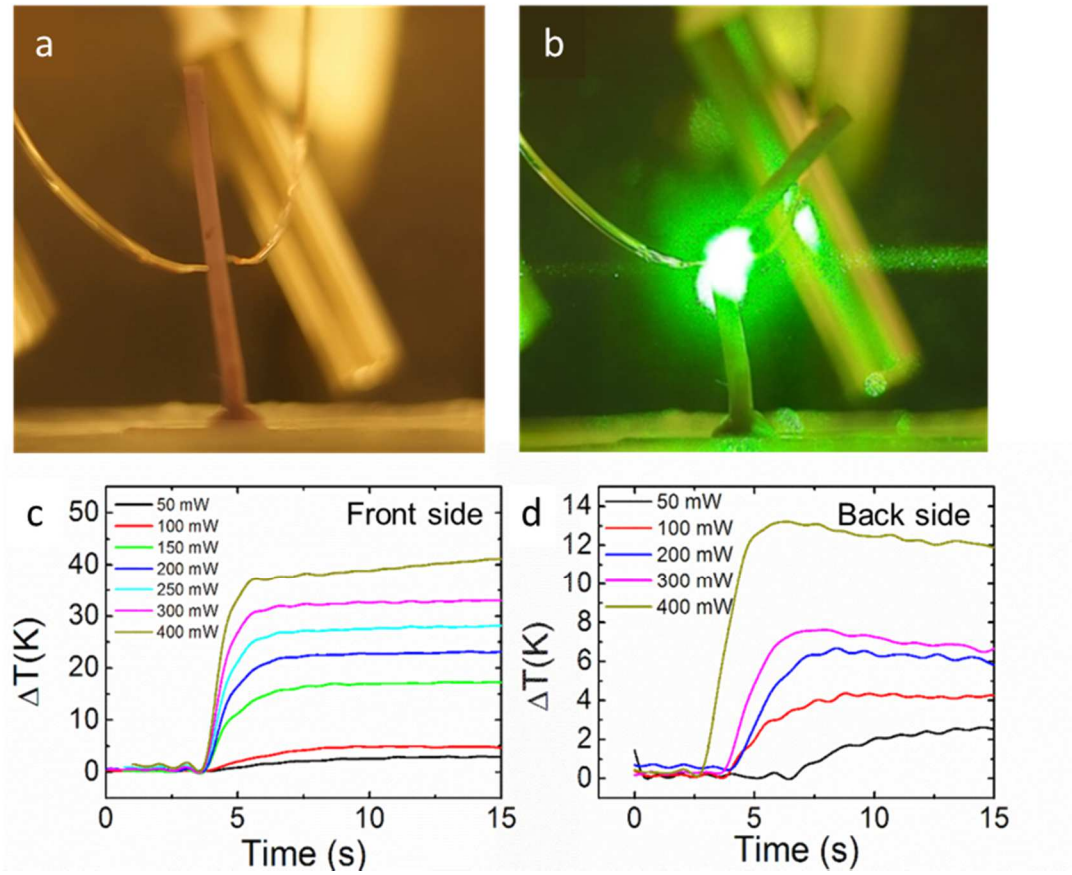

Figure 2.9 The temperature recording during the illumination on the SunBOT. a-b: The temperature measurement setup before (a) and during (b) illumination. c-d: The recorded temperature variation on the illuminated front side (c) and the shaded back side (d) of the SunBOT under illumination.

Overall, artificial phototropism is a self-regulatory effect that results from an elegant balance of fully-coupled participating physical processes: photo-thermal conversion, thermal diffusion, mass (water) diffusion, and mechanical deformation. Comprehensive theoretical efforts, specifically a multiphysics model that couples the light, heat, mass transfer, and mechanics across nano-to-millimeter scales, have been developed to understand the fundamentals of the phototropic process and to guide the rational design predictively.

2.4.2. System generality and tunability

SunBOT is a versatile platform that can be constructed using almost any reversibly photo-responsive soft materials, *e.g.,* hydrogel, LCE, and azobenzene/spiropyran-based polymer. Here we demonstrate the generality of the principle with three different photo-thermally responsive polymers. They are i) a thermo-responsive hydrogel PNIPAAM with homogeneously distributed nano-photo-absorbers, either gold nanoparticles (AuNPs) or reduced graphene oxide (rGO), which act as photo-receptors and photo-thermal converters simultaneously, respectively termed AuNP-PNIPAAm-based SunBOT and rGO-PNIPAAm-based SunBOT, ii) poly(2-dimethylamino)ethyl methacrylate (PDMAEMA) hydrogel with homogeneously distributed polyanaline (PANI) as photo-absorbers, termed PANI-PDMAEMA-based SunBOT and iii) LCE specifically based on diacrylate mesogen RM257 with homogeneously distributed indigo dye as photo-absorber, termed indigo-LCE SunBOTs.

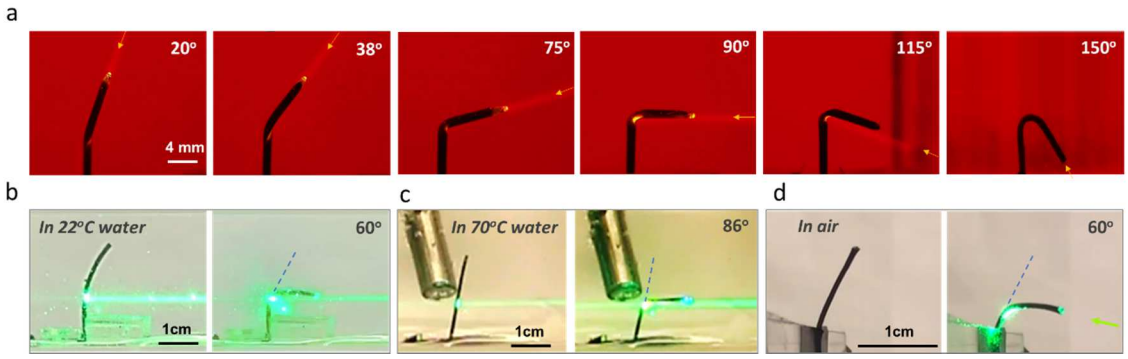

Figure 2.10. Material generality and tailorability. (a) Photos of an AuNP-PNIPAAm hydrogel-based SunBOT in water aiming to a laser illuminating from various zenith angles from 20° to 150°. (b-d) Photos of phototropic movement of SunBOT based on, respectively, PANI-PDMAEMA in RT water (b), PPy-(Pam-co-PNIPAAm) in 70 □ water (c), and indigo-LCE in air (d) tracking a laser illuminating from various zenith angles as labels.

Operational Temperature Range: The SunBOT can operate at a broad and tunable temperature range of -2.8~70 □, as shown in Figure 2.11 (laser, small spot size) and Figure 2.12 (white light, large spot size). These have covered an ultra-low temperature below water freezing point and elevated temperatures above 32 □.

These were achieved by (1) tuning the transition temperature of PNIPAAm as broad as 1~90 ^{o}C according to extensive previous reports, via tailoring the composition with co-monomers such as hydro-philic/-phobic small molecules or ionic liquids selective from abundant well-documented methods, such as acrylamide (AM) as a hydrophilic co-monomer to increases the LCST of PNIPAAm (Figure 2.11d), (2) using other photo-thermal responsive polymers with a broad range of responsive temperatures covering 20~50^{o}C, for example using PDMAEMA (Figure 2.11c) and POEGMA, as well as broad choices of photo-absorbers such as PANi (Figure 2.11c) and PPy (Figure 2.11d) in addition to nanomaterials, or (3) simply tailoring the medium liquid covering 1~50 □ , such as water/ethylene glycol mixture to realize operation at -2.8 ^{o}C (Figure 2.11a) and water/acetone mixture to increase the LCST of PNIPAAm to >45 ^{o}C and enable operation at 43.5 ^{o}C (Figure 2.11b). Besides these demonstrated photothermo-responsive polymers, one can employ photo-responsive polymers (*i.e.*, spiropyran-based and azobenzene-based polymers) to have even less constraints on operation temperatures. In addition, the temperature range can be always further tuned by tailing the photo absorption of hydrogel (*i.e.*, absorber species and concentration), pillar diameter, or power density to achieve phototropism.

Besides using photothermally-responsive hydrogels, there are many photo-responsive hydrogels to use, without the constraint of operation temperature range, such as spiropyran-based and azobenzene-based hydrogels. The hydrogel photo absorption, pillar diameter, and input light power density can all be tuned to jointly facilitate the temperature operation window tuning to fit various ambient temperatures.

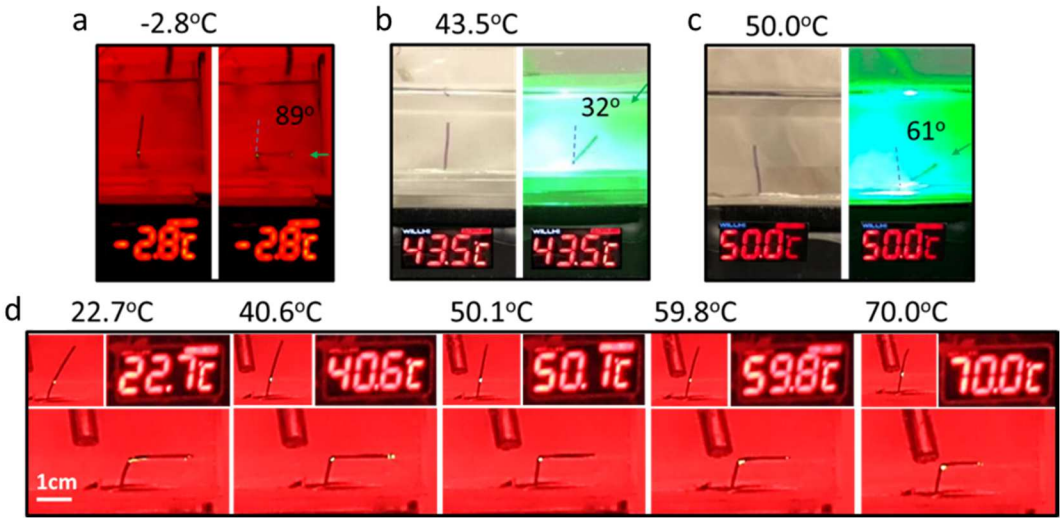

Figure 2.11. The successful tracking of light (laser) incident from a series of arbitrary incident angles (as labeled) at a broad range of bath temperatures spanning from -2.8 °C to 70 °C, which are below the freezing point of water (a) and above the original 32° LCST of PNIPAAm (b, c, d). (a) AuNP-PNIPAAm pillar in -2.8 °C water/ethylene glycol mixture, (b) AuNP-PNIPAAm pillar in 43.5 °C 1:1 water/acetone mixture, (c) PANi-PDMAEMA pillar in 50 °C water, and (d) PPy-(PAM-co-PNIPAAm) pillar in 22.8 °C, 40.6 °C, 50.1 °C, 59.8 °C, and 70 °C water. The dimension of all the pillars is 2.3 cm in length and 0.97 mm in thickness.

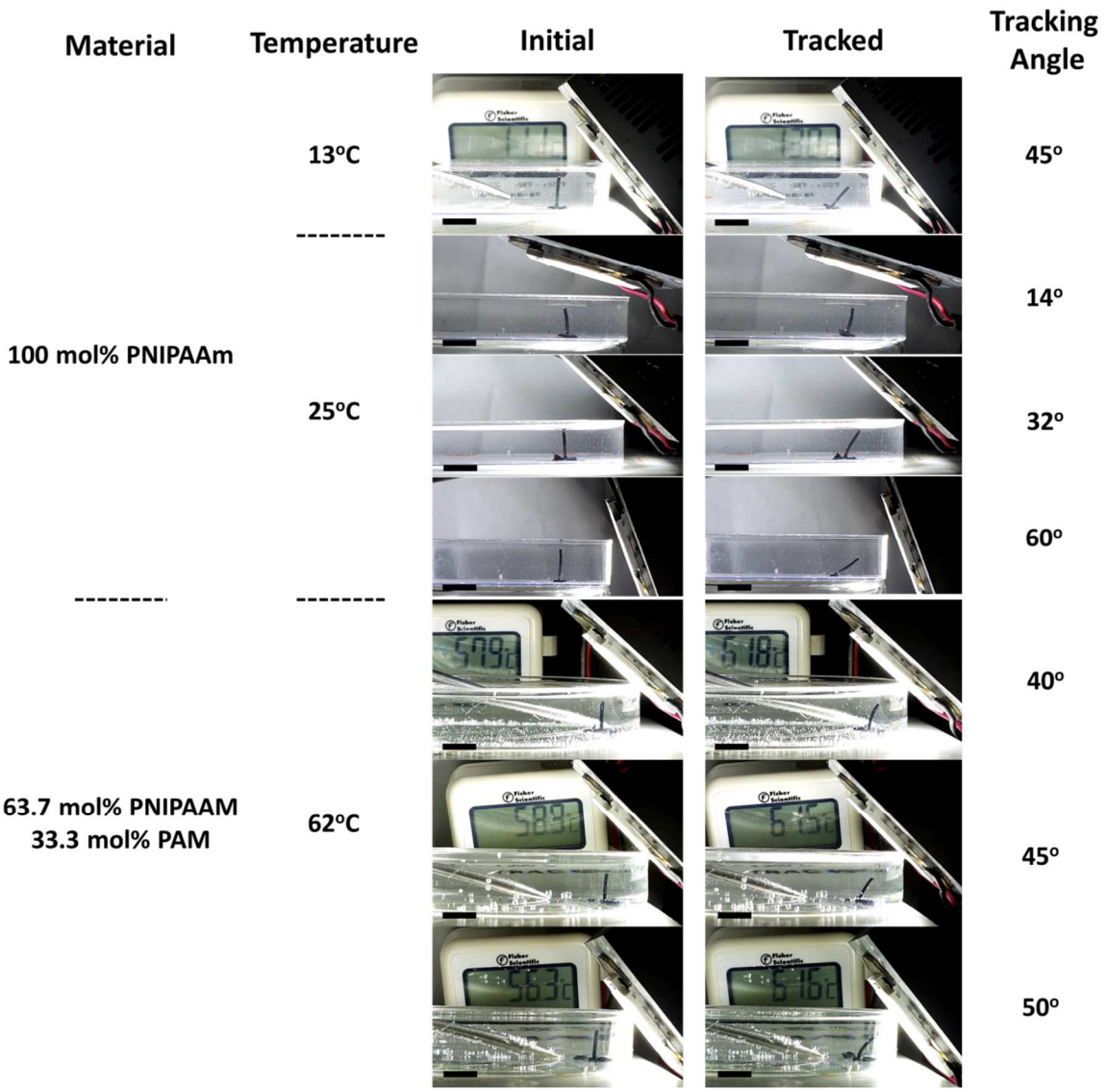

Figure 2.12. The successful tracking of light (laser) incident from a series of arbitrary incident angles at a broad range of bath temperatures spanning from 13 °C to 62 °C. The hydrogel used for tracking at T>32 °C is PPy-coated PAM-co-PNIPAAm, where PPy serves as the photo-absorber and acrylamide (AM) increases the LCST of PNIPAAm as a hydrophilic co-monomer.

2.4.3. Omnidirectional tracking

The omnidirectional phototropic capabilities of the SunBOT were demonstrated and investigated by using the 532 nm laser as the light source. The SunBOT was positioned at the center of a rotary stage. The laser was directed from a 60° zenith incident angle onto the center point of the rotary stage. The stage revolved (with the SunBOT on it) for 360° to vary the horizontal incident angles,

either continuously or intermittently to investigate respectively the tracking and aiming performance. *(1) The continuous revolving* demonstrated the smooth "tracking" of SunBOT. *(2) The intermittent revolving*, comprised of alternating rotating-and-pausing steps, demonstrated the high precision and remarkable controllability of the "aiming", as shown in Figure 2.13. Notably, as soon as the rotation paused (*i.e.*, incident angle stopped), the bending motion of the SunBOT terminated instantly upon meeting the light, without over-bending. In detail, the entire 360° omnidirectional tracking process was divided into six 60°-rotation steps. Each 60°-rotation took 2-3 seconds. As the SunBOT rotated with the stage, it sensed the corresponding changes of the incident direction of the light, and adaptively re-configured itself to point to the light. This tracking motion took tens of seconds. Once the SunBOT was aligned with the light, the motion terminated; the SunBOT maintained a stable state of aiming, as long as the light maintained shining on it from that direction. In each pausing step, we kept the incident angle for tens of seconds, to demonstrate the aiming state is stable and robust. Overall, this demonstrated SunBOT's remarkable capabilities of omnidirectional tracking and steady aiming with high self-controllability and precision.

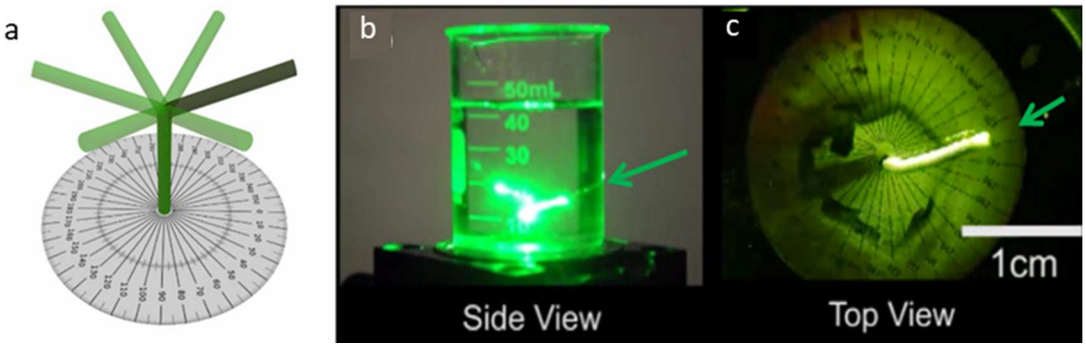

Figure 2.13. Experiment demonstration of the real-time, omnidirectional phototropism of the SunBOT. a, The Schematic of the SunBOT in the state of aiming to the light source from the different incident angles. b, c, The side view (b) and the top view (c) of the demonstration during the experiment procedures, at the same time. The green arrows indicate the direction of the incident light.

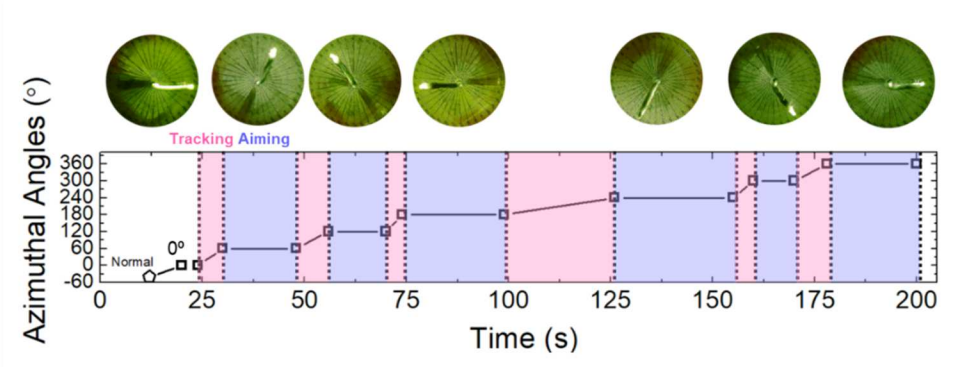

Figure 2.14. The time-lapse of SunBOT trajectory in the omnidirectional light tracking of SunBOT shows high self-controllability and precision in the tracking.

SunBOTs can adaptively re-configure to follow and orient themselves perpendicular to the incident light from arbitrary and constantly varying directions (-150°–150° zenith, 360° azimuth) at room temperature. This artificial phototropism capability achieves remarkably high tracking accuracy (*i.e.*, the ratio of pillar final bending angle and light incident angle) of > 99.8% (Figure 2.15).

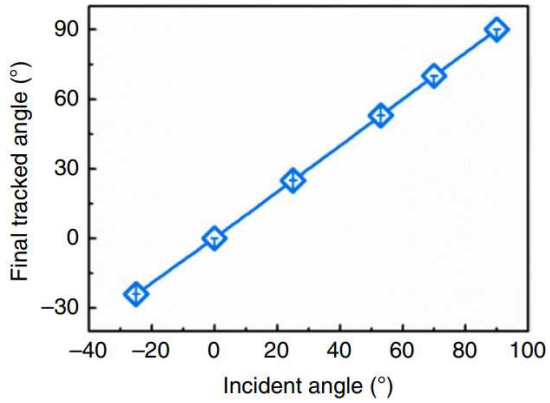

Figure 2.15. The design and mechanism of the SunBOT. The SunBOT aims to the light source with high tracking accuracy (< 0.2% error).

2.4.4. Broad and tunable operation

The SunBOT has a truly broad and tunable operation window that can guarantee successful phototropism over a wide range of light intensities, ambient temperatures, lighting conditions, irregular geometric shapes, and spatiotemporal rhythms of illumination. These can be achieved by

tuning the material properties, including the nano-photo-absorber concentration, transition temperature, dimension of the material, and the coupling between the properties. Figure 2.16 presents the versatility of SunBOTs through more complex direction-cognitive behaviors under various conditions. The SunBOT can track not only spot light but also large-area lighting, showing applicability to ambient light conditions. The optical beam width can also effectively manipulate bending curvatures, which are accurately reproduced by multiphysics modeling. Interestingly, SunBOTs with arbitrary contorted pillar shapes can be straightened by the light. Such high-fidelity tropism presents adaptive learning and self-optimization through continuous dynamic light-material interactions. Ultimately, attributed to the fast recovery (re-swelling) of the hydrogel when not being illuminated, the SunBOT can successfully track a light source in real-time continuously moving 360^{o} azimuthally at a fast speed up to 0.03 second/degree. At these intentionally designed pausing steps, the fast-moving SunBOT precisely stops at the light source direction without any over- or under-bending, confirming an extremely strict spatiotemporal control of the tracking behavior by the light. Being both compositionally and geometrically symmetric, the design simplicity of SunBOTs endows its infinite degree of freedom fulfilling truly omnidirectional tracking and energy harvesting.

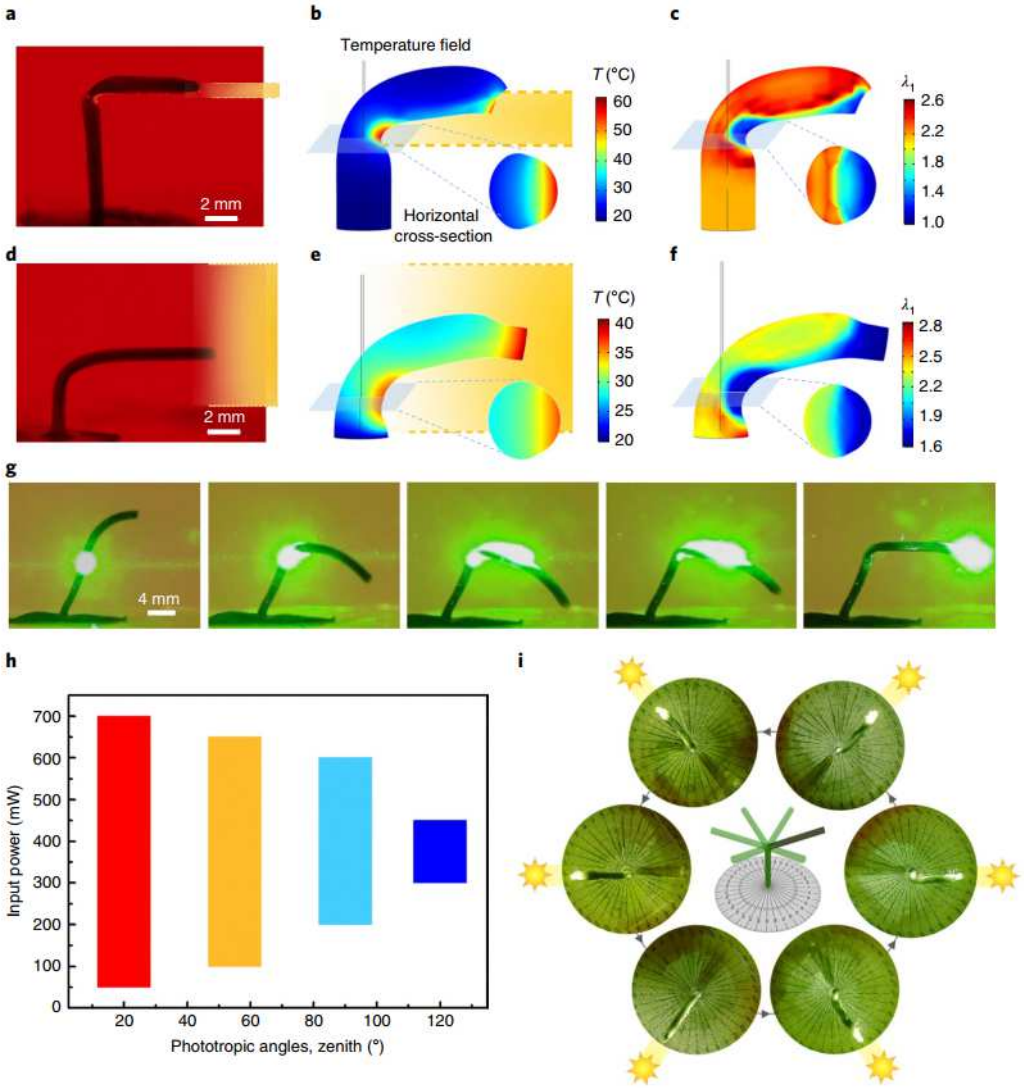

Figure 2.16. Complex and robust phototropic behaviors of SunBoTs. a–f, The SunBOT can track both a spotlight (1 mm beam width) (a–c) and an area light (20 mm beam width) (d–f), which exhibit different curvatures. The simulated temperature distribution (T) (b and e) and stretch field (λ1, primary stretch in the 1-direction; at a fully dried state, λ1 = 1) (c and f) of the steady aiming state captured the experimental results (a and d). Insets: cross-sections at the illumination sites. g, Snapshots of the process of an irregular-shaped SunBOT being straightened after bending (from left to right), which demonstrates the self-correction ability of a robust artificial phototropism. h, The operation windows of input power to successfully track the light of different incident angles (20–120° zenith). An input power smaller than the colored histogram is not sufficient to allow the pillar to achieve tracking. i, Top-view snapshots of a SunBOT continuously tracking light that revolves azimuthally around the SunBOT

2.4.5. Kinetics study of the SunBOT

How fast a SunBOT can track the directional variation of the emissive energy is directly correlated to the ability to aim at the moving light source and hence the final energy production. Based on steady-state studies, we have further investigated the kinetics of the dynamic tropistic locomotion, which was jointly determined by the thermal diffusion and the mass (water) diffusion. The time scale associated with thermal diffusion in the hydrogel remained the same during the deformation, and its dynamics have been simulated in the multiphysics modeling (Figure 2.17). On the other hand, mass diffusion can be manipulated by controlling the nano/micro-structure of the hydrogel. Figure 2.17a and b exhibit distinct phototropic kinetics with different diffusion-dominated mechanisms. When the mass diffusion is relatively fast, *i.e.,* the water diffusion in the hydrogel matrix is completed by the time the steady-state temperature gradient is established; thus, the tracking speed is limited by the thermal diffusion, and the SunBOT is thermal-diffusion dominated (TDD). As shown in Figure 2.17a, the TDD SunBOT can track to 90° within 3.5 seconds (much faster than its natural counterparts), which is comparable to the time required to reach a thermal steady state (Figure 2.17c). By contrast, the mass diffusion dominated (MDD) SunBOT has much smaller pore sizes (Figure 2.17d), hence much slower water diffusion. Consequently, it takes a longer time to reach 90^{o} tracking than for the TDD SunBOT (Figure 2.17b).

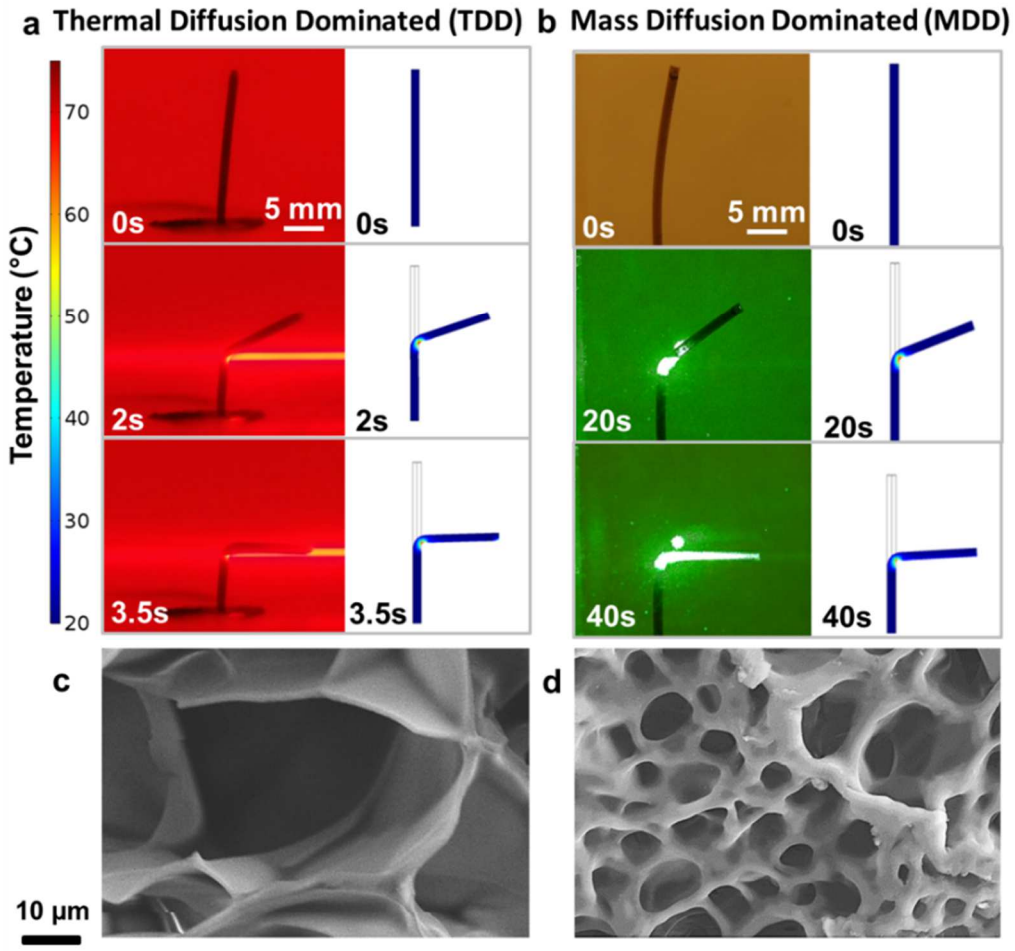

Figure 2.17. The tracking kinetics of the SunBOT. (a) The kinetics of a thermal-diffusion-dominated (TDD) tracking process, evaluated by experiment (left) and finite element analysis (FEA) simulation (right), which perfectly synced. (b) The kinetics of a mass-diffusion-dominated (MDD) tracking process. (a and b share the color bar.) (c, d) The SEM images of PNIPAAM hydrogels were used respectively in the TDD SunBOTs with 50 μm pore size (c) and in the MDD SunBOTs with 5-10 μm pore size (d).

To better understand these dynamic phototropic behaviors, we studied the temporal evolution of temperatures T_f and T_b near the incident site of SunBOT experimentally and numerically (Figure 2.18a). With the quantitative agreement between simulation and experimental results of the kinetic studies (Figure 2.18a, b), we validated our numerical model, which applies the recorded dynamic swelling ratio of the hydrogel (Figure 2.18b) to fit the mass diffusivity. The validation enabled the

rational design and dynamic behavior prediction by providing comprehensive insight and a clear physical picture of the fundamental mechanism.

As the microstructure of the hydrogel matrix provides flexible tunability of the phototropic kinetics, the SunBOT achieves once the material system has been fabricated, one can still readily control its temporal response by varying the incident light power. The time cost of the successful 90-degree tracking of the SunBOT is varying from hundreds of seconds to seconds, as long as the input power falls into the operation window discussed above.

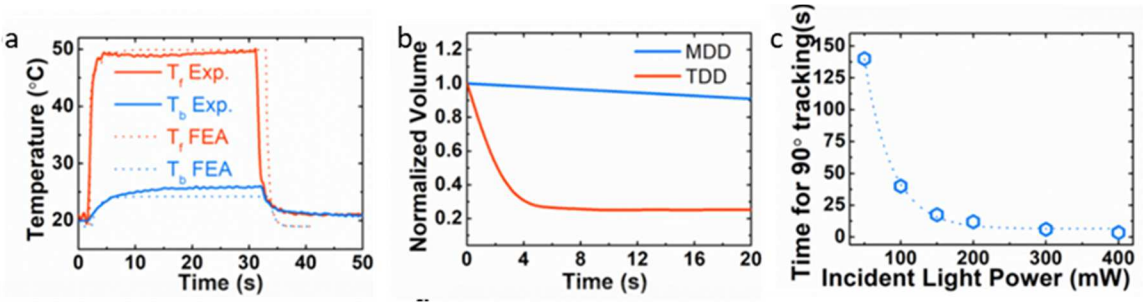

Figure 2.18. Thermal and thermomechanical characterizations of SunBOTs (a) The experimental and simulation results of T_f and T_b of the TDD SunBOTs under 30-second illumination. (b) The kinetics study of the thermal-shrinkage of the hydrogels used respectively in MDD and TDD SunBOTs. (c) The time used to achieve 90° tracking at different incident light powers.

2.4.6. In-air operation

Although omnidirectional SunBOTs using PNIPAm-based hydrogels containing reduced graphene oxide (rGO) or gold nanoparticles (AuNP) have been successfully demonstrated, hydrogel materials used in this work are mechanically weak to self-stand in air and support additional optical devices if held on top of them. Single LCE pillars and liquid-vapor phase transition phototropic actuators have been reported for wide tracking operation windows, but are limited by the high-power, laser-driven requirement that exceeds the intensity of that specific wavelength in the solar spectrum.[34,35] Therefore, it is highly desirable to develop a simple, low-cost intelligent system that

can utilize sunlight (at or lower than 1000 Wm^{-2}) to achieve large-angle phototropic reorientation, while remaining mechanically strong enough to support and drive optical devices.

Therefore, we modified the material system to an LCE bimorph structure as legs in a double-leg design to support the optical devices on top to achieve large actuation and high load-bearing ability (Figure 2.19). Such LCE-based phototropic material system can be applied for enhancing light harvesting and thus the performance of various optical devices such as solar cells.

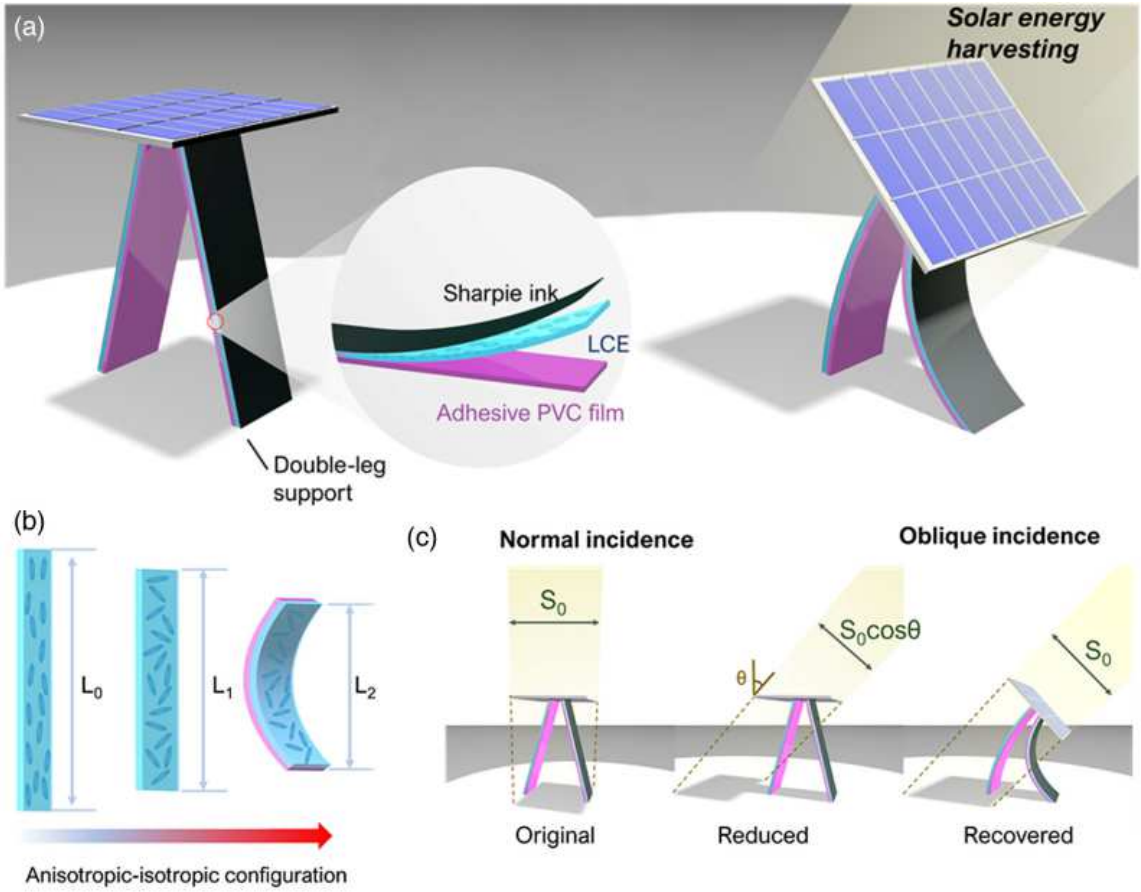

Figure 2.19. Design principle of in-air operation of light tracking device that can support a heavy object. (a) Schematic illustration of the general design of the phototropic system based on LCE. (b) Illustration of the LCE configuration change and bimorph design. (c) Illustration of OEL.

To demonstrate the system's ability to reorient towards light and recover the OEL, solar panels were mounted on the top of the phototropic device. Light generated by a solar simulator of various

intensities (700 – 1000 W m^{-2}, 0.7 – 1.0 sun) and various incidence angles (30°, 45°, and 60°) was used to test the final equilibrium bending angle of the phototropic device (Figure 2.20b). At 30° and 45°, the device showed remarkable tracking performance, able to accurately reorient itself toward sunlight with an error of less than 0.2° even at 900 W m^{-2} intensity (lower than one sun). At a 60° incidence angle, it could bend to 53° and 57° final angle at 700 W m^{-2} at 1000 W m^{-2} intensity, respectively; this still represents significantly improved tracking performance, considering 99.86% (for 57° final angle) of light is recovered compared to its vertical position. It could also bend under natural sunlight condition, where the intensity is less than 1000 W m^{-2}. The phototropic device not only accurately reorients itself towards light, but also does so in a prompt manner. At the 60° and 45° incidence angles (Figure 2.20c, d, respectively), it can reorient itself from a vertical position to the final bending state within 40 seconds, regardless the light intensity. Interestingly, during the phototropic bending process, the device first showed a sharp increase in its bending angle followed by a slow bending backward to the final bending state. Such a phenomenon is believed to come from the momentum on the load (solar panel) sitting on top of the system: during the bending process (Figure 2.20a), the movement of the legs causes the reorientation of the solar panel, which provides the momentum contributing to the overshoot of final equilibrium bending state. After that, the motion of the solar panel is restricted by the LCE legs. Finally, the system reaches its dynamic equilibrium state, and a steady final bending angle can be recorded. Fine-tuning the load weight of the phototropic device can influence the fast bending as well as the overshoot behavior, as both will cease to exist if the load weight is reduced to 2/3 of the optimized weight. At a 30° incident angle (Figure 2.20e), the device took about 90 seconds to reach its final bending state, and a spike of the bending angle was not observed. This could be because the relatively little motion of the 30° reorientation cannot provide enough momentum for the solar panel, and the legs experience less power density at the small incident angle.

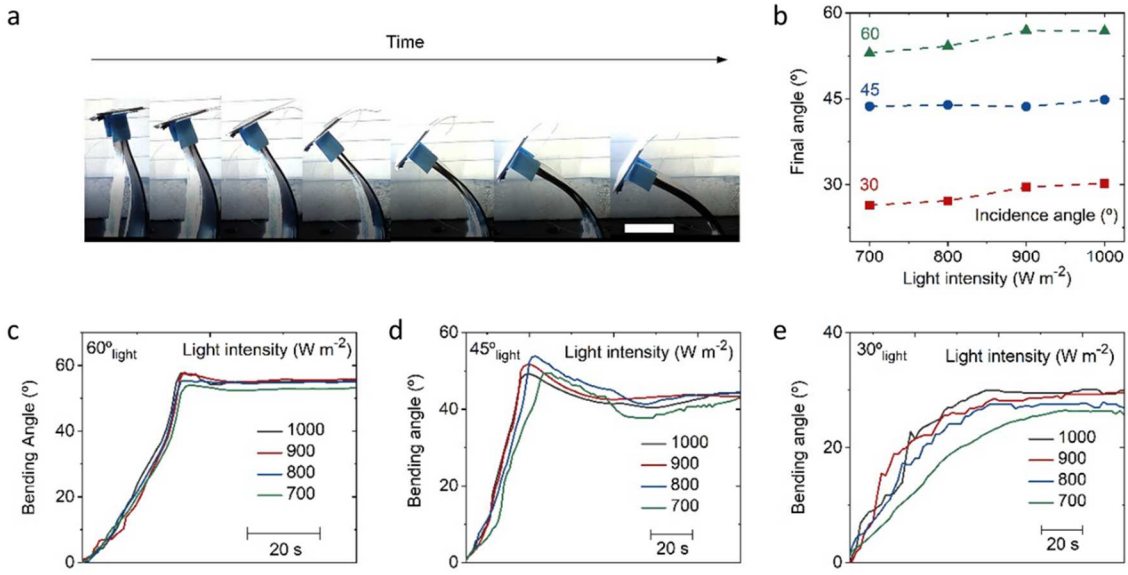

Figure 2.20. Actuation characterization of double-leg designed SunBOT. a) Optical images of the phototropic system during bending. Scale bar represents 1 cm. b) Final bending angle of the phototropic system versus light intensity at different incidence angles. c), d), and e) time-dependent bending angle of the phototropic system at different light intensities at 60°, 45°, and 30° incidence angle, respectively.

2.4.7. Artificial phototropism enhanced energy harvesting: solar steam generation

We demonstrate the efficacy of SunBOTs in solving practical OEL problems (Figure 2.2) by applying an array of micro-SunBOTs (500-μm diameter with a pitch of 1 mm) in solar energy harvesting. The micro-SunBOT array incorporating rGO as a broadband photo-absorber can successfully track white light incidence from the entire hemispheric space. This further demonstrated that the modular design can accommodate either single-wavelength or broad-spectrum light sources. Due to the phototropism, the tips of the micro-SunBOT fibrils are always receiving the maximum photonic power density and thus compensate for the OEL. Compared with a non-tropistic textured surface as the control sample, we evaluated the benefits of the tropistic oblique-loss compensation (OLC) enabled by the SunBOT.

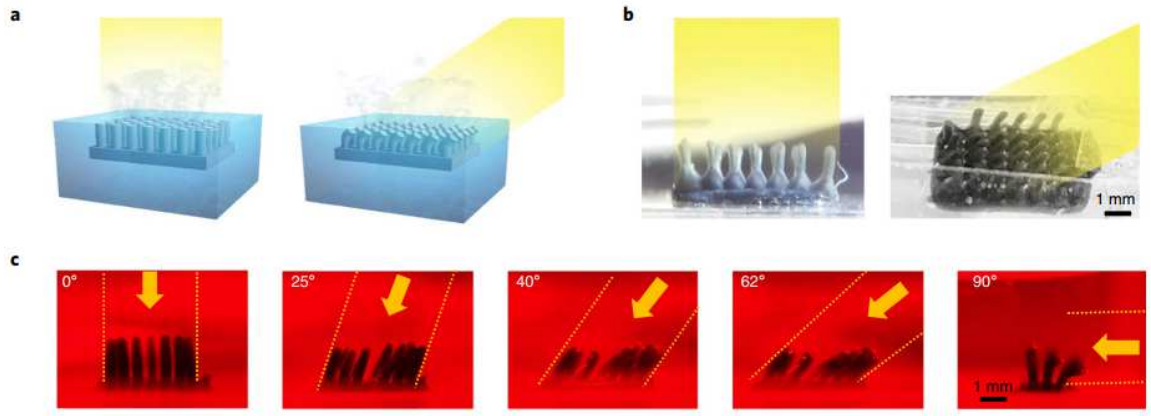

Figure 2.21. A demonstration of the energy maximization function of phototropism: oblique-loss compensation (OLC) in the solar vapor generation (SVG).

By keeping the SunBOT array at the water-air interface under variable-angle illumination, serving as a phototropic solar vapor generation (SVG) system, we evaluated the angle-dependent performances of the photonic energy absorption and conversion, by measuring the generated water vapor mass flux (G_θ, the mass of vapor produced per unit area per unit time). The area used to characterize G_θ is the effective area of the SVG device, *i.e.*, the area positioned at the water-air interface and contributing to vapor generation due to the localized heating at the interface. To exclude the contribution to the vapor generation from the photo-thermal energy produced by water (thermal mass) under illumination, the G_θ has the baseline subtracted. The baseline was measured by recording the evaporation rate of a water bath with a total area equivalent to the total footprint of the SunBOT sample (including the pillar-top and gap areas) under the same illuminating power but without the SunBOT. For non-tropistic surface, the angle-dependent input photonic power density $P_\theta = cos\theta \cdot P_{max}$ decreases as incident angle (θ) increases (Figure 2.2b). This work focuses on studying the angle-dependency of the energy harvesting by maximizing the input power density, instead of the absolute SVG efficiency. Hence, we evaluate the phototropism-enabled OLC via defining a dimensionless value derived from G_θ, the *normalized SVG* ($N = G_\theta \cdot h_{LV}/(P_{max} \cdot C_{opt})$), where h_{LV} is the specific enthalpy of water vaporization (in J/kg), C_{opt} is the optic

concentration, which uses the constant photonic power density at normal incidence $P_{max}= P_{\theta}(\theta=0^{o})=1kW/m^{2}$ as the normalizing factor, instead of an angle-dependent P_{θ}. Under normal incidence, the normalized SVG degenerates to the efficiencies regularly defined in other previous reported SVG studies[36–38](mostly under normal illumination).

When θ=0°, the SunBOT exhibited SVG efficiency of 70% under 1-sun illumination and 80% under 2-sun illumination, which are comparable to the previously reported values[36–43]. When θ=60° ($P_{60°}$ = 50%·P_{max}), for non-tropistic surfaces, the vapor flux G_{θ} reduced to 50% of $G_{\theta=0°}$. By contrast, the SunBOT array maintained 90% of $G_{\theta=0°}$ under normal incidence, which compensated the lost 40% of the input (Figure 2.22c).

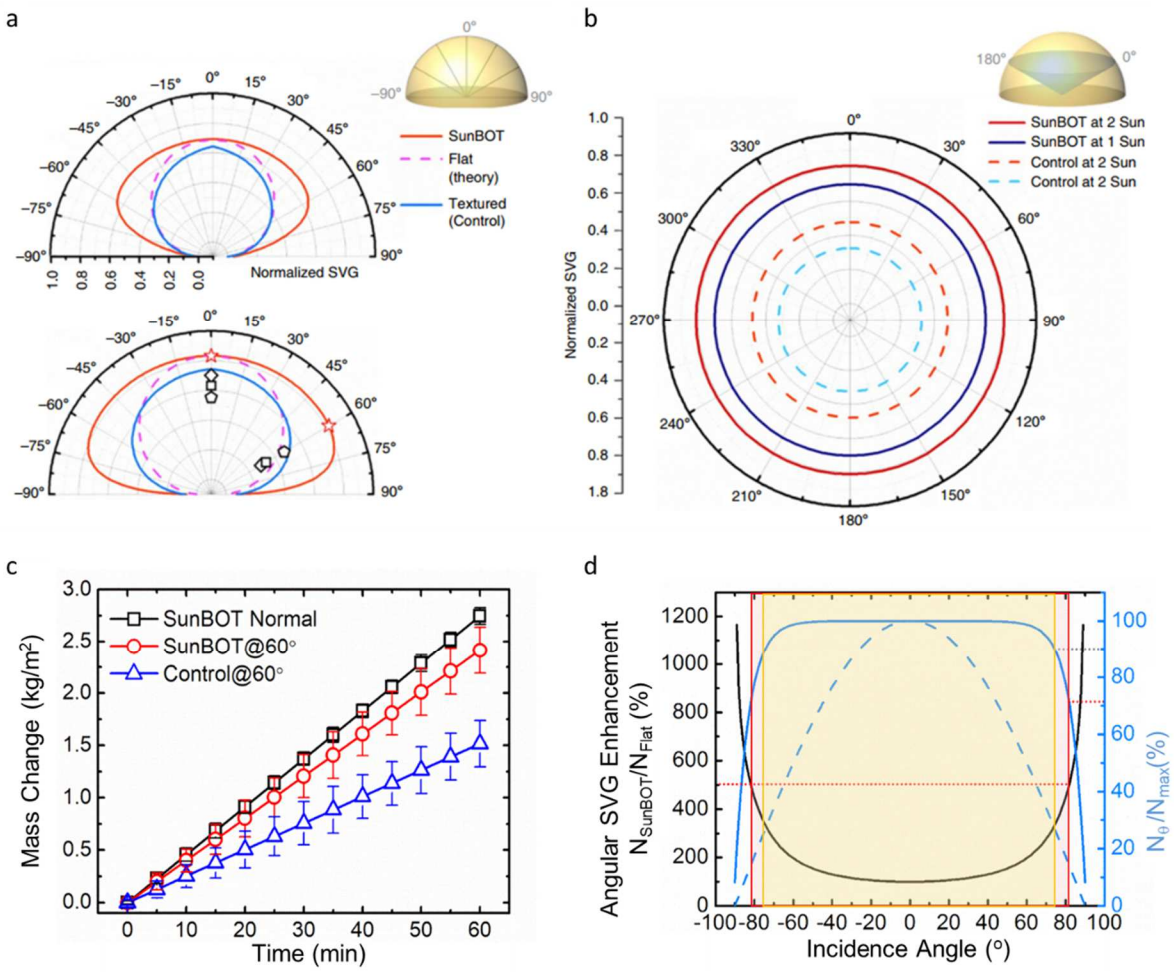

Figure 2.22. SVG performance based on the SunBOT design. A) The measured normalized SVG of SunBOT (rGO) under 1 Sun (top) and 2 Sun (bottom) illumination at various zenith angles from -90 to 90°, in comparison to control samples of a flat surface (in theory) and a non-tropistic textured surface and to previously reported SVG systems (diamond, Camacho-Lopez et al.; square, Shastri et al.; pentagon, Qin et al.; star, this work). B) The SVG of a SunBOT (rGO) array under illumination from 0 to 360° azimuthal angles (zenith angle = 60°). C) Time-dependent SVG mass change per unit area by SunBOT(rGO) under a 60° (zenith) illumination is comparable to that under normal incidence, whereas the control sample exhibits a 45% reduction in SVG. Plots are centered on the mean and the bars indicate the s.d. D) The angle-dependent SVG of a SunBOT (blue solid line) and a flat surface (blue dashed line) and the enhancement ratio that compares the two (black curve), where N_θ is the normalized SVG under the light of an incident angle θ. The red and purple frames indicate two exemplary operation angle windows with >75% and >90%, respectively, of the input energy density harvested.

Under 1-sun and 2-sun illuminations, the SunBOTs-based phototropic SVGs outperformed the control samples at all incident angles (zenith and azimuth) in the entire hemisphere (Figure 2.21a, b). At 60° (zenith), the phototropic SunBOT generates SVGs doubles that of theoretical flat surface, control samples and previous reports. The SunBOTs show omnidirectional SVG (OSVG), which is defined as generating >90% of maximum SVG (θ=0°) under oblique incidence, over a wide operation window of angles, *i.e.*, -60°–60° for 1-sun and -75°–75° for 2-sun, in contrast to the drastic reduction in both theoretical estimation and control samples. In addition, the SunBOT array demonstrates up to 400% enhancement (5-fold) of SVG with an operation window of 164° (-82°–82°) (Figure 2.22d).

2.4.8. Artificial phototropism enhanced energy harvesting: Photovoltaics

The OEL recovery ability of the phototropic device is demonstrated using a two-legs design as previously mentioned. I-V curves are tested and recorded from the solar panels mounted on top and compared to a non-phototropic control (stationary solar panel in horizontal position), recorded for 1000 Wm^{-2} light with an angle of 60°, 45°, and 30° (Figure 2.23a, b, c, respectively). At all voltages, the phototropic device can output up to 200% current, indicating that it can deliver more energy compared to the non-phototropic control. The maximum power output is calculated from the I-V curve data by multiplying the current with the respective voltage and finding the largest value. The maximum output power of the solar panel is also calculated for 60° light illumination and compared to that of 0° light illumination of that intensity. Compared to the phototropic device, the power output of the non-phototropic device at 60° is approximately half of the former, consistent with the cosine relationship. The tracking solar panel illuminated with 60° light gave a 95.7% - 99.2% power output compared to 0° light of the same intensity. The power recovery percentage (defined as the device output power with angled light divided by that with vertical light) of the non-phototropic device (Figure 2.23e) and phototropic device (Figure 2.23f) at various light intensities and angles are also tested. Regardless of the light intensity, the non-phototropic device can recover around

86%, 70%, and 50% of light at 30°, 45°, and 60° incidence angles, respectively, consistent with the cosine relationship. The phototropic device can recover more than 95% of the power for almost all combinations of the incidence angle and intensity, showing its significant strength of recovering OEL, even at a light intensity lower than one sun (1000 W m^{-2}). Incidence angle-dependent power recovery was also examined (Figure 26g). For the phototropic devices, the "front-bending" (0 - 90°) and "back-bending" (-90 - 0°) have similar power output, showing symmetric performance and the ability to track light across the entire hemisphere above the horizon. At nearly all incidence angles, the phototropic device can produce larger power output than the non-phototropic counterpart. At the large incidence angles of 70° and 80°, the phototropic device can generate 2.85 and 4.47 times the power of the non-phototropic device, respectively. At an incidence angle of 90° where the non-phototropic device can barely get any power output, the phototropic device could still generate power comparable to the non-phototropic device illuminated at 40°. All results were indicating that the phototropic device can effectively recover OEL.

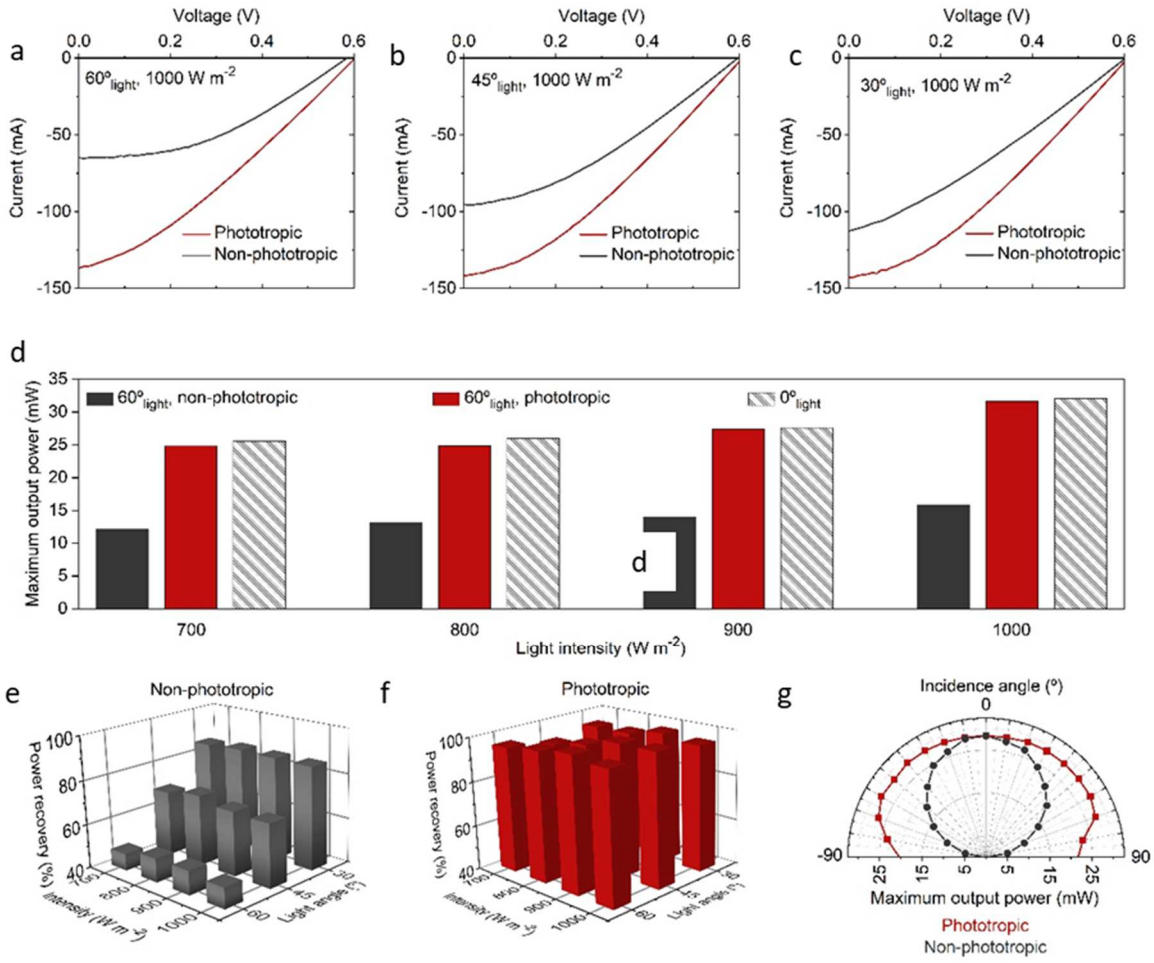

Figure 2.23. photovoltaic performance based on the phototropic design a), b) and c) I-V curves of the phototropic solar panel and the non-phototropic solar panel illuminated with 60°, 45°, and 30° light, respectively. d) Maximum output powers of the phototropic solar panel and non-phototropic solar panel illuminated with 60° and 0° incidence light. e) and f) Power recovery percentage, for 0° incidence, of the phototropic solar panel and the non-phototropic solar panel, respectively. g) Maximum output power of the phototropic solar panel and the non-phototropic solar panel under 1000 W m^{-2} illumination at different incident angles. h) Maximum output power enhancement of the phototropic solar panel at different hours of the day relative to the non-phototropic solar panel.

An outdoor experiment further demonstrated the ability of the solar panel phototropic device to capture more power (Figure 2.24) compared to the non-phototropic device. The I-V curves of the phototropic solar non-phototropic devices are recorded from 9 a.m. to 4 p.m. on a winter day. At 3 p.m., the phototropic device delivered a 55% higher output compared to the non-phototropic device,

which is the result of the combination of a relatively large incidence angle and large light intensity. At larger incidence angles, at 9 a.m. or 4 p.m., the enhancement is slightly decreased to around 45%. Although the incident angle is larger, the light intensity is reduced, so bending may not fully lead to the exact alignment with the incident light. Still, for such a device with low-cost components and simple fabrication, it is remarkable that it can show a real-life application with enhanced power recovery. The bimorph design helps with the large actuation angle despite the relatively low temperature and sunlight intensity during winter, and the double-leg support design allows it to stand firm against the wind and other air turbulence that might be present in the outdoor environment.

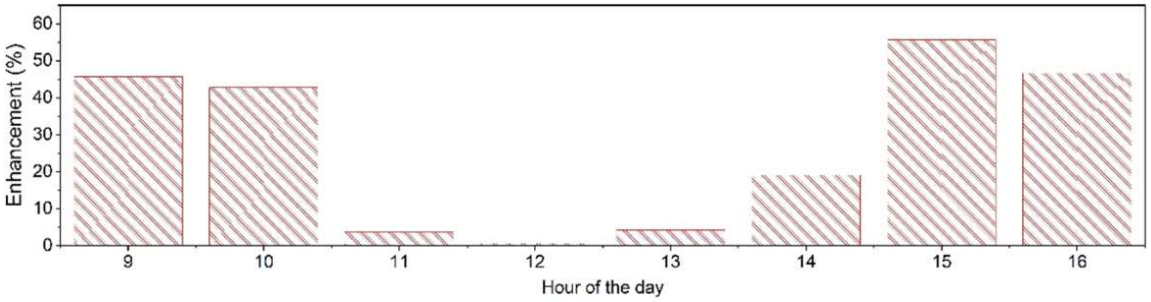

Figure 2.24. An outdoor demonstration of the solar panel phototropic device. Maximum output power enhancement of the phototropic solar panel at different hours of the day relative to the nonphototropic solar panel.

2.5. Conclusions and perspectives

Nature-inspired, synthetic phototropic material has been achieved by the self-adaptively reconfigurable material system with a built-in feedback loop. The phototropic material features omnidirectional self-orienting capability and demonstrates a successful breakthrough of the uncontrollable or preprogrammed motions of the state-of-the-art actuating systems for energy harvesting, exhibiting a sunflower-like behavior. Fundamentally, the experimental-numerical investigation generates new insight into the mechanism behind the plant-like phototropic motion and also establishes a predictive model to guarantee high fidelity and energy efficiency in the harvesting of broad forms of energy. The SunBOTs present biological sensorimotor-like behaviors,

controlled by a feedback loop inherent in the intricate coupled photo-chemo-mechanical interactions. This behavior presents a step toward matching artificial autonomy with the elegant agility of living systems, leading to next-generation intelligent materials. Practically, our SunBOT structures provide a long-sought solution to energy harvesting *via* autonomous input power-density maximization. The nearly infinite degree of freedom in their agile adaptive locomotion may lead to self-sustained, untethered soft robots[44], capable of real-time learning and performing complex tasks in various environments[45,46] autonomously.

3. Light-driven self-excited oscillation for untethered sustainable robots

3.1. Introduction

Oscillation is a classic mechanical motion used to generate kinetic energy in propulsion and directional locomotion for various applications such as robots, wind-powered drones, sensing, and energy coupling. Current human-made oscillations are typically generated by stimuli variation or intermittent power transmission, such as utilizing AC signals on a piezoelectric transducer. Thus, these systems require a tethered or battery-connected power source and complicated mechanisms. By contrast, living organisms can directly harness energy from a constant ambient environment and produce autonomous oscillations like flapping wings, heartbeats, neuron impulses, circadian clocks, and cell division.[47,48] Biological oscillations are mainly out-of-equilibrium phenomena arising from built-in negative feedback loops, which can interconvert between two or more kinetically stable states. Likewise, if human-made oscillations could be generated using a similar life-like mechanism and powered by constant environmental sources, it would be extremely advantageous for robotics, especially untethered autonomous robots; however, it remains another great challenge. Hence, the above two challenges in realizing environment-dictated movement directionality and generating oscillatory motion from non-oscillatory ambient input make realizing artificial phototaxis prohibitively difficult.

In recent years, several new materials and mechanisms of oscillation have emerged from attempts to create synthetic active systems that can autonomously oscillate under respective constant stimuli. Examples include chemo-mechanical oscillation based on the Belousov-Zhabotinsky reaction and non-redox reaction, chemo-mechano-chemical self-regulation, thermo-mechanical oscillation, humidity-driven mechanical oscillation, and pressure-induced mechanical oscillation. [49–54] Nevertheless, few of these materials and mechanisms could be applied to create autonomous soft robots, due to constraints on their ability to realize remotely and precisely controlled locomotion.

Photonic energy has been utilized due to the synergetic capabilities of wireless signaling, remote powering and directional control. Light-driven oscillators have been realized using the self-shadowing effect of photo-responsive polymers during photo-actuation and demonstrated untethered operation with omni-directional controllability,[5] wide operation bandwidth (1-270 Hz),[55] and great deformation programmability under broad-band optical input (400~2500 nm).[17,56,57]

3.1.1. Challenge 1: Limited DOF with in-air operation

Currently, most of the reported work on photo-actuation under unsteady state is focused on liquid crystalline networks (LCNs), using pre-oriented mesogens to induce significant configuration change associated with the photon-induced phase transition. However, limited by the mesogen alignment prerequisite, the LCN-based oscillators are predominantly shaped into thin films, which suffer from single-direction actuation, low available thickness (20~50 μm) for generating sufficient forces, complicated fabrication with strict requirements, and limited capabilities to operate with a load or in an ambient environment with a high damping coefficient, i.e., in fluids. Moreover, relying on an anisotropic-isotropic phase transition to power macroscopic motion, the current material systems are quite selective in the input photonic energy, which usually bears high requirements in polarization, wavelength, and narrow operation windows.

3.1.2. Challenge 2: High energy input for autonomous soft robots

In terms of the actuation strategy of LCNs, photochemical mechanisms suffer from a specific range of wavelengths and/or polarization, unsuitable for practical ambient energy operation.[58–60] Alternatively, photothermal oscillation are suitable for sunlight application, yet requires high light input (>4 suns). Fundamentally, the input energy is used to photothermally heat the material, to overcome the bending stiffness to activate the bending, and to compensate the energy dissipation from damping, such as viscoelasticity of materials and air resistance. LCNs with densely crosslinked network possess high storage modulus (>100 MPa), lower contraction strain (<5%),

and relatively high nematic-isotropic transition temperature (T_{NI}, >60 ^{o}C), demanding higher energy input to reach the critical temperature and thus a high onset power density to trigger the oscillation (>4 Suns).[59,61]

3.1.3. Challenge 3: Low output power production

There remain insurmountable obstacles to be used as a high-performance and robust actuation strategy. The output power density, a vital metric for flapping performance, of light-driven oscillators (<0.5 W/kg) on the insect scale (10-100 mm) is not sufficiently high to match the flight muscle of insects (>29 W/kg),[62] piezoelectric actuators (>150 W/kg),[63] dielectric elastomer actuators (2-600 W/kg),[64,65] and liquid-amplified zipping actuators (200W/kg).[66] This is considered extremely challenging because leveraging the photomechanical Multiphysics energy transduction to produce a dynamic out-of-equilibrium system requires low bending stiffness to improve angular deflection, which constitutes a contradiction to delivering high output that requires high bending stiffness, corresponding to high modulus and high thickness.[67]

3.2. Proposed method

3.2.1. Omnidirectional oscillation with in-water operation made by photoresponsive hydrogels

We propose a visible light-triggered self-sustained oscillation effect of a hydrogel system to operate under fluids with a high damping coefficient, such as water. We will polymerize hydrogel with chemical homogeneity and construct shape with geometric symmetry, which will overcome the single-direction actuation issue. The newly designed hydrogel pillar is aimed to show arbitrary directional oscillatory motion triggered by the light coming from 3D omnidirectional space, which has a similar working principle of previously reported hydrogel-based SunBOTs. Typically, we utilize a facile one-step synthesis strategy to incorporate the thermally-responsive poly(N-isopropylacrylamide) (PNIPAAm) hydrogel, which undergoes volumetric change as high as 70% at elevated temperatures (~32^{o}C or other tunable transition temperatures), with gold nanoparticles

(AuNPs) embedded as visible light absorbers. We achieve oscillatory behavior by establishing a built-in negative feedback loop through self-shadowing and efficient diffusion/mass transfer. We will also utilize computational analytical modeling, a quantitative model, to study and establish the oscillation dynamics.

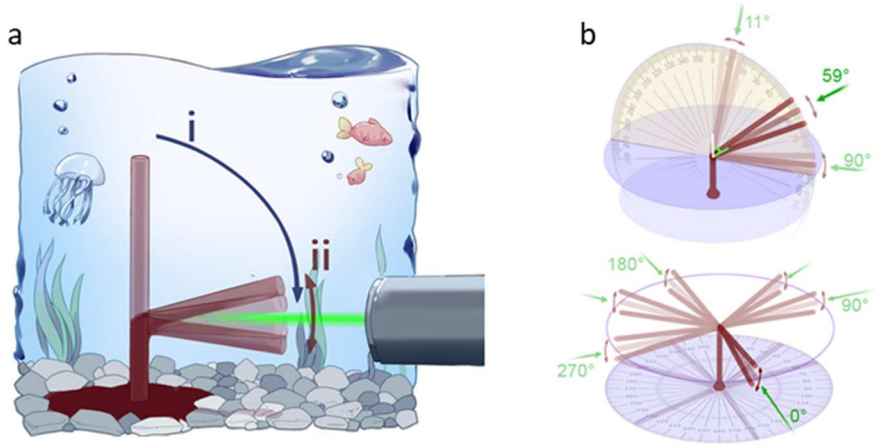

Figure 3.1. (a). Schematic representation of the gel oscillator and the setup. Initially, the gel-made pillar is placed vertically on the ground in water. As the light is switched on, the gel pillar bends toward the light (step i) and then starts the oscillation (step ii). (b) Geometrically symmetric and chemically homogeneous hydrogel pillar is designed to achieve oscillation by arbitrary light coming from upper hemisphere.

3.2.2. Low energy input oscillators by LCE bilayers with programmed thermomechanical properties

We will address the high energy input challenge with a new design of light-driven oscillators and achieve sunlight-powered self-sustained oscillation with diverse autonomous soft robotic behaviors, based on a candle soot-doped LCE/polydimethylsiloxane composite. Specifically, the LCE, synthesized via thiol-ene Michael addition, features low modulus, low response temperature (T_{NI}=40 □), large uniaxial contraction, containing well-dispersed candle soot (CS) as a high-efficiency broad-spectrum photothermal agent. The CS-LCE thin films are 3D printed by direct ink writing (DIW) for the advantages of facile fabrication and the precise control of molecular orientation and geometry. To facilitate high-response out-of-plane bending, we employ a CS-

LCE/PDMS bimorph structure, which boosts the speed and ratio of bending and recovery, critical factors for high-performance oscillation.

Such a design principle will be established with the assistance of theoretical modeling, which elucidates the multiphysics of complex dynamic photo-thermal-mechanical process, and thus guided the system design and the optimization of the key characters, including the oscillation amplification, onset power, frequency, amplitude, and phase angle.

3.2.3. High output power oscillators by the development of responsive materials and structural configuration

In nature, flying insects generate flapping-wing motion based on antagonistic muscle pairs, where the longitudinal and vertical muscles contract and relax (Figure 28a).[47,48] The synergy of the muscle structure and resonant actuation has been proved to amplify the flapping stroke and increase mechanical output power, [68,63] which benefits high-performance actuation.

We resemble the antagonistic muscle structure of insect wings and employ a trilayer construct of a light-driven oscillator to enable a high power density. The trilayer comprises two photo-responsive liquid crystalline elastomers (LCE) layers sandwiching a passive elastic PDMS layer, named flapping LCE-and-PDMS trilayer oscillatory robot (FLaPTOR). The oscillation is produced by opposite-side LCEs being exposed to light alternatively, performing antagonistic contraction and relaxation with anti-phase deformation, resulting in film bending and unbending periodically. These advancements (i) enhance output power density up to 200-fold compared to LCE monolithic oscillator (LMO) and LCE-PDMS bilayer oscillator (LPBO), (ii) exhibit wide light spectrum operation from blue to near-infrared light and using simulated solar light, (ii) permit multifunctionality, such as proprioceptive actuation, energy harvesting, and robotic locomotion. The FLaPTOR possesses both transmission-free configuration and autonomous resonant actuation, enabling a class of simple, high-performance, and multifunctional actuation suitable for future microscale robots.

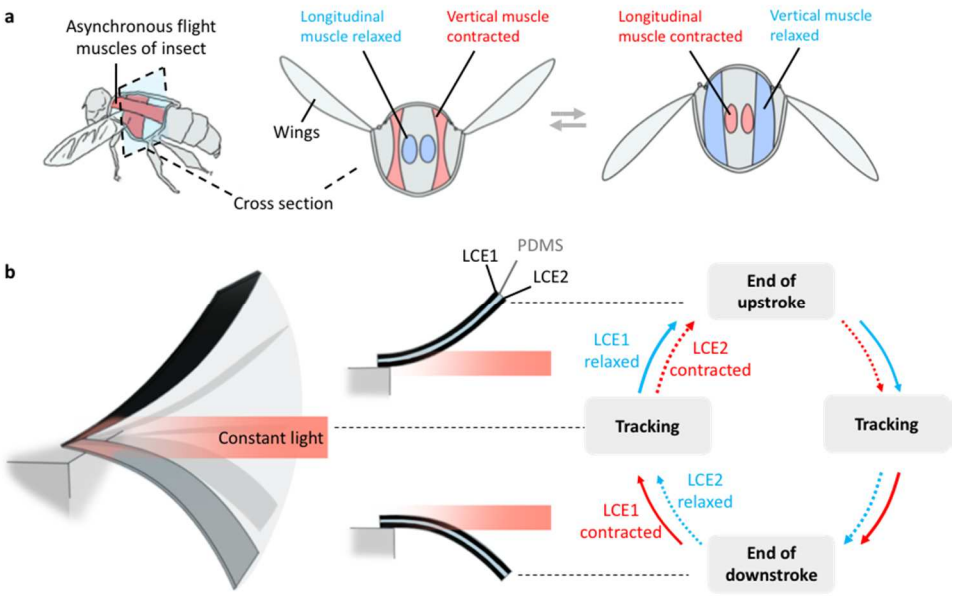

Figure 3.2. Design schematics of flapping LCE and PDMS trilayer oscillating robots (FLaPTOR). a) Illustration of insect's wing stroke using indirect asynchronous muscles. Muscles in the process of contraction and relaxation are shown in red and blue colors, respectively. B) Illustration of the operation mechanism of FLaPTOR. Two photo-responsive LCEs are used to perform antagonistic actuation during self-excited oscillation under constant light input.

3.3. Hydrogel oscillator under water operation with high DOF

3.3.1. Experimental and characterization Section

3.3.1.1. Chemicals and materials

PDMS prepolymer (Sylgard 184 Silicone Elastomer kits) was purchased from Ellsworth. Chloroauric acid, sodium citrate dehydrate, N,N'-Methylenebis(acrylamide) (BIS), dimethyl sulfoxide (DMSO), 3-(Trimethoxysilyl)propyl methacrylate (TMSPMA) and allyl disulfide were purchased from Fisher. 2-Hydroxy-2-methylpropiophenone (Darocur 1173) was purchased from TCI. N-isopropylacrylamide (NIPAAm) was purchased from Sigma Aldrich and recrystallized using n-Hexane. Except for NIPAAm. All chemicals were used as received.

The templates for molding the hydrogel pillars were disposable hypodermic needles purchased from Exel International. The masters of soft swimmer were prepared by 3D printing using Stratasys

3D printer, Objet 24. The Green laser (532nm) was generated by Genesis MX532-1000 STM. The temperature measurement used the K-trype thermocouple coupled with the DC millivolt amplifier and the oscilloscope (Wavesurfer 454, Lecroy). Videos were recorded using a digital camera with a red color filter. The tip displacement and angle were measured by using tracking software.

3.3.1.2. Fabrication of the hydrogel pillars under green light

For the oscillating pillar, the poly(N-isopropylacrylamide) (PNIPAAm) precursor solution was synthesized by mixing 40 wt.% NIPAAm monomer, 1.5 wt.% BIS in DMSO. For the tracking pillar, the concentration of BIS was increased to 2.0 wt.% and 3.0 wt.%, leaving others unchanged. Then, 0.5 wt.% AuNPs, 0.07 vol.% Allyl disulfide and 0.5 vol.% photoinitiators Darocur 1173 were added in PNIPAAm precursor solution, respectively. The prepolymer solution was injected into PDMS mold and covered by TMSPMA-treated cover glass. The UV polymerization was undergone for 80 seconds. Then, the cured AuNP/PNIPAAm pillar gel was carefully squeezed and pulled out from the mold, and immersed in DI water to remove the DMSO residue.

3.3.1.3. Fabrication of the hydrogel pillars operated under white light

The PNIPAAm precursor solution was prepared and injected into PDMS mold, followed by UV polymerization of 40 seconds. Then, the cured PNIPAAm gel was carefully pulled out from the mold and immersed in DI water to remove the DMSO solvent.

Subsequently, to incorporate polyaniline (PANi) into the as-prepared PNIPAm hydrogel, we used the *in-situ* polymerization method. Typically, 182 μL (0.2 M) of aniline monomer was dissolved in 5 mL of a 1M HCl aqueous solution to form Solution A. The PNIPAm hydrogel pillar was placed into the solution A for 2 hours. After the two-hour soaking, 456 mg of ammonium persulfate (APS, 0.2 M) was dissolved in another 5 mL of 1M HCl aqueous solution, to form Solution B. Mix solution B into Solution A under stirring at room temperature for 8 hours to *in-situ* grow polyaniline in the PNIPAm gel. Then, the PANi-embedded PNIPAm gel was taken out of the solution and

rinsed with water to remove excess reactants. The dimension of the PANi-PNIPAm pillar for testing was 29 mm in length and 0.48 mm in diameter.

3.3.1.4. Fabrication of the OsciBot

The OsciBot was made by injecting the prepolymer solution in the PDMS mold, covered with cover glass without treatment. To polymerize the hydrogel homogeneously, the UV light was irradiated from the top and bottom of the PDMS mold for 40 s each.

3.3.1.5. Characterization of hydrogel (de)swelling kinetics

Three different hydrogel pillars of different crosslinker concentrations (1.5 wt.%, 2.0 wt.%, and 3.0 wt.% BIS) were prepared in the PDMS mold, via the same procedure of preparing all hydrogel pillars. Subsequently, a segment from each cured hydrogel pillar was cut into a rod with a diameter of 0.53 mm and length of 0.90 mm. The kinetics of deswelling and swelling were characterized by recording the volume changes of the hydrogel rod during temperature change under an optical microscope (Leica DMI 6000B).

As shown in Figure 3.3, the test of deswelling and swelling rates indicated that the 1.5-wt.% BIS hydrogel shrunk to 33.7±1.7% of its original swollen-state volume when submerged in 45 □ water bath for 30 seconds. By contrast, the 2.5- and 3.0-wt.% BIS hydrogels shrunk to 48.7±4.9% and 62.3%±2.1%.

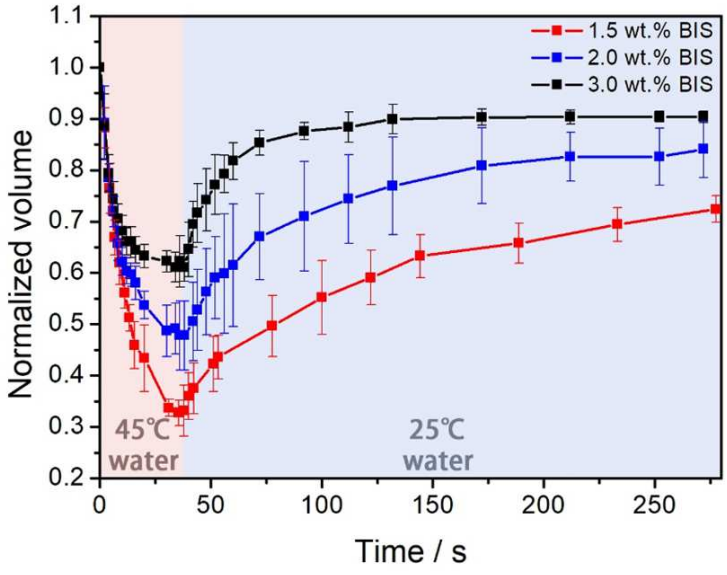

Figure 3.3. Deswelling/swelling kinetics of oscillating hydrogel and tracking hydrogel. Volume changes of reversibly actuating hydrogel disks below/ above the LCST (25 and 45□) are shown with 1.5% wt.% BIS (red square), 2.0 wt.% BIS (blue) and 3.0% wt.% BIS (black square). The AuNP/PNIPAAm composite hydrogel with low crosslinking density possesses a faster deswelling rate and ratio.

3.3.1.6. Characterization of hydrogel microscopic morphologies

The morphologies of the tracking and oscillating hydrogels were observed via Supra 40VP scanning electron microscope. The SEM images used secondary electron mode, with a working distance (WD) of 8.9 mm and Acceleration Voltage of 10.0 kV. As Figure 3.4 shows, the average pore sizes of hydrogels were 4.61 μm, 3.58 μm, and 2.07 μm for 1.5, 2.0, and 3.0 wt.% BIS hydrogels, respectively. Hydrogels with higher crosslinking density had smaller pores.

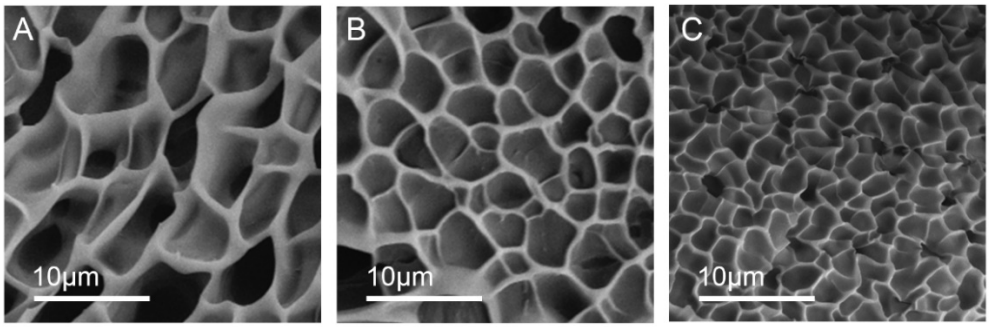

Figure 3.4. Scanning electron microscope images of hydrogels with (a) 1.5 wt.% BIS, (b) 2.0 wt.% BIS, (c) 3.0 wt.% BIS.

3.3.1.7. Characterization of hydrogel mechanical properties

The stress-strain curve of AuNP/PNIPAAm hydrogel was measured using the dynamic mechanical analyzer (DMA, TA Instruments, Q800). Hydrogel samples were cured together with the treated glass slides which acted as the holders at two ends of the hydrogel. As Figure 3.5 shows, the hydrogel with lower crosslinking density (1.5 wt.% BIS, the oscillating hydrogel) has a higher fracture strain of 63% and Young's modulus of 6.3 kPa.

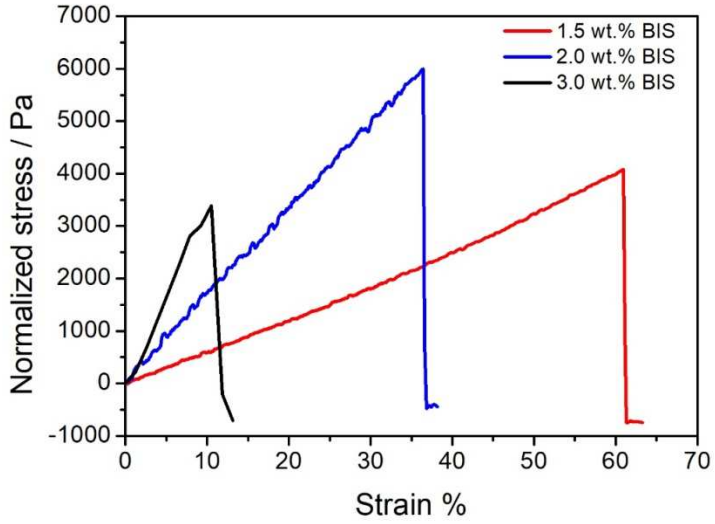

Figure 3.5. The stress-strain curves of hydrogels with different cross-linking densities: 1.5, 2.0, and 3.0 wt.% BIS, respectively.

3.3.2. Time-resolved temperature/ tip displacement of the hydrogel pillar

The temperature was measured by a thermocouple connected to an oscilloscope (wavesurfer 454, Lecroy). The tip of the thermocouple was placed on the hydrogel, as close to the illumination spot as possible. The time-dependent tip displacement and temperature were recorded simultaneously. Pillar dimensions: L=17 mm, d=0.90 mm and input power = 500 mW.

3.3.3. Design principle and operation mechanism of hydrogel oscillation

For the typical oscillation, an AuNP-embedded PNIPAAm (AuNP/PNIPAAm) hydrogel pillar is mounted vertically on the ground of a water bath. Upon exposure to a horizontal green laser (532 nm, input power 175 mW~900 mW, beam diameter = 1 mm), the photonic energy is absorbed and converted into thermal energy. With an appropriate pillar diameter, photo-absorber concentration, and light power, the illuminated site of the pillar (referred to as the "hinge" hereafter) reaches a local temperature above the lower critical solution temperature (LCST) of PNIPAAm (~32□), whereas the back side of the hinge remains at a temperature lower than the LCST. The illuminated side with T > LCST therefore shrinks as a result of the expulsion of water through diffusing out of hydrogel network, whereas the non-illuminated side remains swollen. Such a photo-triggered asymmetric stretching field induces the pillar to bend towards the light source, followed by continuous and stable oscillation.

The mechanism of self-sustained oscillation is rooted in the photothermally-induced self-shadowing effect coupled with the high speed of hydrogel actuation, regulated by a built-in negative feedback loop shown in Figure 3.6. At **State 1**, an arbitrary spot of the pillar is illuminated and heated above the LCST. The front side of the pillar rapidly shrinks due to fast water diffusion, leading to the over-bending (past the equilibrium position determined by the incidence angle) (**State 1- State2**) and thus an initial speed caused by inertia. Then the over-bent tip blocks the light source from illuminating the hinge (in the shade), resulting in a decrease of the hinge temperature. At **State 2**, the tip is at the lowest position with the largest elastic energy and the temperature is at the LCST. The shadowing by the tip then allows for continuous cooling of the hinge below the

LCST, leading to the rapid re-swelling of the gel and pillar unbending (recovery) back to **State 3**, where the hinge is exposed to light again. Since the hinge temperature is still below LCST and there is an upward velocity, the gel keeps recovering until the temperature reaches the LCST (**State 4)**. At **State 4**, the tip is at the highest position, also re-storing the largest elastic energy. With the light exposure on the hinge, the temperature keeps increasing to above the LCST, which bends the tip back down to **State 1** to start the next cycle. Overall, the mechanism of out-of-equilibrium actuation has two folds: during the dynamic light-material interactions, a self-shadowing-enabled negative feedback loop makes the bending pillar inclined to stay aligned with a light source, similar as SunBOT with photo-tracking property; however, meanwhile, the fast and substantial volume change of the photo-responsive hydrogel generates the (un)bending driving force that is large enough to overcome the water damping, breaking the equilibrium and thus presenting an out-of-equilibrium behavior, oscillatory actuation.

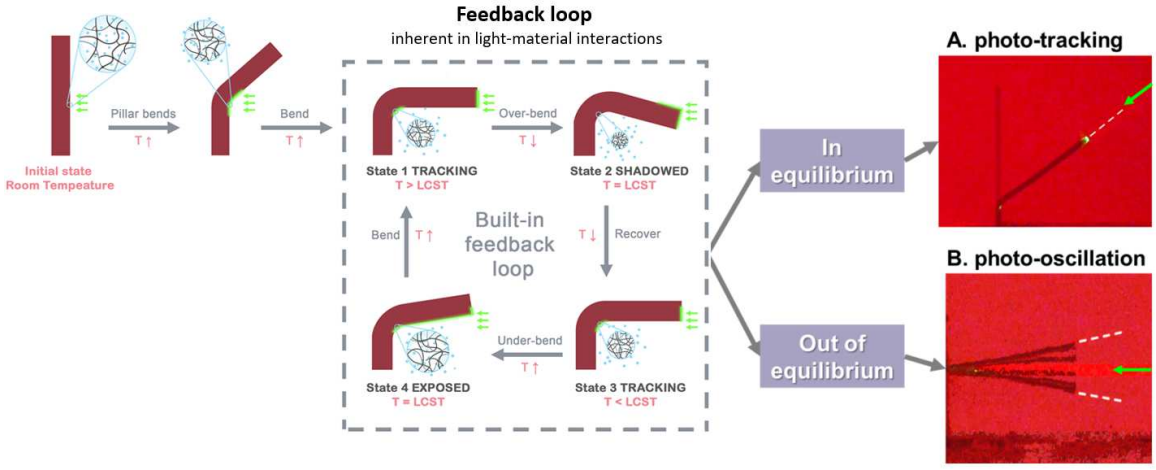

Figure 3.6. Self-shadowing mechanism of light-driven oscillation and tracking of hydrogels.

3.3.3.1. Influence of (un)bending kinetics

To understand the bending and unbending kinetics of the oscillating pillar and tracking pillar, hydrogels with different responsive volume-change rates were prepared by tuning their cross-linking densities (*i.e.*, different water diffusivities and moduli) and tested on their photo-actuation

behaviors. Three pillars with respectively 1.5, 2.0, and 3.0 wt.% BIS cross-linker concentrations were actuated by a 300-mW light. Pillars experienced bending, tracking/oscillation and recovery.

As Figure 3.7 shows, the 1.5 wt.%-BIS hydrogel pillar could bend towards the 90° incident light within 8.7±1.3 s and then started oscillating. By contrast, the 2.0 wt.%- and 3.0 wt.%-BIS pillars bent to 90° more slowly, within 15.7±1.3 s and 56.7±2.9 s respectively and both remained static, aiming at the light in its incident direction. As the light was turned off (t = 60 s), the oscillating pillar abruptly recovered towards the original upright position within the first few seconds, since the initial velocity of the upstroke (unbending) motion promoted the water diffusion into the hydrogel and tip promptly bounced up due to the inertia. The light-tracking pillars, however, swelled progressively back to the vertical state.

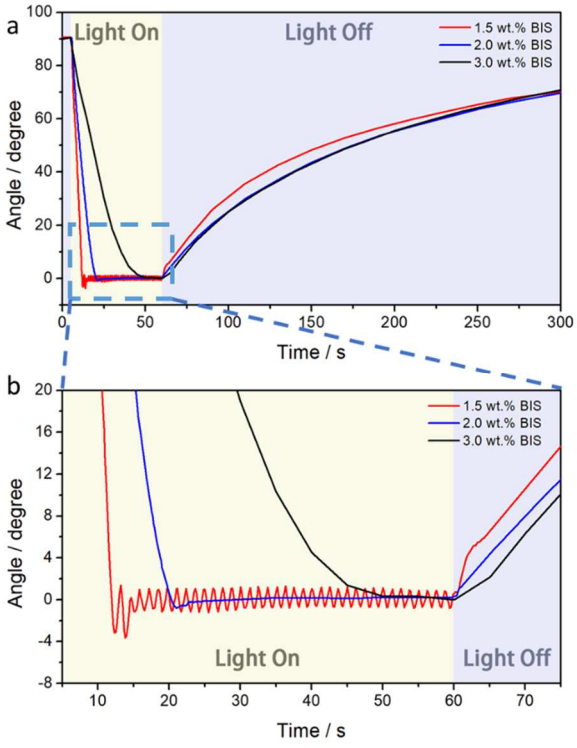

Figure 3.7. Comparisons of the bending and unbending kinetics of oscillating pillar and tracking pillar. The hydrogel pillar with 1.5 wt.%-, 2.0 wt.%- and 3.0 wt.%- BIS could bend towards the 90° incident light within 8.7±1.3 s, 15.7±1.3 s and 56.7±2.9 s, respectively. Only the 1.5 wt.%-BIS sample could oscillate, and 2.0 wt.%-BIS, 3.0 wt.%-BIS samples were tracked the light.

Based on the experimental results above, we have summarized the effect of crosslinking density on materials properties and the boundaries of oscillation and tracking. We found that with a lower crosslinker density, the pore sizes from SEM images were increased, indicating a macroporous structure to enhance the diffusion. Due to the larger pores with lower crosslinker density, we observed that the hydrogels became softer from 27.3 kPa of Young's modulus for 3.0 wt.% BIS to 6.3 kPa for 1.5 wt.% BIS. In the meantime, the elasticity of hydrogels is also enhanced from 12% to 63%. We thereafter found that the volume changes of 1.5 wt.% BIS was 1.84 times greater in comparison to the 3.0 wt.% BIS. The volume shrinkage time scale of 1.5 wt.% BIS was 2.69 times faster than that of 3.0 wt.% BIS. Under the fixed laser intensity, only the 1.5 wt.% BIS hydrogel was capable to oscillate, whereas the other two stayed as tracking. It is worth pointing out that even though the hydrogels with crosslinking density smaller than 1.5 wt.% is expected to have faster response kinetics and magnitude. However, it is experimentally difficult for hydrogels with such small crosslinking density to be cured and come off from the mold. The materials would also be too soft to be able to realize robotic functions or other practical applications.

crosslinking density	**1.5%**	**2%**	**3%**
Pore sizes (μm)	4.61	3.58	2.07
Young's modulus (kPa)	6.3	16.3	27.3
Elongation at break	63%	37%	12%
Deswelled volume/original volume	33.70%	48.70%	62.30%
Volume shrinkage time scale (s)	7.14	9.22	19.2
Tracking time (s)	8.7	15.7	56.7
Oscillation vs. Tracking	Oscillation	Tracking	Tracking

Table. 2. Summary of the effect of crosslinking density on materials properties and oscillation performance.

Based on the materials characterization and oscillation examination, we conclude that the hydrogels with such large pore sizes (>4.5 μm), large volume shrinkage magnitude (<33.7% in 30 seconds),

fast response kinetics (t<7s) can produce the oscillatory motion. Specifically, the loosely cross-linked hydrogel (1.5 wt.% BIS) possesses relatively larger pores, which facilitates fast water diffusion in and out of the hydrogel network, resulting in higher diffusivity (D) and thus rapid volume change. In addition, larger pores also lead to a larger degree of volume change than the dense gel under an identical illumination condition. Hence, given the same deflection angle (90°) of the pillar, the loosely cross-linked hydrogel deforms a smaller amount across its thickness compared to the relatively dense hydrogels. Smaller deformation depth (t) and the higher diffusivity (D) enable a smaller diffusion time scale (t^2/D) required for reaching a certain deflection angle. This ultra-fast deswelling and swelling generate large driving forces for deflection and recovery, respectively, which are sufficient to overcome water damping (*i.e.*, the frictional force from the surroundings) and produces the overshoot of the pillar. This driving force breaks through the equilibrium for the light-tracking state exhibited by the slower-responding gel, facilitates an out-of-equilibrium motion, and also maintains the oscillation.

3.3.4. Oscillation properties study

To describe the fundamental physics of the oscillation, we performed analytical modeling to establish a governing equation. First, to characterize the oscillation frequency, we consider the oscillating pillar as a cantilever beam. Since the hydrogel is submerged in water, the damping due to the water cannot be neglected. The angular frequency of the first bending mode of the damped cantilever beam can be calculated as,

$$\omega_d = \omega_1 \sqrt{1 - \frac{c^2 L^4}{4\rho AEI}} , \qquad (1)$$

where $\omega_1 \approx 3.5\sqrt{EI/\rho AL^4}$ is the angular frequency of the first bending mode without damping, c is the damping coefficient per unit cantilever length, E is the Young's Modulus, I is the area moment of inertia, ρ is the hydrogel density, A is the cross-sectional area of the cantilever and L is

the cantilever length. The oscillation frequency ($f_d = \omega_d / 2\pi$) for a pillar with a circular cross-section of diameter d is then written as,

$$f_d = \frac{3.5}{8\pi}\frac{d}{L^2}\sqrt{\frac{E}{\rho}}\sqrt{1-\frac{64c^2L^4}{\rho E\pi^2 d^6}}, \qquad (2)$$

According to our experimental data, E=6.3 kPa, ρ=10^3 kg/m^3, L≈10 mm, d≈1 mm, and the natural period of the cantilever vibration without damping is $t_1 = 2\pi/\omega_1 \approx 0.29$ s. Solvent diffusion in the hydrogel has a different time scale of t_{diff}=d^2/D, where D is the diffusivity. Based on our measurement D≈10^{-7} m^2/s, the diffusion time scale t_{diff} can be estimated as around 10 s, which is larger than the inertia time scale. Thus, this model has revealed that the oscillation frequency is dominated by inertia, and less influenced by diffusion.

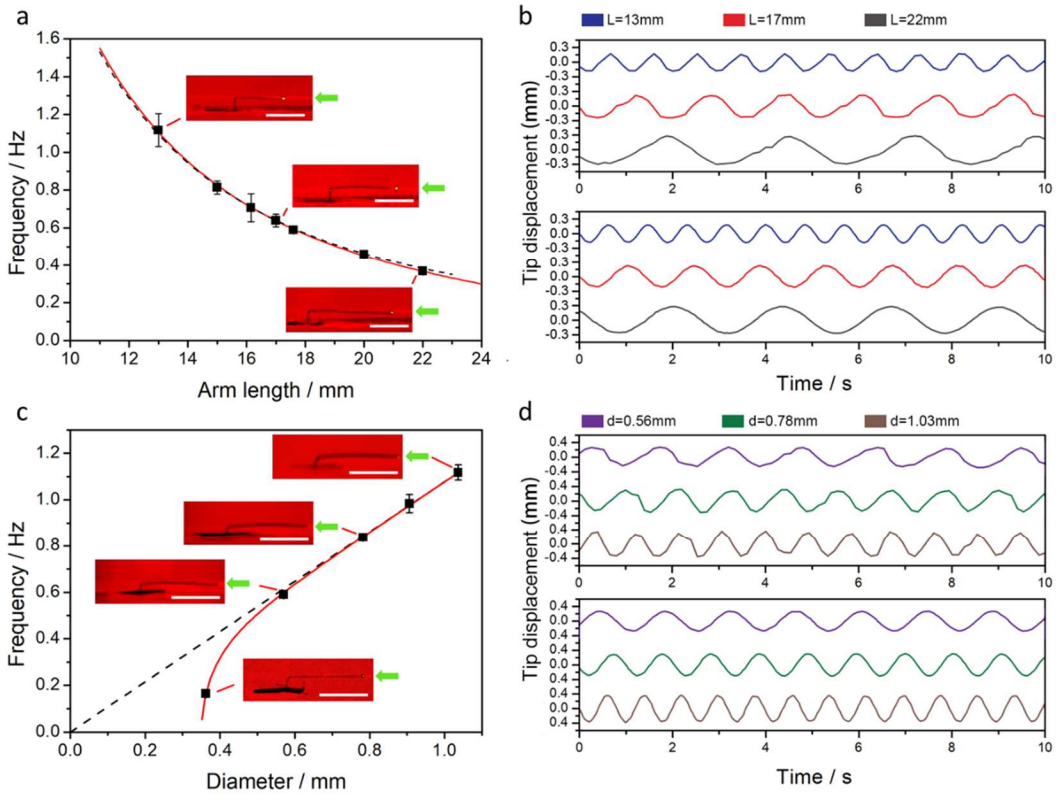

Figure 3.8. The frequency of the oscillator dependent on the geometry. (a) The frequency as a function of arm length. The fitting curve with water damping consideration matches better with the

experimental data (red curve, R^2=0.987) compared with no water damping (black dash curve, R^2=0.983); (b) Comparison of the experimental (upper) and computer simulation (lower) result of the time-resolved tip displacement. The dimensions of pillars: d= 0.56 mm, L = 11 mm (blue), 15 mm (yellow), 22 mm (red). The scale bar in inserts = 1 cm. (c) The frequency as a function of diameter; (d) Comparison of the experimental and theoretical results. The dimensions of pillars: d= 0.56mm (purple), 0.78mm (green), 1.03mm (brown) and L = 17 mm. Input power = 300 mW.

With this model, we further investigate the contributions of inertia and diffusion in oscillation. Figure 3.8 illustrate the theoretically and experimentally measured frequency as a function of arm length and diameter. As the arm length increases, the frequency for an undamped cantilever drops in a scaling of $f_1 = \omega_1 / 2\pi \approx L^{-2}$, as shown by the black dashed curve of Figure 35A. Considering the water damping of the system, the fitting curve of experimental results will be modified to the red solid curve. To explore the diameter effect, pillars with different diameters but the same arm length were fabricated. The frequency-diameter profile is linear when the diameter is relatively large, consistent with the frequency formula in Eq. (2). However, the water-damping term becomes dominant as the diameter decreases, leading to a deviation from the black line. By fitting the experimental results of the frequency vs. diameter plot (Figure 3.8C) and the frequency vs. arm length plot, we obtained the damping coefficient per unit length *c* to be 3.265×10^{-4} and 1.272×10^{-4}, respectively, which validates the formula of the vibration frequency, Eq. (2). Furthermore, the experimentally observed oscillation frequency agreed well with the theoretical prediction, verifying the domination of frequency primarily by inertia rather than diffusion. On the other hand, for the pillar to bend to a large angle such as 90°, the water does not need to diffuse through the entire thickness of the hydrogel, but only through a thin layer on the surface. This is sufficient for the hydrogel to bend to a relatively large angle in an oscillation period. Generally, during the oscillation, the diffusivity and speed of bending determine whether there is oscillation or tracking, while the inertia determines the frequency of the oscillation.

In addition, we numerically solved the dynamic oscillation equation for the damped cantilever beam under constant light illumination. The tip displacement for different values of arm length and diameter are shown in Figure 3.8b and 3d. The simulated and experimental results for variations in both diameter and arm length show very good agreement, with only ~10% mismatch.

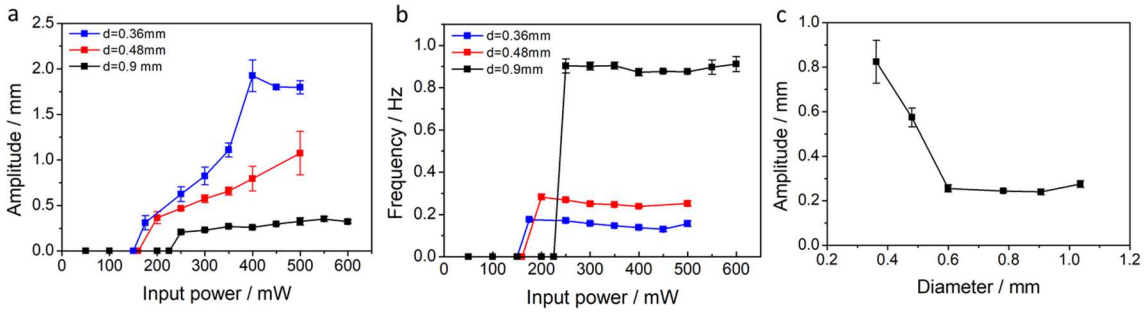

Figure 3.9. Input energy dependency and long-term stability of oscillation. (a, b) Amplitude and frequency as a function of input power. When the input power was higher than the threshold energy, the amplitude increases as input power increases. The frequency, however, was maintained at a relatively same value. Also, the thinner pillar could oscillate with larger amplitude at the same power input. (c) Given the same power input of 300 mW, a thinner pillar oscillated at larger amplitude due to a smaller diffusion time scale t^2/D.

The oscillation performance can also be affected by light intensity. For a hydrogel pillar of a certain response rate/ratio and dimension (L=17 mm, d=0.36 mm~0.9 mm, 1.5 wt.% BIS), an input power lower than a certain threshold (150 mW~225 mW) yielded only light tracking. As the input power increased above the threshold, the vibration was amplified cycle by cycle and eventually reached a stable oscillation. A higher light intensity allowed for a broader temperature fluctuation and thus a larger pillar over-bending angle, leading to a higher oscillation amplitude (Figure 3.9a). Increasing the input power initially induced a slight frequency drop (Figure 3.9b), which may arise from the longer traveling distance required to overcome the water damping and slow down the bending/recovering speed. As the light intensity was increased further, the frequency drop was then compensated by the higher bending speed at a higher light intensity (Figure 3.9b). Therefore, the oscillation frequency of the current system solely depends on the geometry and the mechanical properties of the pillar. Moreover, our study indicates that a lower pillar diameter can initiate a

higher oscillation amplitude at a given input power (Figure 3.9c). The higher amplitude for thinner pillars is due to the smaller t_{diff} for a thin pillar, which results in considerable bending kinetics and magnitudes.

3.3.5. Optimal operation conditions of oscillation

The diameter, arm length, and photo-absorption are the key parameters that affect the range of operation input power. We have conducted an experiment using a series of light intensities on hydrogel pillars of different arm lengths, diameters, and photo-absorber concentrations. Below we summarized their effects and identified the optimal operation conditions of oscillation.

First, we define the range of operational input power for clarification. For photo-induced oscillation, there exists a threshold intensity beyond which the self-sustained oscillation occurs. The threshold intensity determines the lower limit of the operation window of oscillation. Below the threshold intensity of oscillation, there is a range of intensity where the pillar can steadily track the laser direction, as shown in the yellow regime in Figure 3.10. When the laser intensity is overly low, the energy is not sufficient to induce tracking or oscillation, as shown in the grey regime in Figure 3.10. By contrast, if the light intensity is overly high, we observed unstable oscillation with chaotic behavior, as shown in the red regime in Figure 3.10. This implies the deviation of oscillation from the steady position is amplified and the pillar tip may not perfectly shadow the hinge if any lateral fluctuation happens. Here, the unstable intensity determines the upper limit of the operation window. Thus, we determine the range of operation input power between the threshold intensity of oscillation and unstable intensity, as shown in the blue regime in Figure 3.10.

To investigate the effects of the key parameters on the operation input condition, we first fixed the diameter of the pillar as 0.9 mm and changed the *arm length* from 17.7 mm to 10.6 mm, equivalent to the aspect ratio changing from 20 to 11.8. With a higher aspect ratio, the threshold intensity was gradually reduced, especially to 122 mW for the aspect ratio of 20. In the meantime, the unstable intensity was also reduced. It is noteworthy that when the aspect ratio was decreased to 10.6, no

oscillation was observed even if the highest laser intensity was applied. This may be because the oscillation can be generated only if the pillar has a sufficiently high aspect ratio to provide inertia.

Second, we examined the correlation between the operation condition and *arm diameter* (pillar thickness). As expected, with a smaller diameter of pillar, a lower threshold intensity was needed to realize oscillation, due to the lower t_{diff}. Also, for the thin pillar, the unstable intensity was also lower. Beyond the unstable intensity, we observed that the pillar started to oscillate irregularly, with more random and chaotic motion. This implies that when the diameter is smaller, the water-damping part becomes more significant. And such a thin pillar could induce a larger actuation magnitude, indicating a larger amplitude. As both the driving force and resistance increase, the deviation of oscillation from the steady position is amplified, resulting in more unstable oscillation.

Third, we investigated the correlation between operation condition and photo-absorber (AuNPs) concentration. As expected, a higher concentration of AuNP had lower threshold intensity, due to the stronger photothermal effect. On one hand, it is interesting to point out that the absorber concentration (0.5 mg/mL) with 10 times diluter than current recipe (5 mg/mL) could still provide sufficient photothermal efficiency to initiate the oscillation, indicating the robustness of our oscillation system. On the other hand, an absorber concentration higher than 5 mg/mL would cause increased aggregation and undesirable segregation of AuNP during the centrifuge and hydrogel photo-curing process. Without such a technical limit in the fabrication process or with photo-absorbers of higher photothermal efficiency, a higher light absorption effect together with lower threshold intensity to start oscillation could be expected.

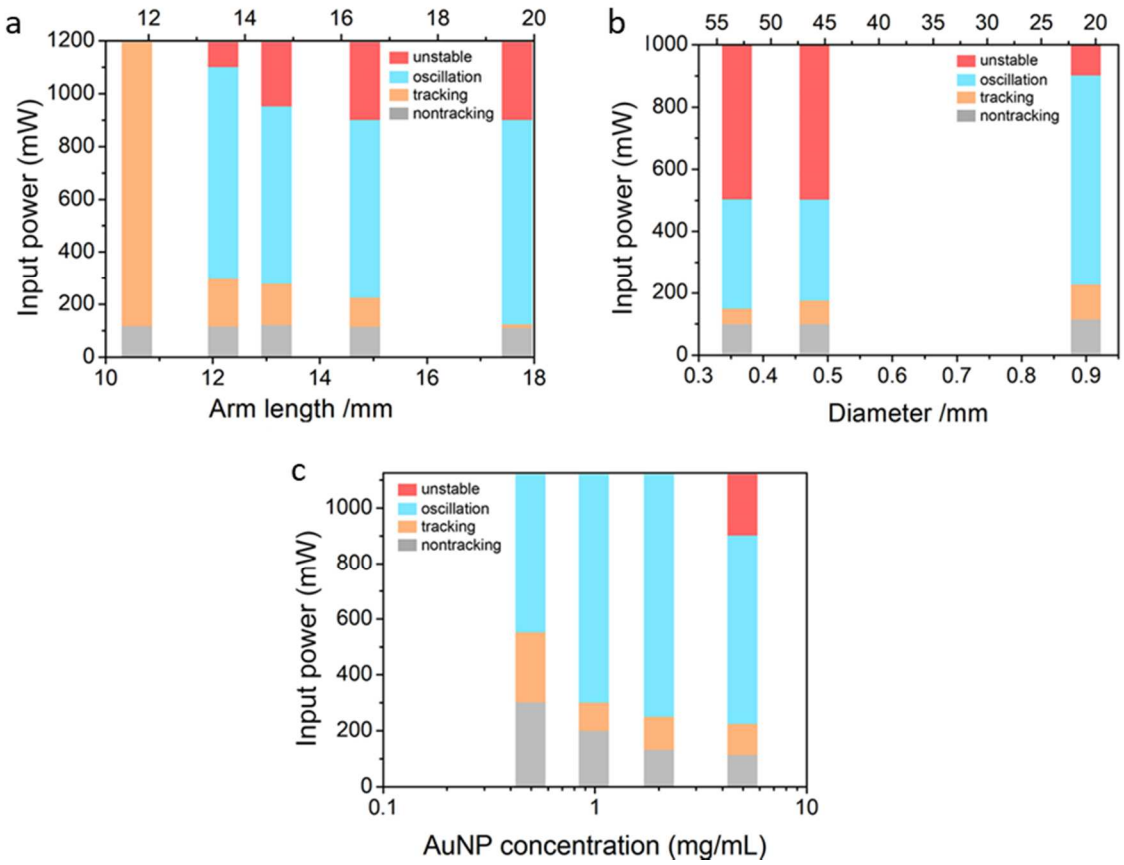

Figure 3.10. Range of operation input correlated to (a) arm length, (b) diameter and (c) AuNP *photo-absorber* concentration. The grey, yellow, blue and red regimes stand for non-tracking, tracking but oscillation, oscillation and unstable oscillation, respectively.

3.3.6. Omnidirectional oscillation

To date, most soft actuators and oscillators can achieve only single-directional motion, limiting the degrees of freedom (DOF) in robotic motion. To realize an omnidirectional response to stimuli coming from arbitrary zenith angles and azimuthal angles, a chemically homogeneous and geometrically symmetric hydrogel pillar was designed. For an originally upright pillar (d=0.9 mm), the 500mW light approached from different oblique angles. We found that an oscillation could be generated with any deflection angle in the range of 59°~90° (Figure 3.11**a**) with approximately the same frequency (Figure 3.11**b**). At this particular light power and pillar diameter, an angle smaller than 59° resulted in light tracking. To achieve the oscillation at a smaller deflection angle, one approach is to increase the power density of incident light, which increases the driving force as a

result. Alternatively, when the pillar diameter was reduced to 0.36 mm, oscillation was realized for deflection angles as small as 8° (Figure 3.11**a**).

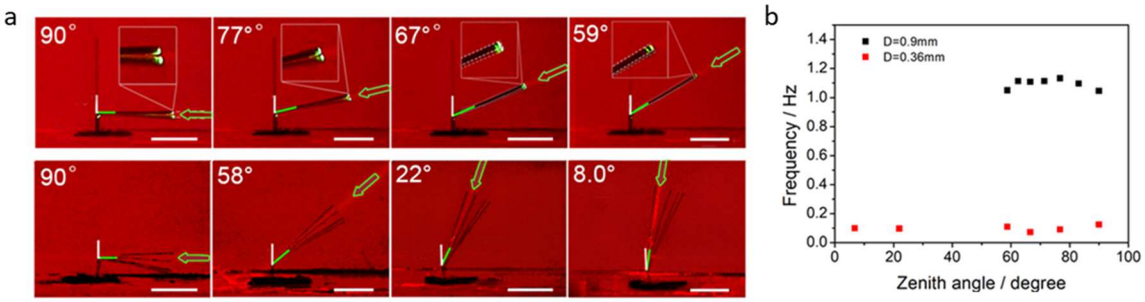

Figure 3.11. Oscillation in response to different zenith angles. (a) Zenith angle test for a pillar with a diameter of 0.9 mm. Under the exposure of 500 mW of light, the oscillation could be initialized ranging from 90° to 59°. Deflection angle ≤ 56° resulted in tracking. As the diameter was reduced to 0.36 mm, the oscillation with 90° to 0° deflection angle and a large oscillation amplitude have been observed. Each frame represents 1.3s for all four different angles. (b)The frequency dependence of oscillation at different zenith angles

Moreover, we showcased the hydrogel oscillation in response to multiple azimuthal angles (Figure 3.12**a**). The light coming from four different angles covering the entire horizontal plane could all initiate oscillation with the same frequency (Figure 3.12**b**). The oscillation frequency under various zenith angles and azimuthal angles is governed by the frequency formula eqn (1), which is close to the natural frequency of the oscillator. At this stage, we have achieved omnidirectional oscillation at arbitrary zenith and azimuthal angles, exhibiting photo-induced kinetic energy generation in the entire 3D space.

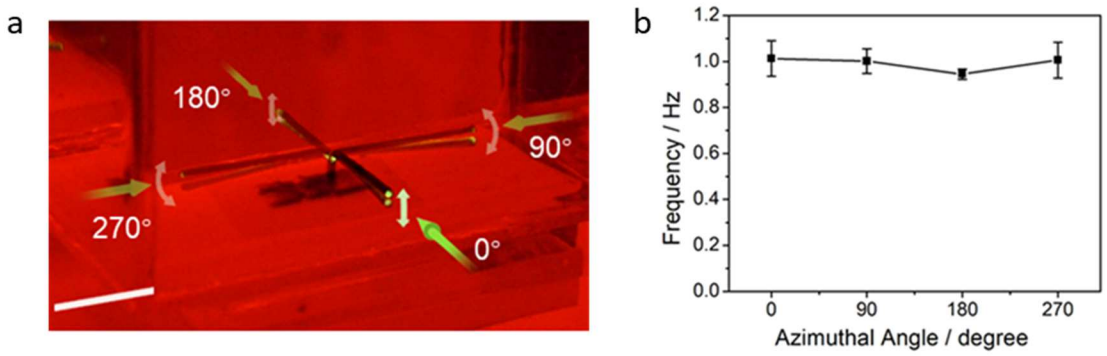

Figure 3.12. Oscillation in response to different azimuthal angles. a) The superimposed snapshots of a pillar in response to the different azimuthal angles of light. b) The frequency dependence of oscillation at different azimuthal angles.

3.3.7. Long-term stability of oscillation

Figure 3.13 demonstrates the long-term stability of the AuNPs-PNIPAm hydrogel oscillation under prolonged green light exposure. We monitored the motion of the hydrogel oscillator over 3600 s of continuous illumination. It displayed highly stable and relentless long-lasting motion with nearly no noticeable fluctuation. Being continuously fueled by light in a stable environment, the hydrogel pillar is anticipated to oscillate perpetually.

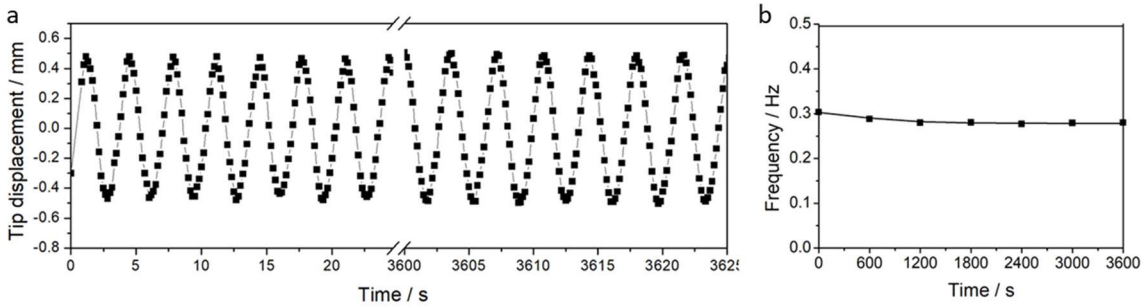

Figure 3.13. long-term stability of oscillation. (a) Tip displacement and (b) frequency upon irradiation of 200 mW over a long period time. The dimensions of the pillar: are L=22 mm, d=0.56 mm. Once reaching steady oscillation, the long-lasting oscillation could be maintained stably over a long period with little frequency and amplitude fluctuation.

3.3.8. Phototactic robot based on the hydrogel oscillator

Phototaxis is a spontaneous and directional movement towards or away from light. It has been observed in many living organisms, such as Platynereis dumerilii, jellyfish, and insects for navigation and photosynthesis. Such stimuli-dictated and environment-powered directional locomotions, if realized with human-made robots, would open new avenues for fully autonomous remotely-steered robots. However, artificial phototaxis, the locomotion following illumination direction, has never been realized, despite considerable efforts on photo-actuation which are typically non-directional (nastic movement). Biological phototaxis is typically realized by helical swimming or oscillatory propulsion.

With the powerful hydrogel oscillator, we successfully created an all-soft phototaxis swimming robot, the OsciBot, capable of propulsion-based high-speed locomotion (Figure 3.14**a**). It is worth pointing out that although there are a couple of propelling robots based on temperature-responsive hydrogels, they mainly rely on alternating stimuli to achieve motion. However, we can convert the constant energy input into a periodically moving unit in the quest to generate energy-efficient and robust 'robotic materials. Our swimming robot is made entirely of the same hydrogel material; the design includes a long hydrogel strip, serving as the paddle, attached perpendicular to a planar hydrogel sheet. As Figure 3.14**b** shows, the robot can float on water due to surface tension on the hydrogel sheet, despite the slightly higher density of hydrogel than that of water. The strip of OsciBot serves as an active flipper to kick water backward and generate propulsion, providing the force to swim away from the light source. When shining light on the arbitrary position of the flipper, it immediately bent upwards followed by continuous oscillating, and propelled the OsciBot to move away from light precisely following the illumination direction.

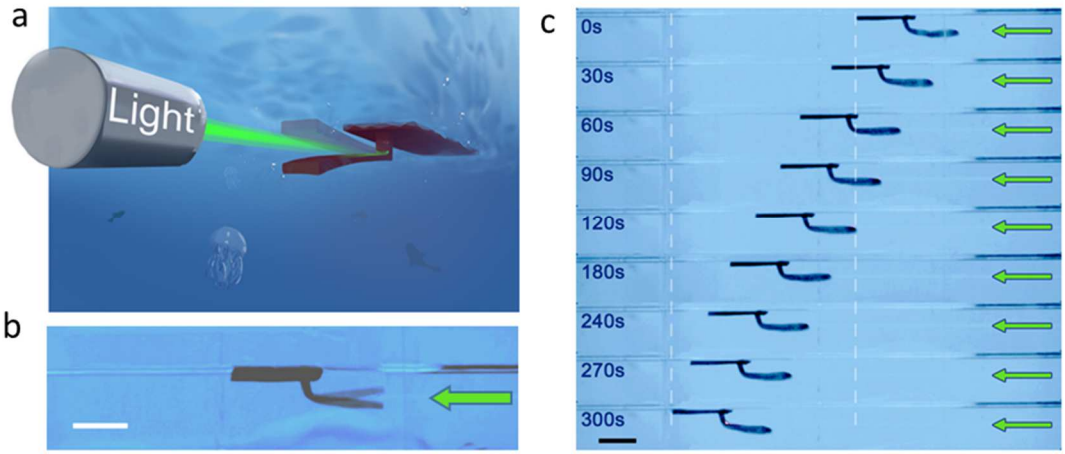

Figure 3.14. Self-sustained oscillator-based soft swimming robot (OsciBot) powered and controlled by visible light. (a) The scheme of the soft swimmer and (b) the real oscillation in water. The green arrows denote the light direction. (c) Sequential snapshots of swimmer shining the constant light. The input power was 450 mW.

Figure 3.14**c** depicts OsciBot's movement fueled and controlled by light. The maximum measured swimming speed was 18.3 mm/min, equivalent to 1.15 body lengths/min, which outperforms previous photo-responsive soft robots inspired by cilia and flagellum with swimming speeds of 0.08 body lengths/min and 0.32 body lengths/min, respectively.

We have further investigated the robotic performance quantitatively and found that the oscillating parameters including the frequency, the amplitude, and the tip velocity or the thrust all affect the swimming velocity. From the different oscillation amplitudes of the same Oscibot with a fixed thickness and aspect ratio of the arm, we observed that the Oscibot swam faster with a larger oscillation amplitude in a linear fashion (Figure 3.15**a**), since the strip propelled more water backward during one cycle. The larger amplitude also indicates a longer distance for the stripped tip to travel, leading to a slight frequency drop, consistent with our experimental observation in Figure 3.15**b**. Thus, the swimming velocity inversely correlates with the oscillation frequency. Furthermore, we established the correlation of the swimming velocity of the Oscibot and the velocity of strip tip displacement. With the strip beating faster, the thrust of the cantilever is

calculated to increase in a quadratic law. Experimentally, such faster beating resulted in higher swimming velocity. Therefore, a larger thrust leads to a higher swimming velocity of the Oscibot. By further increasing the light intensity, improving the light absorption efficiency, and rationally optimizing the geometry of the paddle, as well as the substrate, the swimming performance can be further enhanced. In addition, potentially the speed could also be tuned with the fluid properties and flow structure. For instance, a symmetric, reciprocal oscillation is likely to generate directional movement more efficiently in a non-Newtonian fluid of a low Reynolds number, where the net propulsion is caused by the differential apparent fluid viscosity under asymmetric shearing conditions.

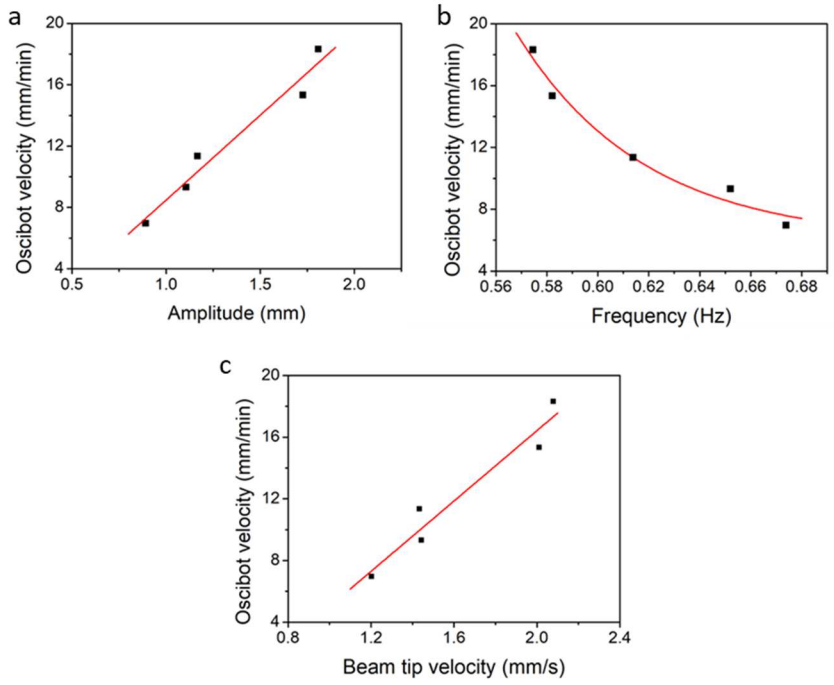

Figure 3.15. The effects of oscillation parameters on swimming performance of the Oscibot. The Oscibot velocity is the function of (a) the amplitude, (b) the frequency, and (c) the beam tip velocity of the oscillation.

To demonstrate the controllability and flexibility of the light-induced motion, we examined the swimming behavior by intermittently switching the light on and off (Figure 3.16). The swimming

robot moved forward at constant speed while the light was on. In the absence of the light, it instantly slowed down and rapidly stopped. Another remarkable point is to determine the dependency of the Oscibot's motion on the upstroke and downstroke during a single cycle. As illustrated by the inset in Figure 3.16**,** the robot swam forward quickly during every upstroke (deswelling) and moved slowly during every downstroke (recovery, reswelling), exhibiting a stepwise motion. This suggests that the beating-flipper system features a small reciprocating motion effect.

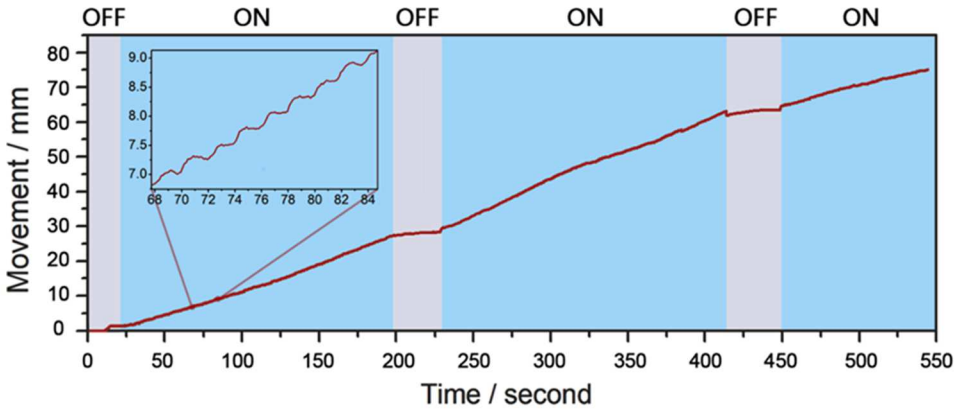

Figure 3.16. On/off control of the soft swimmer. As the light was switched on, the swimmer keeps moving forward. Once the light was switched off, the swimmer stopped in response. During every cycle of the oscillation, mainly the downward stroke (via deswelling) pushed the swimmer forward, resulting in step-by-step movement over time.

From the preliminary test, we have realized the directional control of the swimming robot guided by light. Particularly, we designed the container into a V-shape with an angle. The entire Oscibot was made of the same hydrogel including the strip and substrate. The substrate floated on the water due to surface tension. Guided by light, the Oscibot swam along the long axis of the container as shown in Figure 3.17, 1-4. As the Oscibot swam to the corner, the light direction changed to allow the Oscibot to steer its body and turn left (Figure 3.17, 5-8), to continue swimming to another end of the container.

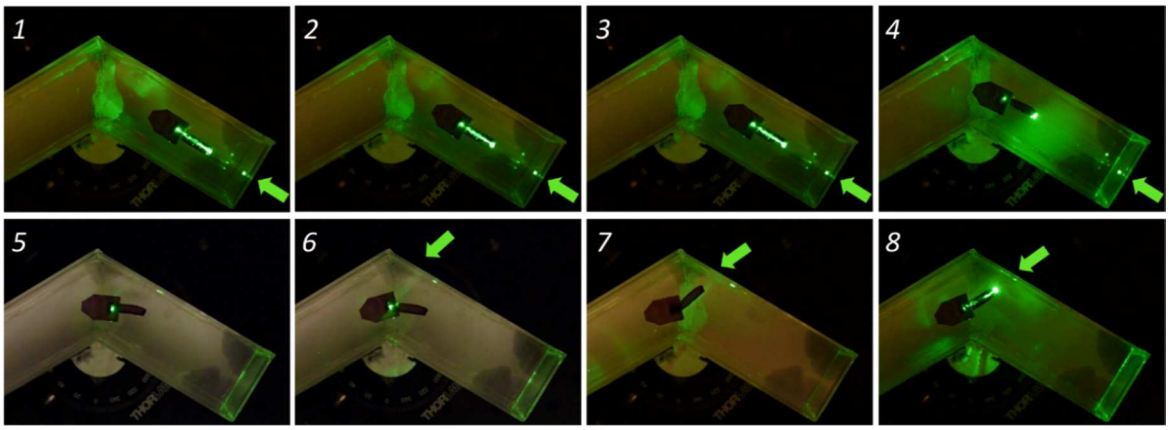

Figure 3.17. Maneuverability of the Oscibot.

3.3.9. Discussion

In terms of materials design, this particular photo-oscillation is achieved by combining photo-absorbers of high photothermal efficiency with fast and reversible thermally-responsive hydrogels. The modular design of responsive materials allows the oscillator platform to be customized and expanded by incorporating a variety of absorbers and stimuli-responsive soft materials that transduce many continuous input stimuli such as light, pH, (electro)magnetic fields, electric fields, and microwaves into kinetic energy, in the form of the oscillatory movements and resulting directional locomotion. In addition, the homogeneous featureless structure of the oscillator makes it convenient to be fabricated by additive manufacturing. It can be easily scaled down as a micromachine, or scaled up and integrated as an active element into large autonomic systems to meet the requirements of different environments. The untethered, environmentally-energy-powered robots can perform solar-powered water sampling for oceanographic applications.

In terms of robotic motions, the oscillation frequency and amplitude can be tuned by the gel geometry and dimensions and light intensity, as well as captured by our established governing equation. With our predictive analytical model, a broad range of oscillatory behaviors can be achieved by tuning or optimizing the oscillator design, oscillation mechanics, and ambient conditions to meet different users' demands. The self-sustained oscillation provides a versatile

capability that can be used in autonomous soft robots such as submerged swimmers with cilia-like motion and transporting devices. It also can be scaled up or integrated into large marine vehicles as the active component. Such a self-sustained, tightly controlled, synthetic oscillatory material system may lead to advances in developing robotic counterparts of natural systems. For example, this system can be potentially used for maintaining homeostatic control and generating autonomous oscillations for biomedicine and surgical applications.

3.4. Sunlight-powered self-sustained oscillators for self-sustainable autonomous soft robotics

3.4.1. Experimental and characterization Section

3.4.1.1. Candle soot

Candle soot (CS) was deposited by placing an aluminum foil above the flame. Then, CS particles were collected and soaked in hexane. CS was used after the removal of hexane solvent.

3.4.1.2. PDMS and silane containing double bonds

PDMS was made by mixing 1:5 of precursor solution (Sylgard 184 silicone elastomer), degassed under vacuum, spin-coated on a clean glass slide with 2min and different speeds. Samples were subsequently placed on a hot plate at 80 □ for 1.5 h and then transferred in a 50 □ oven overnight. Then the film was treated with oxygen plasma for 5 min, and placed under vacuum with TMSPMA vapor for 2h to grow a thin layer of silane with double bonds.

3.4.1.3. LCE printing

LCE was made by thiol-ene click reaction, which was reported previously.[69] Typically, 0.857g RM82, 0.25g RM257 were preheated to melt, and then 0.387g EDDET, 0.056g TATATO, 0.024g BHT, 0.03g I-369, and 0.008g CS were added in the solution and mixed for 10minutes. The CS was dispersed under a probe sonication (20% of 500W, 1s on and 1s off) for 1.5min. Then 25μl TEA was added in the solution with a well mixture. The ink was cured in a syringe at 65□ for 3h to form oligomerized ink. We used a DIW printer (Cellink, BIO-X) to print LCE directly on PDMS. This process helped LCE conform to the PDMS surface and successfully yielded prescribed alignment with low thickness (t<100um). The printing speed was 7mm/s, the distance between the print head and substrate was 0.1mm, and the extrusion was based on pneumatic pressure of 700kPa. The printing pattern was a 3mmx25mm thin strip. After printing, the sample was UV polymerized under UV light for 5min on two sides to fix the orientation. The LCE/PDMS film was peeled by a

razor and used as a single oscillating cantilever or as a hinge material. For butterfly wings, we used a laser cutter to obtain identical wing shapes.

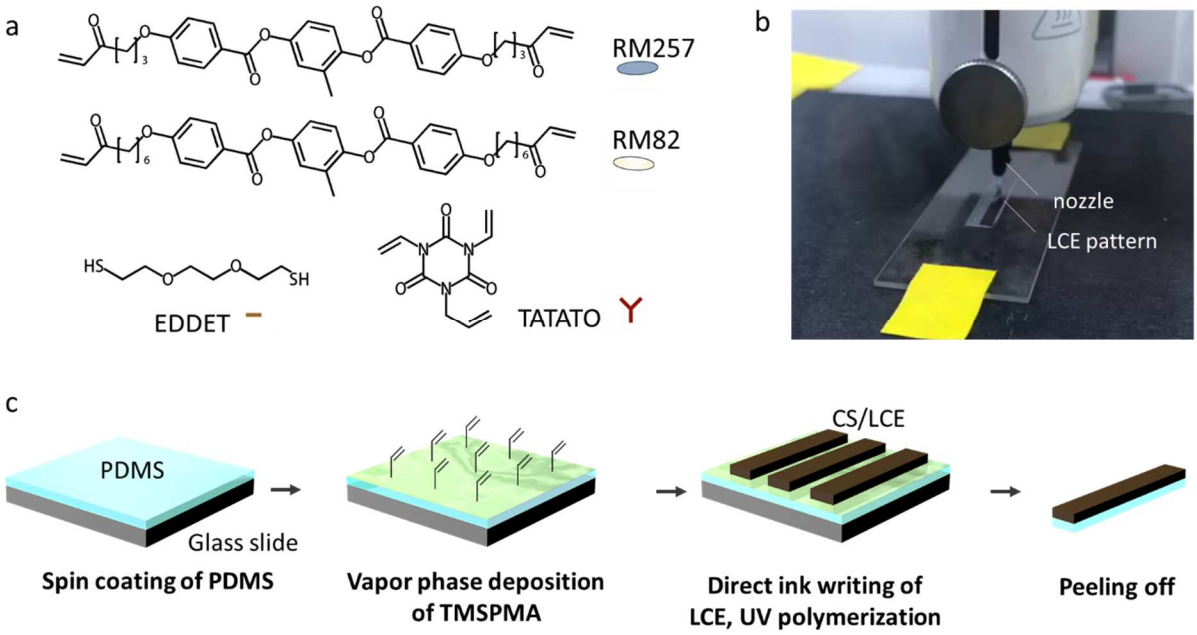

Figure 3.18. Synthesis flow of LCE and CS/LCE/PDMS bilayer. (a) chemical structure of precursors of LCE, (b) photographs of DIW printing setup, (c) Fabrication flow of bilayer.

3.4.1.4. SEM characterization

Cross-sectional images of CLP film were taken by a ZEISS Supra 40VP SEM.

3.4.1.5. Differential scanning calorimetry

Differential scanning calorimetry (DSC-Q8000) was used to measure the cold crystallization temperature (T_{cc}) and nematic-to-isotropic transition temperature (T_{NI}) of LCE liquid ink. Samples with 11mg weight were heated to 100□ to remove thermal history and cooled to -30□. Data was collected by reheating the sample from -30□ to 100□ at a ramp rate of 10□/min.

3.4.1.6. Dynamic mechanical analyzer

Storage modulus and loss modulus were measured by a dynamic mechanical analyzer (TA instruments, DMA850) using an oscillatory temperature ramp mode. The temperature was heated

at a ramp rate of 5□/min and the sweep frequency was set to 1Hz. Data was collected at room temperature to 95□.

3.4.1.7. Optical and photothermal properties

Absorbance spectrums of CLP films were measured by UV-vis-NIR spectroscopy (Shimazu, UV-3101PC). Temperature changes upon NIR laser were measured by placing a thermocouple on the surface of a CLP film.

3.4.1.8. Thermal actuation

Linear contraction and bending in response to heat were carried out by placing the samples (CS/LCE film for contraction and CLP film for bending) on a hot plate and waiting for the actuation to an equilibrium state. The actuation ratio was recorded by an Apple iPhone X and analyzed using PowerPoint.

3.4.1.9. Oscillation performance

Light-driven oscillation was accomplished by hanging samples on a 3D-printed holder and application of light from a horizontal direction. NIR light was provided by an Infrared laser pointer (SKY, 808nm, 1500mW). The intensity of NIR light was controlled by a DC power supply and calibrated by a silicon-based standard photodiode sensor (Thorlabs, PM16-121) with a reflective ND filter (Thorlabs, ND10A). Movies of oscillation were recorded by an Apple iPhone X and a digital camera. All trajectories were analyzed by the software Tracker (version 5.0.5). For the frequency of synchronized butterfly demonstrations, we used Excel to carry out FFT analysis.

3.4.2. Design principle of light-driven self-oscillation with low energy input

In terms of the bending mechanisms of light-driven actuators, three architectures have been widely adopted, namely multilayer,[58] monolith with built-in gradient,[59] and monolith with non-homogeneous light exposure.[55] Among them, we have designed a low-intensity, LCE/elastomer bilayer oscillator “LiLBot” comprising two materials with distinct deformation behavior that

provides a high strain mismatch (Figure 3.19), for higher bending moment and greater design freedom compared to the monolithic layer designs. An elastomer-based passive layer, PDMS, can store elastic energy upon light-triggered shrinkage of the photothermally active layer, which provides an elastic restoration force for the bilayer film to unbend rapidly during the thermal-mechanical relaxation. The photothermal conversion, elastic modulus, viscoelasticity, and thermal conduction of each individual layer can be rationally programmed and broadly tuned; this broad-range tunability is crucial for realizing oscillation under low input energy.[70]

The oscillation was produced by a self-shadowing effect during photo-thermal-mechanical actuation and self-regulated by the resulting built-in negative feedback loop (Figure 3.19). In detail, upon light illumination on the LCE side, LiLBot is locally heated and bends towards the light due to strain mismatch between LCE and passive layer. Then, the tip bends over the incident direction of incoming light and self-blocks the light from shining on the LiLBot. Upon shadowing, the local temperature decreases, and subsequently the LiLBot unbends rapidly, facilitated by the elastic recovery of the passive layer. Such a shape recovery leads to light exposure again, which induces re-bending, the next cycle of the oscillatory motion around the optical beam. However, as observed previously, self-shadowing may also result in static tracking of light (in-equilibrium state) rather than a dynamic, oscillatory state (out-of-equilibrium state). To identify the governing factors in the complex light-material interaction that involves dynamic photo-thermal-mechanical transductions and to identify the condition that enables oscillation upon low input, we have developed a theoretical model. Based on the guiding principle discussed below, we successfully reduced the oscillation onset power close to sunlight for potential self-sustainable robots, which has not been realized nor systematically investigated previously.

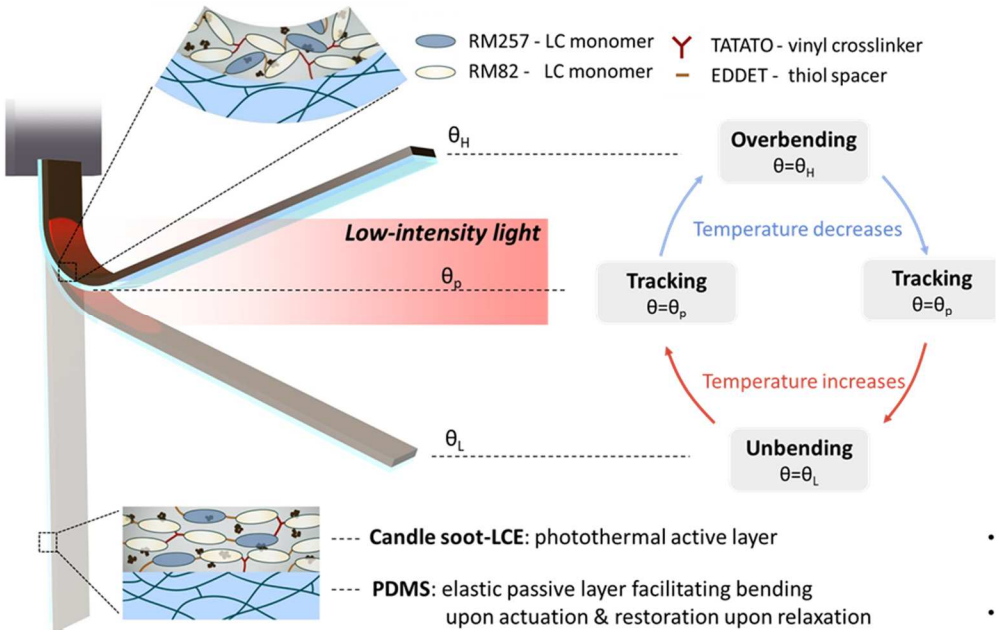

Figure 3.19. Design principle of LiLBot. Schematic of a LiLBot flapping around the incident low-intensity optical beam, presenting a dynamic out-of-equilibrium motion.

The actuation system is modulated by the coupling of i) mechanical equilibrium and ii) thermal equilibrium. Mechanical equilibrium examines the thermomechanical bending capability when the bilayer is heated, without considering the self-shadowing effect. Higher temperature T on the exposure spot leads to a higher bending angle θ, and the temperature-angle (T-θ) profile is determined by the mechanical modulus, damping factor, and thermomechanical response of LCE. For thermal equilibrium, we specifically consider how self-shadowing affects heating on the exposure spot at a given power density. At a high bending angle θ, the tip blocks the light, and equilibrium T will be reduced. The shape of T-θ profile of thermal equilibrium is determined by geometry, the input power density of light, photothermal conversion efficiency, and thermal diffusion of the bilayer.

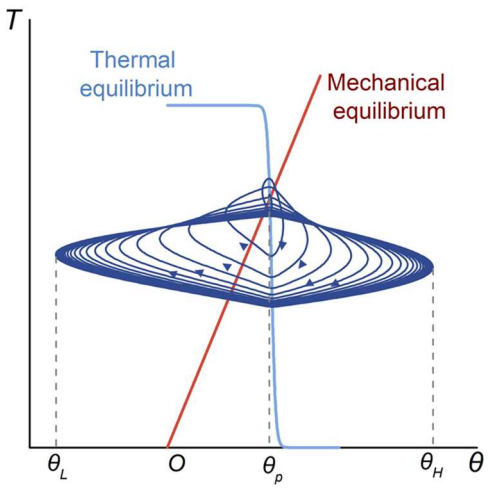

Figure 3.20. The temperature-angle profile of the photo-thermal-mechanical oscillation during an initialization process. The navy-blue curve is time-resolved plotting from perturbation to steady oscillation, produced by simulation. The red curve shows thermomechanical bending (angle θ) of LiLBot as temperature (T) increases and the blue curve shows photothermal self-shadowing effect which leads to temperature drop at higher bending angle.

Due to the different shapes of *T*-θ profile of the two equilibriums, the system tends to dynamically evolute over time. As shown in Figure 3.20, the transition from light-tracking motion to oscillation is governed by comparing the local derivatives of two equilibriums:

$$\text{Tracking (stable):} \quad \beta \left.\frac{\mathrm{d}T_m}{\mathrm{d}\theta}\right|_{\theta=\theta_p} \geqslant -\left.\frac{\mathrm{d}T_t}{\mathrm{d}\theta}\right|_{\theta=\theta_p}$$

$$\text{Oscillation (unstable):} \quad \beta \left.\frac{\mathrm{d}T_m}{\mathrm{d}\theta}\right|_{\theta=\theta_p} < -\left.\frac{\mathrm{d}T_t}{\mathrm{d}\theta}\right|_{\theta=\theta_p}$$

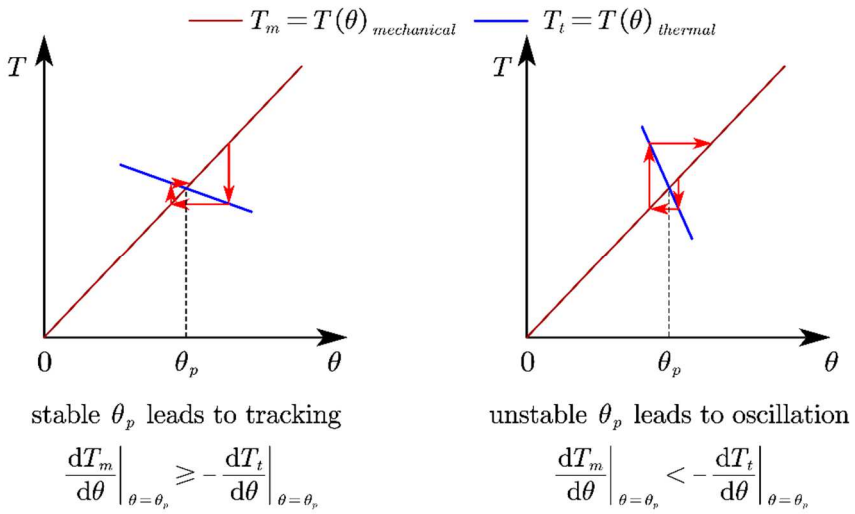

Figure 3.21. Angle-temperature profile of tracking and oscillation scenario

The necessary condition for generating oscillation can be further expressed as:

$$\frac{\beta k}{k_m} \leq \frac{k_p P_{in}}{k_d \theta_0}$$

, where T_m and T_t are temperature elevations compared to the environment at, respectively, mechanical and thermal equilibrium; θ is the instant angle, β is a system damping factor, k_p is photothermal conversion efficiency, P_{in} is input light power, k_d is the thermal diffusion coefficient, k_m is moment coefficient, θ_0 is the incident light angle, and k is the stiffness of the oscillator.

From the mechanical equilibrium, a smaller storage modulus (lower k), smaller loss modulus (lower β), and higher responsiveness to temperature change (higher k_m) favor producing oscillation. From the thermal equilibrium, higher photothermal efficiency (higher k_p) and higher light input (P_{in}) are desired for oscillation. Following this theoretical guide, to realize oscillation at a low light intensity, we designed, fabricated, and optimized the oscillating material system through the following three aspects:

(a) Adopting high photothermal efficiency agent

Candle soot produced from incomplete combustion of candles (paraffin wax) is comprised of carbon nanoparticles, saturated hydrocarbon, and carboxylic compounds, which shows high photothermal effect and good chemical compatibility with LCE. No significant agglomeration was observed visually in the printed LCE thin films (<100 μm) (Figure 3.22a). With addition of 0.5wt% CS in a 100 μm thick LCE film, the absorption could reach nearly 100% over visible to near-infrared light range (400-1100 nm, Figure 3.22b). In our work, we specifically used NIR light for demonstration. Under the illumination of 808 nm NIR laser, the surface temperature of CS/LCE film could reach 70 □ at 202 mW/cm^2 and up to 130 □ under 783 mW/cm^2, which suggests efficient photothermal transduction (Figure 3.22c). [71–73]

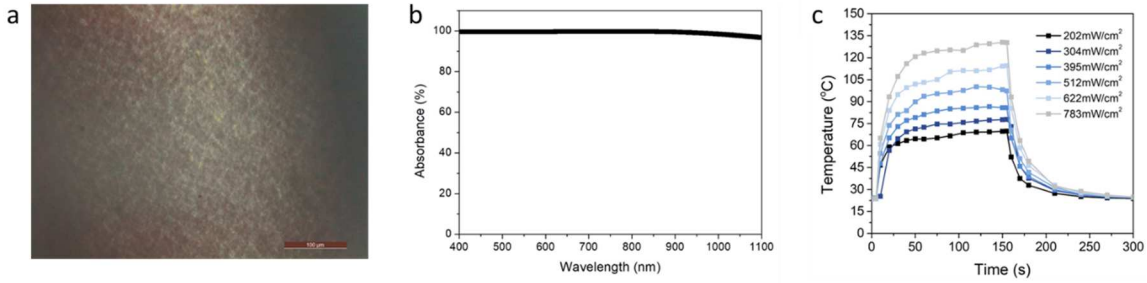

Figure 3.22. Optical characterizations of CS-LCE. (a) Optical microscopic image of a 100um thick LCE film with 0.5wt% CS. Across 400 x 500μm area, no aggregate was found with >5μm size. This demonstrated that photoabsorber CS was well dispersed in printed LCE film. (b) UV-vis-NIR spectroscopy of a 100um thick LCE film with 0.5wt% CS. (c) Photothermal heating over time under NIR light.

(b) Decreasing mechanical moduli

As shown in Figure 3.23, LCE/CS synthesized from thiol-ene chemistry reached a desirably low storage modulus of 1.24 MPa due to the existence of vinyl crosslinker, which are 1~2 orders of magnitude lower than reported LCE[74,75] and 3 orders of magnitude lower than reported LCN.[59] In terms of viscoelasticity, the loss modulus of LCE/CS will drop significantly at high temperatures, suggesting that the damping of the system will be reduced. To further reduce the system damping factor, we incorporate an elastic passive layer, such as PDMS elastomer.

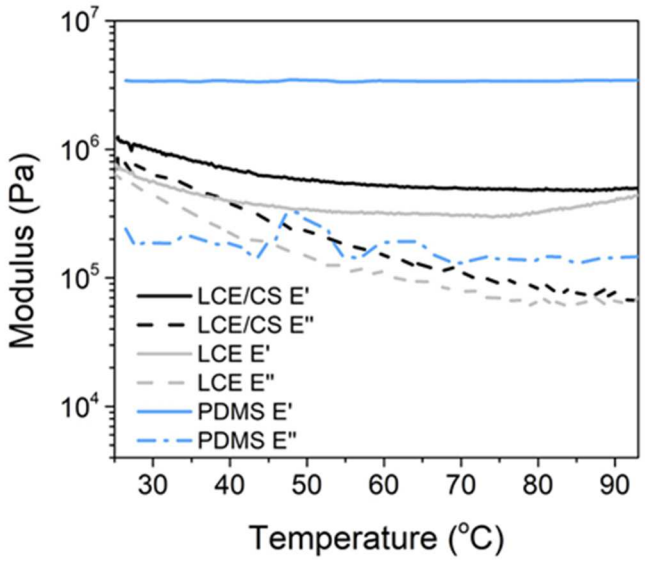

Figure 3.23. Storage modulus and loss modulus of LCE and PDMS

(c) Improving responsiveness with low transition temperature

The LCE made by thiol-ene chemistry was also marked by its low nematic-to-isotropic phase transition temperature (T_{NI}=40 □, Figure 3.24a),[69] substantially lower than LCE synthesized by thiol-acrylate reaction (>70 □)[75] and LCN (90 □).[50] The linear contraction of CS-LCE started from 30□ and reached a plateau at 60-70 □, with a maximum contraction ratio of 30% ($(L-L_0)/L_0$, where L and L_0 are the actuation length and original length) (Figure 3.24b). To construct a bilayer with a passive layer, an LCE oligomerized ink was printed and UV crosslinked on a PDMS film, which was prepared by spin coating and decorated with a silane coating with double bonds. Such an LCE-PDMS bilayer showed good interfacial conformability and adhesion (peel strength ~70 N/m). Due to the thermal contraction mismatch of the two layers, the LCE-PDMS bilayer could bend thermally at high temperatures. A variety of different passive layer materials (different elastomers and polymers) have been explored and tested; the LiLBot with PDMS as the passive layer exhibited the highest actuation and recovery speeds, resulting in the highest amplitude oscillation under the same light intensity. Thickness study showed that LiLBot with 50 μm thick PDMS could reach the highest curvature up to 1.24 mm^{-1} at 70 □ (Figure 3.24c), which was 13 times higher than LCN

(0.095 mm^{-1}) at the same temperature and 4 times higher than LCE synthesized by same chemistry with different alignment configuration.[67] Therefore, we selected CS-LCE/PDMS bilayers for following oscillation characterizations. We named the CS-LCE/PDMS bilayer as CLP bilayer and the corresponding oscillators as LiLBotx, where "x" represented the thickness of PDMS in microns.

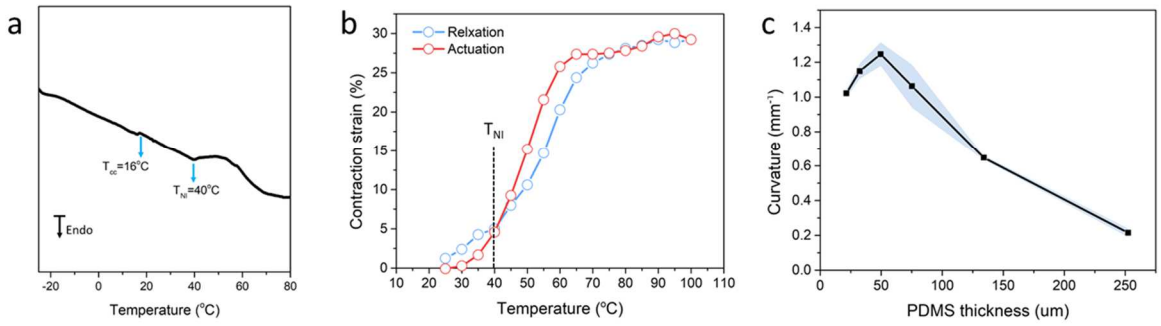

Figure 3.24. Thermomechanical characterizations of LCE. (a) Differential scanning calorimetry curve showing nematic-to-isotropic transition temperature (TNI) of LCE ink, (b) Contraction ratio of LCE as a function of temperature, (c) LCE/PDMS bilayer curvature with different PDMS thickness at 70□

3.4.3. Oscillation performance of bilayers

In a typical experimental setup, the LiLBot was hung vertically, and the NIR light was applied horizontally (Figure 3.25a). It was observed that, as soon as the film bent towards and track the light, oscillation occurred within an appropriate range of input power densities, named as operation window (Figure 3.25b). Below the lower limit, the film cannot oscillate or even track the light. Above the upper limit, the overly high light intensity causes material coiling or unstable oscillation, due to the intense local photothermal effect on the tip and backside of the film as well when the film blocks the light. The middle range that corresponds to steady oscillation is the focus of this study. By varying the PDMS thickness from 21 to 250 μm, the LiLBot50 was found to have the lowest onset power of oscillation (395 mW/cm^2), which agreed with the bending curvature result. We further simulated LiLBot50 for angular change over time, temperature elevation, amplitude in

response to intensity, and onset power of oscillation, showing good agreement with experimental results (Figure 3.25c).

Figure 3.25d describes how the oscillation frequency of LiLBotx changes with the light intensity (400-2000mW/cm^2) and the PDMS thickness (21-250 μm). Previous studies have found that light-driven oscillators vibrate around first-order resonant natural frequency, which is a function of the material's mechanical properties rather than light intensity. For LiLBot, the frequency increased with PDMS thickness but uncommonly decreased with light intensity. This is probably because the film naturally curls up after fabrication due to thermal stress between two layers, and thus the distance between the tip and hinge is shortened at low light intensity, which results in higher natural frequency. Regarding angular amplitude, a threshold power was required to trigger the oscillation and the peak-to-peak amplitude increased nonlinearly up to 60° (angular amplitude=30°) with light intensity (Figure 3.25e).[55] Since the frequency and amplitude changed in opposite directions with increasing energy input, we used *energy density* (kinetic energy divided by volume) of LiLBot to characterize the oscillation strength (Figure 3.25e). Among oscillators with different PDMS thicknesses, LiLBot50 could generate the highest energy density (6.6 J/m^3) at the lowest energy input (below 1 W/cm^2). Combined with all results and analysis above, we used LiLBot50 for subsequent study.

To further reduce the onset power of oscillation, LiLBot was placed from vertical to the horizontal direction and the simulated solar light shone vertically on it from above.[76, 60] Interestingly, light intensity of 100 mW/cm^2 was sufficient to trigger chaotic oscillation, which was likely caused by environmental disturbance, such as external air currents. Light intensity >110 mW/cm^2 could trigger oscillation with consistent periodicity. The successful further lowering of the required light intensity may result from the lower contribution of gravity as restoration force, leading to more substantial bending. Ultimately, with these developments, a sunlight-powered oscillating film was successfully demonstrated, with an input power much lower than that for LCN films based

photothermal effect (450 mW/cm^2)[59], reorientation of photoswitches (1000 mW/cm^2) [57,77], and other derivative works. Note that no LCE-based oscillators were achieved previously.

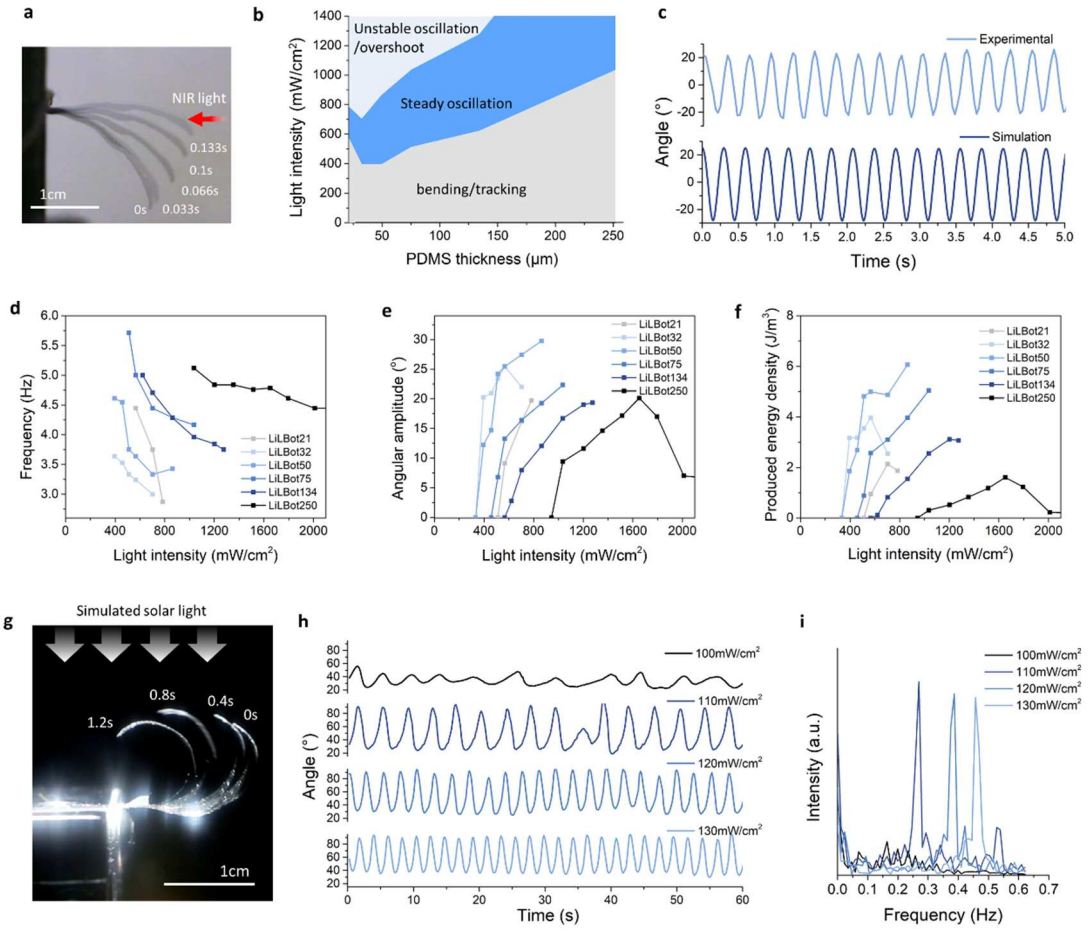

Figure 3.25. Characterizations of CS/LCE/PDMS bilayer oscillators. (a) Schematics and snapshots of the oscillator in half cycle. (b) Oscillation operation window for different PDMS thickness. (c) Comparison of simulation and experimental results. PDMS thickness=50 μm, length=2.2cm, NIR light intensity=700 mW/cm^2. (d) Frequency changes, (e) angular amplitude changes, and (f) produced energy density at different power densities of light. (g) Sequential snapshots, (h) Angle changes, and (i) frequency of overhead oscillation mode powered by a solar simulator. Snapshots were taken at 130 mW/cm^2.

3.4.4. Robotic applications: Sailboat

LiLBot design can be facilely integrated with other materials as an actuation unit for various robotic systems. For example, we have created a flapping wing by assembling a non-active polyethylene

terephthalate (PET) layer as the passive wing with the CLP film exclusively as the active hinge "muscle". Moreover, we designed a phototactic sailboat (Figure 3.26a). To power the sailboat under low light intensity, we chose in-air oscillation over under-water actuation considering the relatively lower thermal diffusion (k_d), thermal conduction, and energy dissipation in air.[5] A CLP-wing, mounted on a plastic boat floating on water and shone by a horizontal NIR light, flaps and provides airflow that propels the boat forward away from the light source, exhibiting a negative phototactic swimming motion. This proof-of-concept sailboat demonstrated a 31 mm/min continuous swimming speed under 567 mW/cm^2 optical input (Figure 3.26b). It presented much faster directional locomotion with significantly lower energy input compared to the oscillating hydrogel-based swimmer (18 mm/min under ~51kW/cm^2).[5] To further improve the speed, the future investigation should focus on the enhancement of the oscillation performance, increasing the number of wings, and breaking reciprocity with a time-asymmetric stroke pattern or non-reciprocal trajectory.[78]

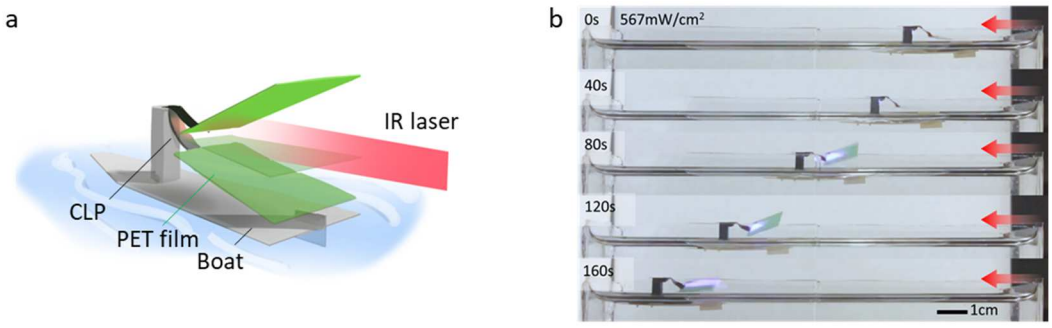

Figure 3.26. Robotic applications: sailboat. (a) Schematics of CLP -based sailboat, walker, and roller under constant light. (b) Sequential snapshots of a sailboat under horizontal light. Light intensity =567 mW/cm^2.

3.4.5. Robotic applications: Walker

Mimicking the traveling wave motions of earthworms, snails, and caterpillars, we demonstrated a territorial walking robot, by using photo-oscillation to produce directional locomotion efficiently.[79] Under an incident NIR light at a tilted angle (~10°), the CLP film constrained by a plastic frame

could perform nonreciprocal wave-propagation motion due to the shadowing of the back wave and continuous regeneration of the new wave (Figure 3.27a,b). Note that the movement does not rely on the asymmetric contact of the robot with the substrate or the surface grating (e.g., ratchet) as previously reported. Over a mild constant light (202 mW/cm^2), this walker demonstrated forward motion at a constant speed of 2.68 mm/min on glass. This moving speed is lower than previously reported LCN wave-propagating walkers, presumably because of the lower modulus of the LCE yielding less stress and lower actuation frequency. Alternatively, we achieved rolling motion at the same light intensity but a much higher moving speed (72 mm/min, Figure 3.27c). The continuous rolling is generated by only one-side illumination on the roller, which caused the curvature change only on the illuminated side. The curvature change induced roller's center-of-mass change, resulting in rolling on the surface.[80]

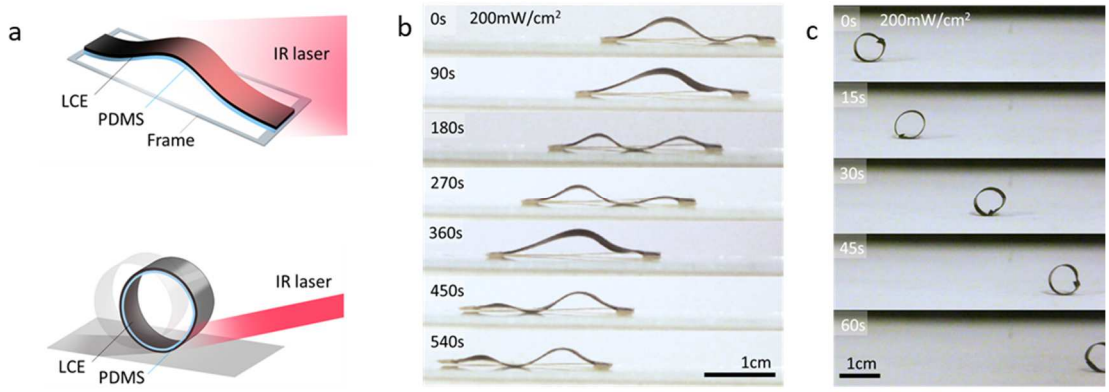

Figure 3.27. Robotic applications: walkers. (a) Schematics of CLP -based sailboat, walker, and roller under constant light. (b) Sequential snapshots of the walker in total 540 s operating time. (c) Sequential snapshots of a roller over time.

3.4.6. Robotic applications: flapping butterfly wings.

Furthermore, we were engaged in the generation of flapping-wings motion for future microscale aerial vehicles. A few concerns remain to achieve the proposed function to interface with potential sunlight condition operation: a) Traditionally, the oscillator needs to align with the light direction, implying that the oscillation direction is parallel to the light direction, which makes it difficult to

initiate oscillation of two wings simultaneously; b) The oscillation frequency, amplitude, and phase angle of the two wings need to be same to enable stable flapping. In doing so, we have constructed an overhead light irradiated with synchronized oscillation mode to power a single CLP film-two butterfly wings system to overcome the above challenges.

In our design, a shadowing strip is placed on the wing with an angle (Figure 3.28). Under the illumination of light from the top side, the CLP film will curl up and lift the wing, which has a tendency to track the light. However, the shadowing strip will block the light in prior to wing tracking to light. With this geometry modification, the oscillation direction does not need to be aligned with the light direction. When we carefully adjusted the light position precisely to the center of the CLP muscle, the two wings displayed oscillation of the same frequency, amplitude, and phase angle. These two flapping wings interact, communicate, and couple the motions into a dynamic steady state (Figure 3.28c).

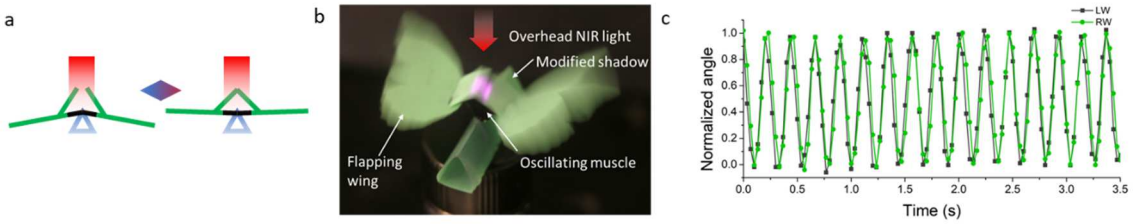

Figure 3.28. Robotic applications: flapping butterfly wings. (a) Working mechanism of the overhead power source and horizontal oscillation motion. (b) Front-view actuation configuration of synchronized oscillation. (c) normalized oscillation angle and phase of two wings under a synchronization state.

The synchronization is based on (1) the symmetry in the geometry and mechanical properties of the wings; (2) the inherent damping in the material; (3) the symmetric excitation induced by the LCE layer. The photo-thermal-mechanical coupling will consistently inject mechanical energy into the symmetric mode, keeping the butterfly oscillating symmetrically with a stable amplitude. The symmetric excitation is perpendicular to and thus injects no energy into the asymmetric motion

pattern in the modal space. The asymmetric motion is only subject to damping (from testbed friction and air viscosity) and restoration (from gravity) forces in the modal space. As a result, any asymmetric disturbance will be damped out, leaving only synchronized symmetric motion.

3.4.7. Discussion and outlook

In this work, we reported a low-intensity LCE bilayer oscillator under constant nonpolarized light. The operation intensity under 1 sun is successfully achieved, ~75% lower than state-of-the-art LC materials. The mild operation window benefits from low T_{NI} LCE while ensuring high photothermal efficiency, high responsiveness, and low mechanical modulus. We demonstrated that LiLBot can be used as powering components of untethered, small-scale soft robots, including walker, roller, sailboats, and synchronized flying wings, presenting the exciting potential for self-sustainable territorial, aerial, and underwater robots.

Although the oscillation frequency (0.3-11 Hz) is within the lower range of natural muscles (1 to 200 Hz), the produced energy density (6 J/m^3) is far below the theoretical energy density of LCE (55 kJ/m^3). This is most plausible because: a) only partial energy storage and release of LCE is used to generate out-of-equilibrium oscillation; b) only the hinge side (one-tenth of the whole cantilever) participates in the energy conversion; c) air damping effect is non-trivial.[77] This can partially explain demonstrated robots with relatively low speed, and our flapping wings can generate relatively low lifting force. Further optimization based on the design principle of oscillation is the next step, which includes improvement of responsiveness in LCE material level[69,74], thermal insulation, photothermal energy conversion, and structural optimization of active-passive configuration.[81]

While a few capabilities and functions of robots are considered transformational using oscillation as a self-sustainable mechanism with low energy input, there still exist many challenges when high power density actuators are required. For instance, to meet the capabilities of flying robots, critical

power density is needed to produce meaningful air thrust. We expect those challenges can be one day solved by cross-disciplinary studies of functional material science and robotics.

3.5. High power output oscillators using a trilayer construct

3.5.1. Experimental and characterization Section

3.5.1.1. Materials

LC reactive mesogens RM257 and RM82 were purchase from Shijiazhuang Sdyano Fine Chemical, Co., Ltd. 2,2-(Ethylenedioxy)diethanethiol (EDDET), 1,4-butanediol bis(thioglycolate) (GDMP), 1,6-Hexanedithiol (HDT), pentaerythritol tetrakis(3-mercaptopropionate) (PETMP), 1,3,5-Triallyl-1,3,5-triazine-2,4,6(1H,3H,5H)-trione (TATATO), I-369, butylated hydroxytoluene (BHT), and tetraethyl orthosilicate (TEOS), Ammonia solution (30%), were purchased from Sigma. Triethylamine (TEA) was used as supplied by EMD. Sylgard 184 PDMS kits were purchased from Ellsworth. Silicone glue (Henkel 908570) was purchased from Amazon.

3.5.1.2. Materials fabrication

Candle soot (CS) was deposited on an aluminum foil above the candle flame, taken into hexane, sonicated till good dispersion, and dried after solvent evaporation. PDMS was made by mixing 5:1 polymeric base and curing agent, spin-coated on clean glass slides with different rotating speeds for 2 mins, and cured on a 110□ hot plate for 2h. Rotating speeds of 180 rpm, 240 rpm, 360 rpm, and 720 rpm resulted in PDMS thickness of 252, 134, 75, and 50 μm. For 320, 460, and 610 μm PDMS, we cured precursor solution between two glass slides with predefined spacers.

3.5.1.3. DIW-TE LCEs

LCE was fabricated by a thiol-ene click reaction[69] with modified chemistry. The functionality of acrylate mesogen, thiol spacer, and vinyl crosslinker are 2, 2, and 3. Molar ratio used was 0.8 acrylate: 1 thiol: 0.133 vinyl. The molar ratio of acrylate mesogens was 0.75 RM82: 0.25 RM257. For thiol spacers, we kept the total molar amount to the same and varied the molar ratio of HDT/(HDT+EDDET) from 0%, 50%, 75%, and 100%. 0.5wt% CS was added as a photothermal

absorber and dispersed by a probe sonicator (Qsonica Sonicator Q500, 25% amplitude, 1 s on, 1 s off pulse for 2 min). Taken 75%HDT recipe as an example, 96.7 mg EDDET, 239 mg HDT, 70.4 mg TATAOTO, 24.0 mg BHT, 250 mg RM257, 857 mg RM82, 8 mg CS, and 25 μl TEA were added, sequentially. After mixing the precursors, oligomerization of ink was completed for 3h at 65□. Oligomerized ink was extruded by a DIW printer (Cellink, BIO-X) on a non-treated PDMS surface with 30mm/s and 170kPa pneumatic pressure. The as-printed samples were post-crosslinked under UV light (134mW/cm^2, 365-400nm) for 5min on two sides.

3.5.1.4. MeS-TE LCEs

We used mechanical stretching to increase mesogen alignment and adopted the thiol-ene click reaction to formulate a UV crosslinking reaction at the second step. The molar ratio of mesogens, thiol spacers, PETMP thermal-induced crosslinker, and TATATO photo-induced crosslinker were 1:1:0.125:0.167. The TATATO concentration was the same as that of DIW-TE LCE. Mesogens were chosen as a mixture of RM82 and RM257, where the RM82 molar ratio was 100%, 75%, 60%, 40%, and 25%. GDMP or HDT were chosen as spacers due to higher modulus compared to EDDET.[82] PETMP was added as a thermally-induced thiol-acrylate crosslinker to form a free-standing film after first-stage thermal oligomerization. The first-stage thermal oligomerization was completed after 4 h at 65□. Then, the partially polymerized films were stretched to monodomain and irradiated under UV light to trigger thiol-ene crosslinking for 30min along two sides.

3.5.1.5. MeS-TA LCEs

We used the Yakacki[75] method to synthesize MeS-TA LCE. The molar ratio of mesogen (also serves as acrylate crosslinker), spacer, and crosslinker were 1.025:0.867:0.067. The first stage of thermal oligomerization was completed under room temperature overnight, and all thiol spacers and crosslinkers completed the reaction. Then the samples were taken from the mold and kept in a 65□ oven overnight to remove the toluene solvent. Finally, the sample was cut to the desired shape,

uniaxially stretched to a monodomain state, and irradiated under UV light to complete the diacrylate crosslinking for 2 h in total.

3.5.1.6. FLaPTOR fabrication

A thin-layer silica coating was grown on LCE to ensure good adhesion between LCE and PDMS. The silica layer was coated by a room-temperature chemical vapor deposition method using TEOS and ammonia solution after oxygen plasma of LCE for 3 min. 10wt% silicone glue was dissolved in hexane to form a dilute solution. For fabrication of the trilayer, PDMS film was sandwiched by two silica-coated LCEs with silicone glue in between. The crosslinking of the silicone glue was carried out at room temperature for 3 days with moisture.

3.5.1.7. FLaPTOR-actuated wing

The passive wing was made of Polyethylene terephthalate (PET) with a thickness of 10 μm and the wing shape was fabricated by a laser cutter (PROVerXL 4030). Two PDMS strips were fabricated by blade casting to produce a thickness of 140 μm. LCE formulation was MeS-TA with RM257-HDT. LCEs and PET film were cleaned using ethanol, activated by oxygen plasma for 3 min, and coated with silica by room-temperature chemical vapor deposition overnight. PDMS was cleaned using ethanol, activated by oxygen plasma for 3 min, and coated with silica for 1.5 h. The multilayer wing was laminated by LCE, PDMS, PET, PDMS, and LCE, sequentially. The interface between each layer was glued with silicone glue to enhance the adhesion.

3.5.1.8. Thermomechanical characterizations of LCE

Before testing, LCEs were annealed at 180□ for 5 min and cooled at room temperature for 5min to remove thermal history. Storage modulus, loss tangent, and actuation strain were measured by a dynamic mechanical analyzer (DMA850, TA instrument) with 25 kPa preload, 1Hz oscillation frequency, 20μm amplitude, 25-210 □ temperature range, and 5 □/min heating rate. Actuation strain was calculated by $\varepsilon = (L-L_0)/L_0$, L and L_0 are the instant lengths and original length. Actuation

stress was measured by an isostrain mode, with a 25-140 □ temperature range, and a 5 □/min heating rate. Work capacity was measured by an isostress mode, with P_0=500 kPa constant load, 25-210 □ temperature range, and 5 □/min heating rate. Lengths at 30 □ and 210 □ were denoted as L_1 and L_2. We assume the material is incompressible and the volume keeps unchanged during actuation. Work capacity was estimated as follows:

$$\text{Work capacity} = \sigma\varepsilon = \frac{P_0(L_1 - L_2)}{L_1}$$

3.5.1.9. Oscillation characterizations

Trilayers were horizontally mounted on a stage by a tape with light illuminated also from a horizontal direction. The light spot was a rectangular shape with dimensions of 3.5x4.5 mm and the light exposure area fully covered the cross-sectional area of the trilayer. A linear translational stage was fixed on the laser to precisely control the height of the light to the trilayer. A power threshold was needed to trigger out-of-equilibrium oscillation of the trilayer. In addition, since the light beam was originally parallel to the LCE surface, the trilayer was manually bent back and forth so that the two LCE surfaces could be exposed and heated to help initiate the oscillation. Then the trilayer could autonomously reach a steady oscillatory state. The oscillation behavior was recorded by a camera with 60 fps. The tip angle of the trilayer was measured by a software Tracker. Frequency, amplitude, and power density were calculated based on the time-dependent angle change.

3.5.2. Design principle of High power output oscillators

The primary purpose of this work is to develop a light-driven oscillation mode with enhanced output power density close to the flight muscle of insects. We utilize photo-thermo-mechanical energy transduction, which permits broader wavelength selectivity, thick-film fabrication, and large actuation strain. To ensure high energy harvesting efficiency, we design a bi-directional actuation mode from both sides of the film where light can activate the deflection both during

upstroke and downstroke for amplification of generated motion. This contrasts with twisted,[57] splayed,[59] and bilayer design[60] with mono-directional actuation. Therefore, a geometrically and chemically symmetric structure (e.g. homogeneous pillar,[17] hollow, and radially symmetrical structure[83]) is anticipated to trigger the bi-directional actuation. The angular bending is achieved by producing a thermal gradient across the thickness direction. However, previous reports demonstrated that axially-aligned LCN films with symmetric configurations were unable to bend due to low thickness and fast heat transfer.[84] The most efficient way to generate a meaningful thermal gradient is by increasing the thickness and increasing the thermal diffusion time scale ($\tau \sim t^2/D$, t is thickness of the film and D is the thermal conductivity). To enable the deformation with the large thickness, we rationally choose LCE instead of LCN considering its large actuation strain. To establish a well-defined strain mismatch given the thermal gradient across the thickness, we inserted a passive PDMS layer in middle and form a FLaPTOR. The two LCE films on both sides can independently contract and relax, and perform antagonistic actuation when bending back and forth (Figure 3.29).

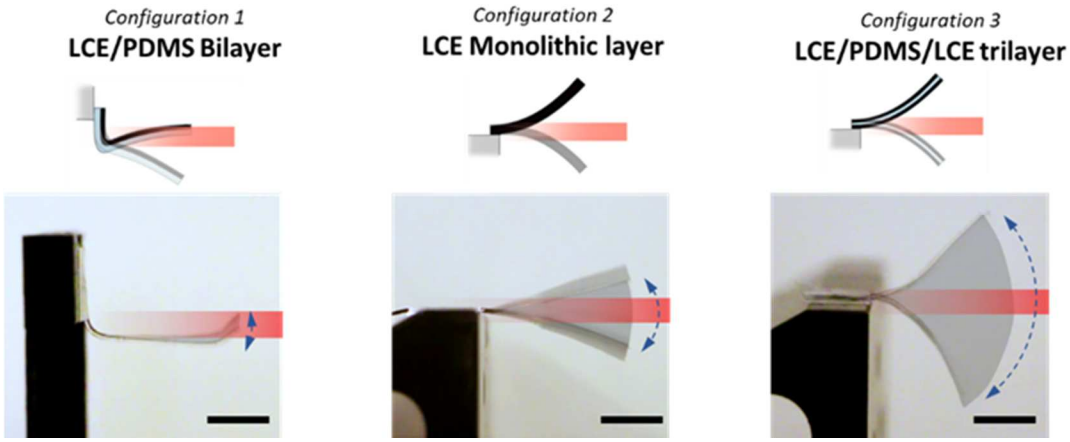

Figure 3.29. Schematic diagrams and superimposed pictures of LCE oscillators based on different configurations: 1) LCE/PDMS bilayer oscillator (LPBO), 2) LCE monolithic layer oscillator (LMO), 3) LCE/PDMS/LCE trilayer oscillator (FLaPTOR).

Configuration	*LCE/PDMS bilayer (LPBO)*	*LCE monolithic layer (LMO)*	*LCE/PDMS/LCE trilayer (FLaPTOR)*
Upstroke	LCE actuates	Upper part of LCE actuates Lower part of LCE relaxes	Upper LCE1 actuates Lower LCE2 relaxes
Downstroke	LCE relaxes	Upper part of LCE relaxes Lower part of LCE actuates	Upper LCE1 relaxes Lower LCE2 actuates
Energy injection	Only upstroke	Full cycle	Full cycle

3.5.3. Improvement of output power density

3.5.3.1. FLaPTOR vs LCE monolithic oscillator (LMO)

FLaPTOR departs from earlier LCE or LCN monolithic oscillator (LMO) by possessing a middle PDMS layer with the same total thickness. Both configurations enable the bi-directional actuation for energy input. For mechanical property, FLaPTOR demonstrated higher and steady storage modulus and lower viscoelasticity (lower tanδ), which were contributed by a stiff and elastic PDMS layer (Figure 3.30a). These are beneficial for high-frequency applications.[68] Since FLaPTOR would delaminate after 140□ due to an overly high thermally-induced stress mismatch between LCE and PDMS, we fitted the modulus above 140□ using the LCE and PDMS data. For thermal property, we observed no obvious difference of temperature and temperature difference across thickness directions under the same NIR light intensity, indicating that both structures have similar thermal transport and energy dissipation behaviors (Figure 3.30b). This is attributed to similar thermal conduction between PDMS (0.15 W/m·K) and LCE (0.24 W/m·K). For thermomechanical actuation of NIR light from one side, we observed the LMO could initially bend to a higher angle, but further increasing power input would lead to unbending (Figure 3.30c). The negative slope of the temperature-angle curve is detrimental to producing amplification of oscillation. In contrast, FLaPTOR demonstrated a more linear and high bending angle up to 200□.

We then studied the time-dependent evolution of oscillation after light exposure Figure 3.30d, e, f, g). The length of the LMO was continuously reduced due to heat accumulation throughout LCE. However, the length of FLaPTOR would maintain steadily upon oscillation due to the rigid PDMS to resist the contraction of LCE. The amplitude and power output of LMO showed peak values at

10s illumination followed by rapid performance deterioration, whereas those of FLaPTOR gradually increased until reaching saturated values. Previous studies showed that length shortening will impede oscillatory behavior because of higher bending stiffness.[5] To decouple the length-shortening effect, we used a longer initial length and ensured the length during oscillation was controlled as 2.5 cm, the same as the length of FLaPTOR. However, the frequency, amplitude, and output power density of the FLaPTOR still outperformed those of LMOs (Figure 3.30h, i, j). This could be explained by: 1) stable and high modulus of trilayer for operation at high frequency; 2) linear thermomechanical bending curve over temperature, and 3) stable length to maintain inertia.

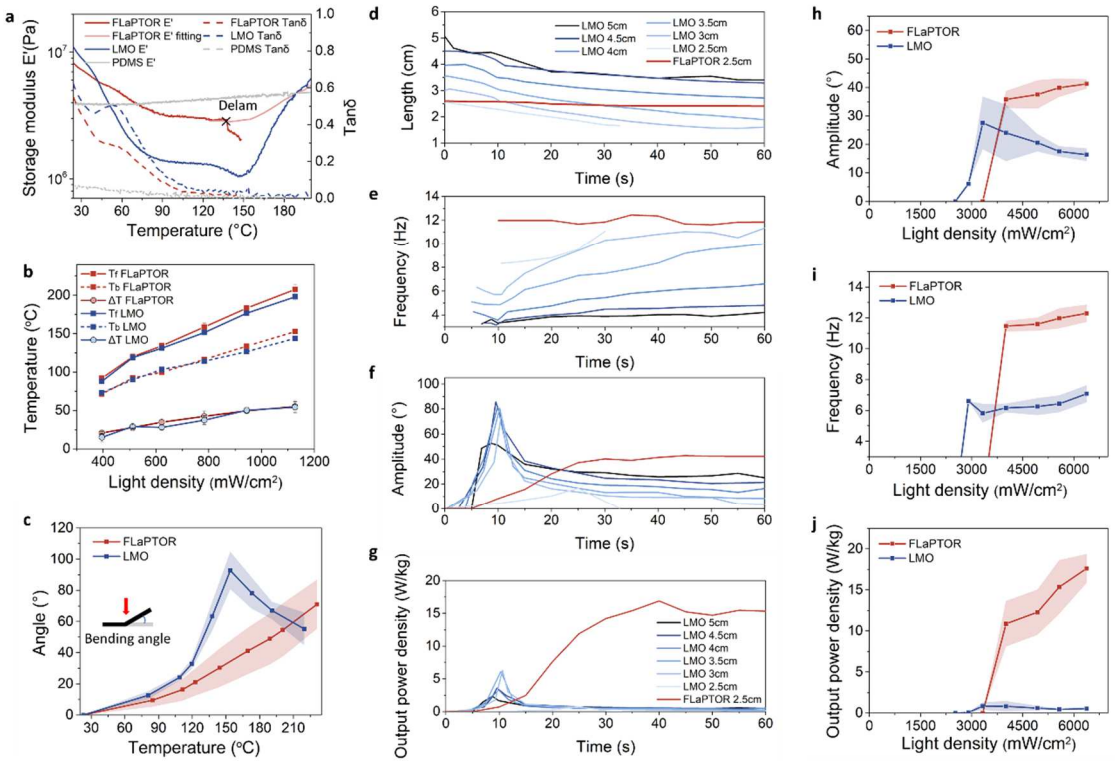

Figure 3.30. Fundamental studies of performance improvement of FLaPTOR over LMO. a) Storage modulus and tanδ of two configurations during temperature ramp. b) Thermal profile of two configurations under different input light intensities. c) Thermomechanical bending at different surface temperatures on the illumination side of LCE. Time-dependent oscillation tests were characterized after switching on the optical beam, including d) length, e) frequency, f) amplitude, and g) output power density. Light intensity was 5580 mW/cm^2.The original length of LMO was changed from 5 cm to 2.5 cm. To decouple the length-shortening effect, oscillation performance was conducted by using a longer

length and ensuring the length during oscillation was 2.5 cm. h) Frequency, i) amplitude, and j) output power density were characterized, respectively.

3.5.3.2. FLaPTOR vs LCE-PDMS bilayer oscillator (LPBO)

We also compared the performance of FLaPTOR and LPBO. Note that the bilayer oscillator has a similar actuation mechanism as splayed or twisted LCN, which possesses a mono-direction actuation mode.[59,84] LPBO with the same total thickness as FLaPTOR could produce a maximum power density of 0.1W/kg (Figure 3.31), more than two orders of magnitude lower than that of FLaPTOR (20W/kg). In addition, above a certain intensity, the bilayer film suffered from tip coiling, leading to a reduction in performance. This implies that the system has broken the upper limit of balance between power input and mechanical energy release.[61]

From an energy-harvesting perspective, FLaPTOR with the antagonistic actuation mode enables energy harvesting and photothermal actuation during the whole cycle instead of a half cycle in LPBO. Concerning the downstroke of FLaPTOR, the shortening of the bottom LCE layer facilitated the lengthening and relaxation of the upper LCE layer at high pacing frequencies, in contrast to the reliance solely on thermal relaxation of upper LCE in LPBO. This effect improves higher flapping speed (v~ ωA), which is proportional to angular frequency ω and angular amplitude A. All these effects lead to better oscillatory stability, improved flapping stroke, high-frequency operation, and large kinetic energy/power.

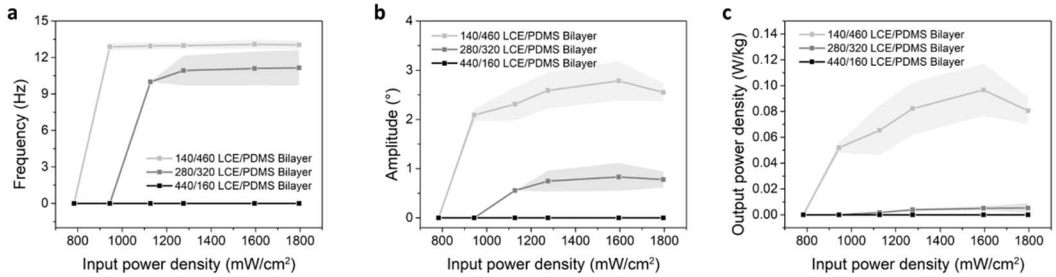

Figure 3.31. Oscillation performance of LPBOs. Thickness in total was 600μm and LCE thickness was 140, 280, and 440μm, respectively. a) Frequency, b) Amplitude, and c) output power density of

three configurations of LPBOs at different input light intensities showed that LPBPO with 140/460 configurations could produce the best performance. The highest power density was ~0.1W/kg.

3.5.4. Structure-property-performance development for high-performance FLaPTOR

The altering chemistry of LCE and the structural configuration of FLaPTOR have various effects on producing high power-density oscillation, which simultaneously requires high frequency and amplitude.

We used three classes of fabrication methodologies and polymerization chemistries of LCEs. We studied the thermomechanical properties. In general, we employed thiol-acrylate Michael addition photopolymerization to obtain randomly-oriented LCE oligomers at the first stage, which were either liquid-like or gel-like. Then, the polydomain oligomers were aligned in a single direction and permanently fixed by photo-crosslinking. Depending on different strategies, these include i) liquid-like oligomers extruded by direct ink writing (DIW) followed by thiol-ene photo-crosslinking chemistry, named DIW-TE;[69] ii) gel-like oligomers followed by mechanically-stretching and thiol-ene photo-crosslinking, named MeS-TE; or iii) gel-like oligomers followed by mechanically-stretching and diacrylate photo-crosslinking, named MeS-TA.[74] We have studied the effects of monomers, spacers, and crosslinkers for each synthesis method. The thermomechanical properties are rationalized by the interaction of diverse chemical components of segments and their packing structures, which modulate the LC phase morphology.[74] Among them, MeS-TA methodology with RM257 as mesogens and 1,6-Hexanedithiol (HDT) as spacers achieved 21.5MPa storage modulus at room temperature, 64% actuation strain at 200□, 1.2MPa actuation stress at 140□, and 311KJ/m^3 work capacity under 500kPa load at 200□, outperforming other fabrication methods, formulations, and reported LCEs (Figure 3.30c). The improved performance is attributed to i) incremental mesogen orientation from the mechanical stretching method, ii) increased modulus while maintaining actuation strain from acrylate crosslinking,[69] and iii) phase segregation of rigid mesogens and HDT spacers.[74]

Then, we investigated the oscillatory performance using these LCEs and assembling them into FLaPTOR configurations. We controlled LCE side layers to be 70-145 μm in thickness and PDMS middle layers were controlled to 50-610 μm in thickness. We named FLaPTORs geometry x/y/x, where x=PDMS thickness in micrometers, and y=PDMS thickness in micrometers. Among all LCE formulations, MeS-TA methodology with RM257-HDT exhibited the highest output power, which was consistent with the above LCE thermomechanical study (Figure 3.30c, d, e, f, g). The output kinetic energy and output power of FLaPTORs outperformed other reported light-driven oscillators, indicating that the chemical development and the unique structural configuration facilitate efficient energy transduction and mechanical output (Figure 3.30g).

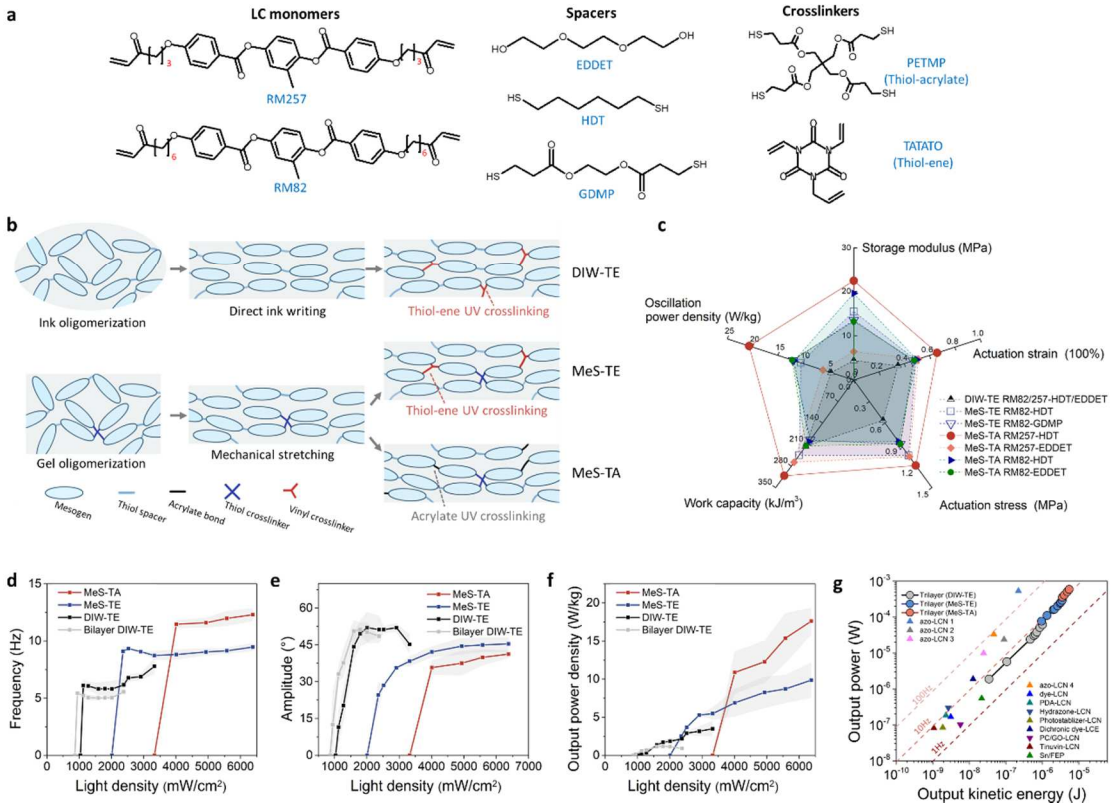

Figure 3.32. structure-property-performance relationship of FLaPTOR. a) Compositions of LCEs, b) Illustrations of polymerization procedures of different LCE synthesis methodologies, c) Thermomechanical properties of LCEs and oscillatory performance after fabrication into FLaPTORs. Geometrical configuration was 120/50 LPBO bilayer using DIW-TE (baseline), 120/134/120-2cm FLaPTOR for DIW-TE, 115/320/115-2.5cm for MeS-TE, and 145/320/145-2.5cm for MeS-TA. d)

Frequency, e) amplitude and f) oscillatory power density as a function of light intensity. g) Output power vs kinetic energy plot showing that the FLaPTOR design outperformed reported oscillators.

We also investigated the geometrical effects of the oscillatory performance, including LCE thickness and PDMS thickness, separately (Figure 3.33). In general, higher input power would produce an unaltered frequency, higher amplitude, and higher output power density, which were analogous to previous light-driven oscillators.[59] With thicker PDMS and/or LCE, the onset light intensity necessary to induce oscillation was increased, suggesting that more energy was needed to overcome the resistive force like damping. Although the oscillation frequency was boosted with a thicker film, the amplitude at a certain input power density was compromised due to the increased moment of inertia. In addition, overly high input power (>6500mW/cm^2) would lead to a risk of LCE fracture, because PDMS provided a geometrical constraint from LCE contraction. When fixing the total thickness and varying PDMS/(PDMS+LCE) thickness ratio, increasing the PDMS thickness ratio will lead to a right shift of the operation window due to less LCE for photo-induced deflection, but the maximum output power density was similar (Figure 3.33g,h,i). Although a low PDMS ratio benefits energy harvesting and could produce a power density of 23W/kg, we observed out-of-plane twisting of the film due to undesired structural instability.[57] In combination of the LCE formulation study, PDMS thickness study, LCE thickness study, and PDMS thickness ratio study, we selected geometry of 145/320/145-2.5cm and MeS-TA methodology with RM257-HDT, and yielded a frequency of 13Hz, amplitude of 42°, and power density of 20.7W/kg, which was close to the power density of flight muscle of insects.

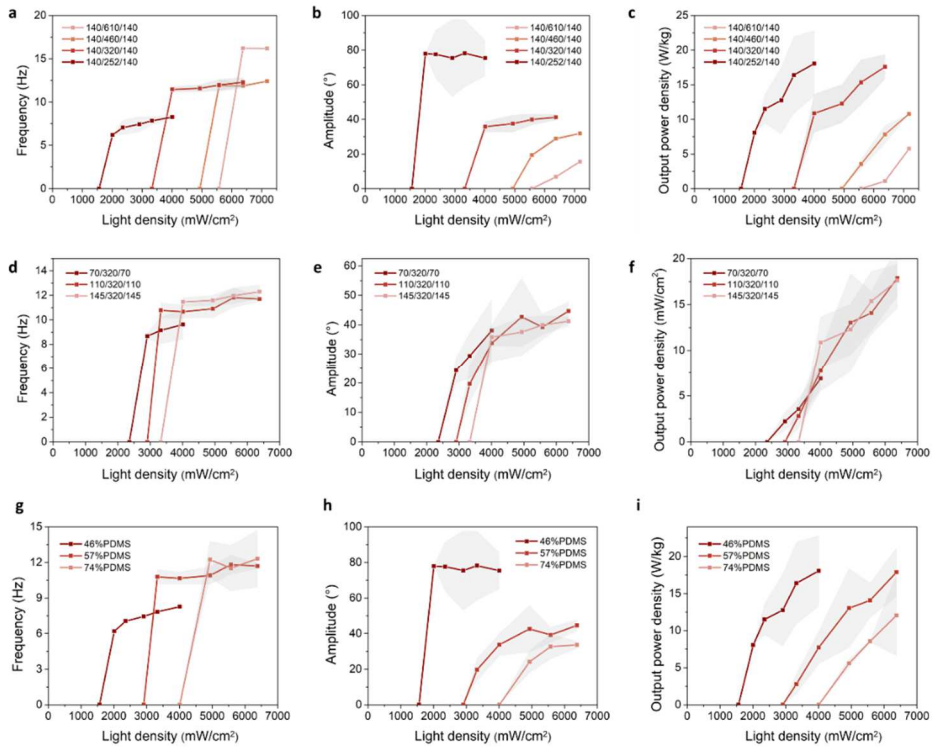

Figure 3.33. Geometrical effects on the FLaPTOR performance. (a, b, c) PDMS thickness, (d, e, f) LCE thickness, and (g, h, i) PDMS/(PDMS+LCE) thickness ratio at a fixed total thickness of 600 μm.

3.5.5. Flapping wing actuator

We have integrated the FLaPTOR with a passive wing fabricated by laser cutting and assembled by multilayer lamination (Figure 3.34a,b). The FLaPTOR-actuated wing performed oscillatory motion in constraint mode (Figure 3.34 c), and partially unconstrained mode by strings (Figure 3.34 d). The FLaPTOR-wing permitted flapping motion under constrained mode (f=10.5Hz, A=38°) and partially-unconstrained mode (f=9.9 Hz, A=16°). We measured the generated thrust by the flapping wing using a force transducer and a balance lever system (Figure 3.34 e, f). The highest average lift force demonstrated 147 μN and the thrust-to-weight ratio was 0.32, given the weight of the FLaPTOR-wing to be 47 mg. The light power delivered to the oscillating wing was 1.1W, implying a thrust-to-power ratio of 0.13 N/kW. Compared with flapping-wing-based MAV systems, the thrust-to-weight ratio and thrust-to-power ratio for the Harvard RoboBee have achieved 1.7 and 41.2 N/kW.[85] Since a thrust-to-weight ratio exceeding 1 is required for vertical takeoff, the

performance of FLaPTOR-wing will be improved by further design investigation, such as 1) molecular engineering of LCE for enhanced thermomechanical properties, 2) structural configuration development of the FLaPTOR to improve the power density, and 3) varying material and geometry of the wing to increase the passive wing pitching and generated thrust.

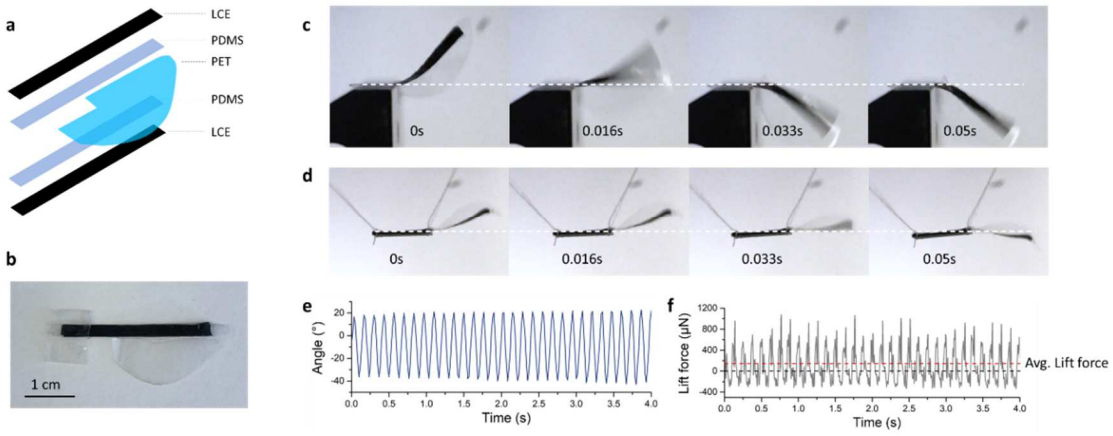

Figure 3.34. Flapping wing application. a) Schematic representation and b) a photograph of a FLaPTOR-wing actuator. Time-resolved snapshots of the flapping wing actuator in one cycle with c) constraint mode and d) partially unconstraint mode. e) Angle change and f) generated instant lift force of the flapping wing actuator.

3.5.6. Discussion and outlook

The achievements described in this work present a major milestone in the development of autonomous, sustained, and untethered flapping motion on an insect scale. Further improvements are expected to aggregate design, manufacturing, actuation, and control to create a fully untethered sustained light-driven flapping robot: ii) reduction of light input without sacrificing the oscillatory power density; i) precise and dynamic control of light input to trigger flapping wings, and iii) investigation of wing-wing interaction to realize synchronized flapping.[86]

4. Exteroceptive sensing and proprioceptive sensing based on stretchable conductive hydrogels

4.1. Introduction

4.1.1. Construction of highly stretchable conductive hydrogels for sensors

Newly developed flexible and stretchable electronics seek to bridge the gap between human and machine, by either performing human functions, such as in artificial skins[87] and multifunctional prosthetics for assisting human movements,[88] or interfacing with clothing or the human body, such as in conductive interconnects,[89] bioelectronics,[90] and wearable sensors.[91] All of these applications require materials that are highly electrically conductive and mechanically compliant. One strategy to enable these functions is structurally designing nonstretchable materials to absorb strain without fracture.[92] Alternatively, intrinsically stretchable conductive materials are highly desired, with intrinsic deformability and reliability at the forefront of concern.

Stretchable conducting polymer-based hydrogels (SCPHs) with a three-dimensionally interconnected microstructure have presented attractive merits for use in sensors and wearable devices.[93] The intrinsically porous structures found in hydrophilic gels, whose large surface areas promote high water content, biocompatibility, and high permeability to ions and molecules. Conducting polymers can be directly made into free-standing and flexible hydrogels by introducing multivalent metal ions or via post-treatment with as-prepared polymers. Despite their high electrical conductivity, the majority of conducting polymers lack stretchability (<10%) and possess limited mechanical compliance under large strains.

In an attempt to improve the stretchability, elastic polymer chains such as polyvinyl alcohol (PVA), polyacrylamide (PAAm), poly(ethylene glycol)diacrylate (PEGDA), and chitosan have been incorporated into rigid conducting polymers in past works. However, these strategies usually suffer from unfavorable electrical and mechanical properties. The introduction of non-conducting polymer chains in this case impedes the conductive pathways. Additionally, since the nucleation

and reaction kinetics are controlled by the Gibbs free energy of nuclei formation, conventional polymerization in the liquid phase suffers from uncontrollable kinetics. The result is a random and loose assembly of disconnected, large polymeric nano-aggregates which lack a dense and continuous packing of conducting polymer chains and highly crystalline networks needed for both electron transport and robustness under tension. Specifically, the limited amount of continuous conductive pathways cannot meet the percolation threshold, as a result of limited electrical and electrochemical properties when serving as electrodes or active materials in flexible electronics. The loosely-packed network is mechanically weak, with a typical tensile modulus of 10 KPa or less. When used as stretchable sensors in particular, their aggregates severely prohibit concurrent deformation along the bulk material upon stretching, thus failing to reflect the actual strain with good fidelity, and ultimately leading to insufficient strain sensitivity.

4.1.2. Molecular integration of sensing unit with actuation component

One of the unique capabilities that sets living organisms apart from artificial materials is the ability of living organisms to perceive and manage their motion to adapt to their environment. This is enabled by locally sensing their movement (kinesthetic) and environment (tactile) by proprio-/exteroreceptors to provide somatosensory feedback for effectors through the reflex arch or neuromuscular systems[94]. For example, octopi exhibit a highly localized and continuous neural system with nonsegmented arms that can accomplish various tasks, ranging from basic arm shortening/elongation to complex object grasping, shape morphing, and accessing the restricted environment.[95] One of the ultimate goals of robotics is to demonstrate sensorimotor-like abilities, by mimicking the receptors and effectors in biological somatosensory systems to achieve simultaneous active motion and perception functions. This requires integrating sensors and actuators with non-interfering and matching sensitivity to the deformation range, without compromising the desirable high mechanical flexibility, fast actuation, and real-time sensation.

Soft robots offer promising opportunities for sensing-actuation unification. Defined by their specific working mechanisms, these sensors and actuators are all single-function units, still unable to realize sensation and actuation simultaneously. Therefore, add-on functionalities to soft robots have been employed to physically integrate the two individual components by welding, 3D printing, embedding, or laminating sensors and actuators. Fabricating such heterogeneous multi-material systems typically involves complex integrating processes with multiple molding and lamination steps and complicated connection terminals. These physically-integrated systems with various material interfaces also have potential stress concentration and adhesion issues. In terms of robotic performance, the sensing and actuation functionalities are predefined with constrained flexibility when handling complex dynamic environment.

It would be highly advantageous to develop a multifunctional monolithic material containing chemically integrated sensing and actuation components at the molecular level, rather than the system level. Such a somatosensory actuatable material can ideally present intrinsic sensing capability and non-predefined actuation simultaneously, without potential delamination or sensing/actuation range mismatching associated with physically-integrated multiplexed design. In addition, the bulk material with molecularly modular design can be chemically customized and physically tuned for optimized mechanical and electrical properties, and further combined with other units for higher-level functionality. However, material designs that seek to accommodate such multifunctionality without a conflict between the signal transductions of the sensing and actuating processes remain limited. Designing complex energy transduction mechanisms in existing soft materials (*e.g.*, conducting polymers) may realize multifunction (sensing and actuation); however, the resulting performance would be rather limited and unsatisfactory for the demanding soft robotics applications (*e.g.*, large, fast, and forceful shape-changing and high strain sensitivity simultaneously).

Among many active polymers, stimuli-responsive hydrogels can undergo a significant volumetric change in response to a variety of environmental stimuli, and thus may serve as a good actuator. To manifest the hydrogel's ability to sense, a piezoresistive mechanism is predominantly utilized, possibly based on ionic or electronic conduction.[96] Although flexible conductive polymers/hydrogels have been explored for soft electronics applications, these materials lack the stimuli-responsive actuation ability required for soft robotics applications.

The hierarchical porous hydrogel network would allow for both continuous electronic conduction for sensation and efficient mass (water) transport for actuation. Although CP-percolated stimuli-responsive hydrogels have been reported, multiple obstacles still remain preventing them from serving as sensory actuators: a) CPs percolation using conventional two-step methods results in high inhomogeneity, typically with CPs formed only on the hydrogel skin, and are hence unable to accurately reflect the actual material deformation. b) Challenges have been found when making materials both electrically conductive and capable of withstanding large mechanical deformation. Their conductivity and mechanical robustness are relatively low, due to the formation of nano-aggregation and discontinuities of the two polymer networks, leading to unstable sensing signals and poor actuation and load bearing. c) The slow actuation due to the slow diffusion in hydrogels with non-continuous channels has a response time of minutes or hours. d) More importantly, although the state-of-the-art conductive hydrogels can reach either high conductivity, good mechanical properties, fast and substantial actuation, or sensing individually, realizing all the desired features simultaneously in one CP-percolated responsive hydrogel composite remains challenging.

4.2. Proposed method

We present an approach to create SCPHs, based on a conducting polymer-hydrogel interpenetrating double network with a hierarchical micro/nano-structure. The unique structure is constructed by an ice-template, assisted low-temperature (ITLP) method, which has not been reported before. We

will characterize mechanical and electrical properties, and compare their performance with materials synthesized by traditional methods. Then, we will demonstrate the highly conductive and stretchable material as high-performance strain sensors.

In follow-up work, we aim for a soft somatosensitive actuator based on a molecularly innervated CP-percolated hydrogel-based material capable of performing a variety of feedback-controlled robotic tasks, including octopus arm–like shortening, elongation, and object-perceiving and grasping (Figure 4.1). We will use the interpenetrating polymer double-network based on poly(N-isopropylacrylamide) (PNIPAAm) and polyaniline (PAni), which combines both photo/thermal actuation and piezoresistive sensing into a monolithic material of "two-in-one" functionality. To achieve the high conductivity and high mechanical robustness necessary for simultaneous optimum strain sensitivity and deformability, we leverage the ITLP polymerization method to construct conductive network. To interface the polymerization chemistry of PNIPAAm, we inspire from the ITLP method and develop a one-pot synthesis method via the ice-templated, ultraviolet (UV) polymerization of PNIPAAm and cryo-polymerization of PAni (ITUC). It solves the aforementioned three issues with (i) distributing the conductive (sensing) and the stimuli-responsive (actuating) components homogeneously distributed at a molecular level throughout the entire bulk material, (ii) maintaining a continuous pathway for electron conduction and so high sensitivity, while remaining strong and stretchable (a result of the suppressed CP-nanoaggregate overgrowth under subzeroreaction and the densified CP packing by ice templating), and (iii) having open pores for high water diffusion and thus fast actuation.

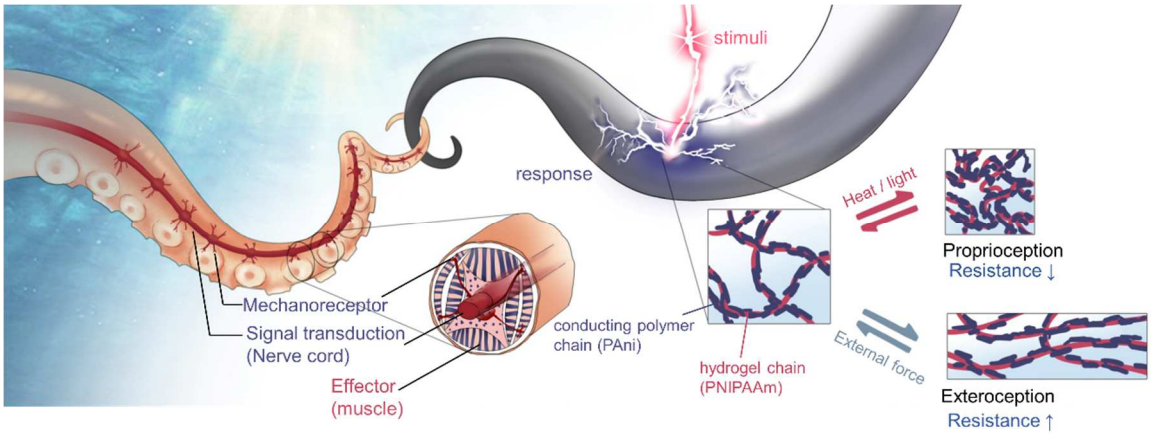

Figure 4.1. Design of the somatosensitive actuator based on conducting polymer hydrogel. (A) Schematic of the bioinspired self-sensing actuator: Resistance change arose from density change or chain elongation of conducting polymer network when exposed to thermal stimulated volumetric change or external stress.

As an actuator, the hydrogel can rapidly change to any arbitrary shape and size in response to stimuli and does so with a substantially improved response rate and a high volume change ratio. We can demonstrate light-responsive actuation properties, such as light tracking, object lifting, and grasping. Based on the enhanced conductivity and stretchability of this hydrogel, we can demonstrate it as a passive strain sensor and pressure sensor, which correspond to the exteroception behavior of the material. Alternatively, because this material has noninterfering sensing and actuation (referred as the e-output and photothermal-input), its actuation can be detected in real-time to provide sensory feedback, undisturbed by the photothermal activity in actuation. Thus, the sensory actuator also has proprioception to monitor its responsive elongation/shortening and bending/ unbending under light stimulation. As a proof of concept, it is demonstrated that the somatosensitive actuator has the potential to help recognize the shape of an unknown object based on the deformation time and resistance evolution. Furthermore, we develop a closed-loop algorithm for actively controlling the artificial arm elongation/shortening, which could be successfully maintained at targeted lengths precisely.

4.3. Exteroceptive sensing based on hierarchically-structured stretchable conductive hydrogels

4.3.1. Experimental and characterization Section

4.3.1.1. Chemicals

Polyvinyl alcohol (PVA, molecular weight = 89000-98000, hydrolysis degree = 99%), aniline, pyrrole, and phytic acid (PA, 50 wt.% aqueous solution) were purchased from Sigma. Aniline and pyrrole were purified by reduced distillation. Lithium chloride, glutaraldehyde (GA, 50% aqueous solution), ammonium persulfate (APS, ACS grade) were purchased from Fisher. Sylgard 184 Silicone Elastomer kits were purchased from Ellsworth.

4.3.1.2. Preparation of precursor solution

10 wt.% PVA solution was prepared by mixing 5 g PVA in 45 g DI water and heating to 85 □ until the solution was transparent. The solution was cooled to room temperature and stored for further usage. 1 wt.% GA solution was prepared by diluting 1 mL 50 wt.% GA solution with DI water. The as-prepared GA solution was kept at 4 □ fridges.

4.3.1.3. Synthesis of PANi/PVA SCPHs

For the synthesis of PANi/PVA composites hydrogel, we used a one-pot reaction to polymerize PANi and chemically crosslinked the PVA simultaneously. Typically, 2000 mg of 10 wt.% PVA solution, 147 μL of purified aniline, 285 μL of 35.5% HCl solution were mixed. DI water was then added and mixed to finally form 3 mL aqueous solution in total, denoted as Solution A. Besides, solution B was made by adding 0.4 mL of 1 wt.% GA and 365 mg APS together, followed by adding DI water to ensure the volume was 1 mL. The solutions were cooled to 4 □ in a fridge and mixed in a water/ice bath.

Then ItG and LpG were cured in different processes. For ItG, the mixture was quickly poured into a 3D-printed plastic mold above a tank of liquid nitrogen. Then the mold was lowered slowly into the liquid nitrogen. After the entire freezing, the mold with the frozen mixture was quickly

transferred to a -20 □ fridge and kept there overnight for sufficient reaction. Then the mixture melted at room temperature to obtain the ItG. For LpG, the mixture was injected into a glass mode with a thickness of 2 mm and cured at room temperature for 15 min. To ensure both ItG and LpG samples have experienced the identical low-temperature condition, the as-synthesized LpG samples were also frozen under a subzero environment in the -20 □ fridge overnight and then thawed at room temperature.

4.3.1.4. Synthesis of PANi/PA/PVA SCPHs

We also used a one-pot reaction to polymerize PANi, PA and PVA. Particularly, solution A was mixed by 2000 mg of 10 wt. % PVA solution, 296 μL of 50 wt.% PA solution, 147 μL of purified aniline, 285 μL of 35.5% HCl solution. DI water was subsequently added to form 3 mL of aqueous solution in total. Solution B was made by adding 0.4 mL of 1 wt.% GA and 365 mg APS together, followed by adding DI water to ensure the volume was 1 mL. Then the fabrication and curing procedure for ItG and LpG were the same as for PANi/PVA SCPH.

4.3.1.5. Fabrication of ItOG-based strain sensor

For ItOG as human-motion sensing and health-monitoring application, two droplets of mixed precursor solution were cast on a plasma-treated glass slide into a thin film. Then the mold and glass slide were carefully placed right in contact with the liquid nitrogen. After the ice was completely frozen, the mold and glass slide were kept in -20 □ overnight, melted at room temperature, rinsed with DI water for 2 days, and immersed in EG for 2 days to form organogel. For strain sensor application, the as-prepared ItOG thin film was connected with two silver wires by silver glue and subsequently covered by a thin layer of PDMS precursor solution (10:1 weight ratio of Sylgard 184 Silicone Elastomer). The film with PDMS precursor was kept in 50 □ oven for two hours to complete the PDMS polymerization.

4.3.1.6. Materials characterizations of ItG and LpG

The morphologies of the gel samples were examined with Supra 40VP scanning electron microscope. The chemical compositions were analyzed with Fourier Transform Infrared Spectroscopy and Raman spectroscopy. The strain-stress curves of the gel samples were measured by a DMA, TA Instruments, Q800. The XRD was conducted using Panalytical X'Pert Pro X-ray Powder Diffractometer.

4.3.1.7. Electrical conductivity measurement of SCPH

The conductivity of SCPHs was measured both by impedance using alternating current and direct current. The SCPH samples were fabricated in a plastic tube with a length of 24 mm and a diameter of 6.7 mm. To avoid ionic conduction through the SCPHs during the test, we purified the hydrogels by exchanging water for a week. The hydrogel was sandwiched with two-terminal platinum electrodes and measured with frequencies of 10000 Hz to 0.01 Hz using CHI660E electrochemical workstation (CH instrument). The conductivity was calculated based on real impedance where the phase angle was zero.

4.3.1.8. Sensing measurement of SCPHs

The sensitivity test was carried out by attaching ItOG strip on two carbon cloths at two ends. Then carbon cloth was connected to CHI660E using the two-electrodes system. Strain sensing of the elbow and throat was done by attaching the device directly to CHI660E. The current was detected using i-t mode with a voltage of 0.4 V. The resistance was calculated based on current data in real-time.

4.3.2. Design and synthesis of SCPHs

The ultimate goal is to create highly compact and interconnected conducting polymer (CP) chains intertwined with stretchable polymer chains in a double network. We aim to mitigate the disconnected nano-aggregation, and instead create a hierarchical structure across nano-to-mm scales continuously for enhanced mechanical, electrical, electrochemical, and piezoresistive

sensing properties (Figure 4.2, lower). Our method uniquely combines two key strategies: ice-templating and low-temperature polymerization.

Firstly, we propose to produce an interconnected, densely packed conducting polymer network by using ice as a template. As the ice is formed continuously through a temperature gradient, the polymer along the ice-crystals also generates a well-defined continuous network. In addition, the in-situ ice growth expels the reactants along the ice-crystals, which densify the polymer chains into a tight packing and result in exceptional electrical and mechanical properties. Secondly, polymerizing at low temperature is key to suppressing unintended nucleation. It has also been demonstrated that conducting polymers synthesized at low temperature possess higher crystallinity, fewer defects, and increased molecular weight, leading to a much greater electrical conductivity.

This prior knowledge makes apparent the feasibility and compatibility of simultaneously ice-templating and low-temperature polymerizing both a hydrogel and a conducting polymer. To prove this concept, we use ITLP technique to create the hierarchical and densified structure with less aggregation (Figure 4.2, lower). Specifically, the reactant solution is first directionally frozen under a temperature gradient with liquid nitrogen (-196 ^{o}C). Subsequently, the frozen sample was placed at low temperature (-20 ^{o}C) for polymerization. For comparison, the control sample was fabricated through room-temperature liquid-phase polymerization (Figure 4.2, upper).

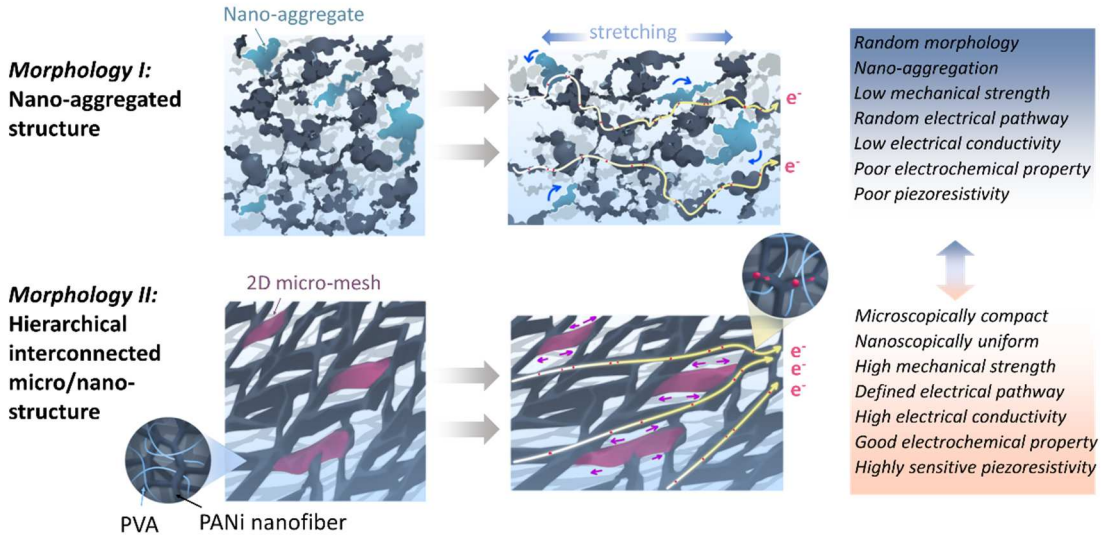

Figure 4.2. Comparison of the morphologies and mechanisms of SCPHs with the conductive components in, respectively, randomly disconnected nanoaggregates (upper, Morphology I, by conventional liquid-phase polymerization) and hierarchically interconnected micro/nano-structure (lower, Morphology II, by ice-templated lower-temperature polymerization). Compared to the former, the latter possess well-defined electron pathways for high electrical conduction. During stretching, the nano-aggregates (sky-blue region) in Morphology I are impeded from deforming in compliance with the bulk material deformation; whereas, the synergic microscopic deformation (pink region) in the hierarchically structured Morphology II can conformably follow and more accurately reflect the macroscopic stretching of the gel, resulting in higher mechanical robustness and sensory capability.

As a representative SCPH, polyaniline (PANi)/PVA hydrogels were prepared by mixing two precursor solutions and reacting them simultaneously (Figure 4.3). As such, aniline was polymerized in the presence of ammonium persulfate (APS), while PVA was chemically crosslinked by glutaraldehyde (GA) both in acidic conditions. The two polymers entangled and formed an interpenetrating network during the *in-situ* reaction. Such a modular material design and fabrication procedure is highly customizable and universal through our successful doping optimization and expansion to diverse polymer systems. Specifically, we optimized the electrical conductivity of the SCPH by utilizing doping engineering, *i.e.,* adding phytic acid (PA) into the precursor solution as the multivalent ionic molecule. Furthermore, we extended this synthesis

method to other stretchable conducting hydrogels (specifically PPy/PVA) and organogels, demonstrating broad applicability across different flexible electronics systems.

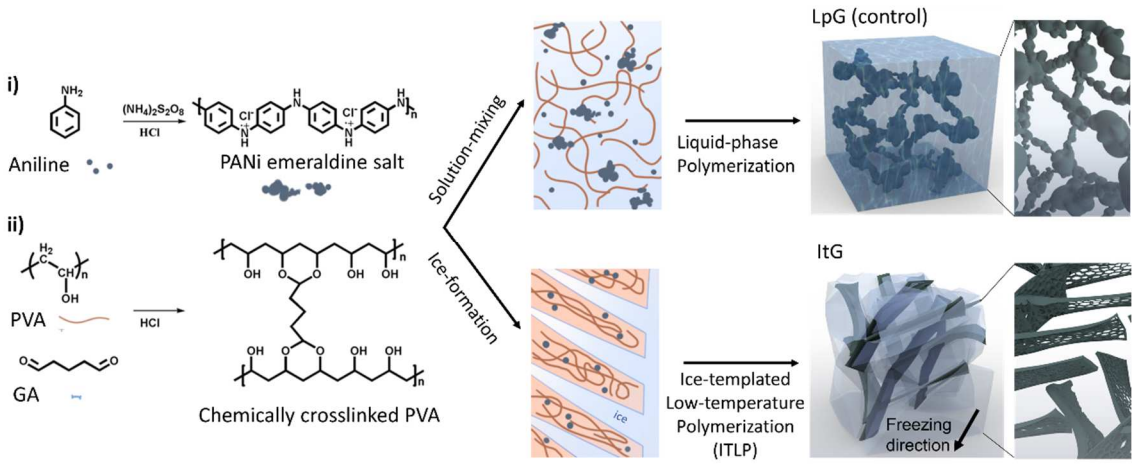

Figure 4.3. Preparation of PANi/PVA-based SCPHs traditional liquid-phase polymerization and ice-templated low-temperature polymerization, leading to morphologies I and II in A. The images of the ItG prepared by the ITLP method show the aligned dendrite microstructure formed with the ice template and the zoom-in view of the branches of the dendrites featuring nano-scale mesh structures.

4.3.3. Material Characterization

The as-prepared PANi/PVA ItGs exhibited remarkable mechanical robustness (Figure 4.4a-c), as they could be easily bent to 180°, stretched to 200% of its initial length, and knotted without breaking. Microscopically, the PANi/PVA ItG displayed a hierarchical structure that was highly ordered from microscale down to nanoscale (Figure 4.4d iv-vi). Specifically, the ItG presented a distinct dendritic microstructure (Figure 4.4d iv), constructed by connected two-dimensional micro-sheets (Figure 4.4d v). Within each micro-sheet are nanofibrils woven into a porous mesh with high uniformity, where the conducting polymer PANi chains are evenly distributed and entangled with PVA chains (Figure 4.4d vi). By contrast, the LpG synthesized with neither an ice-templating nor low-temperature condition possessed irregularly shaped 100 nm-sized nano-agglomerates (Figure 4.4d i-iii) due to the unconfined overgrowth of polyaniline in the liquid phase.

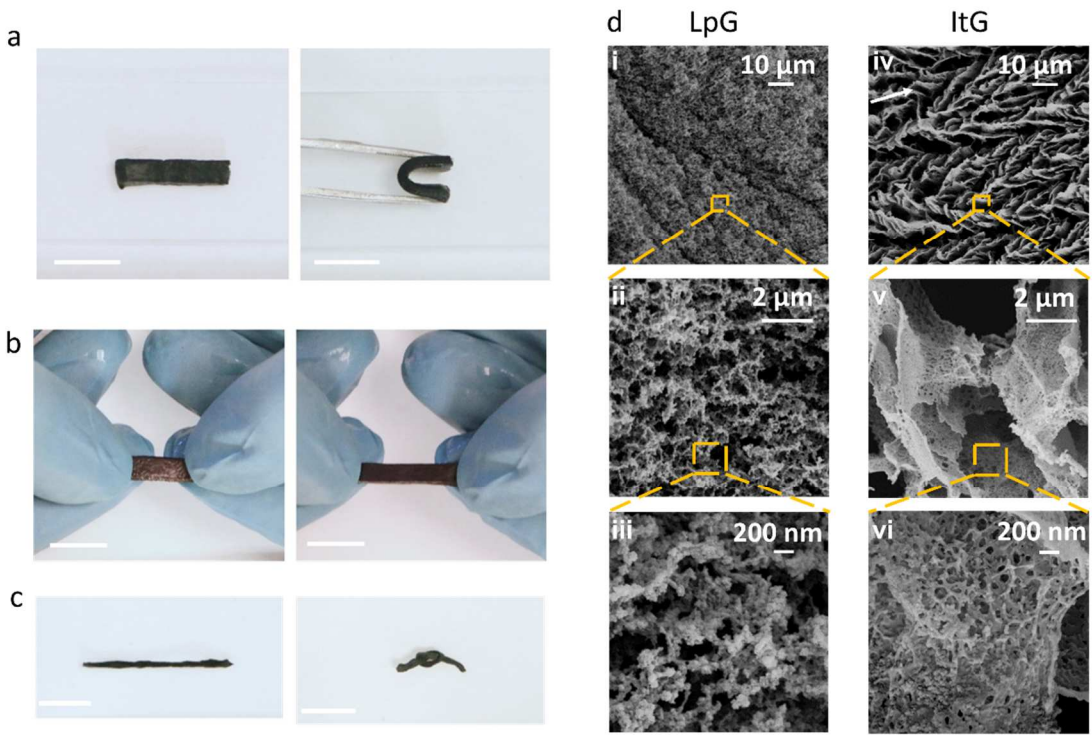

Figure 4.4. Geometrical characterization of ItG and LpG. (a-c) Photographs of ItG show that the gel can be freely bent to 180°, stretched to 100% strain and knotted. (d) SEM images of LpG (left) and ItG (right) at different magnifications. The white arrow in iv indicates the freezing direction.

To investigate the structure formation mechanism, we also synthesized pure PANi (without PVA), to compare ITLP (Figure 4.5a-c) and room-temperature liquid-phase polymerization (Figure 4.5d-f), respectively. The ice-templated PANi presented typically oriented channels, confirming that the morphology of ItG is mainly controlled by directional ice formation; however, they did not exhibit the dendrite structure that PANi/PVA ItG displayed. This confirmed the ice dendrite formation also relied on the presence of a hydrophilic component (PVA here, Figure 4.5b). On the other hand, the room-temperature, liquid-phase synthesized PANi exhibited neither oriented channels nor dendrite structures, instead showing a clustering structure similar to that of PANi/PVA LpG. This indicated that the nano-aggregates were attributed to the presence of PANi (Figure 4.5d-f).

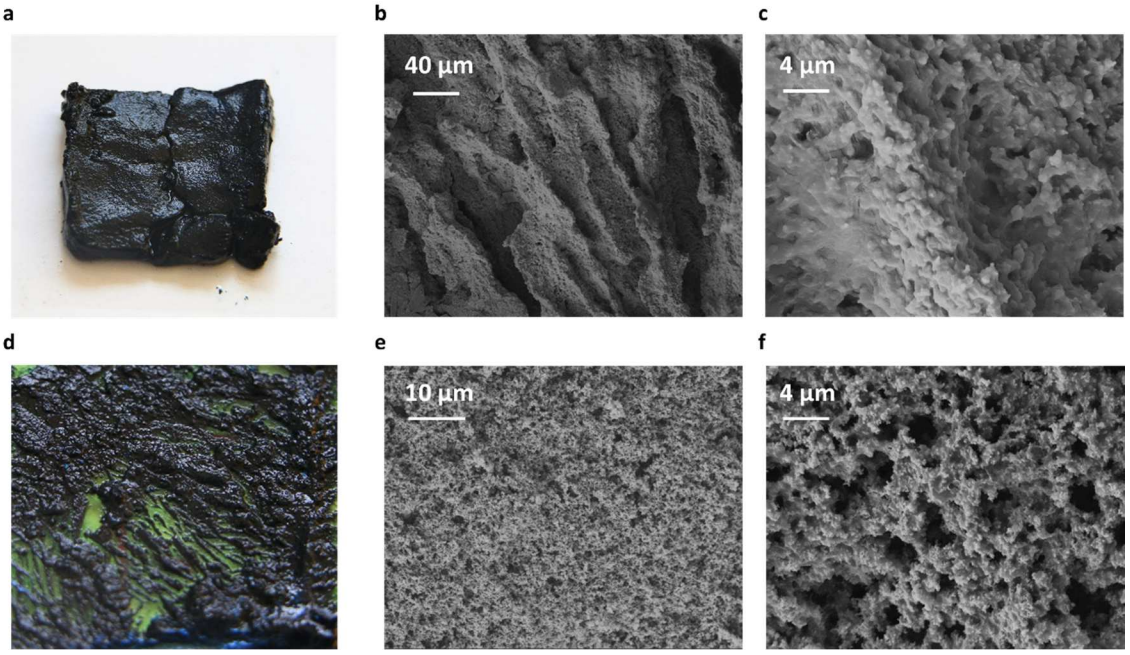

Figure 4.5. Photos and SEM images of pure PANi (without PVA addition) prepared by ice-templated low-temperature polymerization (ITLP) method (a-c) and by conventional room-temperature liquid-phase synthesis followed by freeze-thaw treatment as control (d-f). The ice-templated PANi could form weakly-bonded free-standing hydrogel (a) with well-defined microscale orientation (b). On the surface of the microchannel, the PANi was compactly connected (c). However, the liquid-phase synthesized PANi remained as a viscous slurry (d), because of the loose packing and disconnection of aggregates (e, f).

Fundamentally, these comparisons reveal that such an elaborate hierarchical architecture of the ItG was the result of several mechanisms acting at different length scales. Microscopically, the general morphology was mainly defined by the ice crystals as an effective template and could be easily removed simply by thawing. Typical natural ice has large vertical channels, but here a unique well-connected lamellar structure is formed. Such a structure resulted from the high hydrophilicity of PVA and its fast freezing rate (80-120 µm/s), which require minimum work to create a critical ice nucleus and facilitate the constitutional supercooling of reactant solution.

Nanoscopically, the ice-crystals confined monomers and oxidant agents for aniline polymerization, which facilitated the directional polymerization and also suppressed the growth of the large

crystallites at liquid-solid interface under ultra-low temperature, leading to a nanofibril-connected network. Thermodynamically, the lower temperature (T, in the equation below) resulted in the rise of activation energy (ΔG) and the decrease of the rate constant, hence a controllable reaction kinetics of the polymer chain initiation and growth. These together led to less aggregate formation compared to room-temperature reaction.

$$\Delta G^* = \frac{16\pi\gamma^3 v^2}{3k_B T^2 \left(\ln \frac{C - C_0}{C_0} \right)^2}$$

where △G* is the Gibbs free energy for activation of nucleation, γ is the free energy increase per surface area, v is the volume of each nucleus, k_B is Boltzmann constant, T is the temperature, and C_0 and C are the saturation concentration and actual concentration of the reactants, respectively.

As an extension of this method, using the identical ITLP, PANi/PA/PVA hydrogels led to similar micro/nano-structures as the PANi/PVA hydrogel (Figure 4.6). This demonstrates applicability to a wide variety of components of one's choosing, and also verified the effectiveness of the unique, dendrite-shaped ice template and ultra-low temperature condition to drive the formation of interconnected hierarchical structures for various compositions.

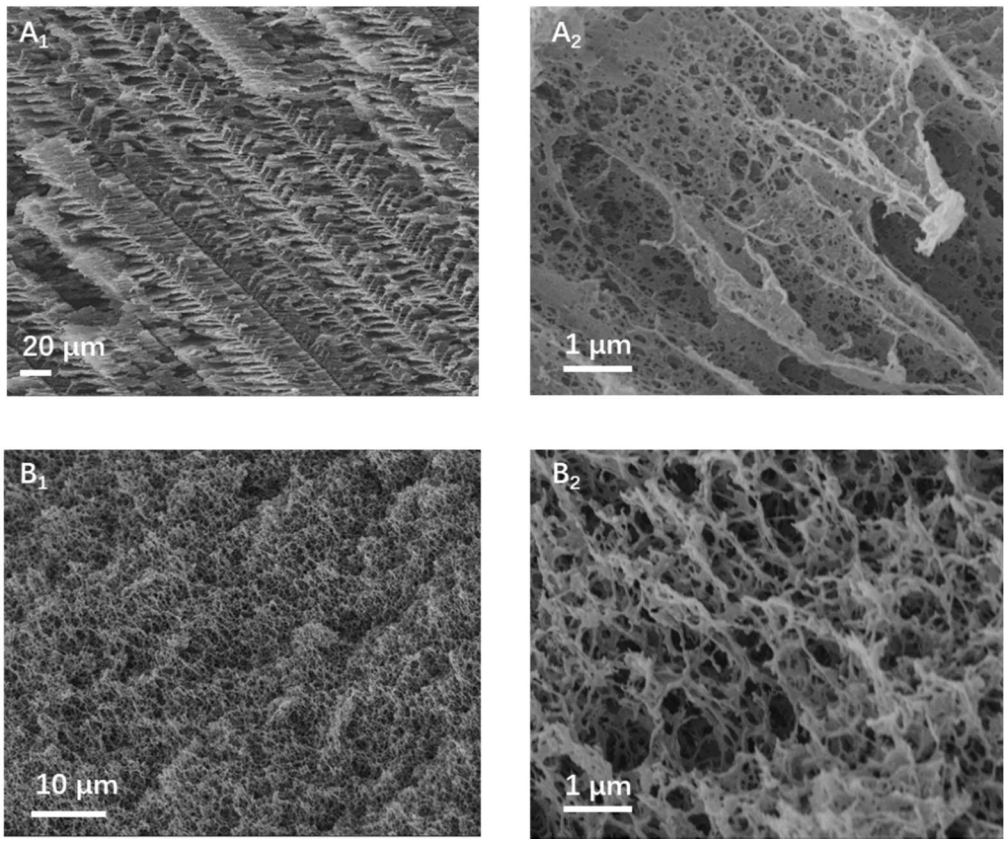

Figure 4.6. Microstructures of PANi/PA/PVA-based ItG (A_1, A_2) and LpG (B_1, B_2) at different magnifications.

To examine whether there were any changes in polymer chemical structures due to the ice-templating process, we first characterized the PANi/PVA-based ItG and LpG with Fourier transform infrared spectroscopy (FTIR) and Raman spectroscopy (Figure 4.7). In FTIR spectra, features at 1638, 1462, 1390, 1290, 1098, and 899 cm^{-1} confirmed that both gels contained typical PANi structures (Figure 4.7a). The peaks at 3449 and 2919 cm^{-1} were attributed to the O-H from intramolecular and intermolecular hydrogen bonds and alkyl groups in PVA. Overall, the ItG and LpG presented identical peak positions according to the FTIR and Raman spectra. This indicated that PANi formed in both gels and there was no obvious difference between the chemical compositions of ItG and LpG. However, the X-ray diffraction (XRD) patterns showed that the ItG possessed a more prominent polyaniline peak compared to the LpG (2 theta=26°), indicating that

the ice-templated gel had substantial close-packing of polymer chains with higher crystallinity (Figure 4.7c), which may suggest their performance differences.

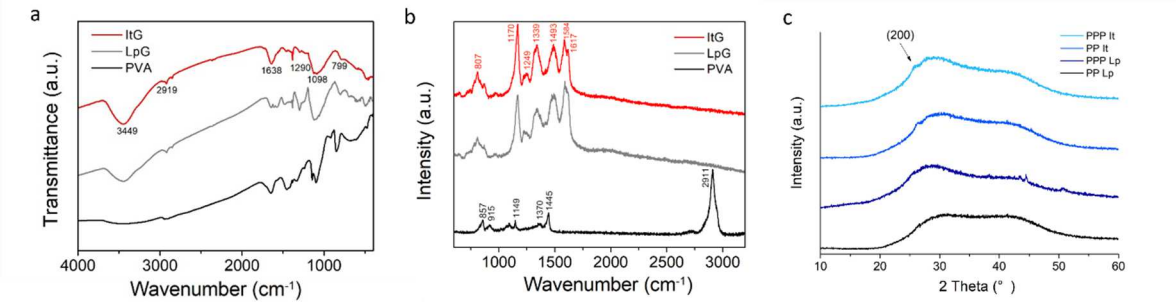

Figure 4.7. Chemical characterization of ItG and LpG. (a) FTIR of ItG, LpG, and PVA in the wavenumber of 400 cm^{-1} to 4000 cm^{-1}. (b) Raman spectra of ItG, LpG, and PVA in the wavenumber of 600 cm^{-1} to 3200 cm^{-1}. (c) The X-ray diffraction patterns of ItGs and LpGs

The mechanical properties ItG and LpG were examined by tensile testing (Figure 4.8, Table 3). The ItG was prepared using a directional freezing process that created an anisotropic morphology, so we conducted stretching tests in both parallel and perpendicular to the alignment direction. Promisingly, the modulus and tensile strength of PANi/PA/PVA ItG parallel to the alignment direction (ItG //) were 119.8 KPa and 118.5 KPa, respectively, which were 12.0 and 12.3 times higher than those of LpGs, demonstrating the effective strengthening in that direction. More importantly, the toughness was improved to 98.2 kJ/m^3, as well, increasing by 29 times due to the ice-templating process. This simultaneous improvement indicates that the hierarchical architecture formed uniformly distributed stiff conducting and elastic hydrogel chains (Figure 4.2, lower) – in contrast to the disjointed aggregates seen in LpG (Figure 4.2, upper) – and can withstand larger forces while being stretched. In addition, the tensile strength and stretchability along the alignment direction were greater than those along the perpendicular direction (ItG ⊥), suggesting that the hydrogel network along the freezing direction had substantial structure integrity with less discontinuity.

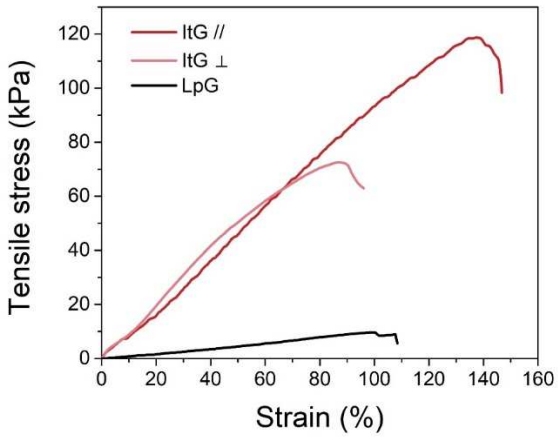

Figure 4.8.Stress-strain curves of ItG and LpG

Table 3 The mechanical performance of PANi/PVA and PANi/PA/PVA hydrogels

Sample	Tensile strength (KPa)	Modulus (KPa)	Toughness (KJ m^{-3})
PP ItG	42.5	45.7	18.8
PP LpG	13.8	7.3	10.1
PPP ItG ⊥	72.6	105.4	35
PPP ItG //	118.5	119.8	98.2
PPP LpG	9.6	8.3	3.4

We measured the electrical conductivity of ItG and LpG using the AC impedance method (Figure 4.9a, b). The conductivity of PANi/PVA ItG along the alignment direction was about 5.99 mS/cm, in contrast to the 0.23 mS/cm of PANi/PVA LpG (Figure 4.9c). The structure modification of ItG presented a 26-fold electrical conductivity enhancement over LpG. After adding phytic acid as dopant, the conductivity of PANi/PA/PVA ItG along the alignment direction was further boosted to 55.5 mS/cm, 83 times of that for PANi/PA/PVA LpG. Using a four-probe measurement, the conductivity of the ItG was 91.0 mS/cm. The conductivity of the PANi/PA/PVA ItG perpendicular to the alignment direction was slightly lower than the parallel direction, presumably due to the

increased structure discontinuity. Notably, this SCPH poses an electrical conductivity comparable to even a pure PANi hydrogel. Similarly, we also measured the electrical conductivity of PPy/PVA gels, showing that ItG experienced a 3.0 times enhancement relative to that of PPy/PVA LpG.

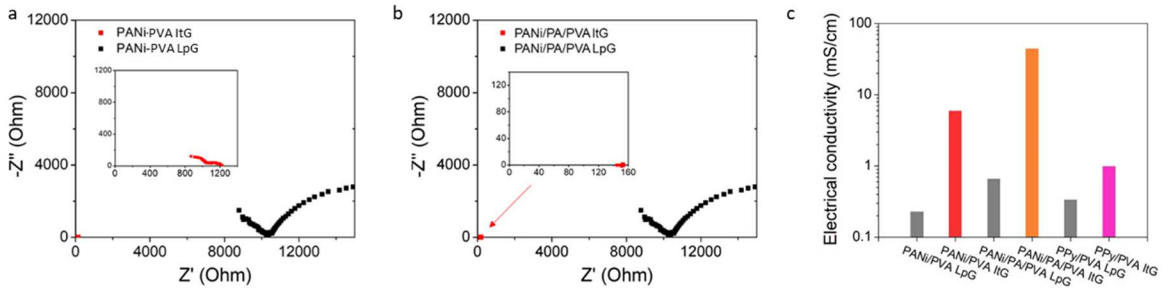

Figure 4.9. Electrical characterizations of LpG and ItG. EIS curves of a) PANi/PVA and b) PANi/PA/PVA gels for electrical conductivity measurement by connecting an SCPH rod-like sample at two platinum electrodes. The conductivity was measured along the freezing direction. (c) The electrical conductivity of ItGs and LpGs based on PANi/PVA and PANi/PA/PVA composites.

To investigate the mechanism behind the electrical conductivity improvement, we synthesized a LpG in liquid phase, but at the same sub-zero temperature condition (by adding lithium chloride in the precursor solution to prevent ice formation). The as-prepared hydrogel demonstrated an electrical conductivity of ~0.45 mS/cm, slightly higher than LpG, but still one order of magnitude lower than ItG. This suggests that the low temperature for polymerization can indeed improve the electrical conductivity, possibly due to a higher molecular weight and crystallinity of conducting polymer. The comparison between LpG and ItG indicates that the drastic conductivity increase of ItG predominantly arises from the hierarchical, interconnected micro-mesh structure induced by ice templating; and the volumetric expansion of the ice crystals would effectively concentrate the reactants into a further denser nano-mesh that provides sufficient percolation of conducting polymer to conduct electrons.

4.3.4. Strain sensors for wearable devices

For stretchable and conductive materials fabricated by nanofiller and elastomer composites, the deformation of aggregated fillers is rather limited during stretching, leading to poor sensitivity. In addition, hydrogel sensors having inevitable ionic conduction suffer from inconsistent resistance changes over time under direct current (DC) due to the ion-derived migration and the formation of electric double layer (EDL). To overcome the aggregation and suppress the capacitance contribution under DC, we explore an ice-templated conductive organogel (ItOG) with uniformly-distributed PANi and solvent exchange from water into ethylene glycol (EG). The ItOG conductor maintained 100.26% of its initial resistance after 400s, presenting ultrahigh stability performance with pure electrical conduction behavior (Figure 4.10).

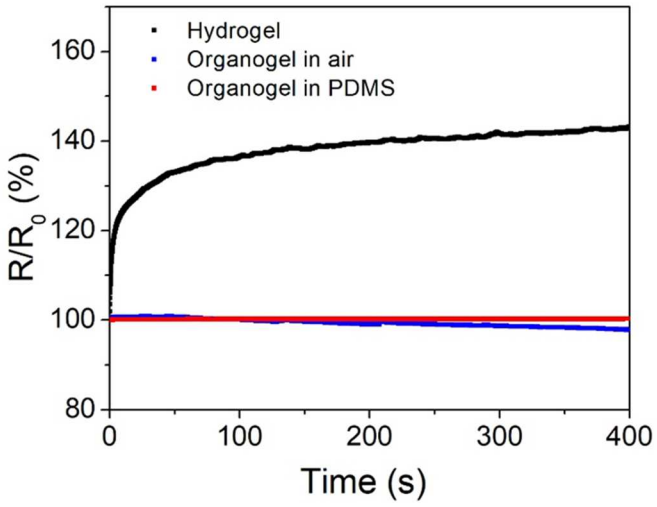

Figure 4.10 Resistance variation of ice-templated PANi/PVA hydrogel (containing water) and organogel (with ethylene glycol instead of water) at different conditions. The hydrogel sample had a great resistance increase due to the formation of the electrical double layer. Organogel sealed in PDMS kept a consistent resistance over the 400s testing duration (even more stable than the organogel without PDMS in air), indicating the pure resistor property.

As the ItOG conductor was stretched while connected to a circuit to measure the resistance, the resistance displayed a continuous and linear increase as the strain increased (Figure 4.11a, b). The

gauge factor ($GF=\Delta R/R_0*\varepsilon$), defined as the ratio of relative resistance change to strain, was as large as 1.43, which is higher than PEDOT/PVA and graphene/PAAm sensor at the corresponding stretching ratio. The gauge factor of ItOG was 1.82 times relative to the liquid-phase synthesized organogel sensor (LpOG). The improved sensitivity is attributed to the mitigated nano-aggregation and thus the enhanced deformation adaptability. Under repetitive stretching and relaxing at strain rates ranging from 0.6%/s to 1.8%/s, the resistance changed periodically and rapidly, capable of reliable, real-time strain sensing (Figure 4.11c). The sensor had over 95% resistance retention after 500 cycles of stretching and recovery (Figure 4.11d). Overall, the ItOG conductor showcased a large range of operations, desirable linearity, high sensitivity, and reversibility, as an ideal material for a high-performance strain sensor.

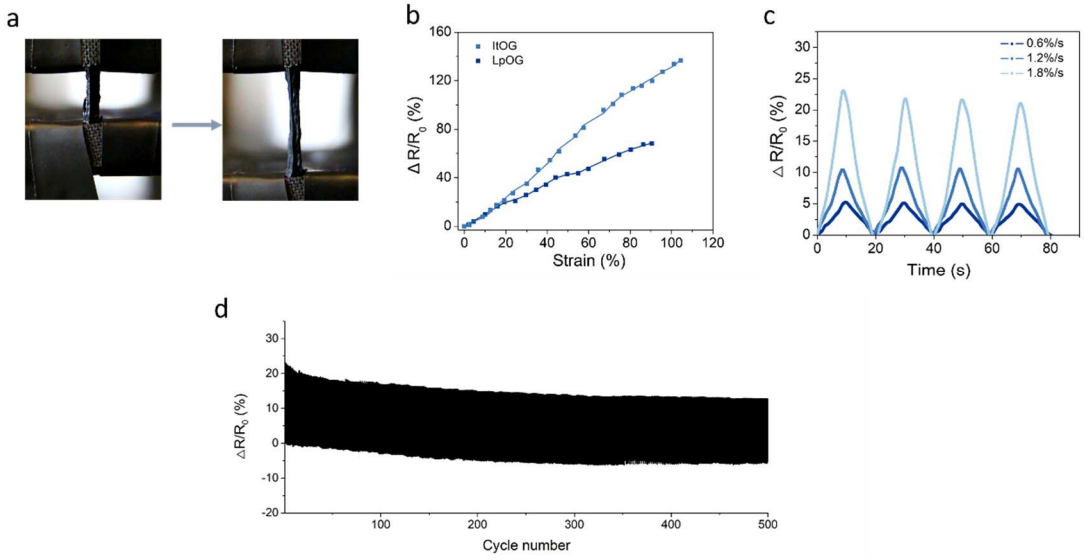

Figure 4.11. Sensing characterizations of ItOG. (a) Photos of ItOG during stretching to measure strain sensitivity. (b) Resistance change (%) upon stretching for PANi/PVA-based ItOG and LpOG. (c) Strain response of ItOG under different stretching rates. (d) The cyclic stretching and recovery test of sensor over 500 cycles.

With such excellent sensing properties, we equipped strain sensors to monitor human body movements. We attached the PDMS-sealed ItOG to a human elbow (Figure 4.12**a**) and the sensor easily conformed to the skin surface – a result of ItOG's high stretchability, flexibility, and light-

weight. We monitored the change in resistance of the sensor during instant bending and gradual straightening of the elbow, presenting well-defined sensitivity and reliability (Figure 4.12**b**).

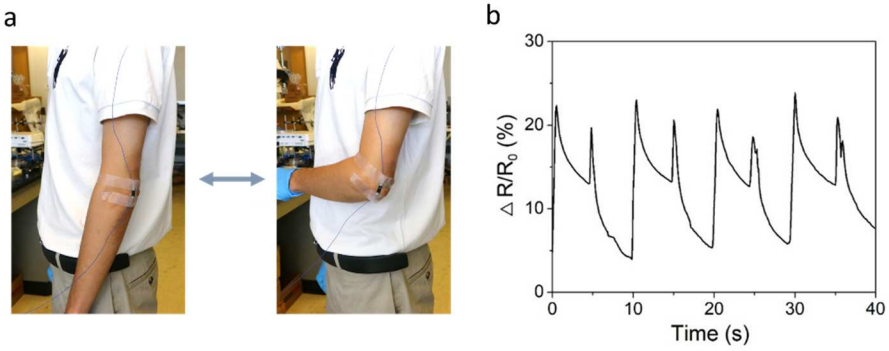

Figure 4.12. Human motion sensing characterization (a) Human motion sensing by attaching ItOG-based sensor on elbow. (b) Sensing of reversible bending and straightening of elbow motion by the sensor.

Furthermore, we examined the sensing performance for recognizing small-scale human motion by attaching the sensor to a human throat (Figure 4.13a). Since the intensity and shape of the signal varied with different motions, we can identify the different motions from the characteristic readout signals of the sensor. Particularly, the heart rate of the human is precisely read by the adjacent lower limit, calculated to be approximately 96 beats/minute. During one typical waveform of a heartbeat, the systolic peak (SP), dicrotic notch (DN) and diastolic peak (DP) were accurately identified (Figure 4.13b). In addition, the sensor could clearly detect respiratory signals during each inhalation-exhalation cycle, swallowing and speaking according to the characteristic pattern and intensity of each movement (Figure 4.13c-e). Overall, combined with the broad sensing range, linearity and sensitivity, ItOG strain sensor can simultaneously monitor multiple daily activities of humans with both small and large strain windows.

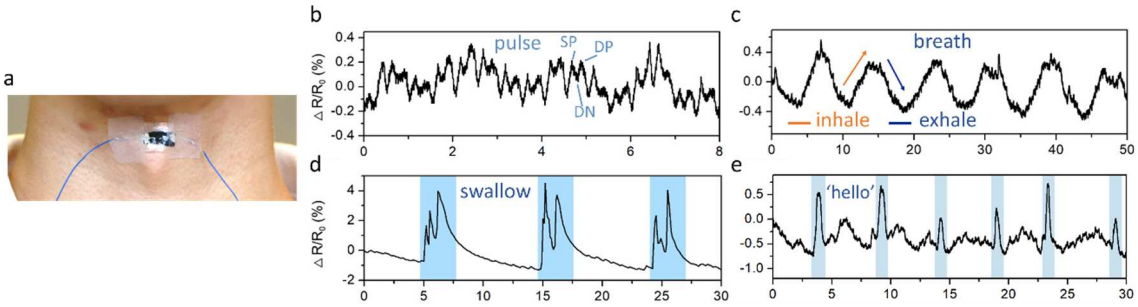

Figure 4.13 Health monitoring demonstration. (a) Health monitoring by attaching ItOG-based sensor on throat. (b-e) Sensing of human pulse, breath, swallowing and speaking by the sensor on the throat.

4.3.5. Discussions and conclusions

This work demonstrates a novel method of ice-templating low-temperature polymerization to synthesize SCPH with a hierarchical architecture comprised of a dense, interconnected, nano-fiber micro-network. Unlike the aggregation widely observed as a consequence of composite fabrication, the uniform and mesh-like distribution of conducting polymer in the elastic networks provides enhanced mechanical robustness, and a well-defined and continuous electrical conduction pathway. Utilized as strain sensors, the conducting hydrogels with less-aggregated structures can accurately capture minute mechanical deformation by transducing piezoresistive signals. In particular, human motions of both large and small strains can be monitored in real-time, demonstrating outstanding broad-range sensory capabilities.

4.4. Molecular integration of sensing and actuation into a somatosensory actuator

4.4.1. Experimental and characterization Section

4.4.1.1. Materials

N-isopropylacrylamide (NIPAAm, ACROS Organics™) was purified by recrystallization from the mixture of hexane and acetone (1:1) and dried in a vacuum, N,N'-methylenebis(acrylamide) (BIS, Aldrich), ammonium persulfate (APS, ACROS), aniline (Ani, Sigma), Phytic acid solution (50% in H_2O, Fisher), dimethyl sulfoxide (DMSO), 2-hydroxy-2-methyl-1-phenyl-1-propanone (Darocur 1173, TCI America), Polyvinyl alcohol (PVA, molecular weight = 8.9-9.8 x 10^4, 99% hydrolysis degree, Sigma), glutaraldehyde (GA, 50% in H_2O, Fisher).

4.4.1.2. Synthesis of ITUC hydrogel

We used a one-pot reaction to polymerize the PANi and PNIPAAm together. Typically, 500 mg NIPAAm, 5, 10, 15, or 20 mg BIS (0.2, 0.4, 0.6, or 0.8 wt%), 183 μL of purified aniline, 100 μL Darocur 1173, and a certain amount of DMSO were mixed into 2 mL solution, denoted as Solution A. Then, 365 mg APS was dissolved in 1 mL water solution, denoted as Solution B. 2 mL of Solution A and 0.5 mL of Solution B were rapidly mixed, cast into a 3D printed mold, and placed in contact with liquid nitrogen for freezing. Then, the frozen sample was illuminated under UV light for 20 minutes to polymerize PNIPAAm while kept on the surface of a -20□ cooling stage to avoid melting. Subsequently, the sample was transferred in a -20□ fridge to complete the cryopolymerization of PANi. Finally, the sample was taken out to melt, and immersed in deionized water to remove excess reactants and salts.

4.4.1.3. Synthesis of UT hydrogel

The solutions used were the same as in the ITUC method. The mixture of Solutions A and B was cast into a PDMS mold, and covered with a glass slide. Then, UV light was applied to the mixed precursor solution to polymerize PNIPAAm (at room temperature, in the liquid phase). Subsequently, the sample (PNIPAAm hydrogel containing the remaining PAni reactants) was left

overnight to complete the thermal polymerization of PANi (also at room temperature, in the liquid phase). The as-prepared sample was soaked in DI water to remove excess reactants and salts.

4.4.1.4. Synthesis of ITUL hydrogel

The solutions used were the same as in the ITUC method. The mixture of Solutions A and B was cast into a 3D-printed mold and placed in contact with liquid nitrogen for ice-templating. The PNIPAAm was polymerized still under UV light on a -20□ cooling stage. Then, the sample was placed at room temperature to let the sample melt and the PAni to be polymerized in a liquid state.

4.4.1.5. Syntheses of ITU in-situ hydrogel

The Solution A excluding the aniline was used to create a PNIPAAm hydrogel first. The ice-templating and polymerization of PNIPAAm at the frozen state were controlled in the same way as we fabricated the ITUC and ITUL hydrogel. Afterward, the PNIPAAm gel was placed in a reacting PAni solution (365 mg APS dissolved in 1 mL water) for in-situ polymerization of PAni in the hydrogel network. The detailed procedures of all the above hydrogels are summarized in Table 4.

Table 4. Comparison of CP-PNIPAAm hydrogels fabricated by different methods

Samples	Step 1	Step 2	Step 3
ITUC	**I**ce-**t**emplating of solution	**U**V polymerization of PNIPAAm	**C**ryopolymerization of PAni
UT	**U**V polymerization of PNIPAAm	**T**hermal-polymerization of PAni at RT	
ITUL	**I**ce-**t**emplating of solution	**U**V polymerization of PNIPAAm	**L**iquid-phase polymerization of PAni at RT
ITU in-situ	**I**ce-**t**emplating of solution	**U**V polymerization of PNIPAAm	**in-situ** polymerization of PAni by placing the PNIPAAm gel in reacting PAni solution

4.4.1.6. Synthesis of PNIPAAm hydrogel in water solution (WaterH)

PNIPAAm hydrogel using water solvent was synthesized by free-radical polymerization of NIPAAm monomer crosslinked with BIS using APS as initiator and TEMED as accelerator at 4□. Specifically, 0.85 g of NIPAAm and 7 mg of BIS were dissolved in 5 mL deionized water. Then, 115 μL of APS aqueous solution (10 wt%) and 20 μL of TEMED were added and mixed thoroughly.

The precursor was then rapidly transferred into molds with desired shape and sealed to allow gelation to occur.

4.4.1.7. General characterizations

Scanning electron microscopy (SEM) micrographs were taken by Zeiss Supra 40VP SEM. The hydrogel samples were frozen in liquid nitrogen, lyophilized and then coated with gold by a sputter coater before being observed by SEM. The mechanical properties of hydrogels, including the stress-strain behaviors and Young's modulus (E), were investigated by a dynamic mechanical analyzer (DMA, TA Instruments, Q800).

4.4.1.8. Actuation characterization

For the swelling and deswelling test, we cut the hydrogel film into a circle and measured the diameter change during heating and cooling. To fabrication the soft gripper, we post-treated the ITUC gel by growing a chemically crosslinked PVA film as a passive layer. The precursor solution was made by mixing 1 g 10% PVA solution, 50 μL HCl solution and 200 μL 1% GA aqueous solution. Then the mixed solution was applied on ITUC gel and covered by a glass slide with a 1 mm spacer. For the object grasping test, the hydrogel strip was tightly attached with two carbon cloth wires at two ends. Then we dropwise the PVA precursor solution on the attaching point for encapsulation.

4.4.1.9. Electrical and sensing characterization

The strain sensing test was carried out by connecting the hydrogel to an electrochemical workstation CHI660E. For measuring the conductivity, the hydrogel film was attached on two parallel carbon cloth wires with a certain distance (L). The AC impedance mode with the frequency sweep from 1-100000 Hz was conducted. The resistance (R) was selected when the phase angle reached 0^{o}. The conductivity was calculated according to the formula: $\sigma=L/Rwt$, where w and t were the width and thickness of the sample. Strain-sensing experiments were carried out by

mounting the hydrogel on a stretching machine (Univert, CellScale) while connecting the two ends into a circuit. For testing the compression and bending sensitivity, the two ends of the hydrogel were attached with carbon cloth wires as electrodes and clamped using a glass slide as a spacer. For proprioceptive shrinking test, we clamped the ITUC gel and carbon cloth wires with a glass spacer. For proprioceptive bending test, the carbon cloth wires were attached on ITUC gel by encapsulating PVA on then.

4.4.1.10. Closed-loop control for adaptive actuation

The sample of the proposed material is shaped as a strip and installed vertically with a weight attached at the bottom. The sample strip narrower than the NIR laser spot size was selected to ensure a more uniform and constant illumination power density upon contraction. The vertical deformation of the sample is controlled by the variation of its stress force, actuated with a laser pointer. The electrical resistance of the sample is measured by a source meter and converted to its vertical deformation through static mapping. It is then sent to the bang-bang controller with a gain scheduler on the target PC to regulate the laser intensity through Arduino.

The real-time sample strain was monitored with a digital camera, recorded as videos, and analyzed with a tracker tool developed by Open Source Physics (OSP) Java framework. The controller is developed with Python script. Three deformation regions are selected and the saturation boundaries of laser intensity is scheduled for each region to deal with actuation nonlinearity. An experiment is conducted for deformation tracking, where the reference signal includes three (A, B, and C) different stages and is ordered in a stepwise ABCBA manner. A complete reference cycle holds at each stage for 300 seconds, and then back to the natural position for deformation reset.

4.4.2. Fabrication and material properties

Traditionally, to obtain a CP-hydrogel composite, people used a two-step synthesis method. Due to the incompatibility of the two syntheses, a hydrogel is formed and subsequently soaked in a CP

prepolymer solution to in-situ polymerize the CP around existing hydrogel chains. However, the sub-micron-sized pores of hydrogels hardly allow for sufficient penetration of CP molecules into the entire hydrogel matrix, which results in a CP-rich shell and a non-conductive core, hindering its application in sensing and actuation (*i.e.*, the ITU in-situ gel). To solve the inhomogeneity issue, we designed a one-pot polymerization technique, whereby the PNIPAAm and PAni precursor mixture was first irradiated under UV light to polymerize PNIPAAm and then kept at room temperature overnight to polymerize PAni (Figure 4.14**a**). The UV- and thermally-polymerized hydrogel, referred to as a **UT gel**.

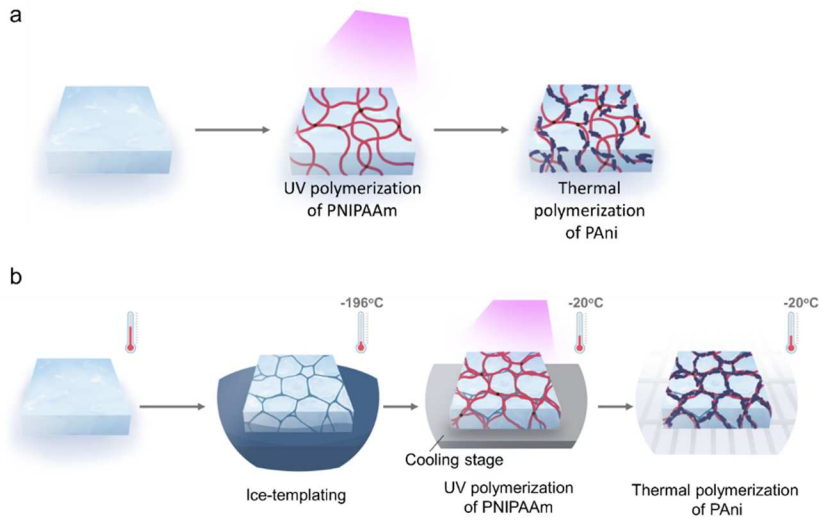

Figure 4.14. Schematic of the fabrication process of UT gel and ITUC gel. Specifically, NIPAAm, BIS, and photo-initiator were used for UV polymerization of PNIPAAm hydrogel, while aniline, ammonium persulfate, and phytic acid could thermally form crosslinked PAni network. (a) For UT gel synthesis, after mixing the above agents, the sample was illuminated under UV light to initiate the polymerization of PNIPAAm. Subsequently, the hydrogel was kept at room temperature overnight to complete the thermal polymerization of PAni. (b) Fabrication of ITUC gel includes the ice-templating after a rapid mixture of the solution, UV polymerization of PNIPAAm and cryopolymerization of PAni.

We measured the conductivity of the UT gels using the AC impedance method first, to minimize the potential electrical double layer (EDL) capacitance due to possible dominant ionic conduction. The conductivities ranged from 0.034-0.06 mS/cm at 0.2~0.8 wt.% BIS crosslinking densities

(Figure 4.15**b**). Under direct current (DC), however, the resistance of the UT gel (1 cm × 2 cm × 0.1 cm) was still unstable over time and at the scale of 1 MΩ, which was close to that of pure water and was therefore unable to accurately reflect the material deformation if it were to serve as a strain sensor. Mechanically, the elastic moduli of the UT gels were 14~44 kPa from the tensile stretching tests (Figure 4.15**c**). Despite the high loading of CP (0.8 M PAni with 20 wt.% of PNIPAAm), the resulting conductivity and mechanical properties were relatively low, compared to pure PAni hydrogels (conductivity=110 mS/cm)[97]. This necessitated modification to further boost the conductivity to 10-100 mS/cm and the modulus to 0.1-1 MPa, to deliver high-performance sensing and powerful actuation. We speculate that the introduction of the non-conducting PNIPAAm and high-water content in the polymer matrix might have impeded the conductive pathway. Meanwhile, the liquid-phase polymerization gels suffered from uncontrollable reaction kinetics, leading to the formation of disconnected CP nano-aggregates, and so, lacked the desirable compact and interconnected packing needed to ensure continuous electron transport and mechanical strength[98].

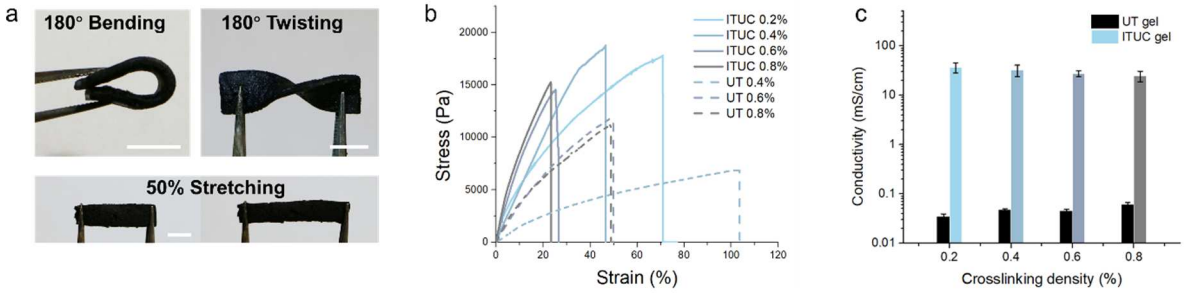

Figure 4.15. Material characterizations of ITUC gels. (a) Images of ITUC gel during bending, twisting and stretching. (b) Strain-stress curve of the ITUC gel and UT gel (control sample, without ice-templating) with difference crosslinking densities. (c) Conductivities of the ITUC gels and UT gels.

To produce dense CP chain packing at micro/nano scale, we modified the UT synthesis by introducing ice-templating and cryopolymerization for PAni (Figure 4.14**b**). Specifically, the mixed solution was rapidly frozen under liquid nitrogen (-196□) to form an ice-template, followed by UV- and cryo-polymerization of PNIPAAm and PAni, respectively, in a sub-zero environment

(-20□). The as-prepared gel is referred to as **ITUC gel**. The modified ITUC gel was much more robust mechanically, capable of bending freely to 180°, being stretched, and twisted to 180° without causing any material damage (Figure 4.15**a**). From the tensile tests, the ITUC gels with different crosslinking densities (BIS concentrations) showed a tunable tensile strength up to 0.18 MPa and a 250%-386% modulus enhancement over the UT gels (Figure 4.15**b**). Meanwhile, the ITUC gel with 0.2 wt.% BIS presented decent deformability with up to 170% stretch at break, suggesting a broad strain sensing and actuation range. At the same time, the ITUC gels exhibited remarkably high conductivities of 24.6-36.8 mS/cm, which were $>10^3$ times higher than those of UT gels (Figure 4.15**c**).

For more clearly identify the key factors that enabled the high conductivity, we have also made another two control samples by, respectively, UV-cryopolymerizing PNIPAAm followed by liquid-state polymerizing PAni from the PNIPAAm-PAni precursor mixture (denoted as ITUL gel), and UV-cryopolymerizing PNIPAAm followed by immersing in PAni precursor and in-situ polymerizing PAni in liquid state as well (denoted as ITU in-situ gel) (Figure 4.16). It showed that both the mechanical property and conductivity of the ITUC gel were significantly improved, compared to properties of UT, ITUL, ITU in-situ (Figure 4.17). The tremendous enhancement of conductivity can be attributed to the ice densification effect and low-temperature reaction of PAni that allowed for substantially denser packing and effectively mitigated nano-aggregation of PAni, facilitating a continuous electronic pathway (as experimentally compared to ITUL gel with liquid-state polymerization of PAni).

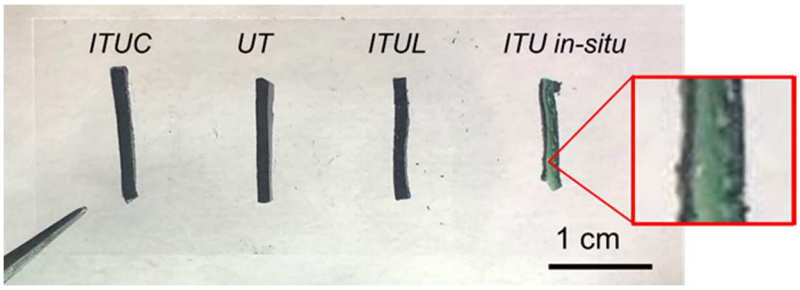

Figure 4.16. Images of hydrogels made by different methods in the cross-sectional view. The ITUC, UT, and ITUL hydrogels were structurally homogeneous across the thickness direction. However, ITU in-situ hydrogel fabricated by the traditional two-step in-situ polymerization method showed a semi-transparent inner part of the hydrogel, indicating the poor CPs percolation.

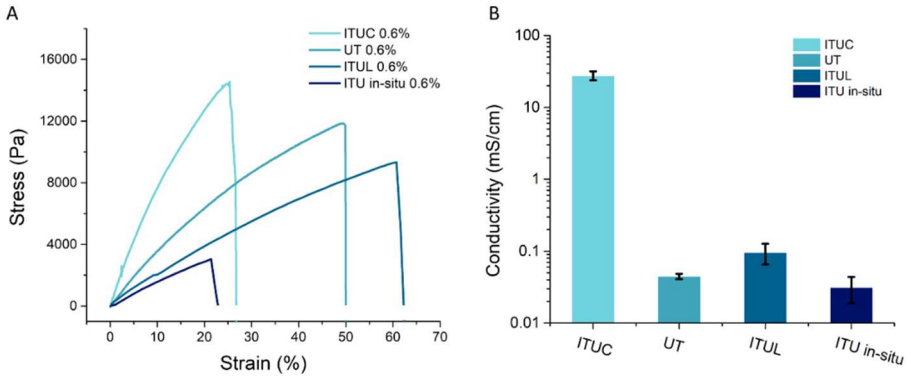

Figure 4.17. Mechanical properties and conductivities of the CPs-percolated stimuli-responsive hydrogels made by different methods.

The SEM images also clearly showed the more compact microstructure with more uniform pore sizes 0.5-2 μm, in contrast with 5-10 μm pores of UT gel (Figure 4.18).

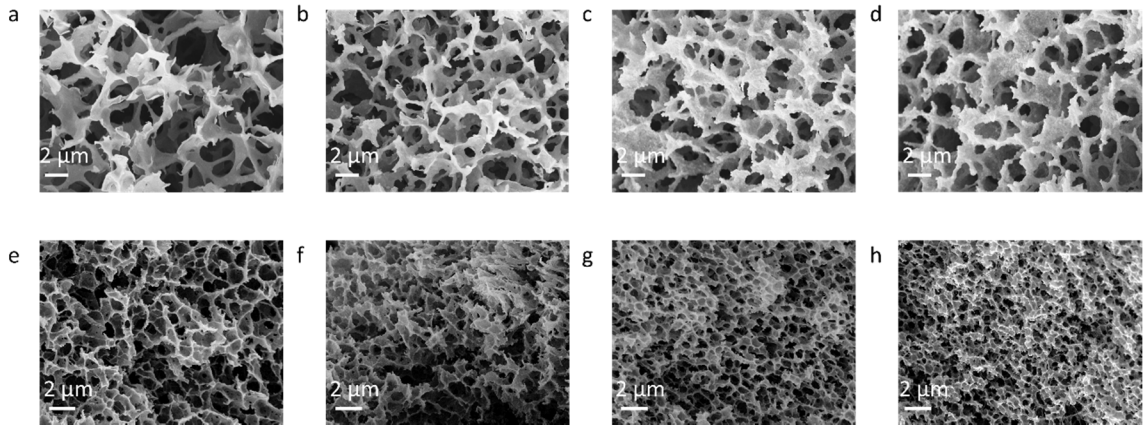

Figure 4.18. SEM images of UT gels (upper row) and ITUC gels (lower row) with different crosslinking densities. (a-d) were UT gels with BIS concentration of 0.2%, 0.4%, 0.6% and 0.8%. (e-h) were ITUC gels with BIS concentration of 0.2%, 0.4%, 0.6% and 0.8%.

Besides, the stability of the ITUC gel constantly soaking in water over time was studied, showing ~46% conductivity drop after a week (Figure 4.19), which is presumably due to the loss of dopant (phytic acid here) under the long-term neutral pH condition. By incorporating PVA in the existing ITUC gel, improved electronic stability has been achieved (~74% conductivity retention), presumably due to the strong hydrogen bonding of PVA to stabilize the dopant phytic acid (Figure 4.19). Further stability improvement studies will be conducted in future research.

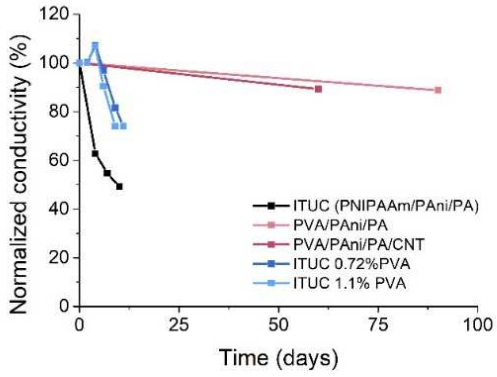

Figure 4.19. The normalized conductivities of different conductive hydrogels.

4.4.3. Actuation performance

To examine the actuation capability of the ITUC hydrogels, we analyzed the hydrogel shrinkage at 40□and recovery rate at room temperature. The ITUC gel (thickness = 0.1 cm) shrunk up to 49.7% within one minute, with a diffusion time scale (duration of shrinkage to 1/*e* of its initial volume) of 8 seconds (Figure 4.20). Notably, although the hydrogel network was toughened by an ice-induced polymer densification effect, the responsive actuation performance was not significantly compromised, compared to the UT gel. Promisingly, the shrinking of the ITUC gel was 10-100 times faster than that of the conventional hydrogels on a scale of minutes to hours. The significantly fast volume changes of our hydrogels arise from the bicontinuous microstructure with open pores, featuring a unique low tortuosity that facilitates rapid water diffusion in and out of the polymeric network, and thus swift actuation is shown as follows.

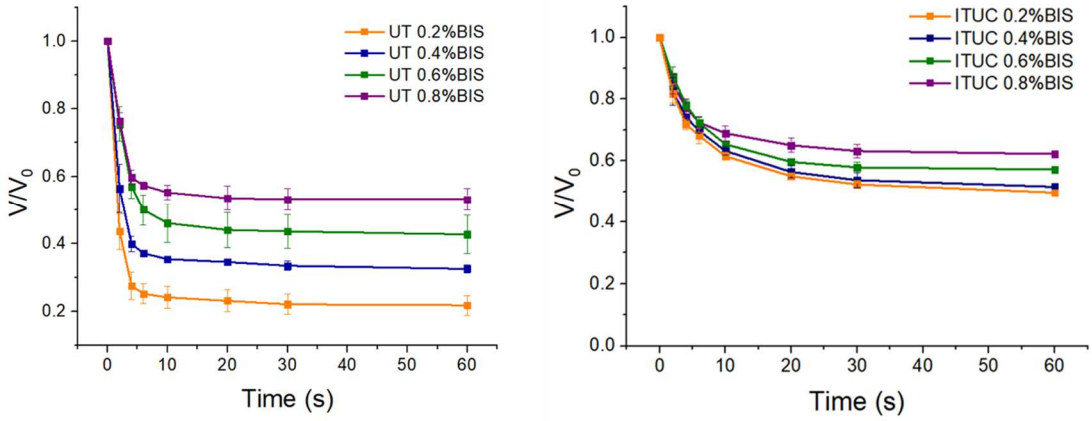

Figure 4.20. The deswelling rate of UT gels and ITUC gels with different crosslinking densities. The samples were placed in 40□ water while being monitored for diameter changes.

The composite hydrogels can be actuated not only by heat but also by light via the photo-thermal-mechanical mechanism due to the photothermal property of PAni. Under NIR light irradiation, the ITUC gel could effectively shrink and lift a weight of up to 171.6 times of its dry polymer weight (Figure 4.21**)**. The hydrogel strip with dimensions of 3.41 mm × 1.36 mm × 7.36 mm can produce a force of 0.055 N and strength of 10.7 kPa, which is 20-time higher compared to conventional PNIPAM hydrogels.

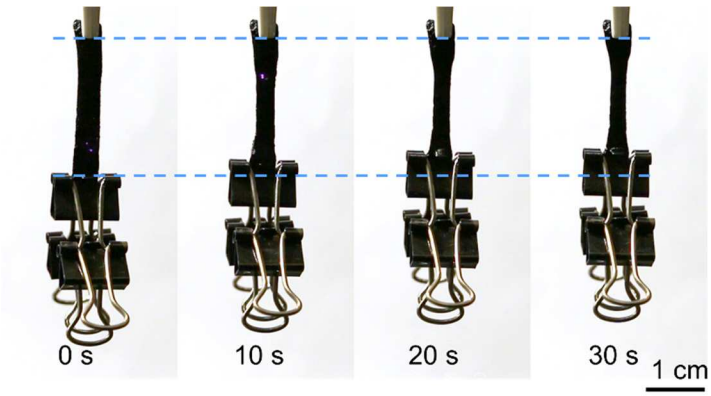

Figure 4.21. Load lifting of ITUC gel under NIR illumination in air.

Furthermore, as the composite hydrogels are chemically homogeneous without any composition gradient or interface like those in conventional physically-integrated systems, they allow for actuation in almost all directions with nearly infinite degrees of freedoms (DOFs). When a NIR light shined on the hydrogel strip at an arbitrary angle, the hydrogel bent towards the incoming light and precisely maintain tracking of the light source via real-time autonomous reorientation (Figure 4.22a). The hydrogel could rapidly recover its original un-deformed configuration when the light was off (Figure 4.22b). As depicted in our simulated graphs with our multi-physics model that coupled the photo-thermal-stress fields, such a directional, asymmetric motion was attributed to the temperature gradient across the hydrogel, where the temperature on the illuminated side increased to above the LCST while the temperature on the shaded side still remained below the LCST, resulting in the local shrinking on the illuminated side and the overall bending of the gel. Once the bending strip reached the light's direction (in that it was parallel to the incident light), it steadily aimed at the incident light controlled by a built-in feedback loop arising from the dynamic light-material interaction. Such an autonomous signal-tracking behavior demonstrated a decentralized, open-loop self-controlled actuation.

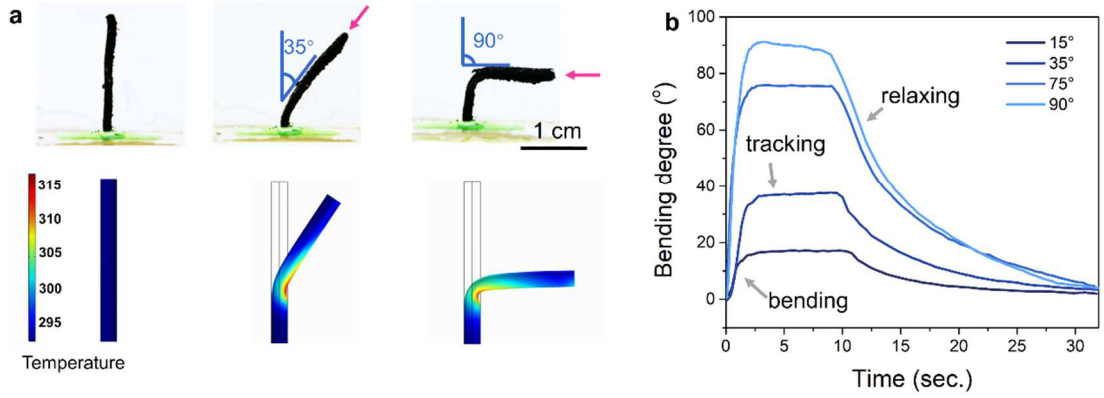

Figure 4.22. Phototropic behavior of ITUC gel that automatically track the light. (a) The gel pillar is exposed to a NIR light and the corresponding computer simulation results based on multiphysics model that captured both the bending angle and kinetics. (b) The angular evolution of hydrogel tracking to different oblique angles.

Apart from the object tracking achieved by the temperature gradient, we also demonstrated that the ITUC gel can bend to a defined direction under elevated temperature by seamlessly adhering the gel with a passive layer in a bimorph assembly (Figure 4.23). By assembling four hydrogel arms, we successfully fabricated a cross-shape soft gripper, which could rapidly grasp an object in hot water. This bimorph also showed that the materials can be facilely combined with other materials to construct a system for complex tasks.

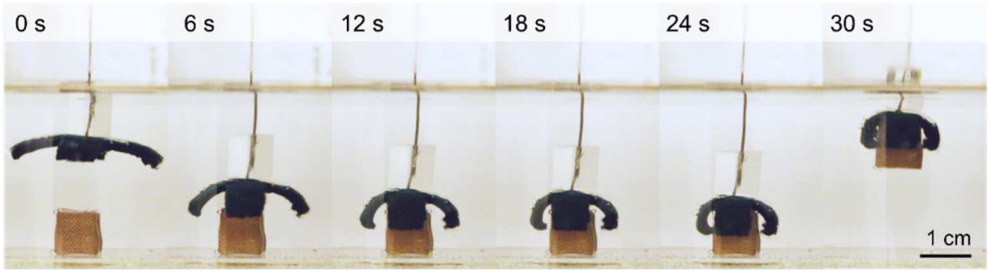

Figure 4.23. Sequential snapshots of the object grasping using the ITUC gel with a PVA passive layer in 45□ hot water.

4.4.4. Sensing performance

The ITUC hydrogel provides high conductivity with stretchability, capable of serving as a piezoresistive strain sensor under mechanical deformation. First, the ITUC gel showed a desirable 0^o phase angle at a broad AC frequency range, whereas the UT gel had a $>40^o$ phase angle at low frequency (Figure 4.24c). The high phase angle in the UT gel indicated more ionic conduction, leading to the electrochemical reaction at the electrode interface. Second, the ITUC gel showed a desirable <0.4% resistance change over 400 seconds at direct voltage, in high contrast to the >650,000% large change of the UT gel (Figure 4.24a). Furthermore, the current-voltage (I-V) curve of the ITUC gel was an ideal symmetric straight line, while the UT gel showed a capacitive behavior with an enclosed area (Figure 4.24b). All these together indicated that the conductivity of the ITUC hydrogel was dominated by ohmic electronic conduction with minor ion-derived conduction, which is highly desired for high sensing performance. This also showed the effectiveness of this new material synthesis method in solving the aforementioned issues of low electronic conductivity presented by UT gels and conventional conductive gels.

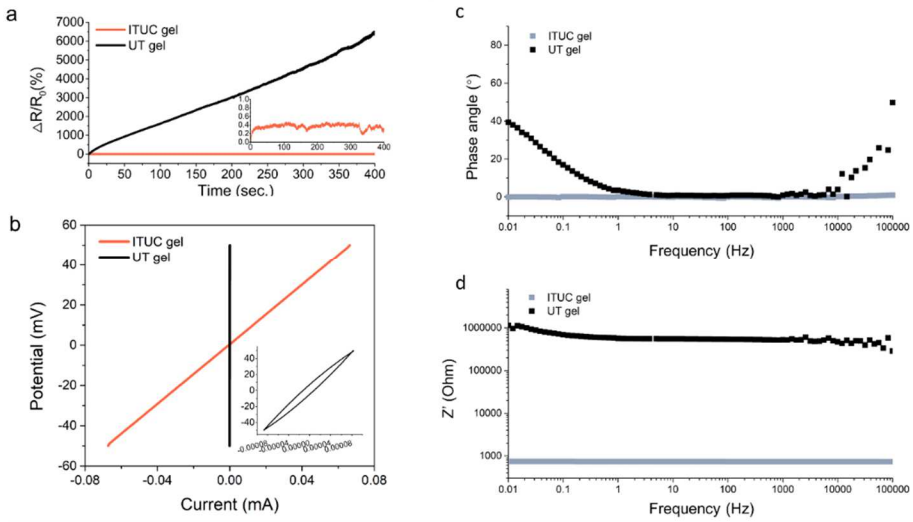

Figure 4.24. Electrical characterizations of ITUC gel and UT gel. (a) The resistance of ITUC gel and UT gel over time. The inset shows the zoom-in resistance change for ITUC gel. (b) The current-voltage sweep of ITUC gel and UT gel from -50 mV to 50 mV. (c) The comparisons of phase angles and (d) real impedance between UT gel and ITUC gel.

The ITUC gels with high stretchability and responsiveness enabled not only the exteroception to sense passive deformations, but also the proprioception to monitor its own motion internally in response to stimulation. For exteroception, we first carried out the strain sensing under uniaxial stretching (Figure 4.25a). The gauge factor ($GF = \Delta R/R_0/\varepsilon$, $\Delta R = R\text{-}R_0$), which is the relative resistance change to strain ratio, reached 2.3 at 70% tensile strain. The sensitivity is comparably higher than PEDOT/PVA and graphene/PAAm gel sensors at the corresponding tensile strain. The improved sensitivity can be attributed to the uniform continuous CPs network without agglomerates by ice-templated low-temperature polymerization. During the passive deformation, the less aggregated microstructure can conformably reflect the macroscopic stretching of the gel, resulting in higher mechanical robustness and sensory capability. Apart from the stretching mode, the hydrogel could also detect the bending and compression, which showed its potential as curvature sensors and haptic (tactile) sensors (Figure 4.25b ,c).

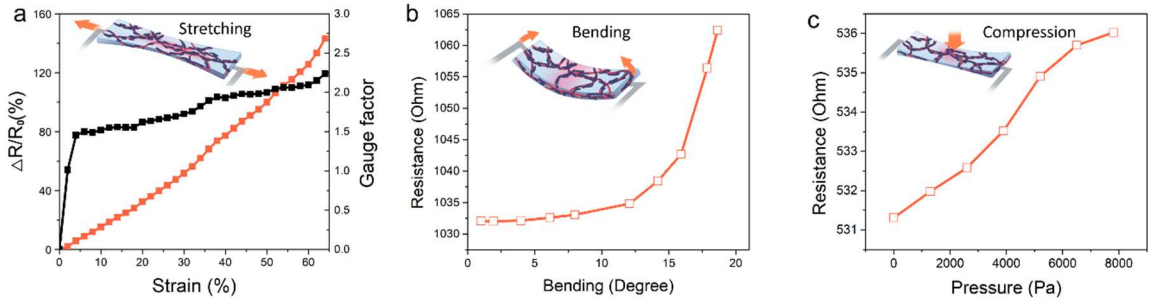

Figure 4.25. Exteroceptive sensing of ITUC gel. (a) The resistance change and gauge factor of ITUC gel during stretching. (b, c) The resistance change of ITUC gel under bending and compression.

Regarding the similar mechanical properties to biological tissues and compatibility of hydrogels, the ITUC gel can be used for human motion monitoring. The ITUC gel mounted on a human finger could precisely sense the motion of human finger during the bending and recovery at different angles reversibly (Figure 4.26).

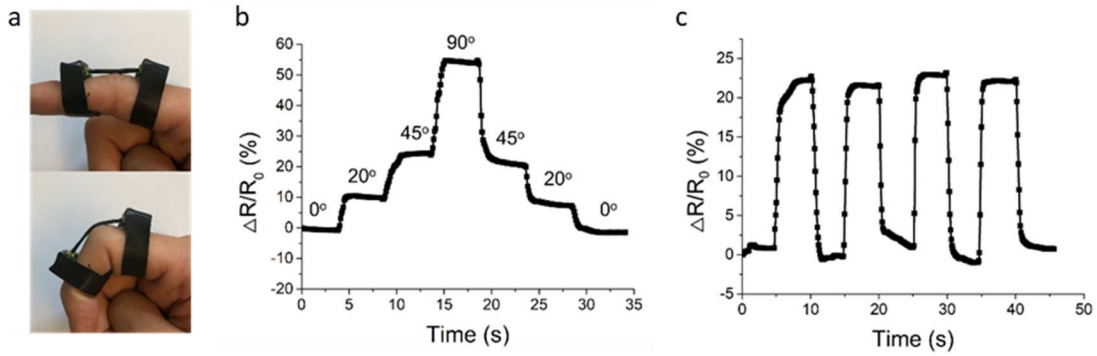

Figure 4.26. ITUC gel as a human motion sensor. (a) Photographs of the sensor during finger bending and straightening. (b) Relative resistance changes of the strain sensor during finger bending and straightening. (c) the reversibility of the strain sensor.

4.4.5. Somatosensitive actuation

Proprioception was further demonstrated through real-time monitoring of its own active actuation behaviors, which mimicked the self-sensing of physical states and motions in living organisms, such as the self-monitored extension or curling of octopus arms. We first demonstrated the kinesthetic shortening/elongation of a hanging ITUC gel by placing a load at the bottom (Figure 4.27). Upon illumination by NIR light, the gel strip shortened. The resistance interestingly increased slightly within the first few seconds and then decreased continuously (Figure 4.27b). We assume the initial relative resistance change ($\triangle R/R_0$) spike was ascribed to the rapid microstructural change of PNIPAAm network into clusters that partially isolated the individual PAni chains. The disconnected clusters resulted in the instant resistance increase of the gel. However, the further shrinkage of the entire dynamic polymer network well enabled the reconnection of the clusters back to the continuous electron pathway, leading to a continuous resistance decrease. Reversely, as the light was switched off, the resistance was initially reduced over the lower limit, followed by a gradual recovery to the initial state.

Similarly, real-time monitoring of photo-responsive bending/unbending actuation was also successfully demonstrated when not mounting a load to the hanging gel (Figure 4.27c). The light-

regulated motion was successfully monitored in real-time by the gel itself. We noticed slight over-bending during its shape recovery upon light shutoff, presumably due to the overheating of the front surface without the restriction of the built-in feedback lock. A similar spike in the resistance change was observed within the first few seconds of turning the light on and off caused by the rapid polymer network change (Figure 4.27d).

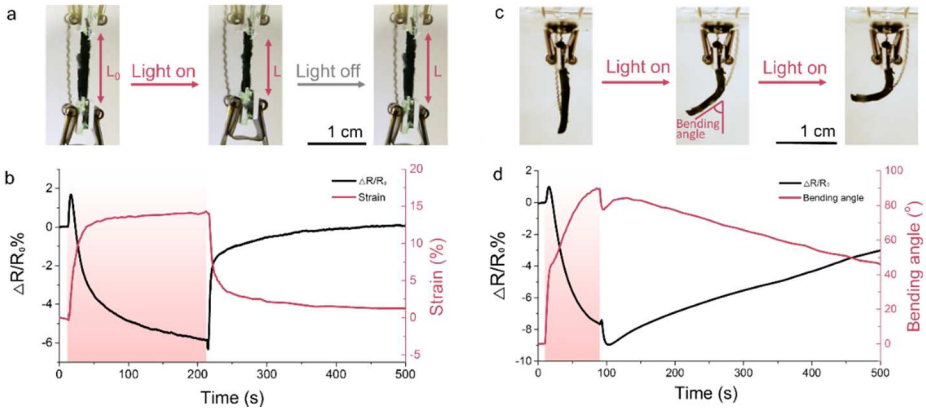

Figure 4.27. Proprioceptive sensing of the ITUC gel. (a) Proprioceptive shortening and elongation under NIR light. (b) Resistance and length change over time. (c) Proprioceptive bending and unbending under NIR light. (d) Resistance and bending angle over time.

To fully demonstrate the utility of the somatosensory feedback in a soft robotic system, we assembled the ITUC gel into an octopus as a soft proprioceptive arm (Figure 4.28a). Starting with a straight inactive state, the octopus arm bent up upon NIR illumination and wrapped around a series of cylinders rods of different sizes. The recorded resistance profiles represent the processes of perceiving and grasping the three objects of different diameters respectively (5, 10, and 15 mm, Figure 4.28b). Specifically, a 7% resistance drop occurred when the arm fully wrapped around the 5 mm cylinder, while a 0.8% resistance reduction occurred over a relatively shorter period of time when perceiving and grasping the 15 mm cylinder, reflecting the relatively smaller required bending deformation (Figure 4.28c). Therefore, both the magnitude and time of resistance change during grasping provide the potential for the shape recognition of unknown objects by the proprioceptive grasping strategy.

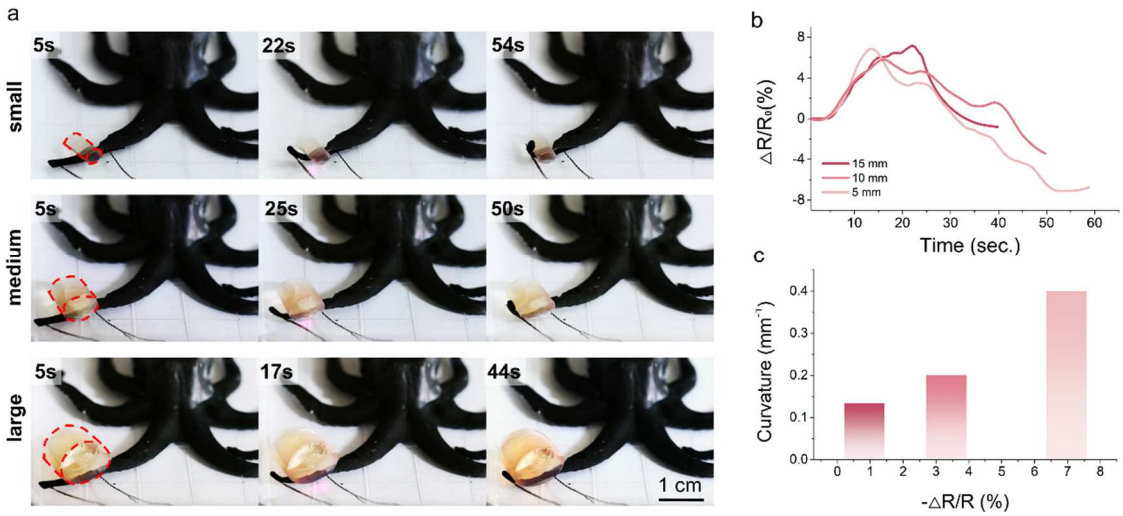

Figure 4.28. Shape recognition of an artificial octopus by wrapping the objects (a). (b) Resistance changes of the gel when wrapping different sized objects. (c) The correlation of resistance changes and curvatures of objects.

4.4.6. Closed-loop actuation

As an ultimate display of the gel's unification of sensory and actuating functions, we developed a closed-loop control system to mimic a biological neuromuscular system, which involves a nerve impulse passing inward from a receptor to the spinal cord and then outward to an effector, much like a muscle or gland triggering an impulsive approach towards or retraction from an external object or environmental stimulus. Control algorithms were designed to precisely regulate the elongation/shortening deformation of a weight-loaded ITUC gel arm, by feeding the controller with the somatosensory feedback pertaining to the real-time length change and controlling the arm shrinking/relaxation motion accordingly (Figure 4.29a). Specifically, we mounted a gain-scheduled bang-bang controller to collect the resistance feedback and correspondingly manipulate the NIR intensity, which successfully held the arm length at three stepwise levels consistently with a 0.16 mm precision ($\Delta L/L_0$= 2.59±0.66%, 5.00±0.63% and 6.75±0.60%, L_0 = 25.0 mm) by controlling relative resistance change ($\Delta R/R_0$ =2.5%, 5.0%, and 7.5%) for two stable cycles (Figure 4.29b).

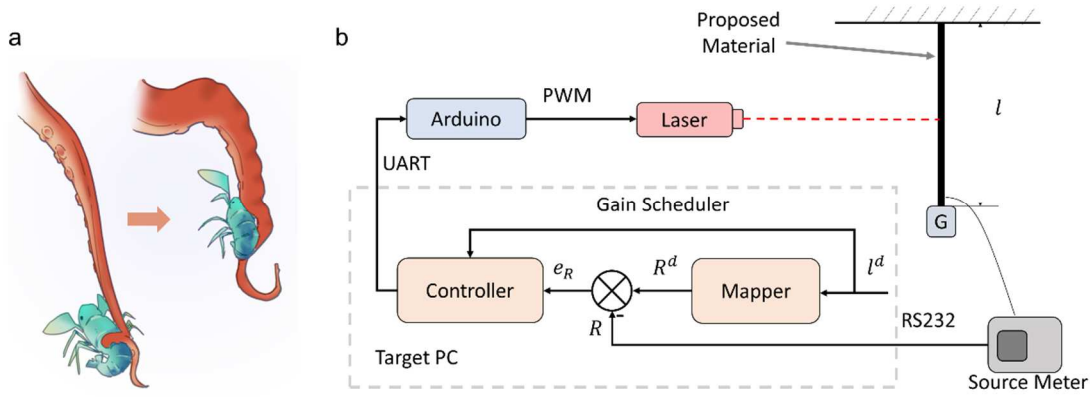

Figure 4.29. Closed-loop control setup. (a) The schematic of hydrogel arm length shortening control. (b) Block diagram of the closed-loop control system. A gain-scheduled bang-bang controller is running on the target PC, taking resistance measurements and sending control command to Arduino, which then generates PWM signals to drive laser intensity.

As shown in Figure 4.30, both the strip resistance and strain oscillated around the target values in response to the light intensity modulation. A slight delay in deformation strain change was observed before reaching the equilibrium of the target length when the relative resistance change ramped down (*i.e.*, gel shrinkage going small, during the 870~1400 second period), while such a delay did not exist during the target length ramp-up, attributed to the relatively faster gel shrinkage over its recovery.

The aforementioned abnormal resistance spikes upon strong illumination, also observed during the controlled arm elongation steps, were well suppressed by lowering the light intensity. Meanwhile, the oscillation was suppressed as well with the effective fine-tuning of light, as the rapid shrinkage of PNIPAAm network occurred mildly. It was found that a background non-zero weak illumination significantly increased the response rate and made the resistance responses to the gel shrinking and relaxation more symmetric, which could be attributed to the higher temperature baseline of the sample from continuous illumination. As the sample was kept warm at a temperature close to its LCST, a smaller temperature change and shorter time were required to trigger sample deformation.

Consequently, such a smaller light intensity difference upon switching also led to smaller oscillation along the target resistance and deformation.

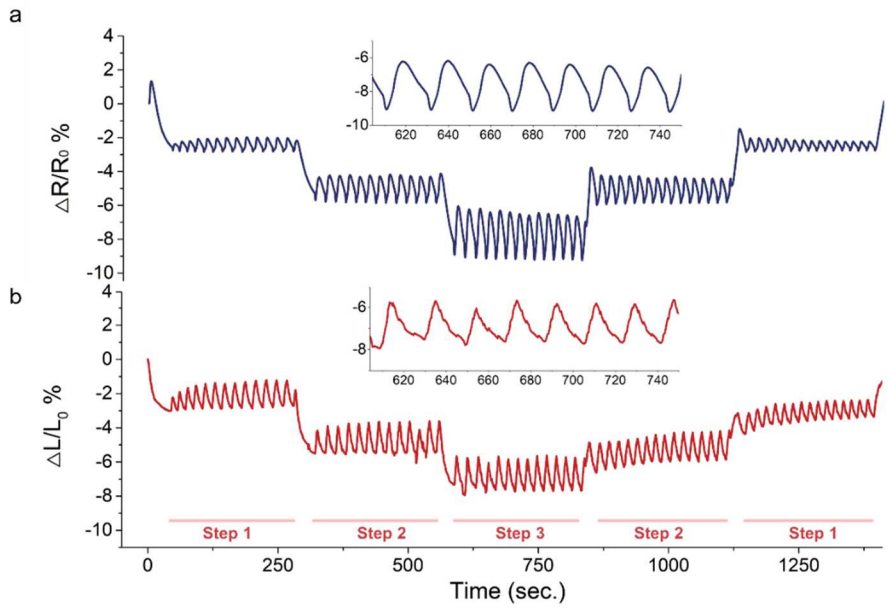

Figure 4.30. Closed-loop control performance. (a) The relative resistance change versus time during closed-loop regulation. (b) The corresponding hydrogel arm strain versus time during closed-loop regulation, to step-wise reach the targeted arm lengths at three steps (original length L_0 = 25.0 mm, targeted lengths at, respectively, step 1 L_1 = 24.35 mm, step 2 L_2 = 23.75 mm, and step 3 L_3 = 23.31 mm). The insets in (a) and (b) showed the magnified curves between 600~750 seconds and their oscillations at a ~20-second period.

4.4.7. Discussion and outlook

In this work, we successfully demonstrated a proof of the concept for implementing molecularly innervated somatosensitive robotic materials, based on conducting hydrogel composites comprised of conductive and responsive polymer networks produced by a one-pot synthesis. Realizing such an integration of both sensing and actuation functions in a single monolithic material was enabled by the unconventional ice-templated cryopolymerization strategy, which effectively resolved the long-lasting conducting polymer hydrogel challenges in inhomogeneity, aggregation formation, and the resulting low conductivity and poor sensory performance under DC voltage. This material

preparation method is highly universal, capable of coupling broad choices of sensing and actuating functional components into a variety of smart materials. This hybrid material design can not only retain the functionalities of each component but also synergistically achieve high mechanical and electrical properties required for sensory actuation. Compared to conventional multi-material integrated systems, the somatosensitive actuating material allows for arbitrary sensing location, offers self-contained multiple sensing nodes, and can be custom-designed for broad applications, including the demonstrated basic robotic tasks of contraction, bending, object lifting, and object grasping with open-loop and closed-loop control algorithms. The method can be also used to fabricate miniature robot with multisensory perception and mobility, which has proved to be a considerable challenge in most current soft robots.

Although promising, the presented exemplary hydrogel system still has several aspects to be optimized in the future investigation: 1) the diffusion-governed response of hydrogel still limits the actuation rate, which can be further improved by morphological or chemical modification, or utilization of other operation mechanisms; 2) in general, the deliverable force of hydrogels is relatively low due to the inherent porous network of high water content, which can be addressed possibly by adding toughening agents; 3) obtaining high electrical conduction without compromising high stretchability, achieving high reliability of conduction over time, and stability of piezoresistive sensing mechanism under cyclic operation need to be considered for broader and practical soft robotics applications. With these goals to be achieved, the exemplary hydrogel-based somatosensory actuatable materials ultimately may be anticipated to perform remote under-water tasks for marine environment applications, such as sensing of the roughness of an object, controllable gripping soft animals like mollusks, bypassing an obstacle, and going through a constrained channel. Beyond this exemplary system, this customizable modular material design can be also extended to other material systems such as liquid crystal elastomers to open up new opportunities.

5. Energy storage based on flexible/stretchable conductive hydrogel

5.1. Introduction

Various natural systems such as muscles, tendons, skins, articular cartilage, and wood exhibit well-defined anisotropic structures.[99] The high order of orientation plays a significant role in multiple functions, including mass transport, surface lubrication, and force generation. Particularly, mass transport is greatly enhanced through vertically-aligned channels due to the low tortuosity. Inspired by nature, considerable efforts focused on the design of aligned micrometer-scale porous structures, showing promising applications in electronics, biomedical engineering, and energy storage devices.[100] Solid electrolytes with aligned structures exhibit low tortuosity and thus facilitate a high ionic transfer, comparable to bare liquid electrolytes. Such ordered structures have also been demonstrated to benefit particularly the rate capability in thick electrodes. In addition, an oriented porous structure provides continuous highways and sufficient surface area for high-mass loading, which is desirable for lowering the manufacturing cost via inactive material reduction. As a pioneering example, Hu group reported an all-wood structured supercapacitor, showing high electrical conductivity, ionic conductivity, ultrahigh areal mass loading, and thus large areal capacitance.[101] However, wood has predefined channels with macro-pores and suffers from rigidity and lack of flexibility. It would be advantageous to possess mechanical flexibility and morphological tenability while maintaining all the above superior electrochemical performance. Therefore, it is highly desirable to obtain a man-made anisotropic structure with similar or even smaller pores, owning high areal-mass loading and high flexibility for energy storage applications.

Hydrogels, comprised of cross-linked polymeric networks with high water content, have become promising matrices for electrode materials and electrolytes in aqueous supercapacitors and batteries, due to the increasing demands for flexibility, wearability, and portability with minimized liquid leakage.[102] Specifically, a hydrogel with three-dimensionally highly-ordered structures further

grant favorable anisotropic properties, such as enhanced directional ion transfer. Currently, anisotropic hydrogels are mainly synthesized through directional stimuli, including mechanical forces, magnetic fields, electric fields, directional freezing, and directional ion diffusion. Particularly, directional freezing, or ice-templating, is a promising and versatile approach to creating well-defined aligned porous channels along the freezing direction. In this process, the hydrogel precursor solution is frozen along a directional temperature gradient. Meanwhile, the monomers are concentrated between crystalline domains and subsequently polymerized in the presence of ice. Since the ice crystals serve as the template for the cross-linked polymer structure, the removal of ice leads to porous monoliths. By manipulating the temperature gradient, solution concentration, viscosity, wetting properties, and incorporating additives, the morphology can be facilely tuned. However, the pore sizes created from the directional freezing method are typically larger than 20 μm even under the most favorable conditions such as crystallization in liquid nitrogen, which limits their applications in energy storage.

Considerable fundamental studies have investigated anisotropic hydrogel structures serving as supercapacitor electrolytes. The Wang group fabricated aligned PEGMA ionogel, PDMAA ionogel and PAAm gel[103] as gel electrolytes through directional freezing. With the same electrodes covering both sides of the gel electrolyte, the device with an anisotropic structure presented improved ionic conductivity and enhanced specific capacitance at a high current in comparison to the isotropic, non-aligned gel. With aligned architecture, the supercapacitor energy loss was significantly reduced. Notably, the electrochemical performance with an aligned structure was comparable to that of a pure electrolyte device.

In addition to the electrolyte, the structural design of the overall device is important for energy storage devices with high mass loading, low tortuosity, and high energy/power density. Conventionally, electrode materials are coated on the surface of electrolyte, which limits ion transport. To maintain high specific capacitance, the electrode mass loading is kept low; however,

the low mass loading inevitably results in low total areal capacitance and increases the fraction of non-energy-storage, inactive materials, which is undesirable for practical energy storage devices. For example, hierarchically aligned nanomaterials based on transition metal oxides/sulfides have displayed outstanding specific capacitance due to the high specific area. A few conducting polymers with nanostructure have also been studied, including PEDOT-PSS, polyaniline, and polypyrrole.[104] However, it still remains a big challenge to efficiently and cost-effectively fabricate materials with high areal energy density and high mass loading. One route to address the ion-transport issue while maintaining the high mass loading is to embed electrode materials in the porous electrolyte matrix. By controlling the morphological orientation and size distribution of the porous matrix, the electrode materials loading can also be optimized, which can effectively improve the device electrochemical performance.

5.2. Proposed method

In the first work, we demonstrate a wood-inspired all-solid-state hydrogel supercapacitor by integrating polypyrrole (PPy) as the electrode material in an aligned polyacrylamide aerogel (APA) matrix. The polyacrylamide (PAAm) hydrogel with unidirectionally-aligned structure was created using an ice-templating method under directional freezing, featuring highly controllable and tunable morphology and good mechanical flexibility. The anisotropic structure enabled ions to freely travel through the channels due to the low tortuosity. The electroactive material PPy was subsequently embedded inside the aligned-structured aerogel film by vapor-phase deposition (VPD), to form a completely flexible all-polymer electrode. The unidirectional and open microchannels generated by directional freezing allowed pyrrole molecules to freely penetrate the PAAm matrix, showing the homogeneous distribution of PPy. When two PPy-embedded aligned-PAAm electrodes were soaked with PVA/LiCl electrolyte and sandwiched with a cellulose-based separator, an all-solid-state supercapacitor was formed. Uniquely, the electrode and electrolyte share the same porous polymer matrix to form an interconnected network, in which gel electrolyte

provides good mechanical flexibility as well as fast ion transfer, and PPy exhibit charge storage capability and chemical stability. These merits are attributed to such an integrated electrode/electrolyte design as proven previously. Additionally, the porous matrix increases the mass loading of the electroactive material (PPy here). Importantly, the aerogel pore size can be tailored simply by adding PVA to the precursor solution, to produce a large specific area desirable for high supercapacitor performance. We will characterize supercapacitor performance, including areal AC impedance, capacitance, cyclic stability, and bending stability.

In the second work, we leverage the highly conductive (55mS/cm), stretchable (150%), and hierarchically structured hydrogels made by ice-templating and low-temperature polymerization. With the remarkable conductivity and mechanical enhancement of the ItG, we study the electrochemical properties for energy storage applications. Particularly, the conductive filler in the ItG network is conductive polymer PAni, which has high pseudocapacitive properties. The stretchability endows the hydrogel electrode with the potential of flexible and stretchable electronic devices.

5.3. Flexible, high areal capacitance, solid-state supercapacitor based on aligned conductive hydrogel

5.3.1. Experimental and characterization Section

5.3.1.1. Chemicals

Acrylamide (Fisher, 98.0%), N,N′-methylenebis(acrylamide) (MBA, Fisher, 98%), Polyvinyl alcohol (PVA, molecular weight = 89000-98000, hydrolysis degree = 99%, Sigma), N,N,N',N'-tetramethylethylenediamine (TEMED, 99%, Fisher), ammonium persulfate (APS, ACS grade, fisher), pyrrole (reagent grade, 98%, Sigma), Iron(III) chloride hexahydrate (Sigma). All chemicals were used as received.

5.3.1.2. Preparation of precursor solution

For the PVA precursor solution, 4 g PVA was dissolved in 40 ml water and heated to 90 □ with magnetic stirring to form a transparent solution with the PVA concentration of 10 wt.%. The PVA solution was cooled down to room temperature for further usage. For the LiCl/PVA electrolyte solution, LiCl was added and mixed in 10 wt.% PVA solution at 90 □. Then, the solution was cooled down to room temperature to form 5 M LiCl/ PVA solution. For the hydrogel prepolymer solution, 1200 mg of acrylamide, 24 mg of MBA (as the crosslinker of acrylamide), 0.67 ml of ethanol, 40 µl of TEMED, and a certain amount of PVA solution were mixed to form Solution A. To study the effect of PVA concentration on hydrogel morphology and supercapacitor electrochemical performance, 0, 0.5, 1, 2, and 3 wt.% PVA were used. After mixing, the solution was degassed under nitrogen for 10 minutes to remove the dissolved oxygen. Solution B was prepared by adding 40 mg Ammonium persulfate (APS, as an initiator) in 1.33 ml water. The prepolymer solutions were kept at 4 □ fridge for further usage.

5.3.1.3. Preparation of the APA

The directional freezing mold was made of polylactic acid (PLA) with dimensions of 3 cm x 3 cm x 2.5 cm and 0.8mm thick hollow side walls. For each sample, 5 ml of solution A and 0.33 ml of solution B were mixed and quickly transferred into the PLA mold. The bottom of the mold was immersed in liquid nitrogen at 1 mm depth, so that the bottom surface was always in contact with a cold source. The mold was fixed and the surrounding container with liquid nitrogen was gradually elevated with 10 µm/s to ensure the advancing ice front had a sufficiently low temperature. As the ice grew to the top surface of the prepolymer solution, the mold was taken out of liquid nitrogen and kept in a -20 □ fridge for 3 hours to complete the cryo-polymerization of the PAAm hydrogel. The sample was subsequently freeze-dried for 2 days to remove the ice crystals and finally form an aligned PAAm aerogel (APA) film. The non-aligned, homogeneous PAAm hydrogel (HomoPA) as the control sample was made by injecting prepolymer solution in a mold with a defined thickness and placing in -20 □ fridge for polymerization.

5.3.1.4. Preparation of the PPy/APA electrode

The APA film was sanded to the desired thickness with sandpaper and cut to the desired size with a razor blade. Then, the film was immersed in a 14 w/v% $FeCl_3$-ethanol solution for 5 minutes. After drying in a vacuum for 2 hours, the film was placed in a vacuum desiccator with 1 ml of fresh pyrrole monomer. Under vacuum, the pyrrole monomer evaporated, deposited, and polymerized on the pore walls of APA aerogel with $FeCl_3$. Then the PPy/APA film was soaked in ethanol for 2 days to remove excessive reactants.

5.3.1.5. Assembly of all-solid-state supercapacitor

Two PPy/APA films with dimensions 1.27 cm x 1.27 cm x 1mm were soaked in 5 M LiCl/ PVA aqueous solution for 1 day. Then a cellulose-based separator was sandwiched between two PPy/APA films and pressed together. The supercapacitor was kept in dry air for 15 hours to form an integrated all-solid-state supercapacitor.

5.3.1.6. Characterizations

The morphology of the APA film was observed via scanning electron microscope (Supra 40VP) after freeze-drying. The electrochemical tests were performed via two electrode method on a CHI660E electrochemical workstation (CH instrument). The cyclic voltammetry (CV) measurements were examined at scan rates of 10, 20, 50, and 100 mV/s. The galvanostatic charge/discharge (GCD) curves were measured with various current densities in the potential range of 0 to 0.8 V. The EIS measurement was performed in the frequency range from 100000 Hz to 0.01 Hz, with a voltage perturbation of 5 mV. The cyclic stability test was performed by cyclic charging and discharging at a certain current density. The areal capacitance (C_A), the areal energy density (E_A), and the areal power density (P_A) of the supercapacitor were calculated according to equations below, respectively.

$$C_A = \frac{2It}{AU}$$

$$E_A = \frac{C_A U^2}{2}$$

$$P_A = \frac{E_A}{t}$$

5.3.2. Synthesis methods of aligned aerogel

The aligned hydrogel matrix in this work is mainly comprised of chemically crosslinked polyacrylamide, polymerized from acrylamide as a monomer, MBA as a crosslinker, APS as thermal initiator, and TEMED as the catalytic agent (Figure 5.1a). During the ice templating process, the prepolymer components in suspension were well mixed and transferred to the mold. The mold was specifically designed with hollow side walls for thermal insulation, enabling the air in between to effectively inhibit the conduction of heat from the side walls into the solution (Figure 5.1b). Thus, the temperature gradient was preferably along the vertical direction. As the ice was nucleated and grown from the bottom to the top surface, the solutes were expelled to the region between the ice crystals. Then the sample was placed in -20□ fridge for cryo-polymerization.

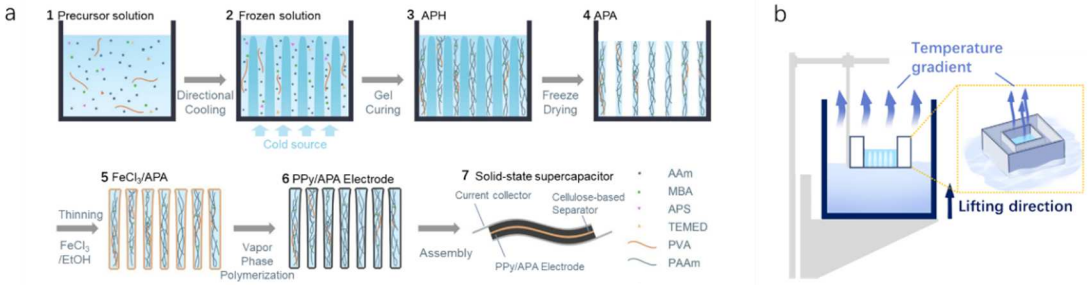

Figure 5.1. Schematic of the fabrication of all-solid-state hydrogel supercapcitors via integration of aligned polyacrylamide aerogel (APA) as the matrix and polypyrrole as the electrode material. (a) Schematic of directional freezing setup. The inset shows the mold which remains hollow in between the inner precursor solution and outer liquid nitrogen, enabling the preferably vertical temperature gradient. (b) Schematic of directional freezing setup. The inset shows the mold which remains hollow in between the inner precursor solution and outer liquid nitrogen, enabling the preferably vertical temperature gradient.

The initiator APS and the catalyst TEMED were controlled as appropriate so that the polymerization predominantly occurred after the ice was completely formed; overly high APS and TEMED content would dramatically increase the reaction kinetics, leading to isotropic hydrogel without alignment, as shown in Figure 5.2a. In addition, a small amount of ethanol was added to the solution to modify the ice formation and mechanical robustness. It is worth noting that the APA without ethanol formed cracks with poor mechanical strength (Figure 5.2b,c).

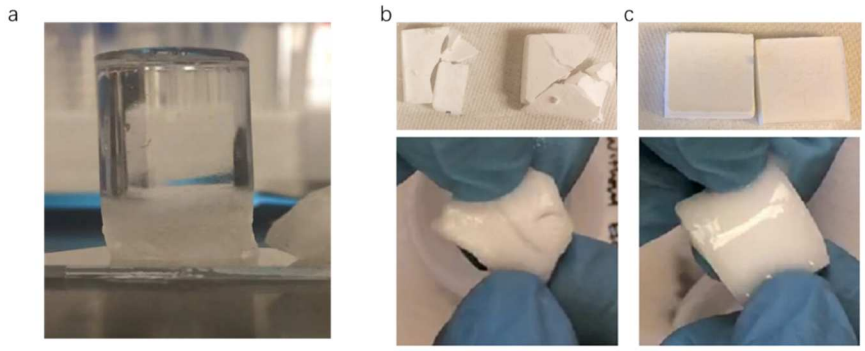

Figure 5.2. Fabrication of APA. (a) Photograph of ice-templated PAAm hydrogels with overly high APS and TEMED content (twice higher). Comparison of APA with and without ethanol addition (b) APA without ethanol formed cracks with poor mechanical strength. (c) After adding 3.33 v/v% of ethanol in prepolymer solution, the as prepared APA was more uniform.

After the ice formation and cryo-polymerization, the frozen sample was placed in a freeze-dryer to remove the ice. Then, the aligned aerogel film was formed. The APA displayed a well-defined anisotropic structure along the freezing direction over a large scale (Figure 5.3b). After swelling in water, the APA film was flexible and capable of freely bending to large angles, demonstrating the potential for a flexible substrate (Figure 5.3a).

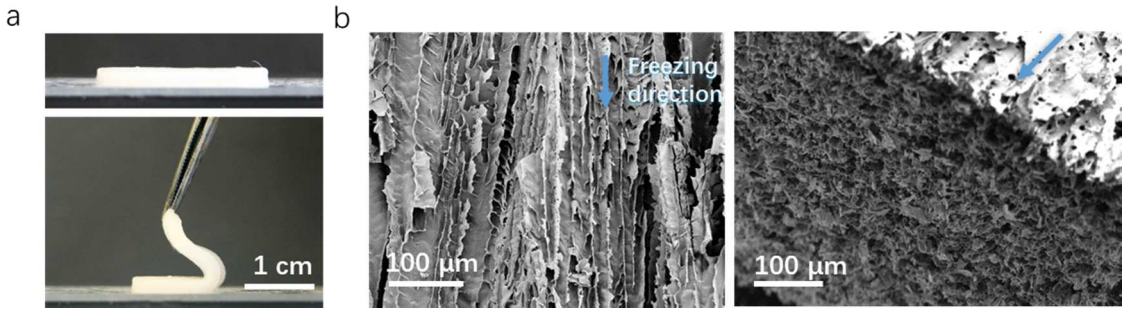

Figure 5.3. Structural characterization of APA. (a) Photographs of swollen APA film on side view (upper) and its high flexibility capable of bending to a large angle (lower). (b) SEM images of APA cross sections, respectively, along the alignment (freezing) direction (left) and the transversal direction (right).

5.3.3. Morphology control of matrix

A small amount of PVA was added to prepolymer solution to control the morphology of the hydrogel/aerogel. For ice templating, the porosity of the materials is a replica of the original ice structure. By modifying the ice crystallization, we achieved a wide tunability of the pore morphology of hydrogel. Here, the pore sizes of the aligned structure were facilely tuned by adding different concentrations of PVA (Figure 5.4a). In Figure 5.4b, the APA without adding PVA had pore sizes of 47 µm. Whereas, the APA containing PVA from 0.5 wt.% to 3.0 wt.% resulted in finer pores with higher PVA content. The smallest pores were 12 µm for 3.0 wt.% of PVA, which was far lower than the channel width of wood (20 ~ 40 µm) and conventional directional freezing pores (>20 µm). The ability to effectively modify the micro-morphology by the PVA addition is due to the increased solution viscosity and hydrophilicity. In addition, the PVA can inhibit ice recrystallization during the gel curing step, which is an unavoidable annealing process. Although adding more PVA is expected to further reduce the pore size, it increases the fraction of electrochemically inactive materials in the electrode and results in more zig-zag ice crystallization due to overly fast ice formation, both not favorable for optimal supercapacitor behavior. Hence, 3.0 wt.% was found the optimum PVA additive concentration in this material system.

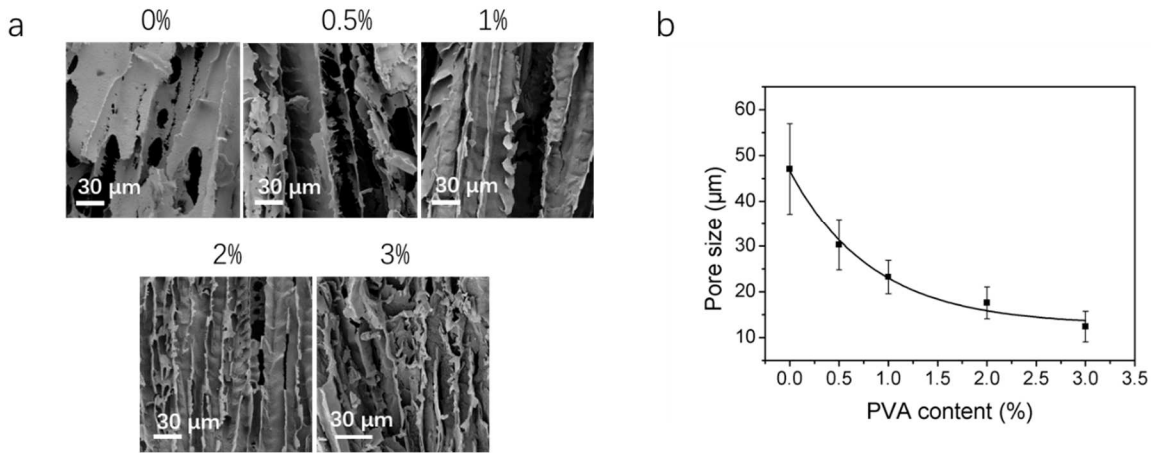

Figure 5.4. Morphology control of APA. (a) SEM images of 6% PAAm containing 0, 0.5, 1, 2, and 3 wt.% PVA. (b) Tunability of the pore size of APA by tuning the PVA content in the precursor solution.

5.3.4. Polypyrrole loading

In recent years, several works have focused on improving electrochemical performance via the structural design of electrode and electrolyte materials. A larger specific surface area can be achieved by reducing the matrix pore sizes of the matrix. Therefore, when coating the same thickness of electrode materials on the matrix surface, the finer structured matrix can accommodate more electroactive materials as a coating due to the higher specific surface area.

We used polypyrrole as an exemplary electrode material to demonstrate the structure tunability and electrochemical improvement due to its high conductivity, electrochemical properties, and facile fabrication. To embed PPy in the substrate, the APA film (Figure 5.5a) was immersed in a $FeCl_3$/ethanol solution to coat the oxidant throughout the entire matrix. After drying the film, it was exposed to pyrrole vapor by VPD. The PPy in the APA film was evenly grown on the inner channel walls. In addition, the PPy was homogeneously distributed throughout the entire film even up to 6.7 mm thickness (Figure 5.5b), showing significantly improved uniformity compared to previous methods with 10-100 μm penetration depth, indicating the formation of a truly interpenetrating network of PPy/APA. The ice templating method creates appropriate open macroporous pores with

orientation, which not only supports the network from being collapsed when drying but also provides sufficient space for gas molecule diffusion, in contrast with most previous close-pore structures.

The chemical structures of pristine APA, APA with the addition of PVA, and the aerogel after coating with PPy were analyzed using the Fourier transfer infrared (FTIR) spectra (Figure 5.5c). All four samples had peak at ~3185 cm^{-1} and ~3327 cm^{-1}, which could be assigned to the characteristic peaks of N-H bonds. The strong peak at ~1650 cm^{-1} was derived from C=O stretching of the amide group, confirming the formation of PAAm structure. The peak at 1093 cm^{-1} from 6APA-3PVA was observed due to the C-O vibration of PVA. For 6APA-PPy and 6APA-3PVA-PPy which were coated with PPy by VPD, the absorption peak at ~1548 cm^{-1} was attributed to the in-plane bending of C=N bonds. The peak located at ~1176 cm^{-1} and ~902 cm^{-1} were due to the stretching vibration of C-N^+ bonds and C=N^+-C bonds, confirming the formation of PPy.

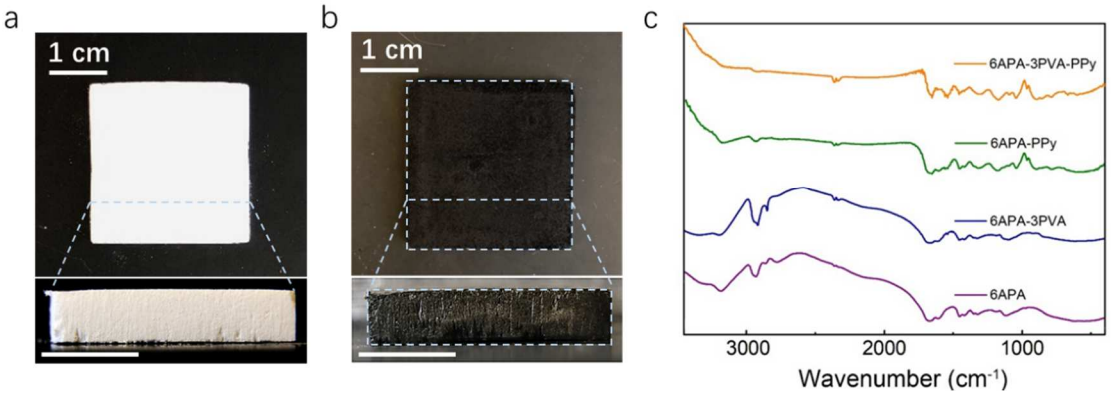

Figure 5.5. Polypyrrole loading into APA film. Photographs of freeze-dried APA film (a) and PPy/APA film after the VPD (b). The PPy can facilely infiltrate into the matrix (up to 6.7 mm thick), attributed to the open porous structure along the aligned direction. (c) FTIR spectra of APA and PPy/APA, with and without PVA addition.

5.3.5. Electrochemical performance of solid-state supercapacitors

To examine the morphology-dependency of the aerogel film electrochemical performance, we prepared PPy/APA films with different PVA concentrations under the identical VPD condition. An

isotropic, non-aligned PAAm aerogel was also fabricated as a control sample. Typically, the PPy was polymerized on the APA matrices which had a constant thickness (1mm) and were soaked with $FeCl_3$/Ethanol of the same concentration (14 w/v%). After the polymerization of PPy on the APA film and removing the excess monomer with an ethanol rinse, the film was immersed in LiCl/PVA aqueous electrolyte and dried in air to remove the excess water. Then, we assembled two electrode layers with a separator to construct a sandwich-like solid-state-supercapacitor (Figure 5.6a). Two carbon cloths were used to cover the two sides of the electrode to connect with the electrochemical instrument.

The electrochemical properties of solid-state supercapacitors were measured as shown in Figure 5.6**b**. The cyclic voltammetry (CV) curves of devices made from PPy/APA matrices with different pore sizes (APA-x PVA, x = 0, 0.5, 3 wt% PVA) and non-aligned, homogeneous matrix (HomoPA), respectively, were measured at 10 mV/s. As shown in Figure 5.6b, all four CV curves demonstrated a nearly rectangular shape, indicating a fast and efficient ion transfer. The enclosed CV area for the APA devices increased with decreasing pore size, an indication of higher loading of electrode materials. By contrast, supercapacitors made from a non-aligned matrix had the smallest enclosure area. For APA-3 PVA, the small equivalent series resistance (ESR= 6.1$\Omega \cdot cm^2$) and charge transfer resistance (R_{CT} = 1.3 $\Omega \cdot cm^2$) in the Nyquist plots indicated a low ohmic contact between the electrode and electrolyte, as well as an enhanced ion transfer. The low ESR and R_{CT} of the PPy/APA electrode benefited from the aligned structure with low tortuosity that allowed for fast ion transport and defined electrical conduction pathways along channel walls. The nearly vertical tail at low frequency in the EIS plot also indicated favorable capacitive behavior. The galvanostatic charging-discharging (GCD) curves were measured with a current density of 9.3 mA/cm^2 with an operating window of 0 ~ 0.8 V. Discharging time of the assembled supercapacitors was longer for smaller pore-sized devices, indicating larger areal capacitance (Figure 5.6f). In addition, the specific areal capacitance at various current densities were shown in Figure 5.6e, which were calculated from

GCD tests. The HomoPA device had an areal capacitance of only 207 mF/cm^2 at 6.2 mA/cm^2, whereas APA-PVA devices all exhibited much larger capacitance throughout the operational current range compared to HomoPA. For the matrix with 12 μm channels (APA-3 PVA), the areal capacitance reached 831 mF/cm^2 at 6.2 mA/cm^2 (332.4 F/g), 259% of the aerogel matrix without PVA addition (47 μm channel width) due to the morphology modification. The high capacitance is attributed to the reduction of microchannels width by morphological control of aerogel matrix.

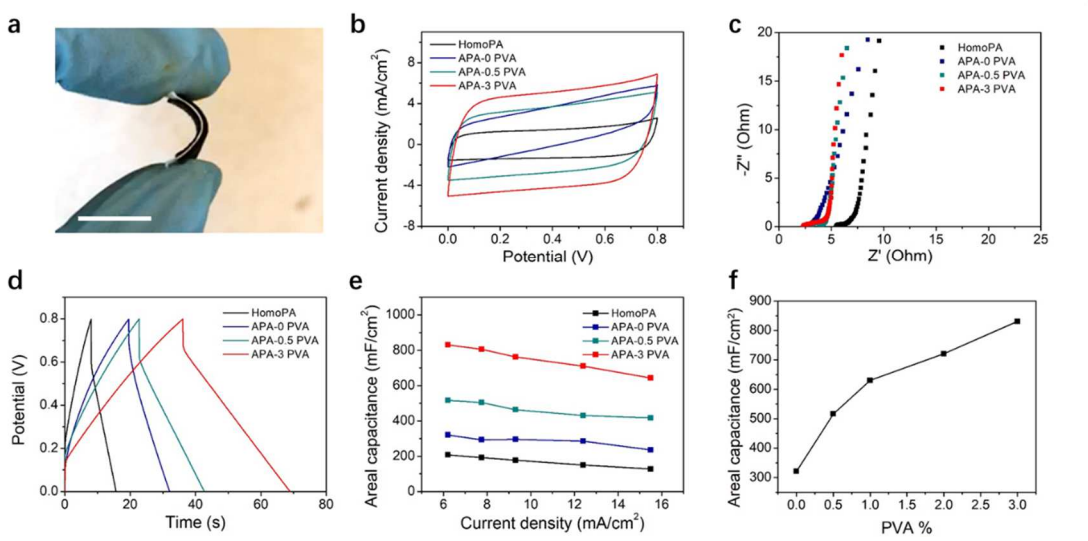

Figure 5.6. Electrochemical performance of supercapacitors with different matrix morphologies. (a) Photograph of a flexible all-solid-state hydrogel supercapcitor. (b) CV curves of the supercapacitors at the scan rate of 10 mV/s. The neat PAAm, PAAm with 0.5 wt. % PVA, and PAAm with 3 wt. % PVA were selected as the hydrogel matrix. (c) Nyquist plots of the three supercapacitors at frequencies ranging from 1M Hz to 0.01 Hz. (d) Galvanostatic charging-discharging (GCD) curves at the current density of 9.3 mA/cm^2. (e) The correlation of areal capacitance with various current density. (f) The areal capacitance of supercapacitors as the function of PVA additive concentration. The current density was 6.2 mA/cm^2.

We then focused on PPy/APA with 12 μm channels in further characterization due to its high performance. As shown in Figure 5.7a, the shape of CV diagrams at different scan rates (10-100 mV/s) was nearly symmetric, indicating good capacitive behavior. The symmetry and triangular shape of GCD curves also demonstrate capacitive properties (Figure 5.7b). Benefiting from the

large mass loading and thick electrode materials, the electrochemical test of the device had a current density range of 3.1 mA/cm^2 to 15.5 mA/cm^2 (Figure 5.7b), which were a considerably larger current value compared to state-of-the-art hydrogel supercapacitors (0.01 ~ 1mA/cm^2). Figure 5.7c illustrates the energy density (E) and power density (P) of such a solid-state supercapacitor, calculated from the GCD curves at different current densities. The largest areal energy density could reach 73.8 μWh/cm^2 with an areal power density of 4960 μW/cm^2. As the areal power increased to 12400 μW/cm^2, the areal energy density was still retained at 57.2 μWh/cm^2. The Ragone plots (Figure 5.7c) compare this device with previously reported state-of-the-art solid-state supercapacitors, presenting its outstanding performance of both high energy density and power density. In addition, the supercapacitor also possessed a high capacitance retention of 86.5% of its original capacitance after 1000 charging-discharging cycles at a current density of 6.2 mA/cm^2 (Figure 5.7d). The EIS after the cyclic stability test showed a slight shift, indicating the relatively small swelling of hydrogel and change in conductivity. The PPy/APA supercapacitor not only exhibited high capacitance but also displayed excellent flexibility under bending, though the device had a larger thickness than the conventional thin film design. Figure 5.7e showcased the good capacitance retention under repeated bending of 90°. Interestingly, the capacitive performance was initially increased to ~118% of its original capacitance and remained 95% after 5000 bending cycles. We attribute the initial performance enhancement under bending to the improved infiltration of electrolytes into electrode under mechanical deformation. In addition, we connected three PPy/APA supercapacitors in series and successfully lit a yellow light-emitting diode (LED) bulb for over 250 s, suggesting promising applications for energy storage devices.

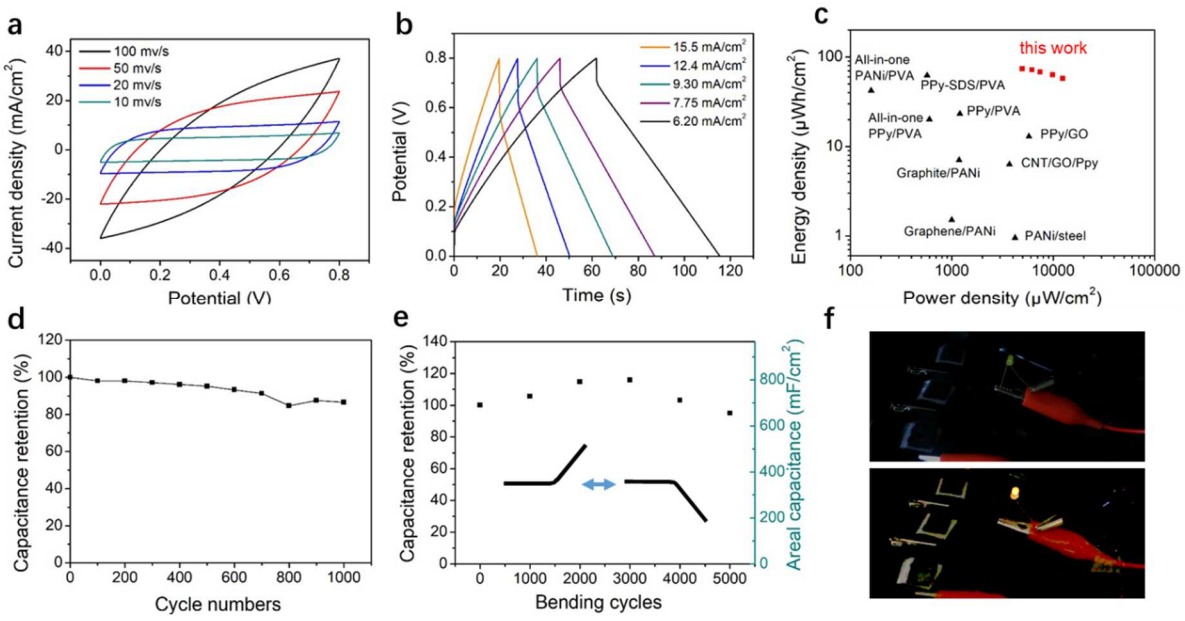

Figure 5.7. Electrochemical performance of the supercapacitor using PAAm hydrogel matrix containing 3 wt.% PVA. (a) CV curves at various scan rates from 10 mV/s to 100 mV/s. (b) GCD curves at various current densities from 6.2 mA/cm^2 to 15.5 mA/cm^2. (c) Ragone plots comparing this supercapacitor with other representative flexible all-solid-state supercapacitors. (d) Capacitance retention during 1000 charging-discharging cycles at current density of 6.2 mA/cm^2. (e) Capacitance retention after 5000 repeated folding cycles. (f) Demonstration of connecting 3 supercapacitors in series to light up a yellow LED.

5.3.6. Discussion

In summary, we have established a new method of creating hydrogel of highly aligned microstructures with tunable fine features and high loading of electrochemical materials. Such a novel method successfully achieved a wood-inspired all-solid-state flexible supercapacitor with an integrated electrode/electrolyte design and significantly enhanced performance. It has the aligned polyacrylamide as the hydrogel matrix and PPy as the electrochemical material. The aligned polyacrylamide hydrogel exhibits low tortuosity, high ionic and electronic conductivity, and flexibility. By modifying the aligned hydrogel with the addition of hydrophilic PVA, the microchannel widths can be drastically reduced from 47 μm to 12 μm, resulting in 259% enhancement in areal capacitance. This value is higher than that of supercapacitor using a

homogeneous matrix (HomoPA). The aligned supercapacitors exhibit high areal capacitance (831 F/cm^2), a high energy/power density (73.8 $\mu Wh/cm^2$ at 4960 $\mu W/cm^2$), and capacitance retention of 86.5% after 1000 cyclic charging and discharging procedures. The PAAm matrix enables the supercapacitors to be flexible and bendable, allowing for 95% retention of capacitive performance after 5000 bending cycles. The rational design of the electrolyte matrix and electrode loading opens new opportunities for the design of novel high-performance materials for flexible energy storage applications.

5.4. Stretchable, high areal capacitance, all-solid-state supercapacitors using hierarchically-structured stretchable conductive hydrogels (ItG)

5.4.1. Electrochemical characterizations of ItG for supercapacitor electrode

We used cyclic voltammetry (CV), galvanostatic charge-discharge (GCD) and electrochemical impedance spectroscopy (EIS) to characterize ItG and LpG as supercapacitor electrodes in a standard three-electrode system. For simplification, we denoted the PANi/PVA system as PP and the PANi/PA/PVA system as PPP. The comparison of CV at a scan rate of 10 mV/s is presented in Figure 5.8**a**. The two pairs of PANi redox peaks are clearly observed both for ItG and LpG, indicating the pseudocapacitor mechanism. The enclosed CV area suggests that the specific capacitance of ItG electrode was larger than that of LpG electrode. Figure 5.9**b** presents the Nyquist plots of ItG and LpG electrodes. The reduction of equivalent series resistance (ESR) was obtained, indicating the improved electrical transfer in ItG electrode. The GCD curves of PPP ItG and PP ItG at a current density of 2 A/g had significantly longer discharging time compared to those of PPP LpG and PP LpG, shown by Figure 5.10**c**. Accordingly, the specific capacitances of the four samples ranging from 0.5 A/g to 20 A/g were calculated (Figure 5.11**d**). The specific capacitance of ItG was considerably higher than that of LpG. Notably, the specific capacitance of PPP ItG reached 888 F/g at 0.5 A/g, which was superior to LpG electrodes (431 F/g for PPP Ft and 295 F/g for PP Ft) and PANi-based electrodes in literature (59.1 - 480 F/g). The improvement in capacitance, and thus energy/power density (Figure 5.12**e**) for ItG is attributed to the lower equivalent series resistance (ESR) and thus lower energy loss during charging and discharging. The PP ItG and PPP ItG also had capacitance retention of 90% and 86%, respectively, after 1000 charging-discharging cycles, indicating the materials' good cyclic stability (Figure 5.13**f**). To further generalize the method, we have also investigated PPy/PVA (Figure 5.15) as electrodes. The GCD and CV results all verified the significant improvement in electrochemical performance by using this strategy. The enhancement of the overall electrochemical property is due to the

interconnected conduction pathway across nano- and micro-scales for high electrical conductivity and thus reduces the energy loss.

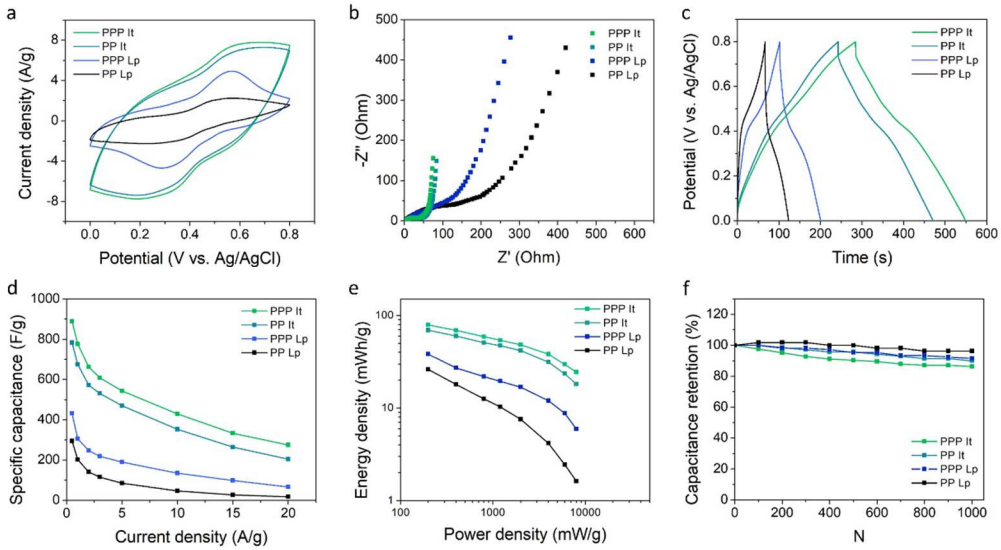

Figure 5.14. Electrochemical properties of ItG and LpG based on PANi/PVA (PP) and PANi/PA/PVA (PPP). (a) CV curves at a scan rate of 10 mV/s. (b) EIS in the frequency range of 10000 Hz-0.01 Hz. (c) GCD at a current density of 2 A/g. (d) Specific capacitance at current densities of 0.5 - 20 A/g. (e) Ragone plot of electrodes. (f) Capacitance retention after 1000 charging-discharging cycles at a current density of 10 A/g.

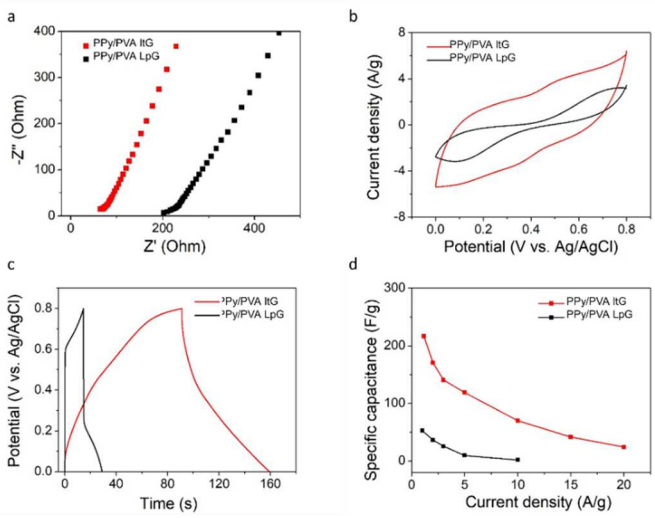

Figure 5.15. Electrical properties and electrochemical properties of PPy/PVA ItG and LpG. (a) Nyquist plot for electrical conductivity measurement. (b) CV curves at 20 mV/s. (c) GCD curves at 2.2 A/g. (d) Specific capacitance at various current densities.

5.4.2. Electrochemical characterizations of ItG for all-solid-state supercapacitors

The hierarchical micro-to-nano structured hydrogel created from this method is a strong contender for practical application in electrochemical devices. Accordingly, we used the PPP ItG as an electrode material for a solid-state supercapacitor (SSC). The areal loading of PANi after pressing was calculated as 5.7 mg/cm^2. To make the device, we sandwiched two PPP ItG films between a PVA/H_3PO_4 film and a cellulose-based separator, before being pressed then dried in air.

The Nyquist plots in Figure 5.16**a** show that the ESR was 5.21 Ω/cm^2 and charge-transfer resistance (R_{CT}) was 0.13 Ω/cm^2, which were very low for a flexible SSC device. In addition, the nearly vertical line at the low-frequency region indicated an ideal capacitive behavior of the ItG electrode. The CV curves at different scan rates (5 – 100 mV/s) showed similar symmetric shape (Figure 5.16**b**), indicating good capacitive behavior of the ItG electrode. The charge-discharge curves at different current densities (2 - 30 mA/cm^2, much higher than the literature with a current density of 0.01-1 mA/cm^2) demonstrated a remarkable performance from the small potential drop (iR drop) at the beginning of the discharging and symmetric triangular shapes (Figure 5.16**c**). The areal

capacitance of the device calculated from the GCD data (Figure 5.16**d**) could reach 2097 mF/cm^2 with the specific capacitance of 367 F/g at the current density of 2 mA/cm^2. Meanwhile, the coulombic efficiency was >95 % covering the entire current density range. Notably, the device, under such a high mass loading, still exhibited 65% capacitance retention even at an extremely high current density of 20 mA/cm^2, which is regarded as an excellent rate capability for devices with ultra-high capacitance. The relatively small capacitance decrease observed at high current density arises from the good conductivity of the electrode which reduces the iR drops. Through calculation based on the capacitance data, the SSC demonstrated a maximum energy density of 186 μWh/cm^2 at a power density of 1600 μW/cm^2 and maintained 95 μWh/cm^2 at a power density of 24000 μW/cm^2. Both the areal capacitance, energy density, and power density of the SSC were among the best in comparison to the previous SSC reports (Figure 5.16**e**). The device also performed 87.7% capacitance retention and nearly 100% coulombic efficiency after 2000 reversible charging/discharging cycles, suggesting excellent cyclic stability of the SSC device (Figure 5.16**f**).

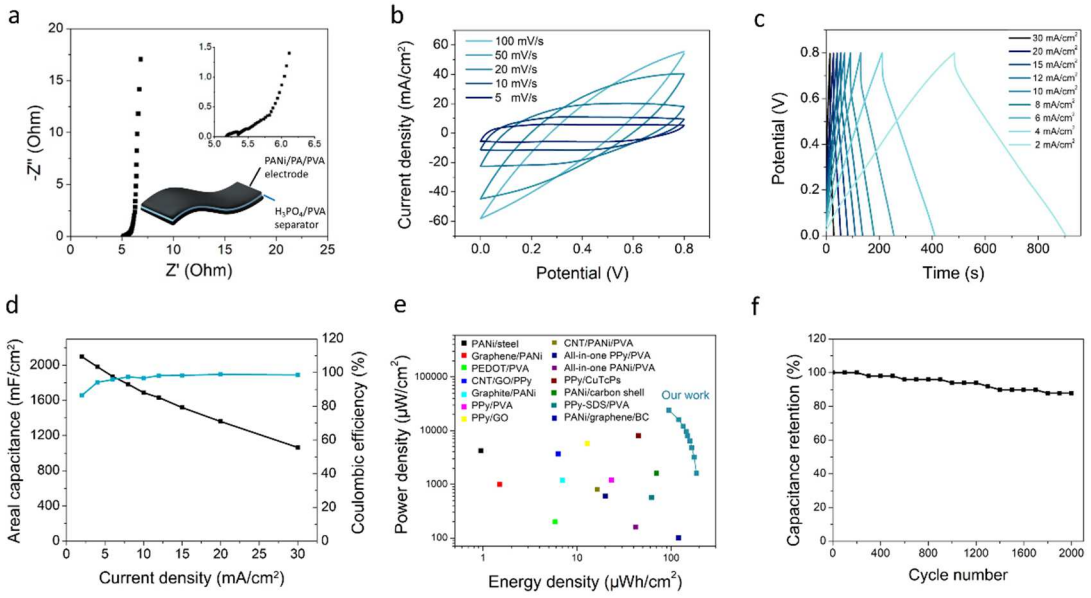

Figure 5.16. Electrochemical characterization of solid-state supercapacitors. (a) EIS curve in the range of 10000 Hz-0.01 Hz. (b) CV curves at scan rates of 5-100 mV/s. (c) GCD curves at current densities of 2-30 mA/cm^2. (d) Areal capacitance and Coulombic efficiency calculated from the GCD

data. (e) Ragone plot of power density and energy density in comparison with literatures. (f) Capacitance retention (87.3 %) of the SSC over 2000 charging-discharging cycles.

Given its promising performance and mechanical softness, we also investigated the ItG's potential for flexible and stretchable electronics applications. During and after bending our devices from 0° to 180° and the twisting from 0° to 90°, the CV and GCD curves showed little variance from static samples**.** Accordingly, the capacitance and Coulombic efficiency calculated from the GCD curves are well retained (Figure 5.17a,b). After 2000 cycles of 90° bending, over 97% of the capacitance retention remained, illustrating excellent bending stability (Figure 5.17c). A stretchable supercapacitor was also fabricated by using a physically crosslinked PVA film as a separator. The device could retain 74% capacitance under 80% uniaxial strain, suggesting potential use for stretchable electronics (Figure 5.17d,e).

As a proof of concept, we have further demonstrated SCPH in wearable applications. Three SSCs connected in series, after charged, could light a red LED for more than 5 minutes. With rigorous bending and twisting of each supercapacitor, the red LED remained lit without any obvious decline in light intensity (Figure 5.17f). Additionally, the device that was wrapped around the arm operated well during regular arm motion (Figure 5.17g).

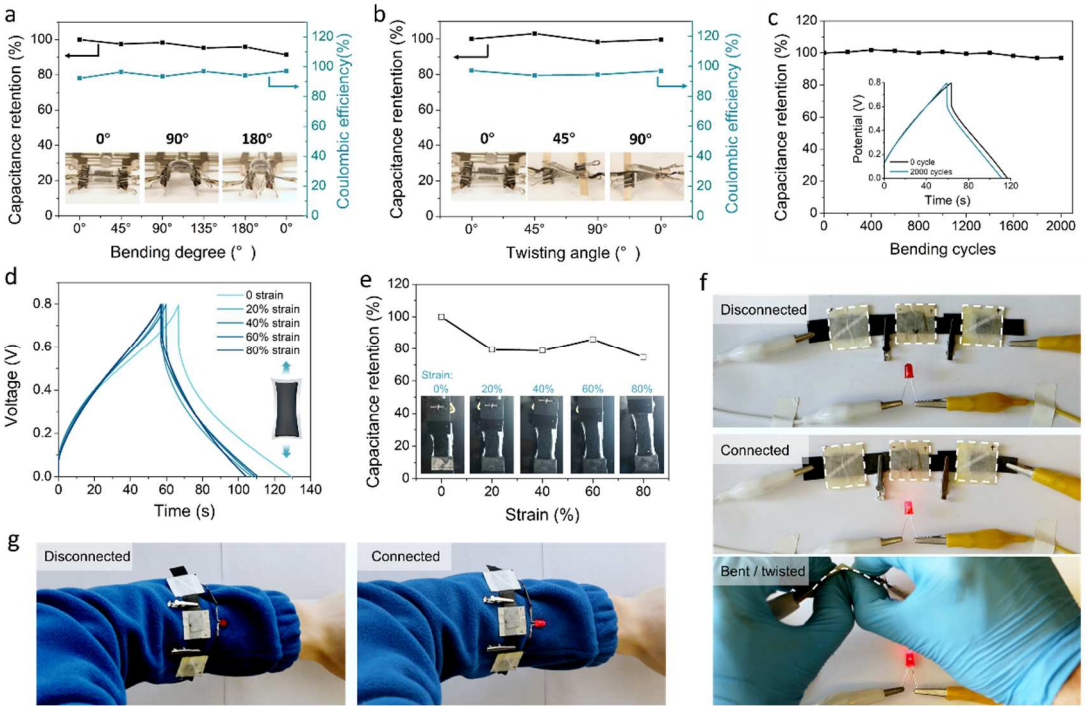

Figure 5.17. Demonstrations of flexible and stretchable supercapacitors as wearable electronics. (a, b) The capacitance retention and the Coulombic efficiency of SSC under various bending angles and twisting angles, respectively. (c) The capacitance retention (97 %) of SSC over 2000 bending/unbending cycles. (d) The galvanostatic charge-discharge (GCD) curves of the stretchable SSC under stretching at various strain (0-80%). (e) Capacitance retention of the stretchable SSC under various strain (0-80%). (f) Three SSCs connected in series to light up a red LED. The device withstood manual bending and twisting without obvious performance deterioration. (g) Wearable demonstration of three connected SSCs that wrap around a human arm functioning well during regular arm motion.

5.4.3. Discussion

Thanks to the continuous highway it provides for electron and ion transportation, the electrochemical performance of the materials being used in the three-electrode system and solid-state supercapacitors are greatly improved. Overall, this facile and universal synthesis method has well addressed some long-lasting challenges in the field of intrinsically stretchable conductive materials, provides a methodology to create a hierarchical, uniform nanostructure-microstructure, and can further facilitate the development of mechanically compliant electronic devices.

6. Conclusion and outlook

In this thesis, we discuss stimuli-responsive polymers and stretchable conductive hydrogels with unique properties and elaborate on the potential applications in soft robotics. We aim to provide an in-depth understanding of the design principle of each system, features of each material, presented function, and potential directions toward self-sustained autonomous soft robots. Regarding the development of each material and specific type of robot, working mechanisms and resulting performance are discussed.

In chapter 2, we introduced an artificial phototropism mechanism to realize autonomous light tracking of stimuli-responsive polymers and hydrogels. The tracking is rationalized by the dynamic feedback loop built in the material and light interaction. The study demonstrated the potential applications for improved energy harvesting, including solar steam generation and photovoltaics. In future work, this mechanism would open new avenues for intelligent energy generations (*e.g.,* biofuel), solar sails, smart windows for energy-efficient architecture, and self-reconfigurable optics, as well as energetic emission detection and tracking with a telescope, radar, and hydrophones.

In chapter 3, following a similar dynamic feedback mechanism in the light-tracking capability, we have been amplifying the feedback loop into an out-of-equilibrium system, named self-excited oscillation driven by constant light input. We have been focusing on the fundamental understanding and pushing the boundaries of the functionality of the oscillation, including i) omnidirectional response with underwater operation; ii) environmental energy source scavenging such as operation under sunlight; iii) high power output close to the flight muscle of insects. Investigation of oscillation through different approaches may make an impact on future autonomous, untethered, and sustainable robots, including walking, rolling, swimming, sailboat, and flapping.

In chapter 4, we were engaged in the development of highly stretchable and conductive hydrogels, which were used primarily for soft sensors. We have come up with an ice-templating, low-

temperature polymerization technique to achieve unprecedented electrical conductivity and mechanical properties simultaneously, which were traditionally a daunting challenge in stretchable electronics. The improvement is realized by the ice-densification effect of solutes along the ice boundaries and mitigated aggregation from low-temperature polymerization. Such conductive material was used for high-performance piezoresistive sensors. Later, we molecularly integrated the highly conductive networks with a stimuli-responsive component, and demonstrated somatosensory actuation performance. From the perspective of the correlation between the complexity and functionality of materials systems, we believe such materials with intrinsic somatosensitive actuating capabilities may open opportunities for intelligent materials with self-regulating functions and computing ability.

In chapter 5, we examined an alternative strategy to achieve self-sustained robot, where the energy storage devices are integrated. Here, we are focused on the hierarchically structured conductive hydrogels as electrodes of supercapacitors. First, we rationalized the morphology of the aligned hydrogel matrix to mimic the low tortuosity wood, and developed a high areal-capacitance flexible supercapacitor. Then, we utilized the previously developed highly stretchable and conductive hydrogels synthesized by ice-templating, low-temperature polymerization technique and assembled into a stretchable all-solid-state supercapacitor. With further development, these energy storage devices may be integrated into the next-generation life-like soft robots with onboard power in challenging and unmanned tasks.

Despite all these achievements, stimuli-responsive polymer-based actuators and hydrogel-based sensors, and supercapacitors are still in its infancy, with many challenges left to be addressed. For example, LCEs exhibit tunable actuation temperature and response rate but are limited by complicated fabrication and a requirement for alignment. Hydrogels exhibit multifunctionality and versatility of chemical modification but usually suffer from diffusion-limited kinetics, small power/energy densities, environmental restrictions, and long-term stability. Addressing these

challenges and fully utilizing the features of each material can allow scientists and researchers to pursue meaningful real-world applications, such as space exploration, environmental monitoring, structural maintenance, social assistance, security, and so on. We believe transformative impacts will be made with future breakthroughs in soft stimuli-responsive actuation, system integration, energy storage, control, and soft robot autonomy.

BIBLIOGRAPHY

1. Brown, E. *et al.* Universal robotic gripper based on the jamming of granular material. *Proc. Natl. Acad. Sci. U. S. A.* **107**, 18809–18814 (2010).

2. Kim, Y., Parada, G. A., Liu, S. & Zhao, X. Ferromagnetic soft continuum robots. *Sci. Robot.* **4**, (2019).

3. Horchler, A. D. *et al.* Peristaltic locomotion of a modular mesh-based worm robot: Precision, compliance, and friction. *Soft Robot.* **2**, 135–145 (2015).

4. Wehner, M. *et al.* An integrated design and fabrication strategy for entirely soft, autonomous robots. *Nat. Publ. Gr.* (2016) doi:10.1038/nature19100.

5. Zhao, Y. *et al.* Soft phototactic swimmer based on self-sustained hydrogel oscillator. *Sci. Robot.* **4**, (2019).

6. Jafferis, N. T., Helbling, E. F., Karpelson, M. & Wood, R. J. Untethered flight of an insect-sized flapping-wing microscale aerial vehicle. *Nature* **570**, 491–495 (2019).

7. Rich, S. I., Wood, R. J. & Majidi, C. Untethered soft robotics. *Nat. Electron.* **1**, 102–112 (2018).

8. Matteo Cianchetti, Cecilia Laschi, A. M. and P. D. Biomedical applications of soft robotics. *Nat. Rev. Mater.* **3**, 143–153 (2018).

9. Banerjee, H., Tsz, Z., Tse, H. & Ren, H. Soft robotics with compliance and adaptation for biomedical applications and forthcoming challenges. **33**, (2018).

10. Neill, C. T. O., Phipps, N. S., Cappello, L., Paganoni, S. & Walsh, C. J. A Soft Wearable Robot for the Shoulder : Design , Characterization , and Preliminary Testing. **02129**, 1672–1678 (2017).

11. Cui, H., Zhao, Q., Wang, Y. & Du, X. Bioinspired Actuators Based on Stimuli□ Responsive Polymers. *Chem. – An Asian J.* **14**, 2369–2387 (2019).

12. Rich, S. I., Wood, R. J. & Majidi, C. Untethered soft robotics. *Nat. Electron.* **1**, 102–112 (2018).

13. Jang, K. I. *et al.* Soft network composite materials with deterministic and bio-inspired designs. *Nat. Commun.* **6**, 1–11 (2015).

14. Tolley, M. T. *et al.* An untethered jumping soft robot. *IEEE Int. Conf. Intell. Robot. Syst.* 561–566 (2014) doi:10.1109/IROS.2014.6942615.

15. Hu, L., Zhang, Q., Li, X. & Serpe, M. J. Stimuli-responsive polymers for sensing and actuation. *Mater. Horizons* **6**, 1774–1793 (2019).

16. Takashima, Y. *et al.* Expansion-contraction of photoresponsive artificial muscle regulated by host-guest interactions. *Nat. Commun.* **3**, (2012).

17. Qian, X. *et al.* Artificial phototropism for omnidirectional tracking and harvesting of light. *Nat. Nanotechnol.* **14**, (2019).

18. Ma, C. *et al.* A Multiresponsive Anisotropic Hydrogel with Macroscopic 3D Complex Deformations. *Adv. Funct. Mater.* **26**, 8670–8676 (2016).

19. Zhang, X. *et al.* Optically- and thermally-responsive programmable materials based on carbon nanotube-hydrogel polymer composites. *Nano Lett.* **11**, 3239–3244 (2011).

20. Taylor, M., Tomlins, P. & Sahota, T. Thermoresponsive Gels. *Gels* **3**, 4 (2017).

21. White, T. J. & Broer, D. J. Programmable and adaptive mechanics with liquid crystal polymer networks and elastomers. *Nat. Mater.* **14**, 1087–1098 (2015).

22. Yu, Y., Nakano, M. & Ikeda, T. Directed bending of a polymer film by light. *Nature* **425**, 145 (2003).

23. Kurihara, S., Ikeda, T., Tazuke, S. & Seto, J. E. Isothermal phase transition of liquid crystals induced by photoisomerization of doped spiropyrans. *J. Chem. Soc. Faraday Trans.* **87**, 3251–3254 (1991).

24. Allinson, H. & Gleeson, H. F. Physical properties of mixtures of low molar mass nematic liquid crystals with photochromic fulgide guest dyes. *Liq. Cryst.* **14**, 1469–1478 (1993).

25. White, T. J., Serak, S. V., Tabiryan, N. V., Vaia, R. A. & Bunning, T. J. Polarization-controlled, photodriven bending in monodomain liquid crystal elastomer cantilevers. *J. Mater. Chem.* **19**, 1080–1085 (2009).

26. Wang, Z., Li, K., He, Q. & Cai, S. A Light-Powered Ultralight Tensegrity Robot with High Deformability and Load Capacity. *Adv. Mater.* **31**, 1–8 (2019).

27. Tian, H. *et al.* Polydopamine-Coated Main-Chain Liquid Crystal Elastomer as Optically Driven Artificial Muscle. *ACS Appl. Mater. Interfaces* **10**, 8307–8316 (2018).

28. Liu, X. *et al.* Reversible and rapid laser actuation of liquid crystalline elastomer micropillars with inclusion of gold nanoparticles. *Adv. Funct. Mater.* **25**, 3022–3032 (2015).

29. Kruusamäe, K., Punning, A., Aabloo, A. & Asaka, K. Self-sensing ionic polymer actuators: A review. *Actuators* **4**, 17–38 (2015).

30. Madden, J. D., Cush, R. A., Kanigan, T. S. & Hunter, I. W. Fast contracting polypyrrole actuators. *Synth. Met.* **113**, 185–192 (2000).

31. Hu, F., Xue, Y., Xu, J. & Lu, B. PEDOT-Based Conducting Polymer Actuators. *Front. Robot. AI* **6**, 1–17 (2019).

32. Yakacki, C. M. *et al.* Tailorable and programmable liquid-crystalline elastomers using a two-stage thiol-acrylate reaction. *RSC Adv.* **5**, 18997–19001 (2015).

33. Atamian, H. S. *et al.* Circadian regulation of sunflower heliotropism, floral orientation, and pollinator visits. *Science (80-.).* **353**, 587–590 (2016).

34. Han, J. *et al.* Untethered Soft Actuators by Liquid–Vapor Phase Transition: Remote and Programmable Actuation. *Adv. Intell. Syst.* **1**, 1900109 (2019).

35. Liu, L. *et al.* Light Tracking and Light Guiding Fiber Arrays by Adjusting the Location of Photoresponsive Azobenzene in Liquid Crystal Networks. *Adv. Opt. Mater.* (2020) doi:10.1002/adom.202000732.

36. Zhou, L. *et al.* 3D self-assembly of aluminium nanoparticles for plasmon-enhanced solar desalination. *Nat. Photonics* **10**, 393–398 (2016).

37. Ghasemi, H. *et al.* Solar steam generation by heat localization. *Nat. Commun.* **5**, 4449 (2014).

38. Zhao, F. *et al.* Highly efficient solar vapour generation via hierarchically nanostructured gels. *Nat. Nanotechnol.* 489–495 (2018) doi:10.1038/s41565-018-0097-z.

39. Li, X. *et al.* Graphene oxide-based efficient and scalable solar desalination under one sun with a confined 2D water path. *Proc. Natl. Acad. Sci.* **113**, 13953–13958 (2016).

40. Zhou, L. *et al.* Self-assembled spectrum selective plasmonic absorbers with tunable bandwidth for solar energy conversion. *Nano Energy* **32**, 195–200 (2017).

41. Chen, Q. *et al.* A durable monolithic polymer foam for efficient solar steam generation. *Chem. Sci.* **9**, 623–628 (2018).

42. Wang, Y., Zhang, L. & Wang, P. Self-Floating Carbon Nanotube Membrane on Macroporous Silica Substrate for Highly Efficient Solar-Driven Interfacial Water Evaporation. *ACS Sustain. Chem. Eng.* **4**, 1223–1230 (2016).

43. Wang, Z. *et al.* Bio-Inspired Evaporation Through Plasmonic Film of Nanoparticles at the Air-Water Interface. *Small* **10**, 3234–3239 (2014).

44. Donald, B. R., Levey, C. G., McGray, C. D., Paprotny, I. & Rus, D. An Untethered, Electrostatic, Globally Controllable MEMS Micro-Robot. *J. Microelectromechanical Syst.* **15**, 1–15 (2006).

45. Liu, Q., Nian, G., Yang, C., Qu, S. & Suo, Z. Bonding dissimilar polymer networks in various manufacturing processes. *Nat. Commun.* **9**, 846 (2018).

46. Le Floch, P. *et al.* Wearable and Washable Conductors for Active Textiles. *ACS Appl. Mater. Interfaces* **9**, 25542–25552 (2017).

47. Pringle, J. Insect flight. in *Cambridge: Cambridge University Press* (1957).

48. Dudley, R. The Biomechanics of Insect Flight: Form, Function and Evolution. in *Princeton, NJ: Princeton Univ. Press* (1999).

49. Mingjing, Q. *et al.* Asynchronous and Self□Adaptive Flight Assembly via Electrostatic Actuation of Flapping Wings. *Adv. Intell. Syst.* **3**, 2100048 (2021).

50. Gelebart, A. H. *et al.* Making waves in a photoactive polymer film. *Nature* **546**, 632–636 (2017).

51. Shin, B. *et al.* Hygrobot: A self-locomotive ratcheted actuator powered by environmental humidity. *Sci. Robot.* **3**, 1–9 (2018).

52. Maeda, S., Hara, Y., Sakai, T., Yoshida, R. & Hashimoto, S. Self-walking gel. *Adv. Mater.* **19**, 3480–3484 (2007).

53. Li, T. *et al.* Fast-moving soft electronic fish. *Sci. Adv.* **3**, 1–8 (2017).

54. Rothemund, P. *et al.* A soft, bistable valve for autonomous control of soft actuators. *Sci. Robot.* **7986**, 1–11 (2018).

55. Serak, S. *et al.* Liquid crystalline polymer cantilever oscillators fueled by light. *Soft Matter* **6**, 779–783 (2010).

56. Zeng, H. *et al.* Light-fuelled freestyle self-oscillators. *Nat. Commun.* 1–9 doi:10.1038/s41467-019-13077-6.

57. Lee, K. M. *et al.* Photodriven, flexural-torsional oscillation of glassy azobenzene liquid crystal polymer networks. *Adv. Funct. Mater.* **21**, 2913–2918 (2011).

58. Yang, L. *et al.* An Autonomous Soft Actuator with Light-Driven Self-Sustained Wavelike Oscillation for Phototactic Self-Locomotion and Power Generation. *Adv. Funct. Mater.* **30**, 1–13 (2020).

59. Gelebart, A. H., Vantomme, G., Meijer, E. W. & Broer, D. J. Mastering the Photothermal Effect in Liquid Crystal Networks: A General Approach for Self-Sustained Mechanical Oscillators. *Adv. Mater.* **29**, (2017).

60. Dong, X. *et al.* Sunlight-Driven Continuous Flapping-Wing Motion. *ACS Appl. Mater. Interfaces* **12**, 6460–6470 (2020).

61. Lan, R. *et al.* Near-Infrared Photodriven Self-Sustained Oscillation of Liquid-Crystalline Network Film with Predesignated Polydopamine Coating. *Adv. Mater.* **32**, 1–8 (2020).

62. Sun, M. & Wu, J. H. Aerodynamic force generation and power requirements in forward flight in a fruit fly with modeled wing motion. *J. Exp. Biol.* **206**, 3065–3083 (2003).

63. Wood, R. J. The first takeoff of a biologically inspired at-scale robotic insect. *IEEE Trans. Robot.* **24**, 341–347 (2008).

64. Duduta, M., Wood, R. J. & Clarke, D. R. Multilayer Dielectric Elastomers for Fast, Programmable Actuation without Prestretch. *Adv. Mater.* **28**, 8058–8063 (2016).

65. Chen, Y. *et al.* Controlled flight of a microrobot powered by soft artificial muscles. *Nature* **575**, 324–329 (2019).

66. Helps, T., Romero, C., Taghavi, M., Conn, A. T. & Rossiter, J. Liquid-amplified zipping actuators for micro-air vehicles with transmission-free flapping. *Sci. Robot.* **7**, eabi8189 (2022).

67. Li, S. *et al.* Digital light processing of liquid crystal elastomers for self-sensing artificial muscles. *Sci. Adv.* **7**, (2021).

68. Cao, C., Burgess, S. & Conn, A. T. Toward a dielectric elastomer resonator driven flapping wing micro air vehicle. *Front. Robot. AI* **6**, 1–11 (2019).

69. Mohand O. Saed, Cedric P. Ambulo, Hyun Kim, Rohit De, Vyom Raval, Kyle Searles, Danyal A. Siddiqui, John Michael O. Cue, Mihaela C. Stefan, M. Ravi Shankar, and T. H. W. Molecularly-Engineered, 4D-Printed Liquid Crystal elastomer actuators. 1806412 (2019).

70. Chen, Y. *et al.* Light-driven bimorph soft actuators: Design, fabrication, and properties. *Mater. Horizons* **8**, 728–757 (2021).

71. Dong, L., Tong, X., Zhang, H., Chen, M. & Zhao, Y. Near-infrared light-driven locomotion of a liquid crystal polymer trilayer actuator. *Mater. Chem. Front.* **2**, 1383–1388 (2018).

72. Xiao, Y. *et al.* A multi-functional light-driven actuator with an integrated temperature-sensing function based on a carbon nanotube composite. *Nanoscale* **13**, 6259–6265 (2021).

73. Tang, R., Sang, W., Wu, Y., Zhu, C. & Liu, J. Multi-Wavelength Light Drivable Oscillatory Actuator on Graphene-Based Bilayer Film. *Macromol. Mater. Eng.* **201600384**, 1–6 (2017).

74. Saed, M. O. *et al.* High strain actuation liquid crystal elastomers via modulation of mesophase structure. *Soft Matter* **13**, 7537–7547 (2017).

75. Saed, M. O. *et al.* Thiol-acrylate main-chain liquid-crystalline elastomers with tunable thermomechanical properties and actuation strain. *J. Polym. Sci. Part B Polym. Phys.* **55**, 157–168 (2017).

76. Kumar, K. *et al.* A chaotic self-oscillating sunlight-driven polymer actuator. *Nat. Commun.* **7**, 1–8 (2016).

77. Serak, S. *et al.* Liquid crystalline polymer cantilever oscillators fueled by light. *Soft Matter* **6**, 779–783 (2010).

78. Qiu, T. *et al.* Swimming by reciprocal motion at low Reynolds number. *Nat. Commun.* **5**, 1–8 (2014).

79. Rogóż, M., Zeng, H., Xuan, C., Wiersma, D. S. & Wasylczyk, P. Light-Driven Soft Robot Mimics Caterpillar Locomotion in Natural Scale. *Adv. Opt. Mater.* **4**, 1689–1694 (2016).

80. Lu, X., Guo, S., Tong, X., Xia, H. & Zhao, Y. Tunable Photocontrolled Motions Using Stored Strain Energy in Malleable Azobenzene Liquid Crystalline Polymer Actuators. *Adv. Mater.* **29**, 1–7 (2017).

81. Kim, Y., van den Berg, J. & Crosby, A. J. Autonomous snapping and jumping polymer gels. *Nat. Mater.* **20**, 1695–1702 (2021).

82. McCracken, J. M., Donovan, B. R., Lynch, K. M. & White, T. J. Molecular Engineering of Mesogenic Constituents Within Liquid Crystalline Elastomers to Sharpen Thermotropic Actuation. *Adv. Funct. Mater.* **31**, (2021).

83. Yang, M. *et al.* Bioinspired Phototropic MXene-Reinforced Soft Tubular Actuators for Omnidirectional Light-Tracking and Adaptive Photovoltaics. *Adv. Funct. Mater.* **2201884**, 1–9 (2022).

84. Vantomme, G., Gelebart, A. H., Broer, D. J. & Meijer, E. W. Self-sustained actuation from heat dissipation in liquid crystal polymer networks. *J. Polym. Sci. Part A Polym. Chem.* **56**, 1331–1336 (2018).

85. Kevin Y. Ma, Pakpong Chirarattananon, Sawyer B. Fuller, R. J. W. Controlled Flight of a Biologically Inspired, Insect-Scale Robot. *Science (80-.).* 603–608 (2013).

86. Vantomme, G. *et al.* Coupled liquid crystalline oscillators in Huygens' synchrony. *Nat. Mater.* (2021) doi:10.1038/s41563-021-00931-6.

87. Yang, J. C. *et al.* Electronic Skin: Recent Progress and Future Prospects for Skin-Attachable Devices for Health Monitoring, Robotics, and Prosthetics. *Adv. Mater.* **31**, 1–50 (2019).

88. Son, D. *et al.* Multifunctional wearable devices for diagnosis and therapy of movement disorders. *Nat. Nanotechnol.* **9**, 397–404 (2014).

89. Feig, V. R. *et al.* An Electrochemical Gelation Method for Patterning Conductive PEDOT:PSS Hydrogels. *Adv. Mater.* **31**, 1–7 (2019).

90. Guarino, V., Alvarez-Perez, M. A., Borriello, A., Napolitano, T. & Ambrosio, L. Conductive PANi/PEGDA Macroporous Hydrogels For Nerve Regeneration. *Adv. Healthc. Mater.* **2**, 218–227 (2013).

91. Lee, Y. Y. *et al.* A Strain-Insensitive Stretchable Electronic Conductor: PEDOT:PSS/Acrylamide Organogels. *Adv. Mater.* **28**, 1636–1643 (2016).

92. Wang, C., Wang, C., Huang, Z. & Xu, S. Materials and Structures toward Soft Electronics. *Adv. Mater.* **30**, 1–49 (2018).

93. Han, Y. & Dai, L. Conducting Polymers for Flexible Supercapacitors. *Macromol. Chem. Phys.* **220**, 1–14 (2019).

94. Wang, H., Totaro, M. & Beccai, L. Toward Perceptive Soft Robots: Progress and Challenges. *Adv. Sci.* **5**, (2018).

95. Hochner, B. An embodied view of octopus neurobiology. *Curr. Biol.* **22**, R887–R892 (2012).

96. Shi, Y., Ma, C., Peng, L. & Yu, G. Conductive 'smart' hybrid hydrogels with PNIPAM and nanostructured conductive polymers. *Adv. Funct. Mater.* **25**, 1219–1225 (2015).

97. Pan, L. *et al.* Hierarchical nanostructured conducting polymer hydrogel with high electrochemical activity. *Proc. Natl. Acad. Sci. U. S. A.* **109**, 9287–9292 (2012).

98. Zhao, Y. *et al.* Hierarchically Structured Stretchable Conductive Hydrogels for High-Performance Wearable Strain Sensors and Supercapacitors. *Matter* **3**, (2020).

99. Zhang, Y. *et al.* High-capacity, low-tortuosity, and channel-guided lithium metal anode. *Proc. Natl. Acad. Sci. U. S. A.* **114**, 3584–3589 (2017).

100. Wang, Y. *et al.* Ice Templated Free-Standing Hierarchically WS2/CNT-rGO Aerogel for High-Performance Rechargeable Lithium and Sodium Ion Batteries. *Adv. Energy Mater.* **6**, (2016).

101. Chen, C. *et al.* All-wood, low tortuosity, aqueous, biodegradable supercapacitors with ultra-high capacitance. *Energy Environ. Sci.* **10**, 538–545 (2017).

102. Li, L. *et al.* Recent Advances in Flexible/Stretchable Supercapacitors for Wearable Electronics. *Small* **14**, (2018).

103. Wei, J., Yin, C., Wang, H. & Wang, Q. Polyampholyte-doped aligned polymer hydrogels as anisotropic electrolytes for ultrahigh-capacity supercapacitors. *J. Mater. Chem. A* **6**, 58–64 (2017).

104. Sun, K. *et al.* A Single Robust Hydrogel Film Based Integrated Flexible Supercapacitor. *ACS Sustain. Chem. Eng.* **7**, 165–173 (2019).